



HAL
open science

Study of the tri-lepton events in the Run II data of the D0 experiment at the Tevatron (FNLA, USA).

Pavel Demine

► **To cite this version:**

Pavel Demine. Study of the tri-lepton events in the Run II data of the D0 experiment at the Tevatron (FNLA, USA).. Physique des Hautes Energies - Expérience [hep-ex]. Université Joseph-Fourier - Grenoble I, 2002. Français. NNT: . tel-00002107

HAL Id: tel-00002107

<https://theses.hal.science/tel-00002107>

Submitted on 10 Dec 2002

HAL is a multi-disciplinary open access archive for the deposit and dissemination of scientific research documents, whether they are published or not. The documents may come from teaching and research institutions in France or abroad, or from public or private research centers.

L'archive ouverte pluridisciplinaire **HAL**, est destinée au dépôt et à la diffusion de documents scientifiques de niveau recherche, publiés ou non, émanant des établissements d'enseignement et de recherche français ou étrangers, des laboratoires publics ou privés.

Université Joseph Fourier – Grenoble 1 – U.F.R. de Physique

Université de co-tutelle: St. Petersburg State Technical University

THÈSE

présentée à l'Université Joseph Fourier
pour obtenir le titre de

DOCTEUR EN SCIENCE

Spécialité: Physique des particules

présentée par

Pavel DEMINE

**Study of the tri-lepton events in the Run II
data of the $D\bar{O}$ experiment at the Tevatron
(FNAL, USA).**

**Interpretation in the R-parity violating
supersymmetry framework (λ coupling).**

Soutenue le 21 novembre 2002, devant le jury composé de :

Yaroslav A. BERDNIKOV

François BRUT

Elemér NAGY

(Rapporteur)

Vyatcheslav P. PROTASSOV

(Rapporteur)

Gérard SAJOT

(Co-directeur de thèse)

Vladimir M. SAMSONOV

(Co-directeur de thèse)

Thèse préparée à l'Institut des Sciences Nucléaires de Grenoble

Contents

Acknowledgments	7
Introduction	9
1 The Standard Model and beyond	11
1.1 The Standard Model	11
1.1.1 Fundamental Particles	11
1.1.2 Fundamental Interactions	12
1.1.3 Gauge Theories and the Electroweak Force	14
1.1.4 Running Coupling Strengths and GUTs	15
1.1.5 Problems with the Standard Model	16
1.1.6 Beyond the Standard Model	17
1.2 Supersymmetry	17
1.2.1 Basics of SUSY	18
1.2.2 Minimal Supersymmetric Standard Model	19
1.2.3 R -parity violation	23
1.2.4 GUT Framework for the MSSM	24
1.3 Minimal Supergravity	25
1.4 Other SUSY Models	29
1.5 Constraints on R -parity-violating couplings and current limits	30
1.5.1 Proton stability	30
1.5.2 $n-\bar{n}$ oscillation	30
1.5.3 ν_e -Majorana mass	30
1.5.4 Neutrinoless double beta decay	32
1.5.5 Charged-current universality	32
1.5.6 $e-\mu-\tau$ universality	32
1.5.7 $\nu_\mu-e$ scattering	32
1.5.8 Atomic parity violation	33
1.5.9 ν_μ deep-inelastic scattering	33
1.5.10 K^+ -decays	34
1.5.11 τ -decays	34
1.5.12 D -decays	34
1.6 Results of R -parity violation searches	34
1.6.1 KARMEN anomaly	35
1.6.2 LEP1	35

1.6.3	LEP2	35
1.6.4	Fermilab Tevatron	37
1.6.5	Perspectives for the LHC	38
1.7	Summary	38
2	Tevatron and DØ detector	41
2.1	Accelerator	41
2.2	DØ detector	43
2.3	Coordinate system and kinematic quantities	43
2.4	Tracking system	44
2.4.1	Silicon Microstrip Tracker	44
2.4.2	Scintillating Fiber Tracker	45
2.5	Preshower detectors	46
2.5.1	Central preshower system	46
2.5.2	Forward preshower system	47
2.6	Calorimeter	50
2.6.1	Calorimeter Electronics	50
2.6.2	Calibration of the Calorimeter Electronics	51
2.7	The Muon Detector	53
2.7.1	Toroid Magnet	54
2.7.2	WAMUS	54
2.7.3	FAMUS	56
2.8	Forward Proton Detector	57
2.9	Luminosity Monitor	57
3	Data Acquisition and Event Reconstruction and Simulation	61
3.1	Trigger system	61
3.1.1	Level 1	61
3.1.2	Level 2	65
3.1.3	Level 3	66
3.2	Luminosity Calculation	67
3.3	Event Reconstruction	71
3.3.1	The Reconstruction Program DØRECO	71
3.3.2	Electron reconstruction	72
3.3.3	Muon reconstruction	72
3.3.4	Jet reconstruction	72
3.4	Monte Carlo Simulation	73
3.4.1	Event Generation	74
3.4.2	Detector simulation	74
3.4.3	Trigger Simulation	75
3.5	Future DØ Analysis Centers	76

4	Electron identification	79
4.1	Introduction	79
4.2	Electron reconstruction in $D\bar{O}$	79
4.2.1	EM Energy fraction	80
4.2.2	H-matrix technique	81
4.2.3	Electromagnetic cluster isolation	83
4.2.4	Sequential electron selection in the data	83
4.3	Association of EM clusters with central tracks	84
4.4	Neyman-Pearson test	86
4.4.1	Probability distributions	86
4.4.2	E/p discriminating variable	87
4.4.3	Using the deposited in the preshower detectors	87
4.4.4	Implementation of Neyman-Pearson test in $D\bar{O}$ reconstruction program	88
4.5	Electron misidentification rate	90
4.6	Electron energy corrections	94
5	Muon identification	95
5.1	Muon hit reconstruction	95
5.1.1	PDT hit reconstruction	95
5.1.2	MDT hit reconstruction	96
5.1.3	MSC hit reconstruction	96
5.2	Muon segment reconstruction	96
5.3	Local track reconstruction	99
5.4	Muon background	100
5.5	Conclusion	104
6	Identification of b-quark jets	105
6.1	Introduction	105
6.2	Particularities of the b -quarks jets	105
6.3	Topological tagging	106
6.3.1	Impact Parameter tag	107
6.3.2	Secondary vertex tag	111
6.4	Tagging with muons	113
6.5	Combined tagging	116
6.5.1	Description of the method	116
6.5.2	Tagging algorithm	118
6.5.3	Discriminating variables	118
6.5.4	Decay length significance	118
6.5.5	Performance of the combined tag	122
6.6	Conclusion	122
7	Phenomenology of the \mathcal{R}_p signal and expected exclusion limits	123
7.1	Consequences of an \mathcal{R}_p coupling	123
7.2	SUSYGEN a \mathcal{R}_p Generator	123

7.3	Effects of the R-parity violating couplings in the decay	124
7.4	Study of the \cancel{R}_p signal with fast MC simulation	128
7.4.1	PGS. Fast D \emptyset detector response simulation	128
7.4.2	Signal simulation	129
7.4.3	Background simulation	130
7.5	Tri-electron selection and its effect on the signal and on the background . .	130
7.6	Limit in the m_0 - $m_{1/2}$ Plane	132
7.7	Conclusion	133
8	Run II Data Analysis and Background Estimation	135
8.1	Data Sample	136
8.2	Selection of reliable data sample at early stage of the experiment	136
8.2.1	Runs selection for tri-electron channel analysis	136
8.2.2	Runs for di-electron one muon channel analysis	137
8.2.3	Single electron trigger efficiency	137
8.2.4	Selection of reconstructed physics objects	139
8.2.5	Di-lepton Event Selection Criteria	140
8.3	Tri-lepton selection	142
8.3.1	Effect of the selection criteria on the signal and on the background	142
8.3.2	Candidate events	148
8.4	Estimation of the background	148
8.4.1	Standard Model Background	151
8.4.2	Instrumental Background	152
8.5	Conclusion	155
9	Conclusion and Outlook	157

Acknowledgments

It is a great pleasure to express my gratitude to the people who have helped me achieve this point.

I wish to extend my sincere thanks to my supervisor, professor Gérard SAJOT, for his guidance and constant support. Despite being incredibly busy, he always has time to answer my questions, give excellent advice, and provide appropriate word of encouragement. This work could not have been accomplished without the open and friendly atmosphere in the group $D\emptyset$ of the ISN, which is always a source of inspiration and new ideas. I appreciate very much the constant help and very useful advices of my colleges: Yannick ARNOUD, Auguste BESSON, Sabine CREPE-RENAUDIN, Oleg KOUZNETSOV, Arnaud LUCOTTE, Anne-Marie MAGNAN, Nirmalya PARUA. Working together with them has been a pleasure.

I thank Christophe ROYON for the fruitful discussions about SUSY and muon identification and for his multiple comments to the manuscript. I would like equally to thank Laurent DUFLOT, Elemér NAGY, Pierre PETROFF for their help and their kindness and I also thank all members of the group $D\emptyset$ -France with whom I have been working.

Running a modern particle physics experiment is a huge team effort. The $D\emptyset$ experiment is made up of nearly 600 especially talented collaborators. Though this thesis carries my name alone, it would not have been possible to write without their contributions to $D\emptyset$. I would also like to thank all the members of the $D\emptyset$ collaboration for maintaining such a wonderful facility.

Finally, I thank my parents and Yulia for their support during the time it took to accomplish this work and for their trust in me. I cannot think of words to thank them enough for all they have given me.

Introduction

This thesis presents the work I have done on the DØ experiment, one of the two detectors at the Tevatron collider situated at Fermi National Accelerator Laboratory (near Chicago, IL, USA). The DØ experiment has already taken data in 1992–1996 and together with the CDF experiment has discovered top quark in 1995 [1, 2]. During the period 1996–2001 Tevatron and both DØ and CDF experiments have been preparing for the second phase of data taking, Run II started in April 2001.

This thesis is devoted to the preparation of the Run II and to the analysis of the first good data (February 2002 – June 2002). Tri-lepton events (electron and muon) have been searched for in view of their interpretation in the framework of the Supersymmetry theory with R-parity violated by λ_{121} coupling.

Chapter 1 starts with a review of the Standard Model and a discussion of some of its problems. The difficulties led to the formulation of Supersymmetry. What Supersymmetry is and how it fixes some of the problems are explained. Supergravity, the particular Supersymmetry model used in this analysis, is presented followed by a brief list of some other Supersymmetry models that have recently been tested. Previous experimental searches for Supersymmetry are also briefly reviewed.

Chapter 2 covers the description of the Tevatron collider and the DØ detector at the Fermi National Accelerator Laboratory located near Chicago, Illinois. The detector subsystems of particular importance for this analysis will be explored in some detail. Algorithms and procedures for identifying particles and measuring the characteristics of events are explained in Chapter 3. Methods for identifying particles of particular interest for the present analysis as electrons and muons are described in more details in Chapter 4 and Chapter 5.

Chapter 6 describes new method for the DØ experiment to identify jets coming for the b quark hadronization. Importance of this method for the search of Supersymmetry is discussed.

If supersymmetric particles exists, what evidence would they leave in a detector like DØ? That question is addressed in Chapter 7, which describes the characteristics of the signal and the overall strategy of the search.

The analysis of the first Run II data is discussed in Chapter 8, which describes the event selection criteria used to select candidates and reject background events, the collider data passing the selection requirements, and the background estimates with the methods used to calculate them. Finally, Chapter 9 covers a summary of the analysis and what may be expected for the future.

Chapter 1

The Standard Model and beyond

1.1 The Standard Model

The Standard Model (SM) [3] accurately predicts all observed phenomena at distances smaller than the diameter of the atomic nucleus (10^{-15} m). It is one of the most successful theories ever invented.

The Standard Model describes particles forming the matter and their interaction. Except gravitational interaction responsible for weight the three fundamental interactions describing observable physical phenomena are included in this model: electromagnetic, weak and strong interactions.

1.1.1 Fundamental Particles

There are two basic types of particles in the Standard Model, fermions and bosons. The fermions have spin $\frac{1}{2}$ and are the building blocks of matter. Fermions adhere to the Pauli Exclusion Principle: only one fermion can occupy a particular quantum state. The fundamental bosons are either spin 0 or spin 1 particles and are thought of as the force carriers.

The Standard Model classify fermions in two categories: quarks and leptons. It does not predict the number of families. Up to now only three families have been observed experimentally. The first family contains quarks u and d , which build protons (uud) and neutrons (udd), and electron and electronic neutrino. Two other families are the replications with higher masses: their quark compositions have limited life-time and do not participate in the surrounding matter.

The quarks have fractional charge: the u , c , and t quarks have electrical charge $+\frac{2}{3}$ e (1 e is the electron charge), and the d , s , and b quarks have charge $-\frac{1}{3}$ e. The quarks make up particles called hadrons. Hadrons with three constituent quarks (such as protons and neutrons) are called baryons, and those with a quark and an antiquark are mesons. An important theoretical advancement was the understanding [4] that quarks must have an additional quantum number called color charge in addition to electric charge, since without color, quarks in hadrons would occupy the same quantum state (since they are fermions, this is not allowed). There are three possible color states: red, green, and blue. There are also anticolors for the antiquarks. Mixtures of a color and its anticolor or of

the three separate colors or anticolors are referred to as colorless. As discussed below, individual free quarks with color are not observed, and the quarks seem to be confined inside colorless mesons and baryons. The type of quark (up, down, charm, etc.) is referred to as the quark flavor. The top quark, the last SM particle to be discovered, was finally observed in 1995 using the DØ [2] and CDF [1] experiments at Fermilab.

Each generation of leptons has a negatively charged particle (electron type) and a massless neutrino. Only particles of the first generation build matter in the everyday world, while particles of the second and third generations can be produced in cosmic rays and in high energy particle collisions. In fact, even when only the u , d , and s quarks were known, the existence of the c quark was theoretically required in order to explain the observed suppression of flavor changing neutral weak interactions. The third generation was needed to introduce CP violation into the SM. Aside for the fact that three generations are needed to make the SM theory work correctly, the second and third generations appear to play no role in the everyday world. Experiments at CERN's LEP e^+e^- collider have shown that there are no more than three neutrinos of masses less than $45 \text{ GeV}/c^2$. [5]

Leptons are particles that are unaffected by the strong force. For each charged lepton, there is a neutrino that is electrically neutral. Unlike charged particles that interact electromagnetically, neutrinos are only affected by the weak force; the force responsible for nuclear decay. As the name suggests, the weak force is the weakest of the three interactions described by the SM (due to the small masses of the fundamental particles, gravity has virtually no effect and is not addressed by the SM) and so neutrinos are virtually undetectable directly. In collider experiments their presence can be inferred by looking for momentum imbalance in events. In the SM the neutrinos are presumed to be massless and therefore travel at the speed of light. The possibility of massive neutrinos, however, is still one of the important questions in particle physics and the subject of much study. Experiments have put constraints on the masses of the neutrinos.

1.1.2 Fundamental Interactions

When fermions interact by the electromagnetic, strong, or weak force, the interaction is transmitted between the particles by a spin one gauge boson. They represent some quantized state of the field of the interaction (i.e. the photon is the quantization of the electromagnetic field). For example, the scattering of two electrons is depicted as one electron emitting a photon which is absorbed by the other electron. For a brief instant, there are three particles present, the two electrons and the photon, representing more energy than what is available in the initial or final states. This situation is allowed, because some energy can be "borrowed" for a very short time as stipulated by the Heisenberg uncertainty principle. The photon is virtual; it only lives for the brief amount of time it takes to carry out the interaction. The gauge bosons couple to the fermions with a strength appropriate with the force. As discussed below, the strengths of the couplings are not constant, but in fact change with the energy scale. The strong force is mediated by the gluon. The gluon is massless and electrically neutral, but does carry color charge. While the quark is characterized by one state of color (red, green, blue, and anticolors for antiquarks), the gluon must carry two states (a color and an anticolor) since it may

be exchanged between two quarks that are interacting via the strong force. The fact that the gluon carries the charge of the strong force implies that it can interact with itself, corresponding to self interacting loop diagrams. The photon does not have this ability, since it is electrically neutral. As mentioned, the quarks and gluons are never observed as free particles. This is because the strength of the strong force increases with distance. For example, if the quarks building a proton are close together, they feel little of the strong force and just "rattle around" inside the proton (this phenomenon is called asymptotic freedom). If one quark begins escaping from the others, it starts feeling the strong force which pulls it back towards the other quarks. The force will increase with the distance between them. This effect is opposite to gravity and the electromagnetic force which weaken as distance is increased.

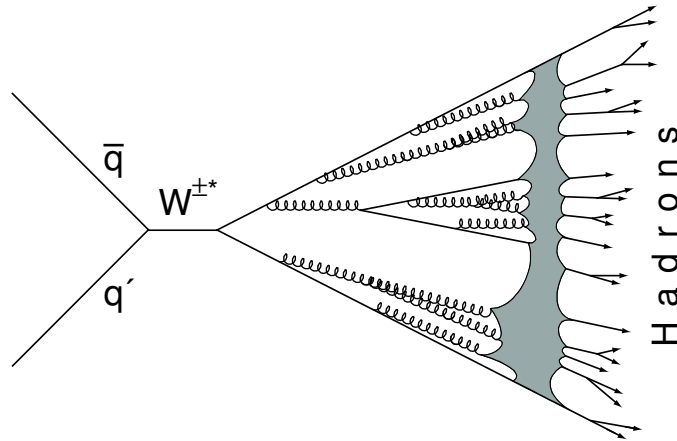


Figure 1.1: An example of Hadronization. Two high energy quarks on the left are shown annihilating into a W boson. The W then decays into two high energy quarks which hadronize by emitting many gluons (curly lines) that emit $q\bar{q}$ pairs. The grey region is where the quarks form hadrons, the particles that are observed in a detector. The direction of the cartoon lines do not represent real particle directions. The final hadrons will be collimated along the direction of their parent quarks or gluons forming jets. There will be at least two jets from the two quarks that decayed from the W . Hard gluons decaying from those quarks may also produce jets (final state radiation). The jets will be balanced in the event if the incident quarks have the same energy (if not, the jets will balance only in azimuthal angle). For example, if two jets are produced and the W is not boosted, the jets will have the same energy and will appear back to back.

If a large enough amount of energy is given to a quark within a hadron so that it could not stay inside (possibly due to a collision at high energy with another quark), the quark may leave the hadron, but the potential energy of the strong force will be so great that a new quark-antiquark pair will appear out of the vacuum. One quark binds with the leaving quark forming a meson and another one stays with the proton remnants. In the end, all the observed particles are colorless hadrons. Since energy must be conserved, the energy of the system is decreased by the energy taken to create the new quarks. High energy quarks will produce many new quarks and antiquarks as shown

in Figure 1.1. Therefore in a detector, a high energy quark is seen as a spray or jet of collimated hadrons moving along the direction of the original quark. The particles within the jet have little momentum transverse to the jet direction, regardless of the energy of the original quark.

The weak force is carried by the weak gauge bosons: the charged W boson and the neutral Z . Unlike the gluons and photons, the W and Z are quite heavy ($\sim 100\text{GeV}/c^2$), which implies that the weak force only acts over short distances. It is difficult to form a picture of the effects of the weak interaction, since it does not attract or repel particles like the other forces. Rather, the weak force is the cause of beta-decay of nuclei, allowing neutrons to transmute into protons. All particles may be affected by the weak force.

1.1.3 Gauge Theories and the Electroweak Force

The Standard Model is built with two separate theories, quantum chromodynamics (QCD) and electroweak. Electroweak unifies the electromagnetic force, described by quantum electrodynamics (QED), with the weak force. All of these theories are gauge theories which means that they involve fields that are invariant under a change of phase or gauge. For example, if the phase of the electron field of QED is changed arbitrarily, the resulting physics is not altered as long as the photon field is changed in the appropriate manner. In fact, to get spin $\frac{1}{2}$ fields invariant under gauge change, there must be a massless spin 1 boson (the photon for QED). This rule would seem to be violated by the weak force with its massive gauge bosons, but there is a fix discussed below.

The manner in which the gauge enters the theory characterizes the interaction. For instance, QED involves phase factors of $e^{i\phi(x)}$, which are members of the symmetry group $U(1)$ — unitary transformations in one dimension. For the weak force, it is convenient to group the particles into doublets,

$$\begin{pmatrix} \nu_e \\ e \end{pmatrix}_L, \begin{pmatrix} \nu_\mu \\ \mu \end{pmatrix}_L, \begin{pmatrix} \nu_\tau \\ \tau \end{pmatrix}_L, \begin{pmatrix} u \\ d \end{pmatrix}_L, \begin{pmatrix} c \\ s \end{pmatrix}_L, \begin{pmatrix} t \\ b \end{pmatrix}_L, \quad (1.1)$$

Instead of using a field for every particle, there is a two-component field for each doublet. The gauge transformations are now quite complicated since matrices are involved. Such transformations belong to the $SU(2)_L$ symmetry group (the L subscript indicates that the weak interactions only affect particles in left handed helicity states). To get a gauge invariant theory, there must be three massless gauge bosons, W^+ , W^- and the W^0 (note these massless bosons are not the same as the massive W and Z bosons described in Section 1.1.2). At this stage, the electromagnetic force can be combined with the weak force by adding in the $U(1)$ group and its gauge boson, the massless and neutral B^0 which will eventually become part of the photon. This $SU(2)_L \times U(1)$ theory with the massless gauge bosons does not reflect the fact that electromagnetism and the weak forces are separated in the everyday world, and that the W and Z weak gauge bosons have mass. Therefore, the symmetry must be broken in some way. The Higgs mechanism provides the method to break spontaneously electroweak symmetry by forcing one to choose a vacuum expectation value (vev) for the Higgs field. The results are that the W^+ , W^- , and the neutral Z (a mixture of the W^0 and the B^0) acquire mass. The photon (a different mixture of the W^0 and the B^0 bosons) remains massless. The price one pays is the introduction

of a new field representing a scalar (spin zero) particle, the Higgs boson, and a new parameter in the model, θ_W , the mixing angle which relates the Z to the W^0 and B^0 . The scalar Higgs couples to any particle with mass: the heavier the mass, the stronger the coupling. The triumph of the Higgs mechanism is the prediction of the masses of the W and Z weak bosons. These particles were discovered at CERN with the UA1 and UA2 detectors in 1982 [6]. Their masses were measured to be right at the SM prediction. This strong evidence for the validity of the Higgs Mechanism is the only evidence, for the Higgs particle which has not yet been observed in an experiment.

1.1.4 Running Coupling Strengths and GUTs

Even if the weak and electromagnetic forces are described by one theory, the electroweak theory, there are still two coupling strengths for the interaction (one for the $SU(2)_L$ part which is mediated by the W^+ , W^- , and W^0 bosons, and another for the $U(1)$ part mediated by the B^0). QCD also has an $SU(3)$ symmetry involving the color charge with its own coupling strength (there are eight generators of the $SU(3)$ symmetry resulting in eight two-color combinations that can be carried by gluons). Note that the name "coupling constant" has been avoided since the couplings are indeed not constant. They change with the energy scale (the scale of the momentum transfer between the two interacting particles) and thus are "running constants". This phenomenon is due to higher order effects of virtual bosons spontaneously forming loops of fermion-antifermion pairs and fermion-antifermion pairs appearing and disappearing from the vacuum. Indeed, the picture that a proton is composed of three quarks is simplistic. The three valence quarks are constantly exchanging gluons, which may transform into quark-antiquark pairs (sea quarks) and back into gluons again. In fact, about half of the momentum of a moving proton is carried by gluons. For QCD, the coupling strength decreases with increasing momentum transfer (shorter distances). That is why the quarks appear to be free within a nucleon when they are probed with high energy electrons. The quarks and gluons within protons are collectively called partons. The root cause of the running coupling strengths has to do with the fact that the higher order effects can cause some calculations to result in infinities. The infinities can be absorbed into quantities that cannot be directly measured and are renormalized, making the theories calculable again [7]. The price to pay is an additional term that must be added to the coupling strengths which is dependent on the energy scale. The renormalized quantities are the running constants.

A goal of a particle physicist is to invent a theory where all of the symmetries of the Standard Model can be expressed by one larger symmetry, and consequently, all the forces are unified into one force. Such theories are called Grand Unified Theories (GUTs). If the running coupling strengths are extrapolated to huge energy scales, they appear to converge at a scale of $M_{GUT} \sim 10^{16} GeV$ (though not all three at the same point, see Figure 1.6). This convergence may be a hint that GUT theories are valid. One also presumes that gravity can be unified at the Planck scale, $M_{PL} \sim G_N^{-1/2} \sim 10^{18} GeV$, where G_N is Newton's constant. Below those scales, the grand symmetry is broken at some point, yielding the particles and interactions observed presently. The Tevatron collider at Fermilab produce interactions with momentum transfers near the weak scale $\mathcal{O}(100 GeV)$ and the soon to be completed LHC collider at CERN will get close to the TeV scale.

Directly probing anywhere near the GUT or Planck scale does not seem remotely possible with current technology. Instead, the predicted effects of the different GUT theories on weak scale physics (new particles and interactions) are subject of searches. So far, no new particles or unexpected interactions have been observed beyond what are included in the SM. Though some proposed GUT models have been ruled out or severely constrained by experiments, it is still unknown what kind of GUT model is correct, let alone if GUTs are indeed the right description of physics at high energy scales.

1.1.5 Problems with the Standard Model

The SM is extremely successful in predicting the phenomena of the subatomic realm. Some aspects of the SM, however, are worrisome [8]. Although the masses of the W and Z bosons are predicted with the Higgs mechanism, the SM gives no hint of the masses of the quarks and leptons. They are input into the model by hand. And though the Higgs Mechanism seems to work, it was added in an ad hoc manner; the SM does not predict electroweak symmetry breaking (EWSB) by itself. This deficiency is addressed by some GUT models that have EWSB built into them.

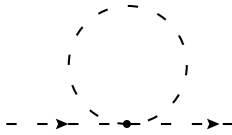


Figure 1.2: Self interaction diagram of fundamental scalars. This diagram is quadratically divergent.

There is a more serious problem. The scalar Higgs boson is a special kind of particle which gives mass to the fermions. Since the Higgs itself is massive, it can be involved in self-interaction loop processes as shown in Figure 1.2. Unlike similar diagrams for gluons, self interaction loop diagrams for fundamental scalar particles involve integrals that are quadratically divergent. When such an integral involved in calculating the Higgs mass is integrated over all momenta, we get an infinity which cannot be renormalized away. A non-renormalizable theory is a disaster, so there must be something that alleviates the quadratic divergence. One can imagine cutting off the integral at some energy scale where new physics becomes important, M_X , which is likely near the GUT scale. The mass parameter of the Higgs from EWSB runs from an energy scale at Q_1 down to a lower energy scale of Q_2 according to,

$$M^2(Q_2) = M^2(Q_1) + C_g^2(Q_2^2 - Q_1^2) + g^2 R + \mathcal{O}(g^4) \quad (1.2)$$

where C_g is a dimensionless constant, g is a coupling strength, and R is some parameter that grows at worst logarithmically as $(Q_1 - Q_2) \rightarrow \infty$. The running of the Higgs mass from the high scale M_X down to the weak scale M_W is thus given by,

$$M_H^2(M_W) \sim M_H^2(M_X) - C_g^2 M_X^2 \quad (1.3)$$

where $M_X \approx \mathcal{O}(M_{GUT}) \gg M_W$. Since the Higgs mass at the weak scale is supposed to be of the order of M_W (that is the scale where EWSB takes place), the terms on the right hand side of Equation (1.3) must be tuned to a precision of $\sim 10^{-26}$ in each order of perturbation theory. A tuning to that degree would be an incredible feat of nature and is unnatural. This difficulty is called the fine tuning problem. A related question is the hierarchy problem: why do the coupling constants of the SM appear to converge at such a huge energy scale ($M_X \gg M_W$)? Nothing in the SM can answer these questions, thus providing the expectation that there must be some theory beyond the Standard Model.

1.1.6 Beyond the Standard Model

There are several schemes to eliminate the quadratic divergence of the Higgs mass [9, 10]. One solution involves treating the Higgs not as a fundamental particle, but composed of fermions. Some force must keep the constituent fermions confined within the Higgs, similar to how the strong force confines the quarks within a hadron. Like QCD, the theory of this new interaction would be renormalizable, thus alleviating the quadratic divergences. Keeping with the strong force similarity, this new force is called Technicolor (recent reviews can be found in [11]), which introduces its own color charge that is carried by the constituent fermions called techniquarks. Technicolor theories predict the existence of technipions and technirhos, particles made up of techniquark pairs. No such particles have been observed and severe constraints can be placed on the validity of this theory. Though Technicolor can alleviate the fine tuning problem, it has nothing to do with unification of forces and does not address the hierarchy question.

A variation of Technicolor, compositeness, postulates that none of the SM particles are fundamental, but are, in fact, made up of preons. If compositeness is reality, then the cross section for some processes would be different from the predictions of the SM. No such significant deviations have been observed. Compositeness also suffers from the same deficiency as Technicolor: it cannot address the hierarchy problem and is constrained by experiments.

The third scheme to eliminate quadratic divergences is Supersymmetry, which adds fermions and scalar particles to the Standard Model to introduce new loop diagrams that cancel out the quadratic divergent loops. Models of Supersymmetry may be based on GUTs that build in EWSB and provide relations between the weak scale and the GUT scale, addressing the hierarchy problem. The Supersymmetry is explored in some detail in subsequent sections of this chapter.

1.2 Supersymmetry

Supersymmetry (SUSY) [10, 12, 13] is a theory that cancels the quadratic divergence from the fundamental scalar Higgs particle by adding new particles to the Standard Model. First, a simple SUSY model is presented to explain how the cancellation is achieved. More realistic SUSY models will be explored in the following.

1.2.1 Basics of SUSY

A simple supersymmetric model is one by Wess and Zumino [13, 14, 15] and shows the basic features of SUSY. This theory involves two real scalar fields (A and B) representing spin zero bosons like the Higgs boson, and a two degree of freedom spinor field (ψ) representing a Majorana (particle and antiparticle are one and the same) spin- $\frac{1}{2}$ fermion. The Wess and Zumino lagrangian describing the theory is,

$$\mathcal{L} = \frac{1}{2}(\partial_\mu A)^2 + \frac{1}{2}(\partial_\mu B)^2 + \frac{i}{2}\bar{\psi}\not{\partial}\psi + \frac{1}{2}m\bar{\psi}\psi - \frac{1}{2}m^2A^2 - \frac{1}{2}m^2B^2 + mgA(A^2 + B^2) - \underbrace{\frac{1}{2}g^2(A^2 + B^2)^2}_{(1)} - \underbrace{ig\bar{\psi}A\psi + ig\bar{\psi}\gamma_5 B\psi}_{(2)} \quad (1.4)$$

where the three particles have the same mass m and same coupling constant g . The A , B , and ψ fields can undergo certain transformations. Transformations are written as,

$$A \rightarrow A' = A + \delta A = A + \bar{\alpha}QA \quad (1.5)$$

where α is the constant parameter of the transformation and Q is the transformation generator. Wess and Zumino define supersymmetric transformations for the scalar fields to be,

$$\delta A = i\bar{\alpha}\gamma^5\psi \quad \delta B = -\bar{\alpha}\psi \quad (1.6)$$

and for the fermion field,

$$\delta\psi = F\alpha - iG\gamma^5\alpha + (\not{\partial}A)\alpha + i(\not{\partial}B)\alpha \quad (1.7)$$

where $F = mA - g(A^2 - B^2)$ and $G = mB - 2gAB$.

The lagrangian (1.4) is invariant under the Wess and Zumino transformations [15]: if the transformed fields are plugged into the lagrangian, it changes at most by a total derivative and thus the resulting physics remains unaltered. The transformations of (1.6) and (1.7) are called supersymmetric, because boson transformations involve the fermion field and the fermion transformation involves the boson fields. This "Supersymmetry" relates bosons to fermions and vice-versa.

Using (1.5), one can identify the transformation generator, Q , in (1.6) and (1.7). Q appears to be an operator which transforms a fermion field into a scalar boson field and vice-versa, altering the spin of the particle by $\pm\frac{1}{2}$. The anticommutation relation for Q is,

$$\{Q_a, Q_b\} = 2(\gamma_\mu P^\mu)_{ab} \quad (1.8)$$

where P_μ represents the translation generators of the Poincaré group (Lorentz boosts and rotations). The a, b subscripts are components of the spinor fields. Since the transformations are involved with space-time transformations, Supersymmetry is a space-time symmetry. This distinction is important, since it differs from the internal symmetries of particles, such as electric and color charge, lepton number, and baryon number. The Wess and Zumino supersymmetric generator acting on a field will only change the spin;

the particle retains its mass, charge, and its other internal quantum numbers. To obtain a lagrangian to be invariant under the SUSY transformations, one particle is needed for each degree of freedom of its partner. The two scalar bosons are the super-partners of the fermion and vice-versa.

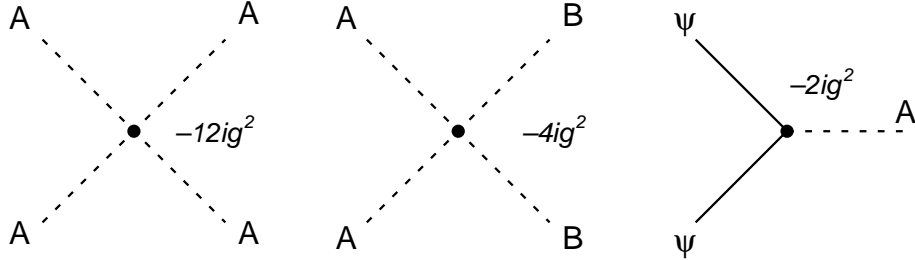


Figure 1.3: Interactions involving the A scalar particle. The vertex factors are shown with each interaction.

The interaction terms marked (1) and (2) in the Lagrangian (1.4) describe how the A scalar particle interacts with the B and the ψ . These terms are expanded below,

$$\mathcal{L} = \dots - \frac{1}{2}g^2(A^4 + 2A^2B^2 + B^4) - ig\bar{\psi}A\psi + \dots \quad (1.9)$$

and predict the interactions shown in Figure 1.3 (the B^4 term is ignored for this discussion). With these interactions, the self interacting one loop diagrams for A can be represented as in Figure 1.4. Diagrams (3), (4), and (5) are separately quadratically divergent, but when their amplitudes are added together, the quadratic divergent terms cancel [15] leaving a logarithmically divergent term that can be renormalized. The self interaction diagrams for B cancel in a similar manner.

Supersymmetry eliminates the quadratic divergences by introducing new particles so that each fermion is paired with two scalar particles causing the divergences to cancel. Clearly, the Wess and Zumino theory is not realistic, since all particles must have the same mass. If this were the case, SUSY could be ruled out immediately: since a scalar electron with the electron mass has not been observed. Supersymmetry must be broken so that there can be mass splitting between the SUSY partner particles. A splitting is allowed because the quadratic divergences do not have to cancel exactly. The fine tuning problem is still alleviated as long as masses are not more than ~ 1 TeV apart. The Wess and Zumino model is too simplistic for the real world, but it shows the basic characteristics of SUSY models.

1.2.2 Minimal Supersymmetric Standard Model

The Minimal Supersymmetric Standard Model [16] (MSSM) is a scheme to introduce Supersymmetry to the Standard Model which adds the fewest number of new particles. Each SM particle receives supersymmetric partners or sparticles, one for each degree of freedom. These additions reflect $N = 1$ Supersymmetry, where N is the number of supersymmetric generators (Q in the previous section) that alter spin by $\frac{1}{2}$ unit. One

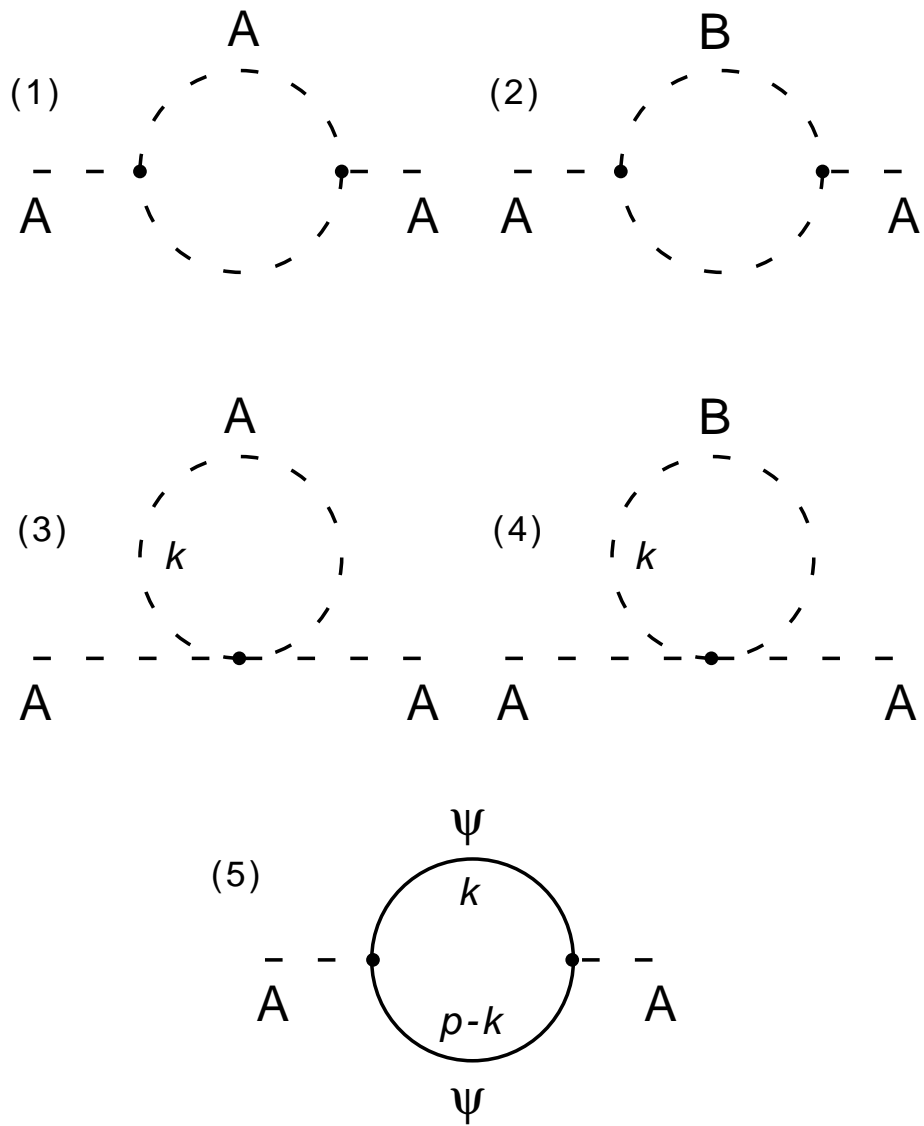


Figure 1.4: Self interaction loop corrections for the A scalar particle.

SM Particles		SUSY Particles				
		interaction eigenstates			mass eigenstates	
Name	Spin	Name	Spin	Symbol	Name	Symbol
q = u, d, s, c	1/2	squark	0	\tilde{q}_L, \tilde{q}_R	squark	\tilde{q}_L, \tilde{q}_R
q = b, t	1/2	squark	0	\tilde{q}_L, \tilde{q}_R	squark	\tilde{q}_1, \tilde{q}_2
l = e, μ , τ	1/2	slepton	0	\tilde{l}_L, \tilde{l}_R	slepton	\tilde{l}_1, \tilde{l}_2
$\nu = \nu_e, \nu_\mu, \nu_\tau$	1/2	sneutrino	0	$\tilde{\nu}$	sneutrino	$\tilde{\nu}$
gluons g	1	gluino	1/2	\tilde{g}	gluino	\tilde{g}
W^\pm	1	wino	1/2	\tilde{W}^\pm	2 charginos of each sign	$\tilde{\chi}_{1,2}^\pm$
H^\pm	0	higgsino	1/2	\tilde{H}^\pm		
photon γ	1	bino	1/2	\tilde{B}^0	4 neutralinos	$\tilde{\chi}_{1,2,3,4}^0$
Z	1	wino	1/2	\tilde{W}_3^0		
h, H, A	0	higgsino	1/2	$\tilde{H}_{1,2}^0$		
graviton G	2	gravitino	3/2	\tilde{G}	gravitino	\tilde{G}

Table 1.1: Particle content of the MSSM.

can conceive $N \geq 2$ models, but one gets into trouble in relating fermions with different helicities incompatible with the left-handed weak interactions.

The particle content of the MSSM is shown in Table 1.1. The particles and sparticles form supermultiplets, similar in spirit to the doublets of electroweak theory in (1.1). There are two kinds of supermultiplets: chiral and vector. A chiral supermultiplet contains a chiral fermion (fermions that couple differently to the weak gauge bosons depending on their helicity state) and two spin zero scalars. The vector supermultiplet consists of a spin-1 vector boson and a fermion. These supermultiplets hold the Standard Model particles and their partners.

For example spin 1 gauge bosons and their spin 1/2 superpartners the gauginos (binos, winos and gluinos) are in vector supermultiplets. In the MSSM, there are only three generations of spin 1/2 quarks and leptons (no right handed neutrino) as in the SM. The left and right handed chiral fields belong to chiral superfields together with their spin 0 SUSY partners the squarks and sleptons.

As shown in Table 1.1, each charged lepton is associated with two spin zero sleptons, since fermions have two degrees of freedom. Each neutrino is paired with only one sneutrino, since neutrinos have only one helicity state. Quarks are similar to leptons and are associated with two scalar squarks each. Squarks and sleptons are labeled left and right handed. Since these particles are scalars, the labels reflect how they couple to the partners of the weak gauge bosons instead of denoting helicity. The massless spin 1 gluon has 16 degrees of freedom (2 helicity states \times 8 color) and is associated with the massive spin $\frac{1}{2}$ gluino, also with 16 degrees of freedom.

The partners of the gauge and Higgs bosons are more complicated. For the MSSM, two Higgs doublets are required in order to give mass to u and d quarks (in the SM, the single Higgs field and its conjugate fulfill this role, but in the MSSM conjugate fields cannot be used [17]). Consequently, five Higgs particles exist: two charged scalars (H^\pm), two

neutral scalars (h and H) and one neutral pseudoscalar (A) as shown in Table 1.1. Since there are two Higgs doublets, there are two vacuum expectation values (vev) $\langle v_1 \rangle$ and $\langle v_2 \rangle$. The vevs are constrained so that $\langle v_{SM} \rangle^2 = \langle v_1 \rangle^2 + \langle v_2 \rangle^2$, where $\langle v_{SM} \rangle$ is the vev of the single Higgs field in the SM. The ratio of the two Higgs doublet vevs is still undetermined however, and is denoted by the parameter $\tan(\beta) = \langle v_2 \rangle / \langle v_1 \rangle$. There is also a free Higgsino mass parameter, μ .

The Z , photon, and neutral Higgses add up to eight degrees of freedom (three helicity states for the Z , two for the γ , and one each for the h , H , and A).

Neutral higgsinos mix with the wino and the bino to give the mass eigenstates, the neutralinos ($\tilde{\chi}_m^0$), where $M_{\tilde{\chi}_1^0} < M_{\tilde{\chi}_2^0} < M_{\tilde{\chi}_3^0} < M_{\tilde{\chi}_4^0}$. The SUSY partners of the W boson (two charges \times three helicities = six d.o.f.) and the charged Higgses (two charges \times one helicity) mix to form two charged spin $\frac{1}{2}$ charginos ($\tilde{\chi}_m^\pm$) which have eight d.o.f. The couplings of the scalar squarks and sleptons to the charginos and neutralinos depend on the chargino/neutralino "gauge content". The parameters $\tan(\beta)$ and μ determine which fraction of the chargino and neutralino mixtures are higgsino and wino/zino/photino. Since the right handed SUSY scalars only couple to the Higgsino part, the branching fractions of the charginos and neutralinos depend heavily on $\tan(\beta)$ and μ .

Since Supersymmetry commutes with the $SU(3)_C \times SU(2)_L \times U(1)$ symmetries of the SM, the gauge interactions between the sparticles are the same as between their partner SM particles with the same coupling strengths, although the difference in spins must be taken into account. For example, if the chargino is mostly wino, it will decay to quarks and leptons with the same branching fractions as a SM W boson. If it is mostly higgsino, it will decay like a Higgs.

The requirement of gauge invariance and renormalisability are sufficient to guarantee that the Standard Model Lagrangian conserves baryon and lepton number. In supersymmetric theories, one introduces a new multiplicative quantum number, R-parity. R-parity is defined to be

$$R = (-1)^{3B+L+2S} \tag{1.10}$$

where B is the particle's baryon number, L is the lepton number and S is the spin. According to this definition, R-parity is $+1$ for SM particles and -1 for their supersymmetric partners. Although R-parity conservation is not required by any model, its violation implies that lepton and/or baryon number conservation are violated as well.

In case of the R-parity conservation, sparticles are always produced in pairs, and each decay of a sparticle yields another sparticle. Consequently, the lightest supersymmetric particle (LSP) must be stable. R-parity conservation is theoretically favored, since it does not allow sparticles to play intermediate roles in processes that involve only SM particles, and so the predictions of the SM remain unaltered. Fast proton decay is also prohibited.

The LSP is generally assumed [18] to be the lightest neutralino, $\tilde{\chi}_1^0$. It must be neutral since charged LSPs would have been seen in atomic physics. The LSP only interacts weakly, like neutrinos, producing missing energy (imbalanced events) in a detector which can be used as an experimental signature for SUSY. It is also a candidate for cold (non-relativistic) dark matter.

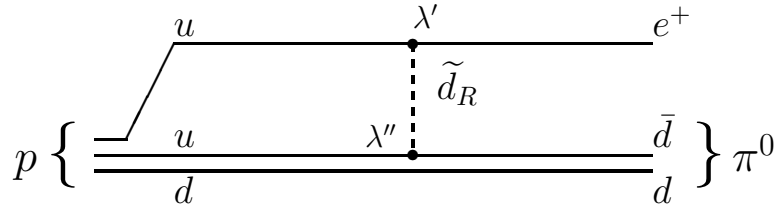


Figure 1.5: Typical diagram for proton decay $p \rightarrow e^+ \pi^0$ through λ' and λ'' couplings.

1.2.3 R -parity violation

Although no violation of B or L has been observed yet, there is no firm theoretical argument which would require exact conservation of them and that of the R -parity. The R -parity violating part of the superpotential can be written as [19]

$$W_{\mathcal{R}_p} = \lambda_{ijk} L_i L_j E_k^c + \lambda'_{ijk} Q_i L_j D_k^c + \lambda''_{ijk} U_i^c D_j^c D_k^c \quad (1.11)$$

Here L and E are isodoublet and isosinglet lepton, Q and D are isodoublet and isosinglet quark superfields, the indices i , j and k run for the three lepton and quark families. The suffix c denotes charge conjugate. The first two terms violate explicitly L while the last one violates B .

One of the immediate consequences of simultaneous violation of B and L is known to be fast proton decay. Most *Grand Unified Theories* (GUT's) which try to unify the strong and electromagnetic interactions within a single (broken) gauge symmetry do predict proton decay as a consequence. In the MSSM too, if R -parity is violated in a maximal sense, i.e., all the couplings in (1.11) are present, one can have proton decay through diagrams such as the one in Fig. 1.5.

The amplitude for this process can immediately be estimated as

$$\mathcal{A}(p \rightarrow \ell^+ \pi^0) \sim \frac{\lambda' \lambda''}{M_{\tilde{d}_R}^2}. \quad (1.12)$$

This is not the only possible diagram, but all others have amplitudes of the same order.

Till date all experimental searches for proton decay have yielded negative results, leading to a lower bound on the proton lifetime of $\sim 10^{32}$ years: this immediately constrains [20] the product $\lambda' \lambda''$ in the above equation to be $\sim 10^{-25}$ or smaller, for $M_{\tilde{d}_R}^2 <$ a few TeV.

To explain such an unnaturally small number, it is enough to assume that one of the factors vanishes, i.e., we can either have L conserved, with vanishing of λ' , or have B conserved, with vanishing λ'' .

Other experimental limits e.g. on lepton number violation: double β decay, or on $N - \bar{N}$ oscillation, etc. indicate that the couplings in (1.11) should not be expected to exceed a few percent, and usually are much smaller than the gauge couplings [21].

Even so, if R -parity is violated the topology of the expected SUSY signal changes substantially. Lepton number terms can result in a significant increase in lepton produc-

tion. The three-lepton terms, λ_{ijk} can cause decay of sleptons into two leptons and decay of the LSP into three leptons (see Section 7.3 and Figure 7.4).

The one-lepton two-quark terms, λ'_{ijk} can cause the decay of squarks into quark plus lepton. They can also lead to the decay of the LSP into a pair of quarks and lepton.

The three-quark terms, λ''_{ijk} correspond to baryon number violating processes.

Out of these three kinds of couplings terms, the B -violating λ'' are difficult to study at the Tevatron; they lead to events with multijet signatures that are difficult to be identified in the presence of huge background from QCD. The L -violating λ and λ' will give rise to multilepton and multijet final states.

1.2.4 GUT Framework for the MSSM

Although the MSSM allows one to add the fewest number of new particles to the SM, it unfortunately leads to a total of 105 new parameters [22]. The MSSM gives no prediction on the masses of the sparticles (of course, they must be heavier than their partners since they were not observed). The mixing angles which enter in the transformation of interaction eigenstate to mass eigenstate are also completely unknown. Such mixing angles appear for example in the stop, sbottom and stau sectors. With so many parameters that must be put by hand, the MSSM is a cumbersome theory to use in systematic searches for sparticles.

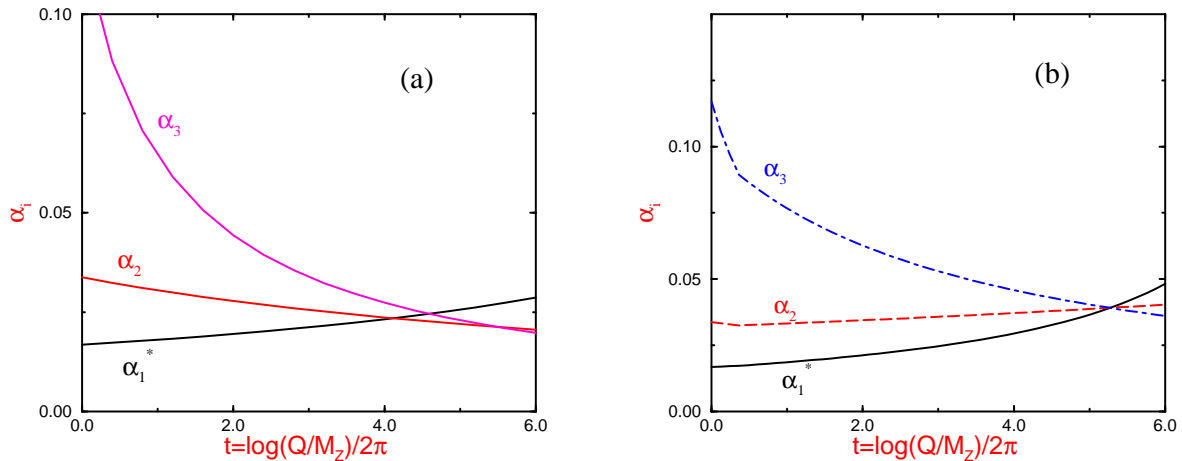


Figure 1.6: Evolutions of the coupling constants. Shown are the evolutions of the U(1) (α_1), SU(2) (α_2), and SU(3) (α_3) coupling constants with the energy scale. Plot (a) shows the evolution in the Standard Model. Plot (b) is the evolution within the MSSM. The addition of the sparticles changes the running of the coupling strengths so that they all converge at the same point, suggesting that the interactions arise from a single grand unified force.

The usual method to reduce the number of independent parameters is to work within the framework of a Grand Unified Theory (GUT). In fact, the MSSM gives a hint that a GUT with SUSY particles may be the correct description of physics at high energy scale, since the additional particles of the MSSM cause the running coupling strengths

to converge at the same point as shown in Figure 1.6. A "GUT inspired MSSM" relies on some symmetry at a high energy scale to give relations between some of the sparticle masses. For example, with such models the masses of the squarks are degenerate except for the scalar top. In GUT models, the gauginos are mass degenerate at the GUT scale, and their masses are related at the weak scale (i.e. typically, $\tilde{\chi}_1^\pm \approx \tilde{\chi}_2^0 \approx 2\tilde{\chi}_1^0$). Although such relations are helpful, one still must put by hand the degenerate squark mass, masses for the sleptons, $\tan(\beta)$, μ and so on.

As it will be seen, the sparticles masses and decay modes are highly dependent on the parameters of the model, and it is advantageous to use a framework with the least number of free parameters possible and most predictive power.

1.3 Minimal Supergravity

In order to decrease the number of parameters, some theoretical prejudice must be imposed. Presumably supersymmetry should be broken spontaneously rather than by "hand" and should be unified with gravity. MSSM fields alone do not permit to construct a phenomenologically acceptable model with spontaneous supersymmetry breaking. Thus it is necessary to introduce a hidden sector to break SUSY and then to communicate the breaking to the MSSM sector using some messenger interaction that couples to both. In supergravity (SUGRA) models gravity is the sole messenger [23].

Minimal Low Energy Supergravity [17, 24] (mSUGRA) is a model that not only unifies the strong, weak, and electromagnetic forces, but also includes gravity at some large energy scale M_X . Typically, M_X is the GUT scale (10^{16} GeV) or the Planck scale (10^{18} GeV). At M_X , the mass parameters for the gauginos are degenerate since for any GUT model, and in the simplest supergravity models, the inclusion of gravity means that all of the SUSY scalars share also a common mass parameter. The only parameters needed to describe mSUGRA models are as follows:

- m_0 — the common mass parameter for all scalar sparticles at the M_X scale.
- $m_{1/2}$ — the common mass parameter for all gauginos at the M_X scale.
- $\tan(\beta)$ — the ratio of the vacuum expectation values of the two Higgs doublets.
- $\text{sign}(\mu)$ — the sign of the Higgsino mass parameter.
- A_0 — a common trilinear coupling constant in the lagrangian (for searches at the Tevatron, A_0 only affects the scalar top mixing).

Along with A_0 there is a bilinear coupling constant, B_0 , but it is recast into $\tan(\beta)$ and μ . Only the sign of μ is needed, because its magnitude is constrained to yield the correct Z mass by electroweak symmetry breaking.

Given the mSUGRA parameters and masses of the SM particles, masses and mixing angles for the sparticles can be determined at the weak scale by solving the renormalization group equations (RGEs) of the model and evaluating loop diagrams. The evolutions of the sparticle mass parameters are shown in Figure 1.7. For many choices of the mSUGRA

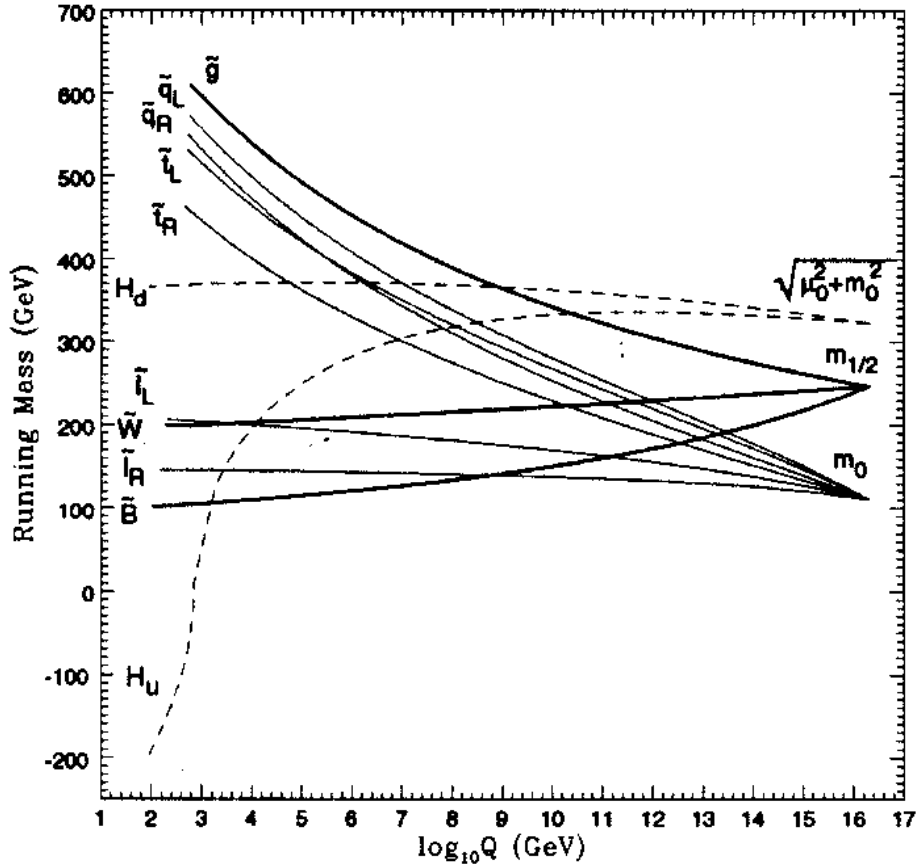


Figure 1.7: Evolution of sparticle mass parameters in Minimal Supergravity. This plot shows the mass parameters of various sparticles vs. energy scale (Q). Note that the gauginos are in states before electroweak symmetry breaking (\bar{W} and \bar{B}). The Higgs mass parameter running negative is at the origin of EWSB. These evolutions are for a particular choice of the model parameters. A different choice of m_0 , $m_{1/2}$, and the other parameters will lead to different evolutions. For some values of the parameters, the Higgs mass stays positive which means that EWSB is not predicted by those models.

parameters, a Higgs mass parameter starts positive at M_X and runs negative, as the energy scale is decreased, thus breaking electroweak symmetry. For the SM, the negative Higgs mass parameter must be put in by hand. The prediction of EWSB is one of the features of mSUGRA that makes these models favored among many SUSY phenomenologists.

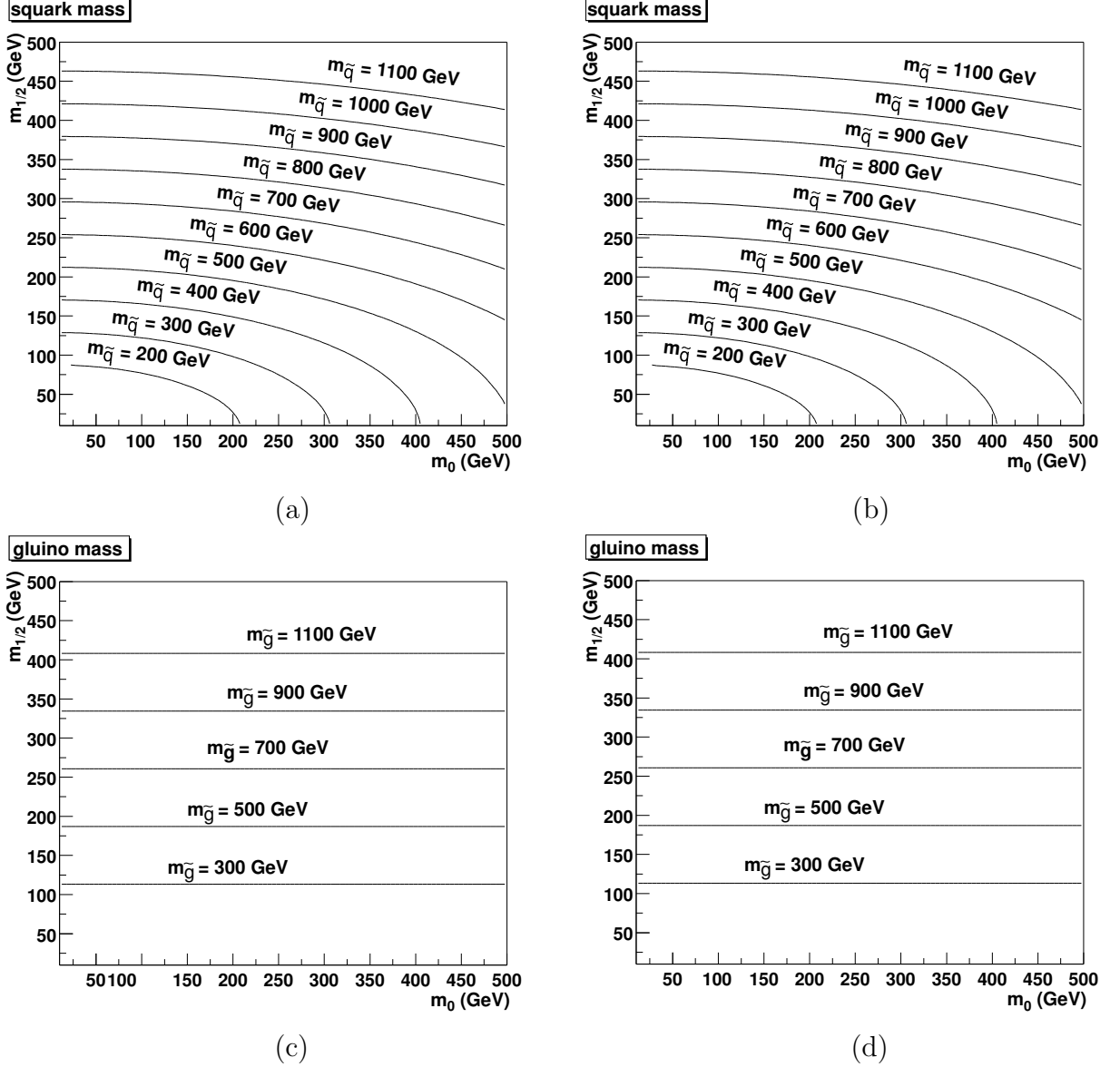
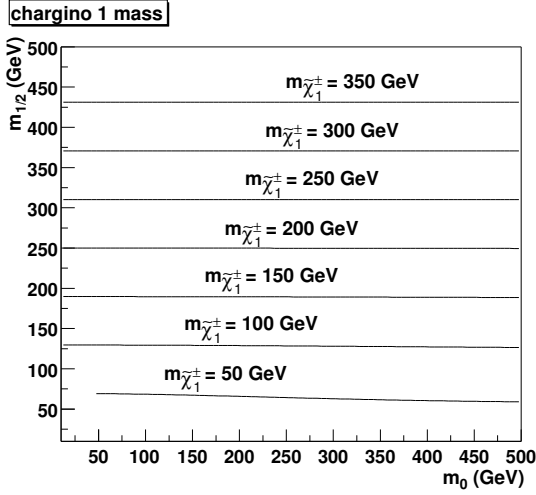


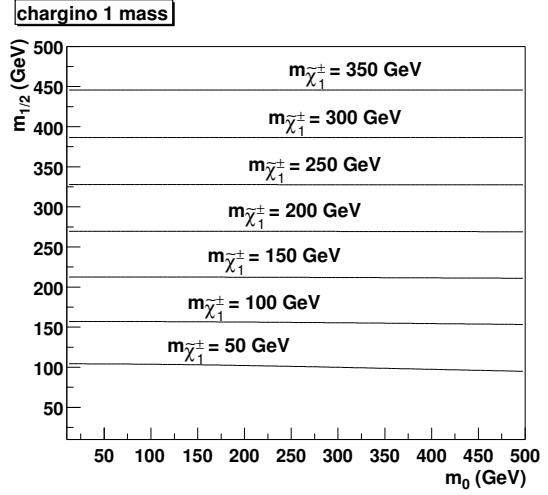
Figure 1.8: Mass contours of squarks (a, b) and gluinos (b, c) on the $m_0 - m_{1/2}$ plane. These contours are valid for parameters $\tan(\beta) = 5$, $A_0 = 0$, $\mu < 0$ (a, c) $\mu > 0$ (b, d).

For a given $\tan \beta$, sign μ and A_0 , describing masses of the sparticles with just m_0 and $m_{1/2}$ is convenient, but one loses the physical aspect of the model.

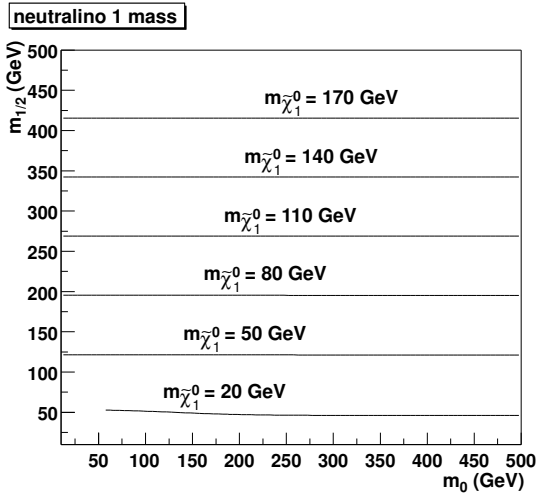
As an illustration Figure 1.8 shows the squarks and gluino masses as a function of m_0 and $m_{1/2}$ for a particular choice of parameters $\tan \beta = 5$, $A_0 = 0$ and $\mu > 0$ or $\mu < 0$. In mSUGRA, the squark masses are not quite degenerate. While the masses



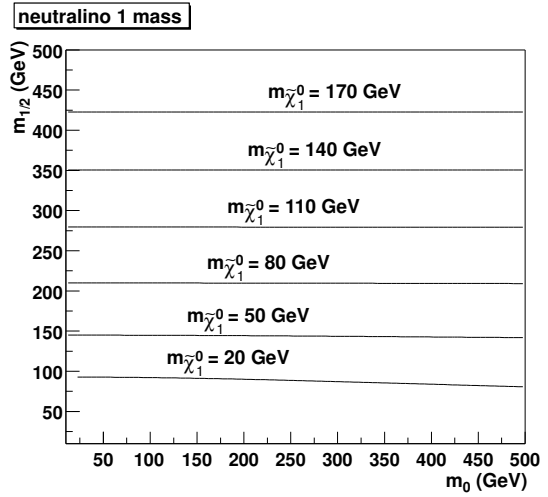
(a)



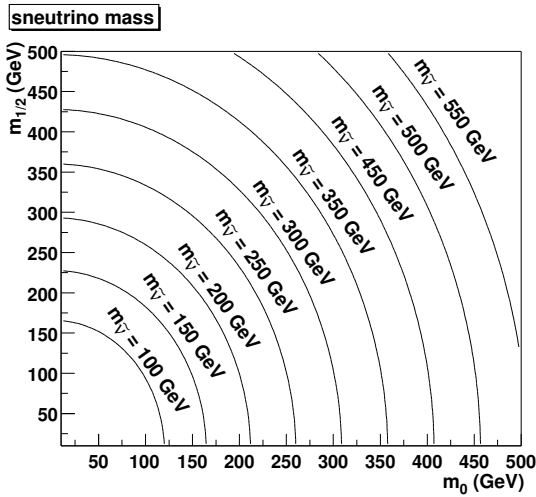
(b)



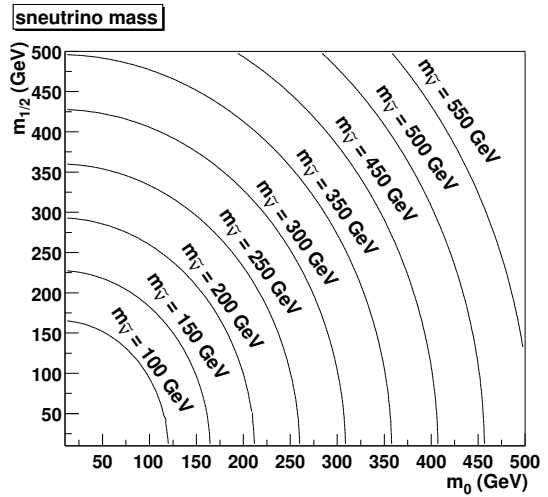
(c)



(d)



(e)



(f)

Figure 1.9: Mass contours of charginos (a, b), neutralinos (c, d) and sneutrino (e, f) masses on the $m_0 - m_{1/2}$ plane. These contours are valid for parameters $\tan(\beta) = 5$, $A_0 = 0$, $\mu < 0$ (a, c, e) $\mu > 0$ (b, d, f).

of the scalar up, down, charm, and strange (both left and right varieties) are typically within $1 \text{ GeV}/c^2$ of each other, the scalar bottom can sometimes mix its left and right states into lighter and heavier mass eigenstates. The lighter sbottom is not more than $15 \text{ GeV}/c^2$ less than the four other squarks. The squark mass contours shown in Figure 1.8 are an average of the masses for left and right squarks excluding scalar tops. As expected, one can see that gluino masses are almost independent of m_0 . Similar plots of mass contours for some other sparticles are shown in Figure 1.9. The values of the other model parameters are $\tan(\beta) = 5$, $A_0 = 0$ for both $\mu < 0$ and $\mu > 0$. For small m_0 and $m_{1/2}$, electroweak symmetry breaking does not occur in mSUGRA, and that region can be ruled out immediately. There are also points where the electron sneutrino is lighter than $\tilde{\chi}_1^0$ and thus becomes the LSP. Cosmological considerations disfavor a sneutrino LSP, but aside from that, there is no evidence why that situation cannot occur.

1.4 Other SUSY Models

Of course, one would like to experimentally test the validity of all SUSY models, but the details of squark and gluino decays are highly model dependent. Therefore Monte Carlo simulations must be performed to test each model. This task is prohibitive for models with many parameters.

The mSUGRA framework requires a minimum of free parameters and is used for the analysis described here. Aside from the fact that mSUGRA is a nice model which has few parameters, includes gravity, and predicts EWSB in many cases, there is no evidence that mSUGRA is the true, correct model of SUSY, assuming that SUSY itself is a symmetry of nature. As Monte Carlo simulations become faster, more models will be able to be tested on a reasonable time scale.

Some new models have been introduced recently which are different from mSUGRA in an attempt to explain one event [25] collected by CDF, the other collider experiment at the Tevatron. The event has an electron, a positron, two photons, and is quite imbalanced (remember that LSPs give rise to imbalanced events). No similar event has been observed at DØ. The SM does not predict the occurrence of such an imbalanced $ee\gamma\gamma$ event. It also turns out that mSUGRA does not predict a significant rate for SUSY processes ending up with photons in the final state. In other models as Gauge Mediated Supersymmetry Breaking (GMSB), the SUSY particles get masses through $SU(3) \times SU(2) \times U(1)$ gauge interactions at a messenger scale $M_m \ll M_{Planck}$ [26].

There are two types of Gauge Mediated SUSY models [27]: those where the LSP is the $\tilde{\chi}_1^0$ and those where the LSP is the gravitino (\tilde{G}), the SUSY partner of the graviton (the spin 2 graviton carries the gravitational interaction and has never been observed). In the $\tilde{\chi}_1^0$ LSP type model, the $\tilde{\chi}_2^0$ is mostly photino and the $\tilde{\chi}_1^0$ is mostly higgsino so that the decay $\tilde{\chi}_2^0 \rightarrow \gamma\tilde{\chi}_1^0$ may occur. If the \tilde{G} is the LSP, then photons are produced when the $\tilde{\chi}_1^0$ radiatively decays via $\tilde{\chi}_2^0 \rightarrow \gamma\tilde{G}$. Both models predict that imbalanced events with two photons should occur more often than what the SM predicts and should be observable in the data sets at CDF and DØ. Searches have been performed and no such excess has been found aside for the one event at CDF, so severe constraints can be placed on these models.

Forming conclusions on the basis of only one event is always a bit dangerous, since the measurements may be fluctuations. Nevertheless, the new SUSY models are interesting in their own right, and, if nothing else, serve as a reminder that there are other possibilities than mSUGRA.

1.5 Constraints on R -parity-violating couplings and current limits

Knowing constraints on the \mathcal{R}_p parameters allows one to estimate prospects of a certain experiment in searching for the \mathcal{R}_p SUSY and, thus, to significantly help in planning new experiments of this type. Many experiments intending to search for the \mathcal{R}_p SUSY signal are now in progress or on the stage of preparation. The constraints for the \mathcal{R}_p couplings and for their products are shown in Table 1.2 and in the following subsections it will be briefly explained how these limits were obtained.

1.5.1 Proton stability

Non-observation of proton decay (mean life $\tau > 10^{31}$ s to 10^{33} s according to the decay mode) places very strong bounds on the simultaneous presence of both L - and B -violating couplings; generically $\lambda'\lambda'' \leq 10^{-24}$. Specific cases have been considered in refs. [32, 33]. Ref. [33] sets an upper limit of 10^{-9} (10^{-11}) for any product combination of λ' and λ'' in the absence (presence) of squark flavour mixing (stop and sbottom).

1.5.2 $n-\bar{n}$ oscillation

The contributions of the λ''_{121} - and λ''_{131} -induced interactions to $n-\bar{n}$ oscillation proceed through the process ($udd \rightarrow \tilde{d}_i d \rightarrow \tilde{g} \rightarrow \tilde{d}_i \bar{d} \rightarrow \bar{u} d \bar{d}$). In ref.[34], the intergenerational mixing was not handled with sufficient care. In the updated analysis [35], the constraint on λ''_{131} has been estimated to be $\leq 10^{-4} - 10^{-5}$ for $\tilde{m} = 100$ GeV, while that on λ''_{121} is shown to be weaker (diluted by a relative factor of m_s^2/m_b^2). It has, however, been shown in the same paper [35] that the best constraint on λ''_{121} comes from the consideration of double nucleon decay into two kaons and the bound is estimated to be $\leq 10^{-6} - 10^{-7}$.

1.5.3 ν_e -Majorana mass

λ - and λ' -type couplings can induce a Majorana mass of ν_e by self-energy type diagrams. An approximate expression for the induced ν_e -Majorana mass, for a generic coupling λ , is

$$\delta m_{\nu_e} \sim \frac{\lambda^2}{8\pi^2} \frac{1}{\tilde{m}^2} M_{\text{SUSY}} m^2. \quad (1.13)$$

Assuming $M_{\text{SUSY}} = \tilde{m}$, the λ_{133} -induced interaction with $\tau\tilde{\tau}$ loops yields the constraint (1σ) $\lambda_{133} \leq 3 \times 10^{-3}$ for $m_{\tilde{\tau}} = 100$ GeV [36]. On the other hand, the λ'_{133} -induced diagrams with $b\tilde{b}$ loops leads to $\lambda'_{133} \leq 10^{-3}$ for $m_{\tilde{b}} = 100$ GeV [37].

Coupling	Bound	Ref.	Coupling	Bound	Ref.	Coupling	Bound	Ref.
$ \lambda_{121} $	0.05	a	$ \lambda_{131} $	0.06	b	$ \lambda_{231} $	0.06	c
$ \lambda_{122} $	0.05	a	$ \lambda_{132} $	0.06	b	$ \lambda_{231} $	0.06	c
$ \lambda_{123} $	0.05	a	$ \lambda_{133} $	0.003	i	$ \lambda_{233} $	0.06	c
$ \lambda'_{111} $	0.001	j	$ \lambda'_{211} $	0.09	p	$ \lambda'_{311} $	0.16	s
$ \lambda'_{112} $	0.02	a	$ \lambda'_{212} $	0.09	p	$ \lambda'_{312} $	0.16	s
$ \lambda'_{113} $	0.02	d	$ \lambda'_{213} $	0.09	p	$ \lambda'_{313} $	0.16	s
$ \lambda'_{121} $	0.035	e	$ \lambda'_{221} $	0.18	r	$ \lambda'_{321} $	0.20	o
$ \lambda'_{122} $	0.06	i	$ \lambda'_{222} $	0.18	r	$ \lambda'_{322} $	0.20	o
$ \lambda'_{123} $	0.20	o	$ \lambda'_{223} $	0.18	r	$ \lambda'_{323} $	0.20	o
$ \lambda'_{131} $	0.035	e	$ \lambda'_{231} $	0.22	o	$ \lambda'_{331} $	0.26	h
$ \lambda'_{132} $	0.33	h	$ \lambda'_{232} $	0.39	n	$ \lambda'_{332} $	0.26	h
$ \lambda'_{133} $	0.002	i	$ \lambda'_{233} $	0.39	n	$ \lambda'_{333} $	0.26	h
$ \lambda''_{112} $	10^{-6}	k	$ \lambda''_{212} $	1.25	m	$ \lambda''_{312} $	0.43	n
$ \lambda''_{113} $	10^{-5}	l	$ \lambda''_{213} $	1.25	m	$ \lambda''_{313} $	0.43	n
$ \lambda''_{123} $	1.25	m	$ \lambda''_{223} $	1.25	m	$ \lambda''_{323} $	0.43	n

- a:** Charged-current universality (1σ) [41];
- b:** $\Gamma(\tau \rightarrow e\nu\bar{\nu})/\Gamma(\tau \rightarrow \mu\nu\bar{\nu})$ (1σ) [41];
- c:** $\Gamma(\tau \rightarrow \mu\nu\bar{\nu})/\Gamma(\mu \rightarrow e\nu\bar{\nu})$ (1σ) [41];
- d:** K^+ -decay (90% CL) [43];
- e:** Atomic parity violation and eD asymmetry (1σ) [41];
- f:** t -decay (2σ) [43];
- g:** ν_μ deep-inelastic scattering (2σ) [41];
- h:** Z decay width (1σ) [45];
- i:** ν_e mass (1σ) [37];
- j:** double β -decay [65];
- k:** $n-\bar{n}$ oscillation (1σ) [35];
- l:** double nucleon decay (1σ) [35];
- m:** constrained from the requirement of perturbative unitarity [35];
- n:** Z decay width (1σ) [46];
- o:** $D^0-\bar{D}^0$ mixing [43];
- p:** $e-\mu-\tau$ universality *e.g.* $\Gamma(\pi \rightarrow e\nu)/\Gamma(\pi \rightarrow \mu\nu)$ [41];
- r:** $\text{BR}(D^+ \rightarrow K^0\mu^+\nu)/\text{BR}(D^+ \rightarrow K^0e^+\nu)$;
- s:** $\text{BR}(\tau \rightarrow \pi\nu)$ [44].

Table 1.2: Upper bounds on \mathcal{R}_p coupling for $\tilde{m} = 100$ GeV. [66, 67, 68, 69]

1.5.4 Neutrinoless double beta decay

It is known for a long time that neutrinoless double beta decay ($\beta\beta_{0\nu}$) is a sensitive probe of lepton-number-violating processes. In R -parity-violating scenario, the process $dd \rightarrow uue^-e^-$ is mediated by \tilde{e} and $\tilde{\gamma}$ or by \tilde{q} and \tilde{g} , yielding $\lambda'_{111} \leq 10^{-4}$ [38, 39]. Recently, a new bound on the product coupling $\lambda'_{113}\lambda'_{131} \leq 3 \times 10^{-8}$ has been placed from the consideration of the diagrams involving the exchange of one W boson and one scalar boson [40].

1.5.5 Charged-current universality

Universality of the lepton and quark couplings to the W -boson is violated by the presence of λ - and λ' -type couplings. The scalar-mediated new interactions have the same $(V - A) \otimes (V - A)$ structure as the W -exchanged diagram. The experimental value of V_{ud} is related to V_{ud}^{SM} by

$$|V_{ud}^{\text{exp}}|^2 \simeq |V_{ud}^{\text{SM}}|^2 \left[1 + \frac{2r'_{11k}(\tilde{d}_R^k)}{V_{ud}} - 2r_{12k}(\tilde{e}_R^k) \right], \quad (1.14)$$

where,

$$r_{ijk}(\tilde{l}) = (M_W^2/g^2)(\lambda_{ijk}^2/m_{\tilde{l}}^2). \quad (1.15)$$

r'_{ijk} is defined using λ'_{ijk} analogously as r_{ijk} . Assuming the presence of only one R -parity-violating coupling at a time, one obtains, for a common $\tilde{m} = 100$ GeV, $\lambda_{12k} \leq 0.04$ (1σ) and $\lambda'_{11k} \leq 0.03$ (2σ), for each k [41].

1.5.6 $e-\mu-\tau$ universality

The ratio $R_\pi \equiv \Gamma(\pi \rightarrow e\nu)/\Gamma(\pi \rightarrow \mu\nu)$, in the presence of λ' -type interaction takes the form

$$R_\pi = R_\pi^{\text{SM}} \left[1 + \frac{2}{V_{ud}} \left\{ r'_{11k}(\tilde{d}_R^k) - r'_{21k}(\tilde{d}_R^k) \right\} \right]. \quad (1.16)$$

A comparison with experimental results yields, for a common mass $\tilde{m} = 100$ GeV and at 1σ , $\lambda'_{11k} \leq 0.05$ and $\lambda'_{21k} \leq 0.09$, for each k , assuming only one coupling at a time [41].

Similarly, from the consideration of $R_\tau \equiv \Gamma(\tau \rightarrow e\nu\bar{\nu})/\Gamma(\tau \rightarrow \mu\nu\bar{\nu})$, one obtains, $\lambda_{13k} \leq 0.10$ and $\lambda_{23k} \leq 0.12$, for each k , at 1σ and for $\tilde{m} = 100$ GeV [41].

1.5.7 $\nu_\mu-e$ scattering

The neutrino-electron scattering cross section at low energies are given by

$$\begin{aligned} \sigma(\nu_\mu e) &= \frac{G_F^2 s}{\pi} (g_L^2 + \frac{1}{3}g_R^2), \\ \sigma(\bar{\nu}_\mu e) &= \frac{G_F^2 s}{\pi} (\frac{1}{3}g_L^2 + g_R^2); \end{aligned} \quad (1.17)$$

where in the presence of R -parity-violating interactions ($x_W \equiv \sin^2 \theta_W$)

$$\begin{aligned}
g_L &= x_W - \frac{1}{2} - \left(\frac{1}{2} + x_W\right)r_{12k}(\tilde{e}_R^k), \\
g_R &= x_W + r_{121}(\tilde{e}_L^1) + r_{231}(\tilde{e}_L^3) \\
&\quad - x_W r_{12k}(\tilde{e}_R^k).
\end{aligned} \tag{1.18}$$

The derived constraints (at 1σ) are $\lambda_{12k} \leq 0.34$, $\lambda_{121} \leq 0.29$ and $\lambda_{231} \leq 0.26$ for $\tilde{m} = 100$ GeV [41].

1.5.8 Atomic parity violation

The parity-violating part of the Hamiltonian of the electron-hadron interaction is

$$H = \frac{G_F}{\sqrt{2}} (C_{1i} \bar{e} \gamma_\mu \gamma_5 e \bar{q}_i \gamma_\mu q_i + C_{2i} \bar{e} \gamma_\mu e \bar{q}_i \gamma_\mu \gamma_5 q_i), \tag{1.19}$$

where, i runs over the u - and d -quarks. For the definitions of the C_i 's in the SM, see any Review of Particle Properties (e.g., ref.[42]). The R -parity violating contributions are ($\Delta C \equiv C - C^{\text{SM}}$),

$$\begin{aligned}
\Delta C_1^u &= -r'_{11k}(\tilde{d}_R^k) + \left(\frac{1}{2} - \frac{4}{3}x_W\right)r_{12k}(\tilde{e}_R^k), \\
\Delta C_2^u &= -r'_{11k}(\tilde{d}_R^k) + \left(\frac{1}{2} - 2x_W\right)r_{12k}(\tilde{e}_R^k), \\
\Delta C_1^d &= r'_{1j1}(\tilde{q}_L^j) - \left(\frac{1}{2} - \frac{2}{3}x_W\right)r_{12k}(\tilde{e}_R^k), \\
\Delta C_2^d &= -r'_{1j1}(\tilde{q}_L^j) - \left(\frac{1}{2} - 2x_W\right)r_{12k}(\tilde{e}_R^k).
\end{aligned} \tag{1.20}$$

Including the effects of radiative corrections, the 1σ bounds are $\lambda'_{11k} \leq 0.30$, $\lambda'_{1j1} \leq 0.26$ for $\tilde{m} = 100$ GeV [41]. Bounds on λ_{12k} are much weaker than those obtained from charged-current universality.

1.5.9 ν_μ deep-inelastic scattering

The left- and the right-handed couplings of the d -quark in neutrino interactions are modified by the R -parity-violating couplings as

$$\begin{aligned}
g_L^d &= \left(-\frac{1}{2} + \frac{1}{3}x_W\right)(1 - r_{12k}(\tilde{e}_R^k)) - r'_{21k}(\tilde{d}_R^k), \\
g_R^d &= \frac{1}{3}x_W + r'_{2j1}(\tilde{d}_L^j) - \frac{1}{3}x_W r_{12k}(\tilde{e}_R^k).
\end{aligned} \tag{1.21}$$

The derived limits, for $\tilde{m} = 100$ GeV, are $\lambda'_{21k} \leq 0.11$ (1σ) and $\lambda'_{2j1} \leq 0.22$ (2σ) [41].

1.5.10 K^+ -decays

Consideration of only one non-zero R -parity-violating coupling with indices related to the weak basis of fermions, automatically generates more than one non-zero coupling with different flavour structure in the mass basis. Consequently, flavour-changing-neutral-current processes are naturally induced. The Lagrangian governing $K^+ \rightarrow \pi^+ \nu \bar{\nu}$ is given by

$$L = -\frac{\lambda_{ijk}^2}{2m_{\tilde{d}_R^k}} V_{j1} V_{j2}^* (\bar{s}_L \gamma^\mu d_L) (\bar{\nu}_{Li} \gamma_\mu \nu_{Li}), \quad (1.22)$$

where V is the CKM matrix. The SM contribution is an order of magnitude lower than the experimental limit. Assuming that the new interaction dominates, one obtains, from the ratio of the $\Gamma(K^+ \rightarrow \pi^+ \nu_i \bar{\nu}_i)$ to $\Gamma(K^+ \rightarrow \pi^0 \nu \bar{\nu})$, the constraint $\lambda_{ijk}' \leq 0.012$ (90% CL), for $m_{\tilde{d}_R^k} = 100$ GeV and for $j = 1$ and 2 [43].

1.5.11 τ -decays

The decay $\tau^- \rightarrow \bar{u} d \nu_\tau$ proceeds in the SM by a tree-level W -exchanged graph. The scalar-exchanged graph induced by λ'_{31k} can be written in the same $(V - A) \otimes (V - A)$ form by a Fierz rearrangement. Using the experimental input

$$\begin{aligned} Br(\tau^- \rightarrow \pi^- \nu_\tau) &= 0.117 \pm 0.004, \\ f_\pi &= (130.7 \pm 0.1 \pm 0.36) \text{ MeV}. \end{aligned} \quad (1.23)$$

one obtains $\lambda'_{31k} \leq 0.16$ (1σ) for $m_{\tilde{d}_R^k} = 100$ GeV [44].

1.5.12 D -decays

The tree-level process $c \rightarrow s e^+ \nu_e$ is mediated by a W exchange in the SM and by a scalar boson exchange in λ' -induced interaction. By a Fierz transformation it is possible to write the latter in the same $(V - A) \otimes (V - A)$ form as the former. Using the experimental input [42]:

$$\frac{Br(D^+ \rightarrow \bar{K}^{0*} \mu^+ \nu_\mu)}{Br(D^+ \rightarrow \bar{K}^{0*} e^+ \nu_e)} = 0.94 \pm 0.16, \quad (1.24)$$

one obtains, at 1σ , $\lambda'_{12k} \leq 0.29$ and $\lambda'_{22k} \leq 0.18$, for $m_{\tilde{q}} = 100$ GeV [44]. The form factors associated with the hadronic matrix elements cancel in the ratios, thus making the prediction free from the large theoretical uncertainties associated with those matrix elements.

1.6 Results of R-parity violation searches

The pioneering experimental search for R-parity violation has been done by the H1 Collaboration on ep data recorded at HERA [47]. Direct production of squarks of each generation by e^+ - quark fusion via a Yukawa coupling λ' was considered. Multi-lepton and multi-jet final states were studied. At 95 % CL, and for the first generation squarks masses up to 240 GeV were excluded for coupling values $\lambda' > \sqrt{4\pi\alpha_{em}}$.

1.6.1 KARMEN anomaly

A light photino has been invoked to explain the Karmen time anomaly [48]. This anomaly is a distortion in the observed time spectrum of neutrino induced events from $\bar{\nu}_\mu$ and ν_e from μ^+ decay at rest. This could be explained by a rare decay of $\pi^+ \rightarrow \mu^+ + X$ ($m_X = 33.9 \text{ MeV}/c^2$) with a small branching ratio in the range $10^{-16} - 10^{-8}$ depending of the lifetime of X . In [49], a supersymmetric solution was considered. The X particle was interpreted as a photino (or zino) and the anomalous pion decay $\pi^+ \rightarrow \mu^+ + \textit{photino}$ was assumed to proceed via the R-parity violating λ'_{211} . The same operator then enables the photino to decay radiatively as $\textit{photino} \rightarrow \gamma + \nu_\mu$ via a one-loop diagram with a d quark and a \bar{d} squark in the loop. This two body decay of the X particle seems disfavoured by the new KARMEN data [50]. Therefore a 3-body decay for such a light photino (neutralino) has been considered [51]. In this scenario one has to invoke 2 non-zero R-parity violating operators. The pion decay $\pi^+ \rightarrow \mu^+ + \tilde{\chi}_1^0$ proceeds through λ'_{211} . The neutralino is assumed to decay as $\tilde{\chi}_1^0 \rightarrow e^+e^-\nu_\mu$ (or ν_τ) through either λ_{121} or λ_{131} . This scenario is not ruled out by other experiments, but as KARMEN acquires only of the order of 10 anomaly events per year, definitive resolution of the problem needs increased statistic.

1.6.2 LEP1

In the R-parity-violating scenario, the LSP is unstable. The OPAL Collaboration at LEP [54] have assumed the photino to be the LSP's decaying *via* a λ_{123} -type coupling. They excluded at 95% C.L. $m_{\tilde{\gamma}} = 4\text{--}43 \text{ GeV}$ for $m_{\tilde{e}_L} < 42 \text{ GeV}$, and $m_{\tilde{\gamma}} = 7\text{--}30 \text{ GeV}$ for $m_{\tilde{e}_L} < 100 \text{ GeV}$.

The ALEPH Collaboration at LEP [55], dealing with a more general λ -type coupling and considering a general LSP rather than a pure photino, have updated the above exclusion zone and have also reported their negative results on other supersymmetric particles up to their kinematic limit ($< M_Z/2$).

A lighter photino ($\sim 2\text{--}3 \text{ GeV}$) in conjunction with a R-parity-violating coupling provides a new semileptonic B -decay mode ($b \rightarrow ce\tilde{\gamma}$). Arranging such that the photino does not decay within the detector, the above channel adds incoherently to the standard semileptonic decay mode. However, the new mode, owing to the massive nature of the photino, arranges a different kinematic configuration compared to the standard channel where neutrino carries the missing energy. A kinematic exploration of the above has been carried out in the context of LEP and CLEO [56].

1.6.3 LEP2

Limits on the couplings

Single gaugino production through λ_{121} and λ_{131} couplings has been studied by DELPHI at LEP2 for several ECM energies (161, 172, 183, 189, 192, 202, 204 and 209 GeV). Such production proceeds through resonant production of a $\tilde{\nu}_\mu$ (λ_{121} coupling) or $\tilde{\nu}_\tau$ (λ_{131} coupling) or via exchange of a selectron or a sneutrino in the t channel. Cross section is (in first order) proportional to λ_{1j1}^2 and allows to obtain limit of the coupling as a function

of the sneutrino mass. Figure 1.10 shows an example (λ_{121} , $\tan\beta = 30$) and demonstrates the improvement one gets compared to indirect determination [28].

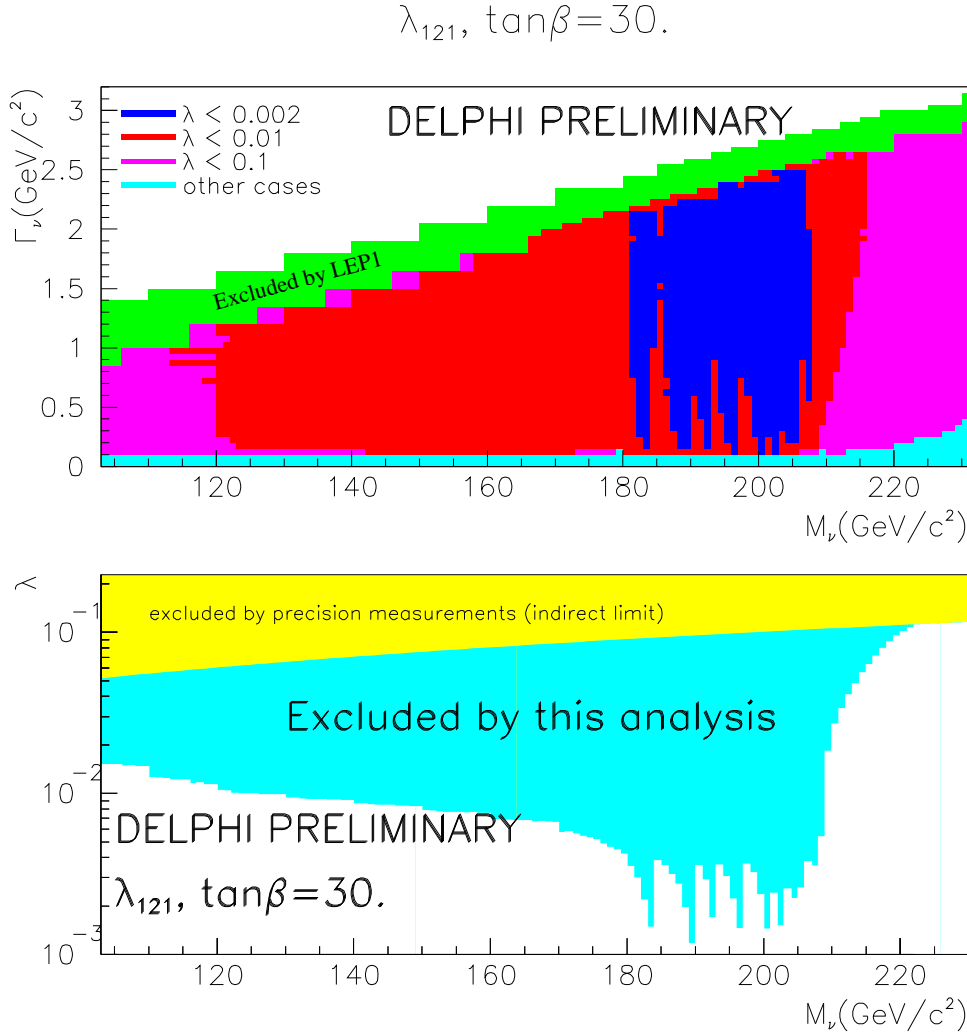


Figure 1.10: For $\tan\beta = 30$, upper limit on λ_{121} as a function of $M_{\tilde{\nu}}$ and $\Gamma_{\tilde{\nu}}$ (top) and as a function of $M_{\tilde{\nu}}$ and assuming $\Gamma_{\tilde{\nu}} > 150 \text{ MeV}/c^2$ (bottom). The indirect limit coming from precision measurements is given assuming $M_{\tilde{e}_R} = M_{\tilde{\nu}}$ [28].

Single Sneutrino production $e\gamma \rightarrow \tilde{\nu}_j$ via λ_{ijk} coupling has been studied by ALEPH. The virtual γ is emitted by one of the incoming electron. The sneutrino can decay directly $\tilde{\nu}_j \rightarrow el$, or if the neutralino mass limit is lower than that of the sneutrino, indirectly via the lightest neutralino, $\tilde{\nu}_j \rightarrow \nu\tilde{\chi}_1^0$ followed by its \tilde{R}_p decay. The cross section depends on the assumed value of λ , the mass of the sneutrino, the mass of the lepton produced in association with the sneutrino and the center of mass energy. Limits on seven out of the nine possible λ couplings as a function of the sneutrino mass can be put by studying such production [29].

In the case of λ_{121} or λ_{131} the resonant production is the process which provides the more stringent limits.

Limits on the masses

The four LEP experiments have put stringent 95 % CL limits on the gauginos masses [30].

For λ_{ijk} coupling the limits are:

particle	95 % CL mass limit, GeV/c ²	experiment
$\tilde{\chi}_1^0$	40.2	L3
	39.5	DELPHI
$\tilde{\chi}_2^0$	84	L3
$\tilde{\chi}_3^0$	107.2	L3
$\tilde{\chi}_4^0$	103	ALEPH
	103	DELPHI
	103	L3

The "highest" lower mass limits are :

particle	95 % CL mass limit, GeV/c ²	experiment
\tilde{e}_R	96	ALEPH
\tilde{e}_L	96	ALEPH
$\tilde{\tau}_R$	95	ALEPH
$\tilde{\tau}_L$	74	OPAL
$\tilde{\nu}_e$	100	ALEPH
$\tilde{\nu}_\mu$	90	ALEPH
$\tilde{\nu}_\tau$	89	ALEPH
\tilde{t}_L	92	DELPHI
\tilde{b}_L	90	ALEPH

1.6.4 Fermilab Tevatron

The impact of the λ' -type couplings in t -quark decay at the Tevatron have been analysed in ref. [43]. One of the consequences is the following: In the SM, the dominant decay mode is $t \rightarrow bW$. The λ'_{3k} -type couplings will induce $t_L \rightarrow \tilde{l}_i^+ d_{Rk}$ (if kinematically allowed), followed by $\tilde{l}_i^+ \rightarrow l^+ \tilde{\chi}^0$ (100%) and $\tilde{\chi}^0 \rightarrow (\nu_i + b + \bar{d}_k, \bar{\nu}_i + \bar{b} + d_k)$ leading to final states with at one lepton, at least one b -quark and missing E_T . The characteristic features of this decay channel are that it spoils the lepton universality in the top decay and for $k = 3$ produces additional b -quark events.

Strategies of setting squark and gluino mass limits from multilepton final states in the absence of R -parity-conservation have been discussed in [58].

The DØ experiment has searched R -parity violating SUSY in events with a tri-lepton signature as it is performed in this thesis [76]. A large domain of mSUGRA parameter space has been excluded for λ_{121} and λ_{122} , in the hypothesis they are greater than 10^{-4} (see Figure 7.5 of this thesis).

DØ has also conducted analysis with λ' couplings in Run I data. One was done by studying events with at least two electrons and four or more jets [59]. Two events were observed, consistent with the expected background of 1.8 ± 0.4 events. This result has been interpreted within the framework of minimal low-energy supergravity supersymmetry

models. For $A_0 = 0$, $\mu < 0$, $\tan\beta = 2$ and for any of the six R-parity violating couplings λ'_{1jk} ($j = 1, 2$ and $k = 1, 2, 3$). Squarks with mass below $243 \text{ GeV}/c^2$ and gluinos with mass below $227 \text{ GeV}/c^2$ have been excluded at the 95 % CL.

Another $D\bar{O}$ analysis but with muons (λ'_{2jk}) has also excluded a large domain of the parameter space [60]. For $\tan\beta = 2$, squark mass below $240 \text{ GeV}/c^2$ and gluino mass below $240 \text{ GeV}/c^2$ have been excluded.

$D\bar{O}$ has also searched for resonant production of smuons or muon sneutrinos in Run I data. Assuming that R-parity is violated via the single coupling λ'_{211} , exclusion contours have been established in the m_0 - $m_{1/2}$ plane for $\lambda'_{211} = 0.09, 0.08$ and 0.07 [128, 61].

The CDF experiment has also searched for like-sign di-electron plus multi-jet events in their Run I data. Finding no events that pass their selection they set limits on $\sigma \times BR$ on two SUSY processes that can produce this experimental signature: gluino-gluino or squark-antisquark production via R-parity violating decays of the c quark or lightest neutralino via non-zero λ'_{121} coupling [62].

Prospective studies concerning the possible discovery of supersymmetry with broken R-parity at Run II of the Tevatron have been conducted in a Run II workshop and the written report is an inspiring guide for any analysis [63].

1.6.5 Perspectives for the LHC

Most of the studies for LHC have been done in the mSUGRA model with the lightest neutralino ($\tilde{\chi}_1^0$) forced to decay to the appropriate quark-lepton combination [64].

For λ coupling the number of leptons in the final state allows to reduce the Standard Model background. For the lightest neutralino decays involving only leptons of the first two generations, the invariant mass of the lepton combinations make it possible to perform a direct reconstruction of some supersymmetric decay chains with good precision. In this case, it appears that the SUGRA parameters are constrained with higher precision than in the R-parity conserving case.

The λ'' coupling studies, have shown that $\tilde{\chi}_1^0$ mass reconstruction seems possible using standard jet algorithms.

The λ' coupling case is intermediate between the two previously considered. If $\tilde{\chi}_1^0$ decay involves a lepton from the first two generations, studies have shown that SUSY could be easily discovered.

1.7 Summary

The fundamental constituents of matter are described by the Standard Model (SM), a theory that has been used with great success to explain the sub-atomic and sub-nuclear regime. Although there has been no experiment that conclusively disputes the Standard Model, the theory has some internal problems and cannot predict some basic, fundamental parameters of nature. Thus, many believe that the SM is not a final theory but is part of some theory of nature at higher scale. Supersymmetry theories (SUSY) are such extensions to the SM. SUSY predicts that there should be more than twice particles than in the SM, and so many experiments have been performed to look for these "sparticles".

Although it eliminates a nagging problem with the SM, SUSY alone is also a complicated theory with more than one hundred free parameters. Therefore, many types of models have been introduced to make SUSY tractable. One such model is Minimal Supergravity (mSUGRA) that only has four free parameters and a free sign. The mSUGRA framework will be used in the present search.

Chapter 2

Tevatron and DØ detector

The DØ experiment studies the products of the proton-antiproton annihilation using the Tevatron collider, located at Fermilab in Batavia, Illinois, USA. This experiment has already taken data at 1.8 TeV in 1991–95 and together with the CDF experiment has discovered top quark in 1995. [2] Tevatron and both DØ and CDF experiments have been upgraded. New period of data taking called Run II has started in April 2001. This chapter briefly describes the technical details of the Tevatron collider and the DØ detector after the upgrade with emphasis on calorimetry and tracking.

2.1 Accelerator

The Tevatron is a $p\bar{p}$ -collider that accelerates both the protons and antiprotons to an energy of 1 TeV, providing a center-of-mass energy of 1.96 TeV. Until the Large Hadron Collider at CERN [78] starts in 2007, the Tevatron will be the highest energy collider in the world. As for all high-energy accelerators, the Tevatron is only the last one in a long chain schematically shown in Figure 2.1.

The proton beam originates in the pre-accelerator, where negatively charged hydrogen ions are accelerated to 750 keV in a Cockroft-Walton accelerator. From there, the hydrogen ions are bunched and led into a 150 meter long linear accelerator (LINAC), which accelerates the ions to an energy of 400 MeV, after which the ions are led through a carbon foil. This foil strips both the electrons from the hydrogen nucleus, leaving the proton. The protons are then led into a circular accelerator, called the booster, in which they are accelerated to an energy of 8 GeV. After this stage, they enter the main injector. This circular accelerator serves multiple purposes:

- It accelerates protons from 8 GeV to 150 GeV for insertion in the Tevatron;
- It accelerates protons from 8 GeV to 120 GeV for the production of anti-protons;
- It accelerates anti-protons to an energy of 150 GeV for injection in the Tevatron.

The anti-protons are produced by colliding the protons that have been accelerated in the Main Injector to an energy of 120 GeV, on a nickel target. These collisions produce many secondary particles, among which are anti-protons, approximately one for every

	Run IB	Run II (Main Injector)	Run II (Main Inj. & Recycler)
Protons/bunch	2.32×10^{11}	3.30×10^{11}	2.70×10^{11}
Antiprotons/bunch	5.50×10^{10}	3.60×10^{10}	5.50×10^{10}
Total Antiprotons	3.30×10^{11}	1.30×10^{12}	1.98×10^{12}
Energy GeV	900	1000	1000
Bunches	6+6	36+36	36+36
Bunch length (rms) m	0.60	0.43	0.18
Typical Luminosity ($\text{cm}^{-2}\text{sec}^{-1}$)	1.6×10^{31}	8.3×10^{31}	2.0×10^{32}
Integrated Luminosity* ($\text{pb}^{-1}/\text{week}$)	3.2	16.7	41.0
Bunch Spacing nsec	3500	396	396
Interactions/crossing (@ 45 mb)	2.5	2.2	5.3

* Typical Luminosity at the beginning of a store—translates to integrated luminosity with a 33% duty factor.

Table 2.1: Parameters of the Tevatron

105 protons. The anti-protons produced are temporarily stored in a circular ring, the Accumulator. When enough anti-protons have been produced to fill the Tevatron ($\sim 10^{11}$ anti-protons), they are assembled, bunched and inserted in the Main Injector to be accelerated to an energy of 150 GeV. The tunnel of the Main Injector also holds the Antiproton Recycler, which is not currently operational. It is designed to decelerate the anti-protons coming from the previous run in the Tevatron and to store them for future use. The recycler will be incorporated into the Main injector project and this will allow to increase the instantaneous luminosity up to $2.0 \cdot 10^{32} \text{ cm}^{-2}\text{sec}^{-1}$ as shown in Table 2.1 [79]. As an added benefit, the Recycler will also allow the existing Antiproton Source to perform more efficiently and produce more antiprotons per hour.

After acceleration of the protons and anti-protons in the Main Injector to an energy of 150 GeV, both beams are inserted in the Tevatron, where they are further accelerated to 1 TeV. The Tevatron uses superconducting magnets with a field strength of 4.2 Tesla to bend the protons and anti-protons through the 1000-meter radius tunnel. The proton beam traverses the Tevatron clockwise, with the antiproton beam moving in the opposite direction. The beams meet at the two interaction points at B0, where CDF is located, and DØ, delivering a peak luminosity of $10^{31} \text{ cm}^{-2}\text{s}^{-1}$. The luminosity measurement at DØ is discussed in the section 3.2. Along the beam, the vertex of the interaction has a Gaussian distribution around the center of the DØ detector with a width of about 25 cm. Some parameters for the Tevatron for Runs I and II with and without "Recycler" are shown in Table 2.1.

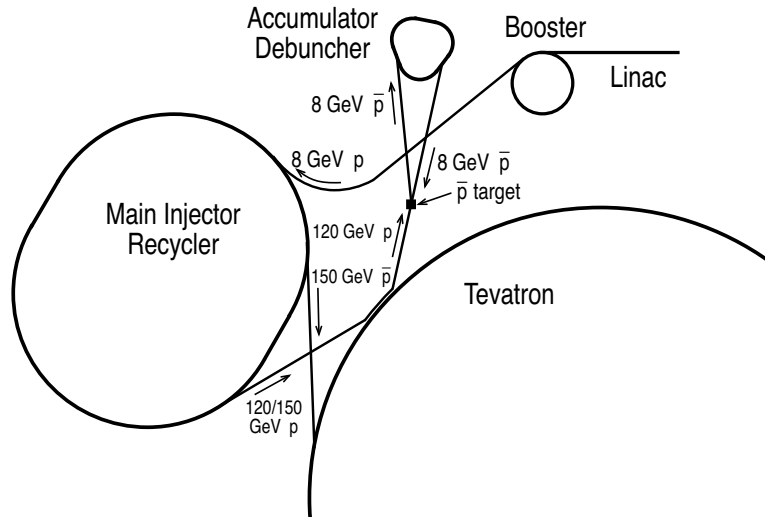


Figure 2.1: The Fermilab accelerator chain.

2.2 DØ detector

The DØ detector [88] consists of four major systems: the tracking system, the preshower detectors, the calorimeters, and the muon system.

2.3 Coordinate system and kinematic quantities

Before describing the DØ detector it is useful to define the coordinate system and angle convention used in the experiment. In DØ a right handed coordinate system is used, with the direction of the proton beam as the positive z axis and the y axis pointing up. The angular coordinates are defined such that $\varphi = 0$ coincides with the $+x$ direction and $\theta = 0$ with the $+z$ direction. In place of θ it is convenient to use the pseudorapidity η defined as

$$\eta = -\ln \tan \frac{\theta}{2} \quad (2.1)$$

The pseudorapidity approximates the true rapidity,

$$y = \frac{1}{2} \ln \frac{E + p_z}{E - p_z} \quad (2.2)$$

in the limit $m/E \rightarrow 0$ where m is the rest mass of the particle.

In $p\bar{p}$ collider, many products of the collision escape detection by going down the beam pipe, thus making the measurement of momentum or energy of the colliding partons impossible. However, as their transverse momenta (p_T) are negligible, one can apply conservation of momentum and energy in the transverse plane. The transverse energy, $E_T (= E \sin \theta)$ and $\cancel{E}_T = |\sum_i \vec{p}_T^i|$, the missing transverse energy, are two quantities used extensively in the analyses of collider data.

2.4 Tracking system

The momenta of charged particles is determined from their curvature in the 2 T magnetic field provided by a 2.73 m long solenoid magnet. The superconducting solenoid, a two layer coil with mean radius of 60 cm, has a stored energy of 5 MJ. To ensure good field uniformity, the current density is larger at the ends of the coil. The thickness of the magnet system is approximately one radiation length.

The tracking system (Fig. 2.2) contained within the bore of the superconducting solenoid consists of an inner silicon microstrip tracker (SMT) [80], surrounded by a central scintillating fiber tracker (CFT) [81].

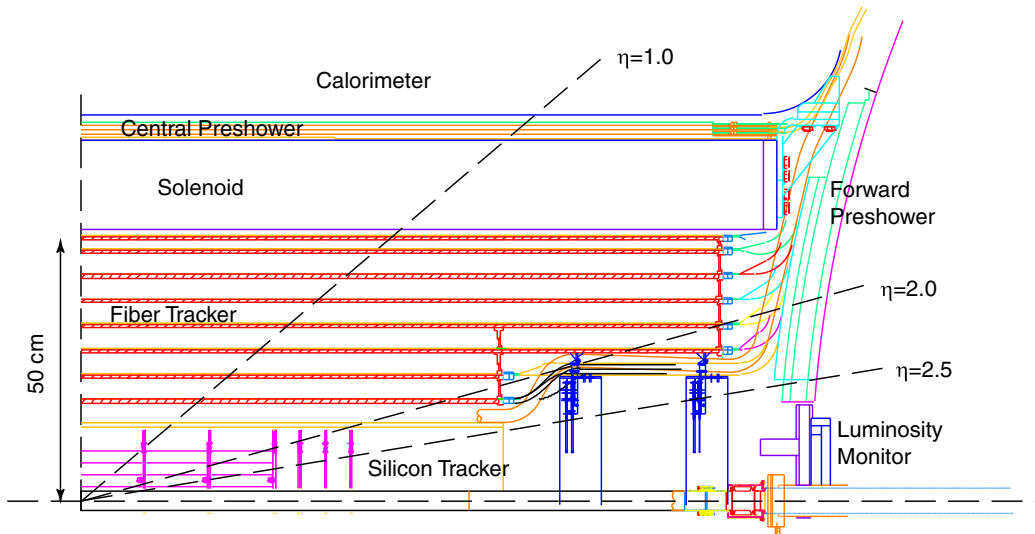


Figure 2.2: $r - z$ view of the DØ tracking system.

The tracking system has been designed to meet several goals: momentum measurement by the introduction of a solenoidal field; good electron identification and e/π rejection; tracking over a large range in pseudorapidity ($\eta \approx \pm 3$); secondary vertex measurement for identification of b -jets from Higgs and top decays and for b -physics; first level tracking trigger; fast detector response to enable operation with a future bunch crossing time of 132 ns; and radiation hardness.

2.4.1 Silicon Microstrip Tracker

The silicon tracking system is based on $50 \mu\text{m}$ pitch silicon microstrip detectors providing a spatial resolution of approximately $10 \mu\text{m}$ in $r \times \varphi$. The high resolution is important to obtain good momentum measurement and vertex reconstruction. The detector consists of a system of barrels and interleaved disks designed to provide good coverage out to $\eta \approx 3$ for all tracks emerging from the interaction region, which is distributed along the beam direction with $\sigma_z \approx 25 \text{ cm}$.

The barrel has 6 sections, each 12 cm long and containing 4 layers. The first and third layers of the inner 4 barrels are constructed of double-sided 90° -stereo detectors with axial

strips and orthogonal z strips at pitches of $50\ \mu\text{m}$ and $153.5\ \mu\text{m}$ respectively. The outer two barrels use single-sided detectors with $50\ \mu\text{m}$ pitch axial strips in layers 1 and 3. In all six barrels the second and fourth layers are made from double-sided detectors with axial and 2° stereo strips at $50\ \mu\text{m}$ and $62.5\ \mu\text{m}$ pitch respectively. The combination of small-angle and large-angle stereo provides good pattern recognition and allows good separation of primary vertices in multiple interaction events. The expected hit position resolution in $r\varphi$ is $10\ \mu\text{m}$, and for the 90° -stereo detectors it is about $40\ \mu\text{m}$ in z .

The forward disk system consists of double-sided detectors with $\pm 15^\circ$ stereo strips at $50\ \mu\text{m}$ and $62.5\ \mu\text{m}$ pitch. The H-disks, which cover the high- η regions, are constructed from two back-to-back single-sided detectors with $\pm 7^\circ$ stereo strips at $80\ \mu\text{m}$ pitch.

The detectors are mounted on beryllium bulkheads which serve as a support and provide cooling via water flow through beryllium tubes integrated into the bulkheads. The silicon tracker has a total of 793,000 channels. Figure 2.3 show a cross sectional view in the $r - \varphi$ plane of a barrel section.

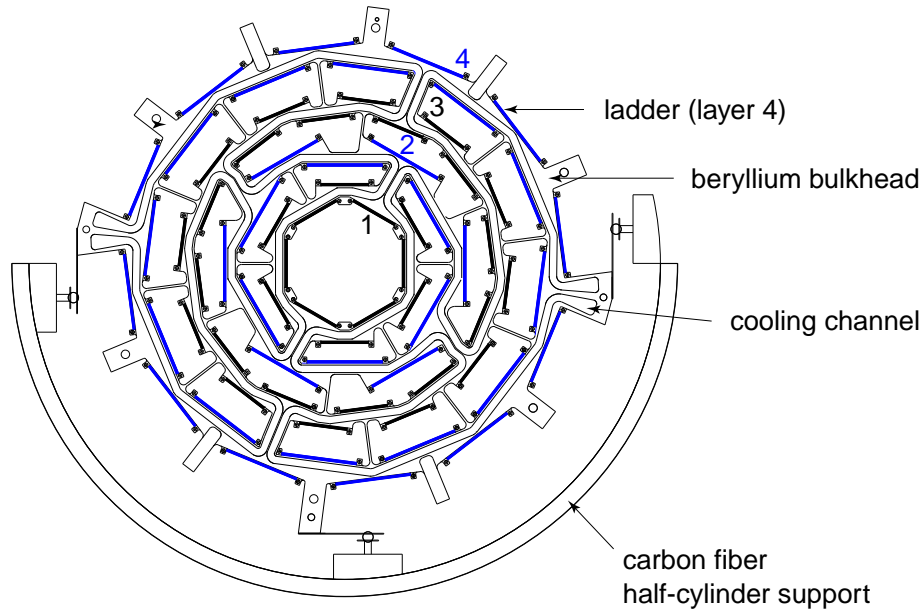


Figure 2.3: Cross sectional $r\varphi$ view of an SMT barrel.

2.4.2 Scintillating Fiber Tracker

The outer tracking in the central region is based on scintillating fiber technology with visible light photon counter (VLPC) readout [82]. The Central Fiber Tracker (CFT) consists of 8 layers, each containing 2 fiber doublets in a zu or zv configuration ($z =$ axial fibers and $u, v = \pm 3^\circ$ stereo fibers). Each doublet consists of two layers of $830\ \mu\text{m}$ diameter fibers with $870\ \mu\text{m}$ spacing, offset by half the fiber spacing. The fibers are supported on carbon fiber support cylinders. This configuration provides very good efficiency and pattern recognition and results in a position resolution of $\approx 100\ \mu\text{m}$ in $r\varphi$.

The fibers are up to 2.5 m long and the light is piped out by clear fibers of length 7-11 m to the VLPC's situated in a cryostat outside the tracking volume, which is maintained at

9 K. The VLPC's are solid state devices with a pixel size of 1 mm, matched to the fiber diameter. The fast risetime, high gain and excellent quantum efficiency of these devices makes them ideally suited to this application.

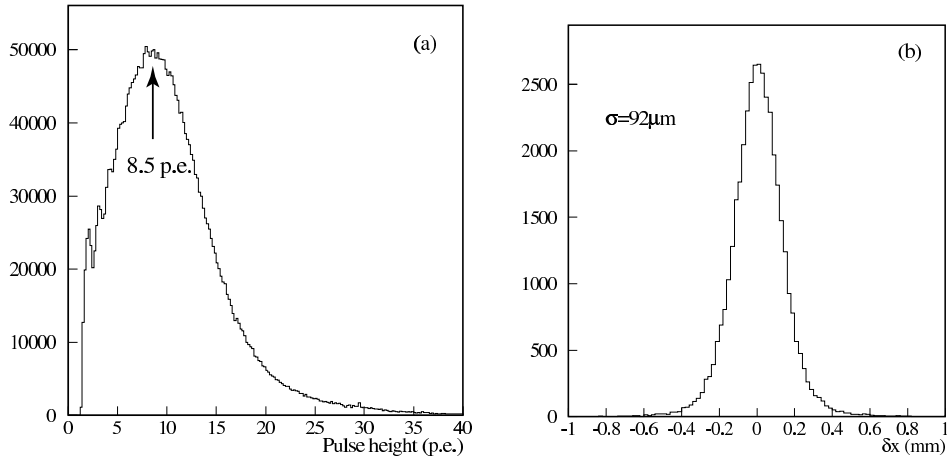


Figure 2.4: CFT cosmic ray test stand results: (a) photoelectron yield per fiber; (b) distribution of doublet residuals from fitted tracks.

The CFT has a total of about 77,000 channels. Since this technology is rather novel extensive testing has been done. This includes the characterization of thousands of channels of VLPC's and the setup of a cosmic ray test stand with fully instrumented fibers. The measured photoelectron yield, a key parameter of the system performance, was found to be 8.5 photoelectrons per fiber, with operation such that 99.5 % of the thermal noise was below a threshold of one photoelectron. This is well above the requirement of 2.5 photoelectrons needed for fully efficient tracking based on detailed GEANT simulations. The tracking efficiency measured in the cosmic ray stand is $\epsilon > 99.9 \%$. Figure 2.4 shows the pulse height distribution for cosmic ray muons [83]. Also shown is a histogram of the fitted track residuals, from which a fiber doublet resolution of $92 \mu\text{m}$ is determined.

2.5 Preshower detectors

The central and forward preshower detectors (CPS and FPS) provide fast energy and position measurements. The preradiator consists of 5.5 mm lead in the CPS and 11 mm of lead in the FPS (see Fig. 2.6).

2.5.1 Central preshower system

The central preshower detector (CPS) [84] is designed to aid electron identification and triggering and to correct electromagnetic energy for effects of the solenoid. The detector functions as a calorimeter by early energy sampling and as a tracker by providing precise position measurements. The cylindrical detector is placed in the 51 mm gap between the solenoid coil and the central calorimeter cryostat at a radius of 72 cm, and covers the

region $|\eta| < 1.2$. The detector consists of three layers of scintillating strips arranged in axial and stereo views with a wavelength-shifting (WLS) fiber readout. The stereo angles for the two stereo layers are $\approx \pm 23^\circ$. Wavelength shifting fibers are used to pipe the light out to a VLPC readout system. In front of the detector there is a lead absorber so the solenoid plus lead total about two radiation lengths of material for particle trajectories.

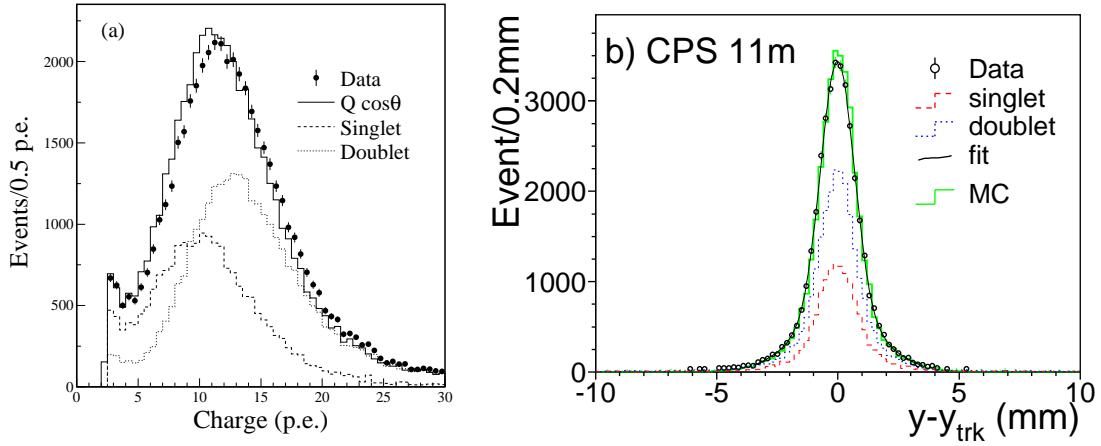


Figure 2.5: Preshower detector cosmic ray muon tests: (a) light yield (p.e. = photoelectrons); (b) fitted track residuals.

The position resolution for 10 GeV electrons is estimated from Monte Carlo to be < 1.4 mm. Cosmic ray tests have been performed to study the light yield and resolution [85]. Figure 2.5 shows some results. The light yield is shown in Fig. 2.5(a) together with the simulated yield for a cosmic ray muon passing through a “singlet” (i.e. a single layer of triangular strips) and a “doublet” (two layers of strips). The readout fiber in this setup was 11 m in length.

The triangular shape of the scintillator strips is a convenient configuration for reconstructing the position of a particle that passes through 2 strips. The distance traversed by the track in each strip has a linear correspondence to the incident position. The cluster position can therefore be calculated by using the charge-weighted mean of the strip centers.

Spatial resolution is investigated with respect to hit positions given by the PDT track and the residuals for the positions of preshower clusters relative to the PDT tracks are shown in Figure 2.5(b). The measured doublet position resolution for cosmic ray muons is $550 \mu\text{m}$.

2.5.2 Forward preshower system

The $D\phi$ forward preshower detector (FPS) [86], like its counterpart in the central region, is intended to enhance electron identification capability by making precision position measurements of particle trajectories using dE/dx and showering information collected just upstream of the calorimeter. Monte Carlo simulations have shown that substantial improvements in off-line electron identification and γ/π^0 separation can be expected when FPS information is appropriately applied [87].

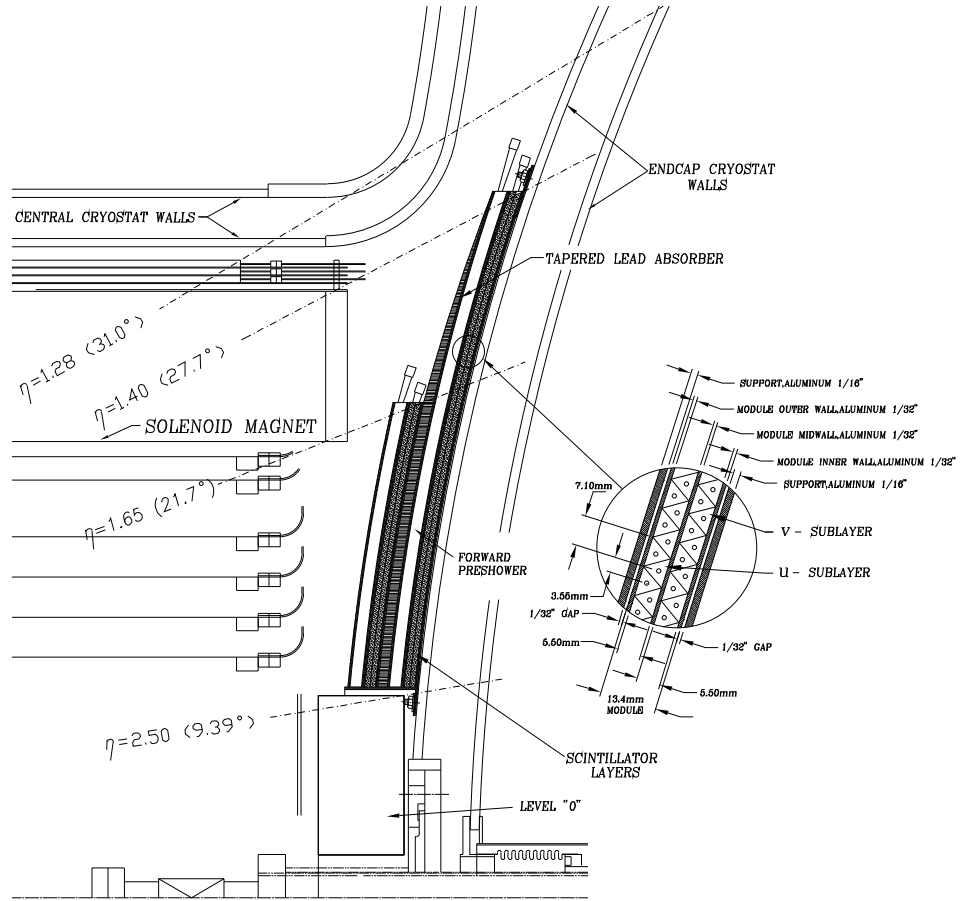


Figure 2.6: One quarter view of forward preshower detector, with detail of scintillator $u - v$ layer.

Two FPS detectors cover the pseudorapidity range $1.4 < |\eta| < 2.5$, with one detector mounted on the inner face of each of the end calorimeter (EC) cryostats (see Fig. 2.6). The detector consists of triangular scintillator strips with embedded wavelength-shifting fibers, read out by visible light photon counters (VLPC). The detector is composed of a layer of lead absorber of two radiation lengths thick sandwiched between two active scintillator planes, with each scintillator plane consisting of one u and one v sublayer.

Since particles traversing the magnet solenoid ($1.4 < |\eta| < 1.6$) are likely to shower upstream of the FPS, the mip-detecting scintillator (or inner) layer in front of the lead absorber is not needed in this pseudorapidity range. The inner (outer) scintillator layer, therefore, covers the pseudorapidity range $1.6 < |\eta| < 2.5$ ($1.4 < |\eta| < 2.5$). The lead consists of two radiation lengths in the high- η region, and is tapered in the region $1.4 < |\eta| < 1.6$ in order to equalize the amount of material traversed as a function of pseudorapidity.

DØ LIQUID ARGON CALORIMETER

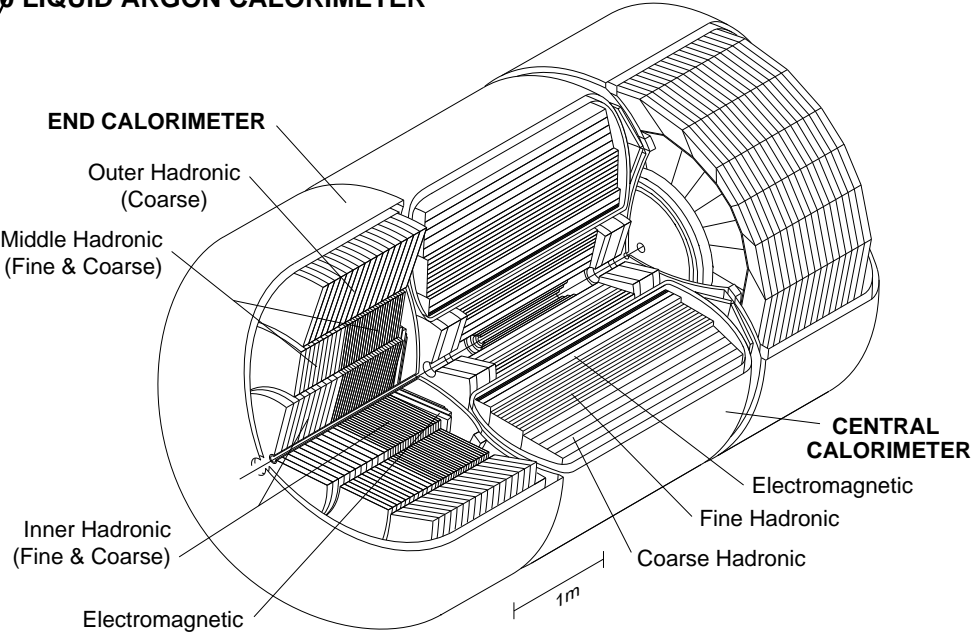


Figure 2.7: Cutaway view of the DØ calorimeter.

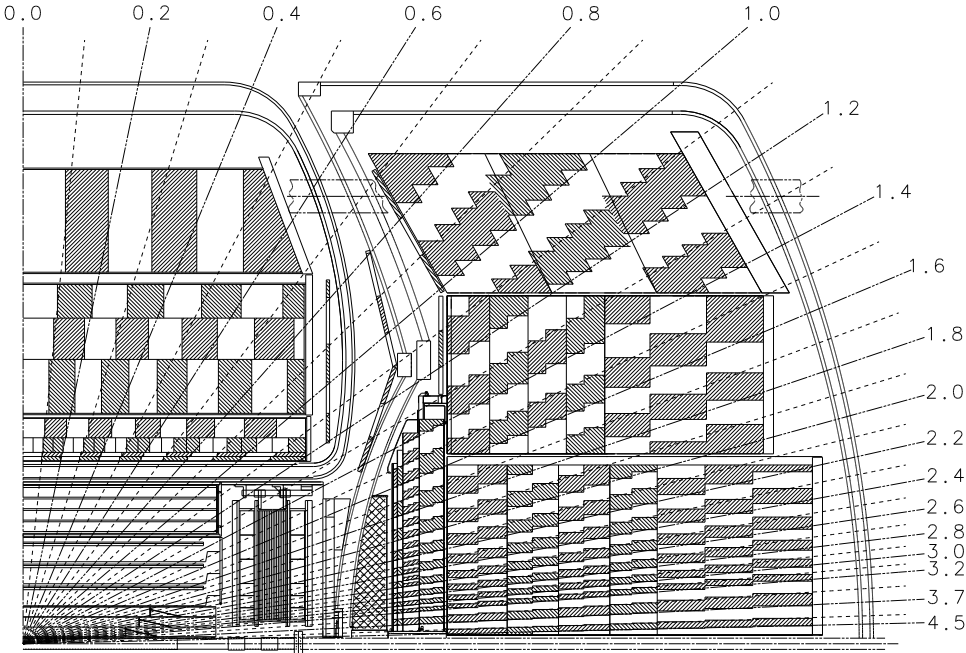


Figure 2.8: One quarter view of the calorimeter.

2.6 Calorimeter

The DØ calorimeters [88] have liquid argon as active medium to sample the ionisation produced in electromagnetic or hadronic showers. The primary absorber material is depleted uranium but in the outer layers stainless steel and copper are also used. There are three calorimeters of roughly equal size: the central calorimeter (CC) and two end calorimeters (EC). The design is shown schematically in Fig. 2.7.

The central calorimeter consists of three concentric cylindrical layers of modules. It is 226 cm long and radially it occupies the space $75 \text{ cm} < r < 222 \text{ cm}$ and covers up to $|\eta| < 1.2$. There are 32 *electromagnetic* (EM), 16 *fine hadronic* (FH) and 16 *coarse hadronic* (CH) modules in it. The transverse segmentation is 0.1×0.1 in $\eta \times \varphi$ space except in the third layer of the EM module where EM shower maximum is expected; the latter has a segmentation of 0.05×0.05 in $\eta \times \varphi$ space. The EM, FH and CH module boundaries are rotated to avoid continuous inter module crack.

Each of the two forward calorimeters has a ring of 16 outer hadronic modules; the next is a ring of 16 middle hadronic modules and in the center there is a single large inner hadronic module (ECIH). In front of the ECIH there is a finely segmented electromagnetic calorimeter (ECEM).

The end calorimeter provides coverage in the range $1.1 < |\eta| < 4.5$. The transverse segmentation is mostly 0.1×0.1 in $\eta \times \varphi$ space, but for $|\eta| > 3.2$ the segmentation is increased to 0.2×0.2 . As in the CC, here also third EM layer has finer segmentation with 0.05×0.05 for $|\eta| < 2.7$, 0.1×0.1 for $2.7 < |\eta| < 3.2$ and 0.2×0.2 for $|\eta| > 3.2$.

2.6.1 Calorimeter Electronics

The electronics receives a signal from a calorimeter cell which is proportional to the energy deposited by the particles passing through the active media. Coaxial cables carry the signal to a feed through port which allows to pass them across the cryostat. The feed through boards reorganize signal from the module builder's scheme to the physics scheme in which signals from all depths in the $\eta \times \varphi$ space are combined to quasi projective 0.1×0.1 towers delivered on two cables each containing 24 channels. The signal is then conducted to the charge sensitive preamplifiers. The preamplifiers integrate the pulse of current flowing from the calorimeter cells over time (by virtue of a small capacitance in the feedback loop) to produce an output which is proportional to the charge flowing into the preamplifier input. The preamplifier outputs go through 30 meters of cable to a baseline subtractor system (BLS) which shapes the signal and samples it before and after the bunch crossing.

The aim of the BLS is to subtract the signal baseline before an interaction from a signal just after it in order to get the exact signal amplitude. The sampled signal is stored in a switched capacitor array (SCA). The SCA resolution allows for a 12 bits dynamic range. In order to obtain a 15 bits range two shaped outputs are provided with $\times 1$ gain and $\times 8$ gain by the preamplifier. Following the Level 1 trigger decision the readout with the appropriate gain factor is digitized by an analog digital converter (ADC).

Figure 2.9 shows a schematic view of the electronics with the changes made for Run II in order to reduce electronics noise and dead time. The readout electronics of the DØ

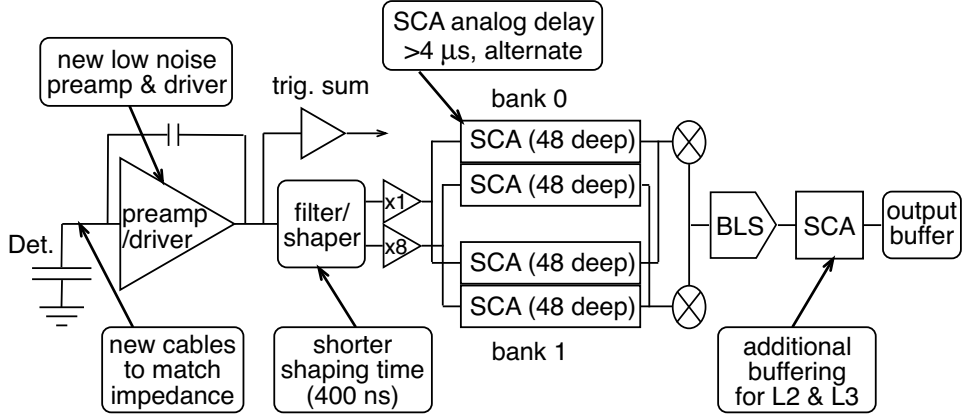


Figure 2.9: Schematic view of the electronics system for the DØ calorimeter at Run II. The added text corresponds to the modification performed after Run I.

calorimeter is composed by 12 crates containing 12 ADC cards. Each card contains 384 channels which are distributed on 8 BLS cards, each treating the signals of 4 Towers of 12 longitudinal depths. In order to calibrate the detector, the response of the different elements needs to be well known. The response before calibration is expected to differ from channel to channel at the level of a few percents.

2.6.2 Calibration of the Calorimeter Electronics

The calorimeter upgrade concerns only its electronics [89] and has been designed to operate reliably at the instantaneous luminosity of $2 \times 10^{32} \text{ cm}^{-2} \text{ s}^{-1}$ and the bunch crossing time of 132 ns. The two requirements of the upgrade are a reduction in shaping and readout time, and analog buffering needed to store data until the Level 1 or Level 2 trigger decisions are available. These tasks needs to be performed while maintaining the properties of low electronics noise, high linearity and good accuracy, i.e. small variations in channel-to-channel response.

The resolution of the calorimeter can be parametrized as

$$\left(\frac{\sigma_E}{E}\right)^2 = C^2 + \frac{S^2}{E} + \frac{N^2}{E^2}, \quad (2.3)$$

where C stands for the calibration errors, S – the sampling fluctuations and N – the Uranium and electronic noise. These values measured during DØ Run I for the electrons in the central calorimeter were:

$$\begin{aligned} C &= 0.003 \pm 0.002; \\ S &= 0.157 \pm 0.005 \text{ (GeV)}^{\frac{1}{2}}; \\ N &= 0.140 \text{ GeV}. \end{aligned}$$

These parameters are expected to be slightly worse for Run II due to the coil addition.

Based on a MC study [90] the present values of the parameters are:

$$\begin{aligned}
 C &= 0.004 \pm 0.002; \\
 S &= 0.23 \pm 0.10 \text{ (Gev)}^{\frac{1}{2}}; \\
 N &= 0.202 \pm 0.006 \text{ GeV}.
 \end{aligned}$$

In order to achieve good energy scale accuracy and resolution, it is essential that the calorimeter readout electronics is highly linear, stable and produces very little electronics noise. There energy calibration consists of two steps. The first one is the online calibration which is a study of a response to a well known injected calibration signal ("pulse"). The second one is the offline calibration which is obtained with physics events characterized by a known energy (for example the Z mass peak).

For the online calibration, a signal given by a pulser is introduced in the electronics chain. This can be done in two ways: either the signal is introduced inside the calorimeter on the reading cell (cold calibration), or it can be generated outside the cryostat just at the beginning of the electronics chain (warm calibration). The first method has the advantage of creating the calibration signal at the same place as a true particle but this method needs an access to the inside of the cryostat which was not foreseen when the detector was built and excludes any repairing in case of problem. Due to the problem of accessibility, the warm calibration has been chosen at $D\emptyset$.

In this case, it is not possible to generate a calibration signal which accurately mimics the physics signal. Moreover due to the reflection, the calibration signal is more sensitive than the physics signal to the cable length and the cell capacitance variations. It was shown however that the calibration can be much better than 1 % [91].

The calibration system of the $D\emptyset$ calorimeter consists of 12 identical subsystems. Each subsystem is composed of one pulser main board which sends the signal distribution, the commands and the DC currents to two cards called active fanouts. They are called active because in addition to perform the signal distribution, they generate the calibration pulse. The pulser main boards are connected to the pulser interface board (PIB) with which the controls of the amplitude and the signal calibration delay are done together with a selection of pulsed channels. The pulser main boards are composed of one serial bus interface, one channel enable register, one digital analog converter of 18 bits, six programmable delays and 96 DC current generators programmable by the DAC.

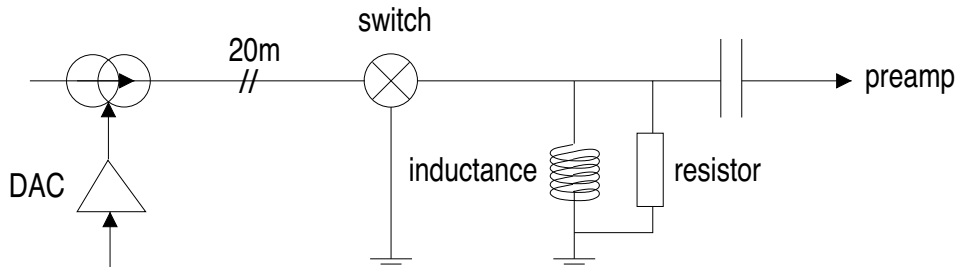


Figure 2.10: Schematic diagram of the measuring chain.

The active fanout is divided into three identical parts. Each part receives one command

signal and 16 DC currents. It schematically works as shown in Figure 2.10. An 18-bit DAC delivers a DC current (1 DAC unit = $0.825 \mu\text{A}$) to a 1 mH inductance. On a command signal whose arrival time is defined by a programmable delay (256 steps of $\approx 1.6 \text{ ns}$), a switch diverts the current from the generator to ground and the inductor releases the energy it stored to send a current to the resistor and it leads to an exponential signal at the preamplifier input (1 DAC unit = $11.5 \mu\text{V}$, 40 ns rising time, 450 ns decaying time [92]). This pulse is in turn distributed to 8 preamplifier cards where it reaches 6 channels per card. Thus, a minimum of 48 channels in the same preamplifier box may be pulsed at the same time.

On the reception of a trigger signal, three commands are sent to each of the two corresponding fanouts. The pulses generated by the active fanouts cards are near the preamplifiers. The shortness of the cable linking the active fanout to the preamplifier prevents losses and perturbations of the pulse. The conversion of the current to the calibration signal is performed on the "switch" cards which consists of an operational amplifier with a little shift register, a transistor and a resistor.

The calibration system has been designed and built by the LPNHE and Orsay laboratories from fall 1998 to fall 2000. It has been installed at DØ in october 2000 [93].

The calibration signal is a precise charge pulse of known value. The level of charge is ajustable to cover the electronics dynamic range. The signal, generated on active fanouts, can be sent to a set of preselected preamplifiers, which allow to conduct the following operations:

- cables and dead or bad channels test;
- determination of the electronics linearity;
- cross-talk study;
- the calorimeter cells intercalibration;
- correspondence of input voltage to ADC counts;
- readout chain non linearity [94].

2.7 The Muon Detector

The muon detector consists of three major parts, as is shown in Figure 2.11:

- Wide Angle MUon Spectrometer (WAMUS), covering $|\eta| < 1$;
- Forward Angle MUon Spectrometer (FAMUS), covering $1 < |\eta| < 2$;
- Solid-iron magnet creating a toroidal field of 1.8 T.

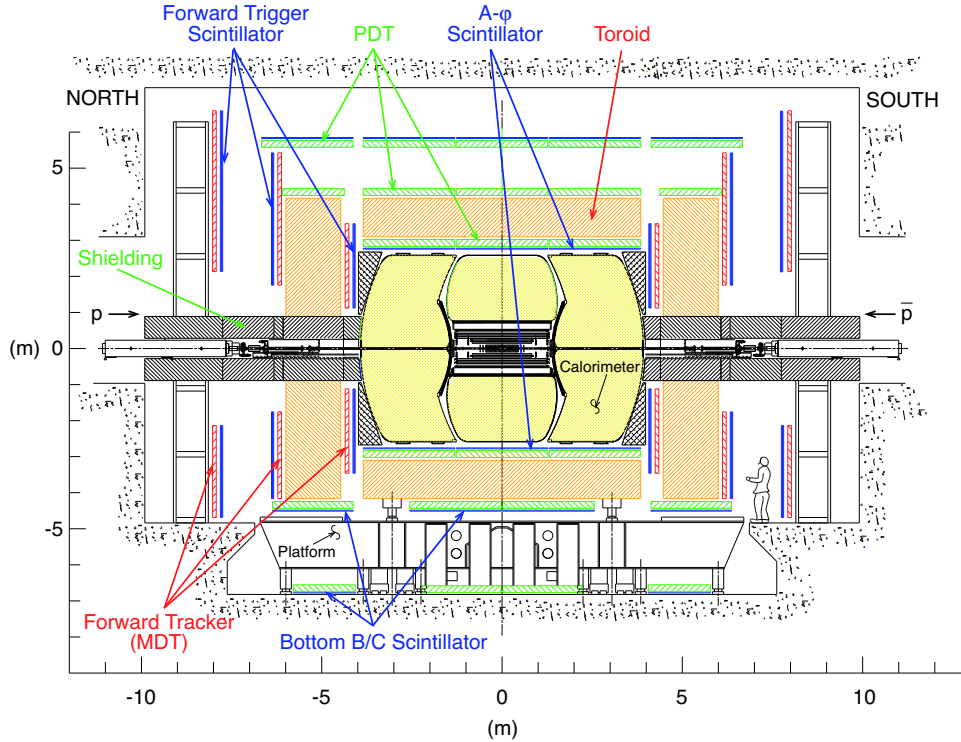


Figure 2.11: Overview of the muon detector elements.

2.7.1 Toroid Magnet

The toroid magnet is a square annulus 109 cm thick, weighting 1973 tons. Running the coils of the magnet at 1500 A, the magnet generates a magnetic field of 1.8 Tesla, with the field lines running in a plane perpendicular to the beam axis, vertically in the side parts of the magnet and horizontally in the top and bottom of the magnet. The iron of the magnet also serves as the return yoke for the solenoid magnetic field.

The magnet is split in a central system, covering the WAMUS region, and two forward systems, covering the FAMUS region.

2.7.2 WAMUS

The WAMUS consists of three detector systems: three layers of drift chambers with proportional drift tubes (PDT's), one inner layer of scintillators (A- φ counters) and outer layers of scintillator (Cosmic Cap) [95].

Proportional Drift Tubes

The three layers of pressurized drift tubes are arranged in a barrel geometry with one layer inside the toroid, normally called the A-layer, and two layers outside the toroid with one meter separation, called the B and C layers. Their purpose is to provide muon identification, and a momentum measurement independent of the central tracker.

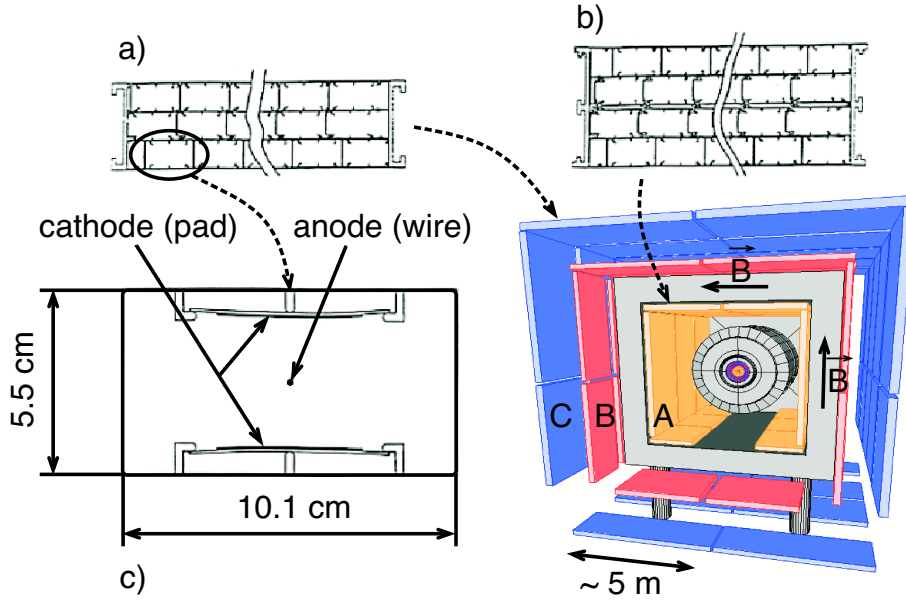


Figure 2.12: WAMUS. (a) is the end view of the 3-deck extrusion. (b) is the end view of the 4-deck extrusion. (c) is the end view of a single cell, including the cathode pad.

The chambers are constructed of extruded aluminum tubes and are of varying size, with the largest being approximately $250 \times 575 \text{ cm}^2$. Each of the B and C layers outside the toroid consists of three decks of tubes; the A-layer inside the toroid consists of 4 decks, with the exception of the A-layer bottom PDT's, which have 3 decks of tubes. The tubes are 10.1 cm across, with around 24 tubes per chamber. The wires in each tube are oriented along the field lines of the magnetic field, in order to provide the position of the bend coordinate for the muon momentum measurement. Besides the anode wire, each tube also contains a vernier pad used as a cathode. Figure 2.12 shows the layout of the chambers of each layer and a tube details.

The tubes are filled with a non-flammable gas mixture of 80 % argon, 10 % CH_4 and 10 % CF_4 . When operated at a voltage of 2.5 kV for the pads, and 5.0 kV for the wires, the drift velocity in this gas is around $10 \text{ cm}/\mu\text{s}$, with a maximum drift time of 500 ns. The uncertainty in the hit position due to diffusion in this gas is around 375 microns. The high voltage wires are 5 cm separated from each other. Each wire has a time readout with a resolution of 0.1 ns on each side, and is connected to a neighboring wire through a 20 ns delay jumper. When a hit occurs on the wire, this setup enables the measurement of the drift time T_d , and the axial time T_a . The resolution with which these times can be measured is dependent on the position along the wire of the hit. If the track passes the wire far from the electronics (near the jumper), the signal has to travel one wire length maximum, and the dispersion of the signal induces a resolution of approximately 10 cm. If the track passed the wire close to the electronics, the signal to the neighboring wire has to travel two wire lengths, and the dispersion causes the resolution to degrade to 50 cm.

A- φ Counters

The A- φ counters are scintillators that cover the WAMUS PDT's in the A-layer between the calorimeter and the toroid magnet. They are segmented in φ -slices of 4.5° , and have a length along the beam axis of ~ 85 cm. A photo-multiplier tube, connected to the scintillator through multiple scintillating fibers. The scintillators have a timing resolution of ~ 4 ns and provide a fast signal for triggering on muons and for rejecting out-of-time cosmics and backscattered particles from the forward region.

Cosmic Caps

The Cosmic Caps cover the top and sides of the muon detector, as well as part of the bottom, and are located outside the toroid. They are located outside the C-layer, and at the bottom also partly on the outside of the B-layer. Their purpose is to provide a fast signal to identify cosmic rays and, together with the A- φ counters, to give a timestamp on a muon to determine in which beam crossing the muon was produced. The time resolution of the scintillators is 5 ns, which can be improved by offline corrections to 2.5 ns.

2.7.3 FAMUS

The FAMUS consists of three major systems: 3 layers of mini drift tubes (MDT's), 3 layers of scintillating material, also known as pixels, and shielding around the beam pipe to reduce trigger rates, fake track reconstruction and aging of the detectors [96].

Mini Drift Tubes

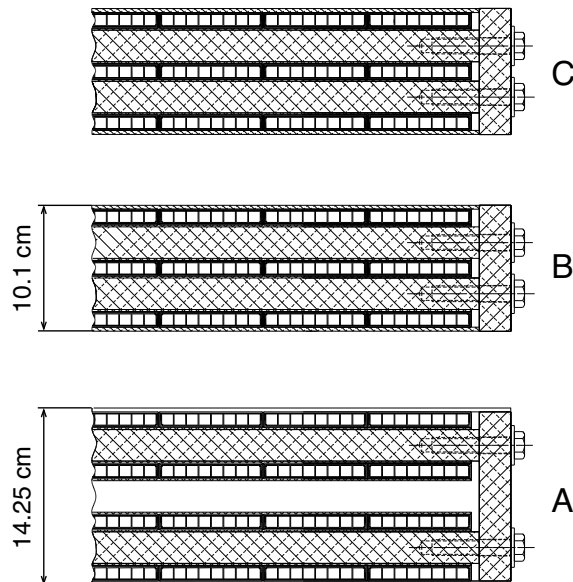


Figure 2.13: Layout of the three MDT planes.

The forward muon spectrometer is built from three layers of Iarocci tubes, which have a position resolution in the drift plane of $\sigma_x \approx 0.7$ mm. The A layer, which is mounted on the inside face of the toroid, consists of 4 planes, while the B and C layers (mounted on the outside of the toroid, with one meter separation) consist of 3 planes, as is shown in Figure 2.13. Each plane consists of tubes, each having 8 cells, and each plane is divided in 8 octants. The individual cells have an internal cross section of 9.4×9.4 mm², and have a 50 μ m tungsten-gold wire as the anode. The gas mixture in the cells is a mixture of 90 % CF₄ and 10 % CH₄, which at a voltage on the cathode of 3.1 kV gives a maximum drift time in the cells of ~ 60 ns, which is well within the 396 ns beam crossing time. The cells are read out on one side of the wire with a 18.8 ns resolution clock. Because the cell is only read out on one side, the time measured is the sum of the drift time and the axial time. Therefore, the position of a hit in a pixel detector along the wire is needed to determine the axial position of the hit, thus allowing the measurement of the drift time.

The efficiency of a single Iarocci tube is measured to be close to 100 %, but this is degraded by the thickness of the wall to an efficiency of 94 % for tracks perpendicular to the MDT plane. For tracks with an inclination to the MDT plane, the thickness of the wall has less impact, and the efficiency approaches 100 %.

Pixels

Mounted on the face of each layer of MDT tubes are single planes of scintillating material, divided up in 8 octants of each 96 slabs of scintillating material [97]. The φ segmentation is 4.5 degrees; the η segmentation for the outer nine rows of counters is 0.12, for the inner three it is 0.07. The scintillators are read out by phototubes with an operating voltage of 1.8 kV. When the threshold for passing particles is set at 10 mV, the efficiency for detecting single particles is 99.9 %, with a time resolution of less than 1 ns.

2.8 Forward Proton Detector

The Forward Proton Detector (FPD) is designed to study diffractive processes, and measures protons and anti-protons that are scattered at small angles [98]. The detectors are located around 30 meters away from the interaction point. They consist of 9 spectrometers, formed by 18 Roman Pots and the magnets of the Tevatron. The Roman Pots are stainless steel containers that allow a piece of scintillating material to be inserted close to the beam, but outside of the machine vacuum. Each piece of scintillator measures the (x,y)-position of the (anti-) proton passing through with a resolution 80 μ m, thus providing a 3-dimensional measurement of the position of the particle, which is used in the reconstruction of the particle trajectory.

2.9 Luminosity Monitor

DØ measures the delivered luminosity by monitoring a specific physics process with known cross section using a specialized detector, the Luminosity Monitor (LM) [99, 100, 101].

This detector measures coincidences between the proton and anti-proton bunches indicative of an interaction.

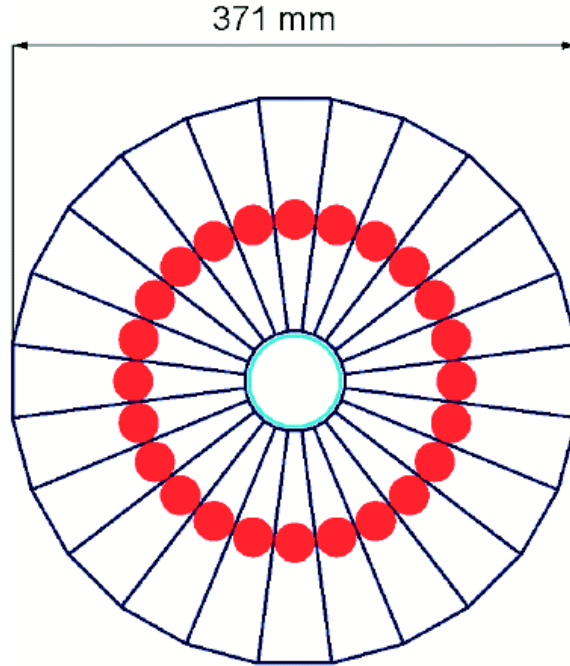


Figure 2.14: Schematic of the Run II Luminosity Monitor (one side). The solid circles represent the locations of the photomultiplier tubes.

The luminosity is measured by identifying beam crossings containing non-diffractive inelastic interactions [102]. Such a system also needs to distinguish between beam-gas interactions and beam-beam interactions, and whether there have been multiple interactions in the crossing. To reach this goal, two hodoscopes are used, located on the inside face of each end calorimeter cryostat, 135 cm from the center of the detector. Each of these hodoscopes is made of 24 wedge shaped scintillators, with photomultipliers mounted on the face of each wedge. Because of the 1 T fringe field, regular photo-multipliers do not work that is why the fine-mesh photomultiplier tubes are used. The wedges are arrayed around the beam pipe as shown in Figure 2.14. The hodoscopes cover the pseudo-rapidity region $2.7 < |\eta| < 4.4$, providing an acceptance of $(98 \pm 1) \%$ of all the non-diffractive inelastic collisions (estimated from Monte Carlo studies).

The LM uses the time difference between signals produced by the north and south detectors to differentiate between collisions (luminosity) and beam losses (halo). To perform this identification the Run I electronics (FastZ system) is currently used [102, 103]. Signals from wedges in each half of the detector are summed together and used as inputs to the FastZ. The FastZ compares the time difference between the summed north and summed south signals to independently identify luminosity and halo.

Protons travel clockwise around the Tevatron, so an errant proton (i.e. proton halo) will first pass through the north LM, and then, ≈ 9 ns later, pass through the south LM. Anti-protons travel counter-clockwise around the Tevatron, so anti-proton halo will

first hit the south LM and then the north LM. On the other hand, particles produced in collisions between protons and anti-protons in the DØ interaction region should strike the north and south LM at approximately the same time.

In case of a single interaction in the beam crossing, the system provides a fast measurement of the position of the interaction along the beam axis, as well as a measurement of the luminosity. The vertex position of the interaction is calculated by measuring the difference in arrival time of particles in the opposing beam jets, according to:

$$z_\nu \approx \frac{c(t_{-z} - t_{+z})}{2} \quad (2.4)$$

The resolution with which the detector measures both times is 194 ps, and accordingly the resolution in the measured z position of the interaction vertex is ~ 6 cm. The trigger rejects events with a vertex position $|z| > 97$ cm, which causes an inefficiency of < 1 % due to the width in the vertex distribution.

All of these signals: luminosity, proton halo, anti-proton halo, and the Z -position of the interaction, are sent to the Trigger Framework for use in the trigger decisions [104].

The luminosity calculation will be explained in detail in Section 3.2.

Chapter 3

Data Acquisition and Event Reconstruction and Simulation

Collisions happen at a very high rate at DØ intersection, but a majority of the events are not interesting for further studies. In this chapter a brief description is given on how the interesting events are selected (Trigger) and written in the storage medium (Data Acquisition System). In the later part we describe reconstruction of physical objects (such as electrons, jets etc.) from the raw data and corrections that need to be applied to the reconstructed parameters of these objects prior to analysis.

3.1 Trigger system

The frequency of beam crossings at the center of the DØ detector is 4.7 MHz. With an average event size of 250 kilobytes [113], this would require too high a bandwidth to write to tape without filtering. An intricate system of triggers is thus needed to filter out interesting events and suppress background. For these purposes the 3 levels of triggers are implemented:

- Level 1: Pipelined hardware stage using tracking, calorimetry and scintillating detectors;
- Level 2: Second hardware stage refining and combining Level 1 output with a pre-processor and a global processor;
- Level 3: Partial event reconstruction on computer farms.

The settling of these levels is specific for each sub-detector. Figure 3.1 represents the elements of the level 1 and 2. These levels will be successively described in the following sections.

3.1.1 Level 1

The level 1 trigger is a hardware system filtering the 4.7 MHz beam crossing rate to an output rate of 10 kHz for level two, with no dead time [111]. The time available for the

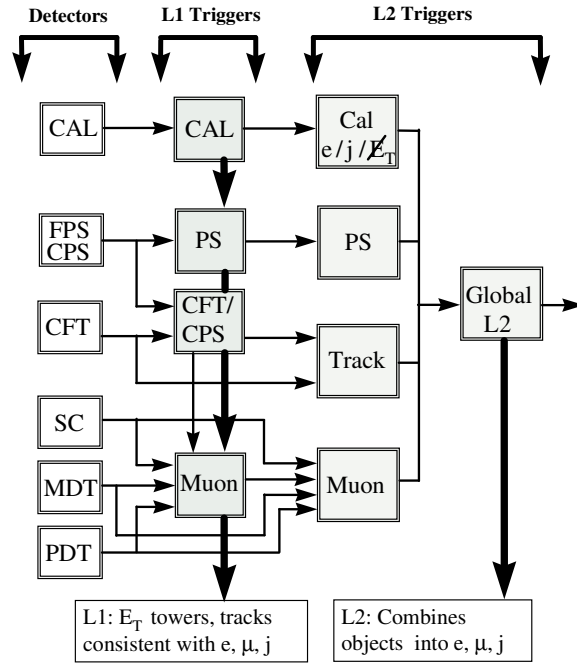


Figure 3.1: Structure of the levels 1 and 2 of the DØ triggering system.

level 1 trigger decision is $4.2 \mu s$. The system consists of a Trigger Framework and several Trigger Subsystems:

- Muon Trigger
- Central Tracking Trigger
- Calorimeter Trigger

Each Trigger Subsystem processes the data from the detector and produces, for every beam crossing, input terms to the Trigger Framework. The Trigger Framework uses this input, together with information about the readiness of the DAQ system to begin another data acquisition cycle, to decide whether the event should be rejected or captured for further processing in Level 2. To minimize the dead time caused by the decision time, the Trigger Framework is pipelined with 32 stages. The Trigger Subsystems use And-Or Input Terms to pass their results to the Trigger Framework. These And-Or Input terms can hold physics information, but also beam indicator signals, cosmic background vetoes, or in general, any event-dynamic or static information that is needed to form a Level 1 trigger decision. There are 256 of these And-Or Input Terms available in the Trigger System, which are combined in the Trigger Framework to form And-Or combinations. For every beam crossing, the Trigger System can evaluate 128 of these And-Or combinations. If any single one of the 128 combinations is positive, and the DAQ system is ready for acquisition, the Level 1 framework issues an accept, and the event data is digitized and moved into a series of 16 event buffers to await a level 2 trigger decision.

Level 1 Central Track Trigger

The Level 1 Central Track Trigger (CTT) uses the following hardware systems [114]:

- Axial fibers of the Central Fiber Tracker
- Axial strips of the Central Preshower
- Forward Preshowers strips
- Forward Proton Detectors

At Level 1, there is no information available from the CFT stereo fibers or the CPS stereo strips. The trigger is split up in a central part, using the Central Fiber Tracker and the Central Preshower, and a forward part, consisting of the Forward Preshower strips and the Forward Proton Detectors.

The central trigger is divided in 80 sectors in φ . For each of these sectors, the central trigger determines the number of tracks per p_T bin, as well as the number of fibers hit. There are 4 p_T bins:

- $1.5 \div 3$ GeV
- $3 \div 5$ GeV
- $5 \div 11$ GeV
- $11 \div 1000$ GeV

In addition, the trigger also reports the number of these tracks that have been successfully matched with a cluster in the central preshower. The tracks found are reported to the Trigger Manager, the L1 Muon Trigger and L2 pre-processors.

The forward trigger combines clusters in the backward u- and v-layers of the FPS with hits in the forward layer of the FPS to tag the clusters as electron or photon like. The number of electron and photon like objects per quadrant is reported to the L1 FPS Trigger Manager. In each of the FPD detectors, track segments are reconstructed and matched to form tracks. The number of tracks found is reported to the L1 FPD Trigger Manager.

Calorimeter Level 1 trigger

From the viewpoint of the L1 calorimeter trigger, the calorimeter is divided in 1280 projective towers, with 32 divisions in φ and 40 in η , resulting in a segmentation of 0.2×0.2 in $\eta \times \varphi$ for each tower [115]. In depth, these towers are divided in three sections: an inner electromagnetic section consisting of about 20 radiation lengths, followed by a hadronic section and a coarse hadronic section. The electromagnetic section is divided in 7 segments in depth while the hadronic section is divided in 3 segments with some variation depending on the position of the tower. Only the electromagnetic and hadronic sections are used for the L1 trigger decision since the coarse hadronic section typically generates too much noise at L1. The inputs for the trigger are the transverse energies deposited in

each of the 1280 electromagnetic and 1280 hadronic sections. These transverse energies are combined in the trigger manager into quantities, which consequently are compared to the trigger criteria to pass or reject the event.

The triggers are known as CEM(1,X) where the argument X ($X = 5, 10, 15$ or 20) refers to a desired energy threshold.

Muon Level 1 trigger

The Level 1 Muon Trigger is divided in three geographic regions: north, central and south [113]. The central Level 1 trigger logic is performed locally in the detector octants. Two trigger algorithms are implemented which run on MTC05 and MTC10 VME cards. The MTC05 trigger algorithm matches the tracks found by the CFT Level 1 trigger with hits in the scintillation counters. The segmentation of the scintillators matches the segmentation of the CFT Level 1 trigger in φ . To veto cosmic rays, high p_T tracks also require a hit in the cosmic ray veto scintillation counters since the tracks penetrate the muon spectrometer iron. A timing gate of 25 ns in the scintillators is used to reject background hits, while a 50 ns timing gate defines cosmic ray veto scintillation counter hits. The MTC10 trigger algorithm finds centroids in the PDT chambers and verifies them with matching scintillation counter hits. The timing information of the scintillation counter hit is needed because the maximum drift time in the PDT's (500 ns.) is greater than the bunch crossing time (396 ns.). A low p_T trigger is defined using only centroids found in the A-layer, while a high p_T trigger is defined using correlations between centroids found in the A-layer and B- or C-layer. Four p_T thresholds (2, 4, 7 and 11 GeV/c) are defined using the CFT information.

The triggering in the north and south regions is also implemented in two algorithms, running locally in each octant on MTC05 and MTC10 VME cards. The MTC05 trigger algorithm matches the CFT trigger tracks with a hit in the A-layer pixel scintillation counters for low p_T tracks, and with hits in all three pixel layers for high p_T tracks. The segmentation of the pixel scintillation counters azimuthally matches the CFT Level 1 trigger segmentation. The pixel scintillation counters have a timing gate of 25 ns to suppress backgrounds. The MTC10 trigger algorithm matches centroids found in the MDT chambers with hits found in the pixel scintillation counters. A low p_T trigger is defined by using only the A-layer, while the high p_T trigger requires correlations between a centroid in the A layer and a centroid in the B- or C-layer. Similar to the central system, four p_T thresholds (2, 4, 7 and 11 GeV/c) are defined using the CFT information.

The information for each octant in each region is combined in the muon trigger manager, which produces global muon trigger information. The muon trigger manager makes a trigger decision based on the p_T threshold (2, 4, 7 and 11 GeV/c), pseudorapidity region ($|\eta| < 1.0$, $|\eta| < 1.5$ and $|\eta| < 2$), quality (Loose, Medium and Tight) and multiplicity information. This trigger decision is send to the L1 Trigger Framework where it is included in the global physics trigger decision. In case of an accept, the L1 Muon Trigger reports the results to the L2 Muon Trigger, and on a L2 Accept, to the L3 Muon Trigger.

Level 1 trigger efficiency

L1 trigger efficiency curves are determined by plotting the fraction of events selected by muon triggers that satisfy the trigger condition under study as a function of the EM object E_T [116]. In the following analysis, we will use the CEM(1,15) trigger when it is unrescaled and the CEM(1,20) for some earlier data. These triggers reach full efficiency at $E_T > 25$ GeV.

3.1.2 Level 2

The Level 2 trigger reduces the 10 kHz Level 1 accept rate by a factor of ten to 1 kHz as an input to Level 3. This is done using multi-detector correlations of objects found in the event [117]. The Level 2 trigger consists of two stages: a preprocessor stage, which processes data from each Level 1 trigger for use in the second stage, which is a global processor that combines this data to make a trigger decision. There is a one-on-one mapping between Level 1 trigger bits and Level 2 trigger bits. Figure 3.1 shows the relation between the Level 1 and Level 2 trigger elements.

In the preprocessor phase, each detector system separately builds a list of trigger information. There are preprocessors for the following subsystems:

- Central tracker
- Preshower detectors
- Calorimeter
- Muon spectrometer

Each of these preprocessors will be discussed in more detail below. For each subsystem, the Level 1 information is gathered and transformed into physical objects like hits, clusters and tracks. The time budget for this preprocessing is $50 \mu s$. After the physical objects are formed, they are transmitted to the global processor. The global processor correlates the information from the different detector systems to make physics objects like jets, electrons and muons, and makes a trigger decision within $75 \mu s$.

Central Tracker preprocessor

The Central Tracker preprocessor reads in the tracks found by the Level 1 CFT trigger, transforms the (η and p_T) bin information into physical measurements and creates Level 2 tracks [118]. These tracks are ordered in p_T and sent to the L2 global processor. The tracks are maintained in memory for Level 3 readout in case of a Level 2 Accept.

Preshower detector preprocessor

The preprocessor for the forward and central preshower will take the clusters found by Level 1, and compute their azimuth and rapidity before sending them to the L2 global processor. The global processor can match the tracks found by the Central Track preprocessor with the L2 preshower clusters to find electron candidates.

Calorimeter preprocessor

The calorimeter preprocessor runs three algorithms in parallel [119]:

- Photon and electron reconstruction
- Jet reconstruction
- Calculation of missing transverse energy.

The jet reconstruction algorithm clusters 5×5 (3×3) groups of calorimeter trigger towers that are centered on seed towers. Each clustered group must pass a minimum E_T cut to be considered a jet candidate. The E_T of the clusters is calculated assuming that the interaction point is at $z = 0$. Jets that pass a minimum E_T cut, as defined in the trigger menu, are passed to the L2 global processor.

The photon and electron reconstruction algorithm processes the electromagnetic towers given by the L1 calorimeter trigger and turns them into seed towers. For each seed tower, it determines which of its nearest four neighbors contains the largest E_T , and the total electromagnetic and hadronic energy in the seed tower and the nearest neighbor is calculated. Based on the total electromagnetic energy, and the ratio of electromagnetic energy compared to hadronic energy, the electromagnetic tower is considered an electromagnetic candidate and passed to the L2 global processor.

The missing transverse energy algorithm calculates the vector sum E_T of the individual trigger towers E_T passed to it from the L1 calorimeter trigger and reports it to the L2 global processor if it exceeds a certain value.

Muon Tracker preprocessor

The muon tracker preprocessor first finds track stubs separately in the A-layer and the BC-layer in both the central and forward regions. This stub finding is done by shifting a 3-tube wide window over all the cells in an octant, looking for wire triplets with a matching scintillator hit (if a scintillator layer is present). The track stubs found are reported to an ALPHA preprocessor board that matches track stubs in the A layer with track stubs in the BC-layer, and creates L2 objects from matched or unmatched stubs. These L2 objects hold the φ , η and p_T of the muon, and are reported to the L2 global processor. Upon a L2 Accept, the L2 objects are sent to L3 to serve as seeds for more precise muon track reconstruction.

For the entire data taking period of interest, this level of requirements was not operated.

3.1.3 Level 3

The level 3 trigger is a software based system characterized by parallel data paths which transfer data from the detector front-end crates to a farm of processors. It reduces the input rate of 1 kHz to an output rate of 50 Hz. At the farm, each event is examined by a processor with a collection of filters.

Each front end crate creates one block of data per event. These data blocks move independently through the data system over the data pathway and are recombined into single events at their assigned Level 3 processor node. The Event Tag Generator, which is notified by a Level 2 Accept, uses the Level 1 and Level 2 trigger bits to assign an event to a certain event class. This determines which filter should be run on the event to pass or reject it. The filters call physics tools that have access to the full event data to search for electron, muon and jet candidates, as well as interesting event topologies.

For this analysis, only electron filter is used. L3 electrons start out using a narrow ($\Delta R = 0.4$) jet algorithm (based on calorimeter towers). This defines the electron cluster. In the next step, only cells with a ΔR of 0.25 around the axis of the cluster are used to define the electron object [120]. The trigger named EM_MX (known at some early stage as EM_HI) requires, in addition to a CEM(1,15) first level trigger, a fully reconstructed EM cluster of transverse energy greater than 15 GeV as well as an EM fraction (see below for definition) larger than 0.9. Both L3 filter efficiencies are essentially 100 % for E_T values in excess of 20 GeV. Some EM L3 triggers use the shower shape. This criteria uses the width of the energy deposit in the EM layers of the calorimeter. The width in each layer is defined as $\text{width} = \sum(E_i \times \Delta R_i) / \sum E_i$ where i is running over cells of the cluster in an EM layer and ΔR_i is the distance in η and ϕ between cell and cluster axis.

3.2 Luminosity Calculation

In the absence of a crossing angle, the instantaneous luminosity is given by the expression

$$\mathcal{L} = \frac{f_{rev} B N_p N_{\bar{p}}}{2\pi(\sigma_p^2 + \sigma_{\bar{p}}^2)} F(\sigma_l / \beta^*), \quad (3.1)$$

where f_{rev} is the revolution frequency, B is the number of bunches in each beam, N_p ($N_{\bar{p}}$) is the number of protons (anti-protons) in a bunch, σ_p ($\sigma_{\bar{p}}$) is the RMS proton (anti-proton) transverse beam size at the interaction point, and F is a form factor that depends on the ratio of the bunch length, σ_l to the beta function at the interaction point, β^* [105]. \mathcal{L} has units of $cm^{-2}s^{-1}$. Extracting \mathcal{L} from this expression requires detailed knowledge of beam characteristics, which is the case for the beam division.

In $D\bar{O}$, the luminosity is measured by identifying beam crossings containing non-diffractive inelastic interactions [102]. Such a system also needs to distinguish between beam-gas interactions and beam-beam interactions, and whether there have been multiple interactions in the crossing. To reach this goal, two hodoscopes are used, located on the inside face of each end calorimeter cryostat, 135 cm from the center of the detector.

Process	cross section (mb)	acceptance
hard	46.69 ± 1.63	0.97 ± 0.02
single diffractive	9.57 ± 0.43	0.15 ± 0.05
double diffractive	1.29 ± 0.20	0.72 ± 0.03

Table 3.1: Cross sections and acceptances of the processes involved in the luminosity calculations.

The luminosity is deduced from the ratio of the coincidence rate between the north and south counters over the effective cross section. For these calculations the following processes are considered:

- single diffractive processes;
- double diffractive processes;
- non-diffractive processes (called hard processes).

The effective cross section is defined as the cross section of the considered processes multiplied by the geometric acceptance and the detection efficiency of luminosity monitor:

$$\sigma_{eff} = \epsilon_{counter} (\epsilon_{SD}\sigma_{SD} + \epsilon_{DD}\sigma_{DD} + \epsilon_{HC}\sigma_{HC}) \quad (3.2)$$

where ϵ_{SD} is single diffractive acceptance, σ_{SD} is world average single diffractive cross section and ϵ_{DD} , σ_{DD} , ϵ_{HC} , σ_{HC} are similar terms for double diffractive and hard core inelastic collisions. The values of these parameters are shown in Table 3.1. The efficiency of the counter is $\epsilon_{counter} = 0.907 \pm 0.02$ and the effective cross section is $\sigma_{eff} = 43.26 \pm 2.07$ mb.

The proper determination of the Luminosity constant, σ_{eff} , has historically been a contentious issue at DØ, and between DØ, CDF, and Beams Division. For the analyzed data sample, presented in this thesis σ_{eff} was set to 43 mb. This value was adopted at the end of Run IB [109]. While the efficiency and acceptance of the Run II luminosity detector are different than the Level 0 detector from Run I, and while the \sqrt{s} is larger and the world average of some of the underlying cross sections have changed, we believe that these effects are probably small ($< 10\%$). So in the present analysis, the uncertainty of the luminosity is set to 10 %.

The output signals from the Luminosity Monitor are counted by a set of scalers, one for each possible crossing (159 total) [110]. The rate at which these scalers increment, folded together with the acceptance and efficiency of the luminosity detector, yields the delivered luminosity.

The number of interactions per crossing follows a Poisson distribution. The probability of n interactions in a given crossing is:

$$P(n) = \frac{\mu^n}{n!} e^{-\mu}, \quad (3.3)$$

where μ is the average number of interactions per crossing. The Luminosity Monitor does not discriminate between single and multiple interactions; a signal is generated if at least one hard scattering occurs in a given crossing. The probability that there be no interaction in a given crossing is $P(0) = e^{-\mu}$. The output signal from the Luminosity Monitor is equivalent to the probability of at least one interaction in the crossing,

$$P(n > 0) = 1 - P(0) = 1 - e^{-\mu}. \quad (3.4)$$

Extracting μ from (3.4),

$$\mu = -\ln(1 - P(n > 0)). \quad (3.5)$$

The product of μ and the crossing rate, $f \approx 7.6$ MHz, is equal to the product of \mathcal{L} and the cross section of the monitored process, σ_{eff} since an equivalent definition of \mathcal{L} to (3.1) is $\mu f = dN/dt = \mathcal{L}\sigma_{eff}$. Solving for \mathcal{L} , one gets

$$\mathcal{L} = -\frac{f}{\sigma_{eff}} \ln(1 - P(n > 0)). \quad (3.6)$$

However, the beam consists of different bunches and μ is not uniform from crossing to crossing; there can be wide disparity between crossings depending upon the characteristics of individual bunches (3.1). It is necessary to measure the luminosity independently for each of the 159 potential crossings and sum the result to extract \mathcal{L} .

$$\mathcal{L} = -\frac{f/159}{\sigma_{eff}} \sum_{i=1}^{159} \ln(1 - P_i(n > 0)) \quad (3.7)$$

Since $P_i(n > 0)$ is the measured number of positive signals from LM, N_{LMi} , divided by the number of crossings one counted over, $N_{crossing}$, one gets

$$\mathcal{L} = -\frac{f/159}{\sigma_{eff}} \sum_{i=1}^{159} \ln\left(1 - \frac{N_{LMi}}{N_{crossing}/159}\right) \quad (3.8)$$

$N_{crossing}$ must be large enough to smooth out statistical fluctuations.

The measurement of the luminosity appropriate for a particular L1 trigger is similar. The primary difference is that the measurement is limited to crossings when the trigger was capable of being satisfied. The luminosity for each L1 trigger may be formulated in the same fashion as (3.8). The problem is that different triggers may be active or inactive during different intervals of time and one needs to calculate the luminosity independently for each trigger. To reduce the number of scalers needed to collect this information, triggers are grouped together so that they have common dead time, *i.e.*, common sources of enable, disable, and readout. These groups are called Exposure Groups [110, 111, 112]. The exposure group definition includes all And/Or terms (AOT) [104] that are highly correlated with the bunch structure (*e.g.*, the live-beam-crossing term). Other such terms include any AOT that causes a bias in the normalization such as requiring a single interaction, a tight Z cut on the primary vertex, or a veto on an LM output (exposure groups containing these AOT terms cannot be normalized). Exposure groups allow the readout to be partitioned so that different triggers may read-out independent portions of the detector.

A L1 trigger is defined by a set of AOT (including all terms required by its exposure group) and belongs to one, and only one, exposure group. The calculation for the L1 trigger luminosity follows from (3.8),

$$\mathcal{L}_{L1}(n) = \frac{N_{decorrelated_n}}{N_{crossing}} \frac{f/159}{\sigma_{eff}} \sum_{i=1}^{159} \frac{N_{Exposure\ Group_i}}{N_{crossing}/159} \ln\left(1 - \frac{N_{LMi}}{N_{crossing}/159}\right) \quad (3.9)$$

$N_{Exposure\ Group}$ includes the effects of all AOT and disables correlated with the bunch-to-bunch luminosity profile including some global disables (*e.g.* skip next crossing after

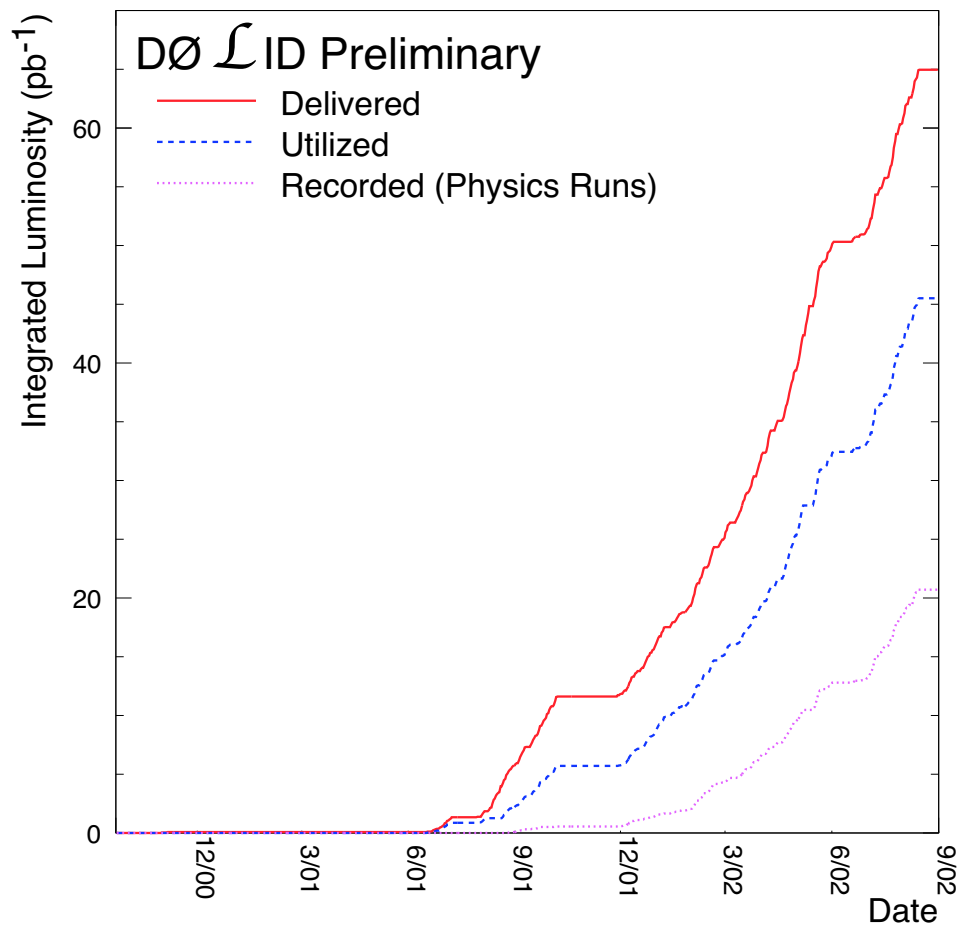


Figure 3.2: Accumulated luminosity as a function of time.

L1 accept) and front end busies [110]. $N_{\text{decorrelated}_n}$ is the number of crossings when the L1 term n was exposed taking in account only the effects of AOT and disables correlated with the bunch-to-bunch luminosity not correlated with the luminosity profile.

The Tevatron delivered $\approx 36 \text{ pb}^{-1}$ of luminosity from October 8, 2000 through April 27, 2002. This luminosity, integrated over time, is display in Figure 3.2. The delivered luminosity is defined using Equation 3.8. Luminosity delivered during operations, that is, luminosity delivered while a run was going (discounting all sources of disable during a run including run coordination program disables associated with pauses) is labeled as utilized in Figure 3.2.

3.3 Event Reconstruction

The events recorded by the data acquisition system (RAW events) contain information like digitised counts in calorimeter cells, hits in the tracking system etc. However, in physics analysis one studies the objects like jets, electrons, photons etc. The process of converting the raw data into interesting physics objects is called the reconstruction. In DØ this task is performed by a huge computer program called DØRECO.

3.3.1 The Reconstruction Program DØRECO

Apart from the raw data, DØRECO needs detector survey and calibration information as its input. The outputs of DØRECO consist of two different sets of files: written in DØ Object Management (DØOM) format and in ROOT format. Size of DØOM files for an event is quite large, typically $\sim 2 \text{ Mbytes/event}$, and it contains the raw information along with the reconstruction results. ROOT files contain those results of the reconstruction and summary of the event data which are likely to be needed frequently for the physics analysis. The size of ROOT file is about $\sim 100 \text{ kbytes/event}$. The enormous volume of data that DØ will collected in the coming years necessitate a further reduction in the size of data files that can be kept on disk. This third set of data files called thumbnail in compressed format contains minimum amount of information ($\sim 15 \text{ kbytes/event}$) needed for further analyses [122].

The reconstruction program performs four major tasks:

- Hit finding, in which, digitised signals from the sense wires of the tracking detectors are converted into spatial locations of hits. Also, signals from calorimeter cells are converted to energy depositions.
- Tracking and Clustering, where the tracking hits are joined together to form tracks and the calorimeter energy depositions in the cells are grouped to form clusters.
- Primary and secondary vertexing. The location of the $p\bar{p}$ interaction is used in the calculation of various kinematical quantities (*e.g.* transverse energy) and the vertexes are essential for particle identification.

- Particle identification, during which the tracking and calorimeter information are combined to form candidates for electrons, photons, jets, or muons. The criteria applied by DØRECO in choosing the candidates are quite loose.

3.3.2 Electron reconstruction

In the calorimeter, hit finding converts the raw information of digitised counts from each cell to energy, with appropriate calibrations. Corrections are applied to account for cell-by-cell variations in gain and pedestals. The cell energies are converted to transverse energy values by using the position of the interaction vertex. Cells with the same η and φ are grouped together to form towers. These towers are used in the next stage for electrons, photons and jets identification.

The electron reconstruction will be described in more details in Chapter 4.

3.3.3 Muon reconstruction

The reconstruction of the muon tracks starts from conversion of the raw hits and time information into three dimensional position information. After the individual hits are found, track segments in each layer are formed by fitting groups of hits in a straight line. The tracking is done separately for segments before and after the magnet. The segments are then matched and the momentum is determined from the measurement of the bend of track while passing through the magnet. Later on the momentum resolution will be improved by a global fitting, using the muon tracks the associated tracks in the central detector and the event vertex. The momentum measured in this way needs to be corrected for the loss of energy in the calorimeter.

The muon reconstruction will be described in more details in Chapter 5.

3.3.4 Jet reconstruction

Most DØ analyses reconstruct jets using a cone jet algorithm [121] which proceeds as follows:

- Preclustering: The calorimeter towers are first ordered in E_T . Starting from the highest E_T tower, for every tower with $E_T > 1$ GeV, a precluster is formed from all adjacent towers with $\Delta\eta < 0.3$, $\Delta\varphi < 0.3$. Preclustering continues until all the towers with $E_T > 1$ GeV are assigned to a precluster. The E_T -weighted centroid of each precluster defines the axis of the corresponding candidate jet.
- Cone Clustering: Starting from the candidate jet axis, all towers within a radius of R in the $\eta - \varphi$ space (for this analysis R is chosen to be 0.7) are assigned to the cluster. The centroid of this new jet and its new axis are recalculated. This process is repeated until it stabilises.
- Merging and splitting: No towers should be shared among jets. But during cone clustering it may happen that few towers are shared among different jets. If two jets share some towers, the fraction of the total energy which is shared between them

is examined. If it is more than 50 % of the E_T of the softer jet then the two jets are merged and jet axis is recalculated. Otherwise, they are split into two jets with each tower being assigned to the closest jet.

- To suppress random noise fluctuations that can produce jets, an E_T threshold of 8 GeV is imposed.

The jet candidates have a large number of quality variables associated with them. The parameters used in this analysis are

- electromagnetic fraction (EM fraction): fraction of the energy deposited in the EM calorimeter to the total energy of the jet.
- hot cell ratio: the ratio of the energy deposited in the hottest to the next to hottest cell,
- coarse hadronic fraction (CH fraction): the ratio of the energy deposited in the coarse hadronic calorimeter to the energy of the jet,

For physics analyses it is necessary that the energy of a reconstructed jet be the same as the energy of the original parton that formed the jet. However, there are systematic effects which lead to differences. Hence an energy scale correction is needed. The energy scale can be affected by the following:

- Jets are usually composed of a large number of particles of different energies, *e.g.*, approximately 67 % of the particles in a 50 GeV jet have energy less than 5 GeV [123]. The response of the calorimeter in this energy region is nonlinear and therefore summing up the response of the calorimeter to each particle does not give the correct result.
- Showering losses of particles outside the jet cone.
- Energy deposited by particles not originating from hard scattering *e.g.*, particles arising from the fragmentation of the spectator quarks (underlying events), or from the natural radioactive decay of Uranium used as absorber in the calorimeter. These sources affect the jets much more than the electrons because they are extended objects.
- The zero-suppression used in the calorimeter readout can produce a shift in the energy.

3.4 Monte Carlo Simulation

In this analysis, for the study of signal and background processes, the Monte Carlo simulation techniques have been used extensively. In general, this proceeds in four steps:

- event generation, in which simulation of the particle collisions is done;

- detector response simulation where the simulation of the interaction of the particles passing through the detector is done. DØ GEANT Simulation of the Total Apparatus Response (DØGSTAR) program [135, 136] has been used for these purposes;
- physical events reconstruction with DØReco program;
- simulation of the trigger.

In the following these four steps will be discussed in brief.

3.4.1 Event Generation

While there exists a number of event generators for the simulation of hadron-hadron collisions, we use in the present analysis Pythia [160] and Susygen [157] programs. Susygen has been used for the generation of SUSY \mathcal{R}_p signal events and Pythia has been used for simulation of various SM background processes (discussed in detail later). The basic steps followed in all these event generators are similar but they differ in the details of their implementation.

- A primary hard scattering is generated according to the appropriate physics process studied.
- QCD radiative corrections are added for both the initial and the final state.
- Partons are fragmented into hadrons independently, and particles with lifetimes less than about 10^{-12} seconds are decayed. This process is known as fragmentation or hadronisation. As this cannot be done in perturbative QCD, different event generators employ different empirical schemes for hadronisation, *e.g.*, Pythia and Susygen use Lund String fragmentation scheme [161].
- The final step in the event generation is to evolve and hadronise the leftover partons known as "spectators". There is no unique way of dealing with the leftover partons. Pythia and Susygen use an extension of the Lund Colour scheme.

3.4.2 Detector simulation

A detailed simulation of the detector response when particles pass through it is necessary to understand the systematic effects. The *DØ GEANT Simulation of the Total Apparatus Response* (DØGSTAR) package [135] relies heavily on the CERN package GEANT [136] program developed at CERN. This program simulates the tracks and interactions of the particles traversing through a volume containing user-specified materials. The interactions included in it are electromagnetic and hadronic showering, decays of short-lived particles, multiple Coulomb scattering, electron and muon bremsstrahlung and production of γ -rays. The DØGSTAR package allows the user to run separately each of the different phases of detector simulation:

- event generation using a MC programs partially described in the previous subsection;

- particle tracking in the detector with hit (position and energy deposition) generation.

Each program phase can be run independently provided the output file from the previous phase is available.

An essential component of the computer model of the detector is the database consisting of the following elements:

- a description of the detector geometry,
- the magnetic field map,
- all material and tracking media definitions,
- sensitive element definitions.

The most critical and error prone step in using GEANT is the coding of the geometrical model. In the DØGSTAR package the complex geometrical model using fortran code has been replaced by a number of ASCII data files which are read by the program and contain all the arguments for the GEANT geometry routines.

Raw data simulation is performed by DØSim [162]. DØSim uses DØGSTAR output as input and does the digitization for each detector, pileup and raw data simulation. It performs following functions:

- Merge hard scatter and minbias events (the number of which is a parameter as well as the mode : fixed number or poisson distribution).
- Add calorimeter pileup from previous events.
- Make L1CalTTowerChunk for L1 simulation.
- Add calorimeter noise.
- Add SMT noise and inefficiencies.
- Add CFT noise and inefficiencies.
- Add Muon noise and inefficiencies.

3.4.3 Trigger Simulation

Not all the events due to hard scattering are recorded by the data acquisition system. Thus, to have a realistic estimation of the efficiency with which a given event can be detected, one needs to treat the events passing through DØGSTAR as raw data and pass them through the trigger generators. To simulate the function of the trigger system, the program TRIGSIM is being developed. The simulator uses the same trigger configuration files which are used at the time of data taking.

The major goals of TRIGSIM are:

- to evaluate trigger efficiencies and rejection on MC and data samples for triggers before they are run online;
- test and debug online trigger software before it goes online.

3.5 Future DØ Analysis Centers

The analysis of data from Run II will be such a significant effort, that it cannot be done by relying on the Fermilab systems alone. Success in this endeavor will require a set of DØ off-site analysis institutions, called Regional Analysis Centers (RAC's). The DØ Remote Analysis Model (DØRAM) consists of three sorts of analysis centers, each with some dependence on the one above it in the hierarchy. In order of their capabilities they would be:

- Fermilab, presumably the sole Central Analysis Center (CAC);
- set of Regional Analysis Centers;
- groupings of Institutional Analysis Centers (IAC), each group associated with a single RAC;
- Desktop Analysis Stations (DAS).

In Run IIa, the current size of a typical reconstructed event from the DØ detector can be as much as 300 KB. The average output rate of the online DAQ system is 50 Hz, which constitutes a 15 MB/s average throughput. The number of events in a mean Run IIa year will be on the order of 8×10^8 .

For Run IIb, the DAQ rate will be 100 Hz and the size of each event will be about 500 KB. The event rate per day is foreseen to be 6×10^6 corresponding to 1.9 TB of raw data. Which in turn will result in 600 GB of reconstructed events and 6 GB of thumbnails. In parallel, 3×10^6 MC events will be processed per day resulting in 1.5 TB of additional data to handle. In total, DØ will produce 5 TB of data per year.

The evolution of the FNAL DØ reconstruction farm is designed to keep pace with this rate. Also, the FNAL storage requirements for processed data and producing the subsequent tiers of derived data are significant, and likewise expected to keep pace. It is anticipated that the FNAL processing farm will be sufficient for all of Run II primary reconstruction needs. RAC's are not envisioned for *ab initio* event reconstruction.

The tasks for a RAC include:

- emergency reprocessing of the data due to a possible coding or calibration error;
- detector element-level analysis (calibrations, alignments, *etc*);
- data caching and delivery (Thumbnail (TMB) and ROOT files);
- production and storage of the MC data.

To accomplish these tasks, the requirements for the RAC might include:

- sufficient connection bandwidth to the outside world for the data exchange with Fermilab CAC, other RAC's and IAC's;
- complete replication of the TMB files;
- mass storage of the ROOT files;

- sufficient computing power;
- complete replication of all necessary databases (detector parameters, calibration constants, data taking information, *etc*).

The RAC's act as gateways for their IAC's both to other RAC's and to Fermilab CAC and also serve as storage (long and short term) sites supporting their associated IAC's. Ideally, resource management should be done at the regional analysis center level. In reality, various institutional priorities and unique queueing strategies make identical IAC activities unlikely and human guidance will be required to forward the requests along the various paths to completion. Just how this interim management of tasks will be handled and how much of it is required is a serious issue for RAC implementation. Accordingly, the actual capabilities of the evolving system need to be carefully planned.

The DØ Remote Analysis Model is still on the preliminary project stage. Test are currently being done at a prototype RAC in Karlsruhe. The beginning of the implementation is planned by 2003 and its full deployment is expected by 2004 [124].

Chapter 4

Electron identification

4.1 Introduction

Electrons are identified by detecting an electromagnetic shower in the calorimeter with an associated energy lost in the preshower detectors and a track in the tracking system. The more detailed explanation of these steps follows.

It is obvious that for a particular calorimeter the shower pattern of an electron depends on its energy and its impact position. Such a dependency complicates the identification of an electron. Another difficulty comes from background EM showers which look like the shower of an electron.

The three most common types of electron background are:

- a charged hadron with a significant energy loss in EM section of the calorimeter;
- a neutral pion with a charged hadron tracking through its EM shower cone;
- an electron–positron pair production by a photon which converted in the material in front of the calorimeter.

4.2 Electron reconstruction in DØ

At the reconstruction stage, EM clusters are defined in the calorimeter as a set of towers. Clusters of towers are constructed with the simple cone preclustering algorithm with a cone size $\mathcal{R} = \sqrt{\Delta\eta^2 + \Delta\phi^2} = 0.4$, a seed E_T of 0.5 GeV and a p_{Tmin} of 1 GeV [126].

Electron candidates are created on purely calorimeter information [127]. The algorithm uses a list of calorimeter tower clusters. It selects those with ratio of the energy in the electromagnetic calorimeter to total energy (EM energy fraction) above a certain threshold (currently 0.9), then an isolation is calculated as the ratio of the energies of towers inside two concentric cones (typically of radius in $\eta - \phi$ space of 0.2 and 0.4). Clusters of towers with an isolation greater than an adjustable value (typically 0.8) are used to create EMparticle objects.

The x , y , z co-ordinates of the EM cluster at each floor is calculated by weighting cell positions with the logarithm of the cell energies. The x , y , z of the EM3 floor is

used together with the primary vertex to calculate the direction of the electron candidate 4-momentum while the energy is set to the total cluster energy. The components of 4-momentum are calculated assuming the mass of the object is 0. At this level as no matching with central tracks is required the ID of the object is set to 10.

The 3D clusters constructed in the central and forward preshower detectors are matched to the electron candidate by requiring them being in an $\Delta(\phi) \times \Delta(\eta)$ window around the electron candidate. If a preshower cluster is matched, its position together with the primary vertex is used to recalculate the direction of the electron candidate momentum.

The track from the central tracking system closest to the electron candidate is matched if it lies within a $\Delta(\phi) \times \Delta(\eta)$ window. The momentum direction is recalculated using the track direction at the vertex and the ID of the object is set to 11 or -11 (electron or positron).

EM showers are expected to deposit a large fraction of their energy in the electromagnetic section of the calorimeter and to have a longitudinal and lateral development compatible with those of an electron. The following subsections describe in more details the cluster characteristics used for the electron selection.

4.2.1 EM Energy fraction

The development of electromagnetic and hadronic showers is quite different so the shower shape information can be used to discriminate electrons and positrons against hadrons. Electrons deposit almost all their energy in the electromagnetic section of the calorimeter, while hadrons are typically much more penetrating.

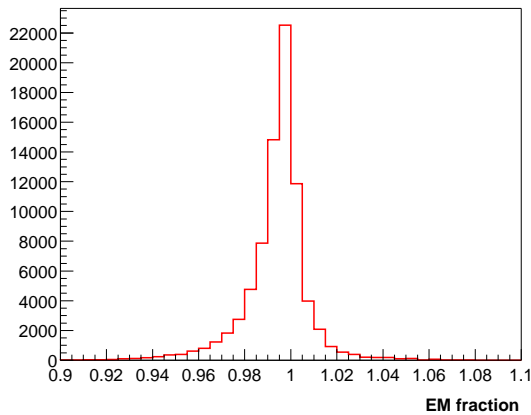


Figure 4.1: Distribution of EM energy fraction for the EM clusters in a MC $\gamma^*/Z \rightarrow ee$ sample.

The EM energy fraction of an electron candidate is defined as

$$f_{\text{EM}} = \frac{E_{\text{EM}}}{E_{\text{total}}}, \quad (4.1)$$

where E_{EM} is the amount of cluster energy in the EM calorimeter and E_{total} is the total cluster energy. Figure 4.1 shows the distribution of f_{EM} for electron candidates from $\gamma^*/Z \rightarrow ee$ MC events. f_{EM} can be higher than one because of the suppression scheme used to take care of multiple interactions. Energy deposited by previous minimum bias are subtracted from the cell energy giving rise to possible negative energy. f_{EM} is greater than 1 if hadronic cell energy is negative for a given EM candidate.

4.2.2 H–matrix technique

The shower shape of an electron or a photon has a distinctive profile from that of a jet. It follows a well known teardrop pattern [125]. Fluctuations cause the energy deposition to vary from the average in a correlated fashion among the cells and layers. To obtain the best discrimination against hadrons, both longitudinal and transverse shower shapes are used as well as correlations between energy deposits in the calorimeter cells. This is done using a covariance matrix technique [128, 129, 130].

For a sample of N Monte Carlo generated electrons one can define the covariance matrix

$$M_{ij} = \frac{1}{N} \sum_{n=1}^N (x_i^n - \langle x_i \rangle) (x_j^n - \langle x_j \rangle),$$

where x_i^n is the value of observable i for electron n and $\langle x_i \rangle$ is the mean value of observable i for the sample. If $H = M^{-1}$, we determine whether a shower k is electromagnetic by computing the covariance parameter

$$\chi^2 = \sum_{i,j} (x_i^k - \langle x_i \rangle) H_{ij} (x_j^k - \langle x_j \rangle)$$

By placing a cut on χ^2 we can separate electromagnetic and hadronic showers.

Figure 4.2 shows the separation power of the H–matrix method when applied on electron and pion samples [131]. Several dimensions of H–matrices have been studied and their performances compared.

In the present analysis the matrix M is 8–dimensional. The first four observables used to build the matrix M are the fraction of shower energy in the first, second, third and fourth electromagnetic layers of the calorimeter. These four variable describe the longitudinal development of the shower.

To characterize the transverse development of the shower two measurements of the cluster size in the third floor are used:

- S_1 – size of the cluster along r -axis for the forward region of the calorimeter or z for the central region;
- S_2 – size of the cluster along $r\varphi$ -axis.

To parameterize the energy and impact parameter dependence of the matrix the logarithm of the total shower energy and the position of the event vertex along the z axis are added as two independent parameters.

Figure 4.3 shows the distribution of the 8–dimensional H-matrix χ^2 for a MC $\gamma^*/Z \rightarrow ee$ event sample.

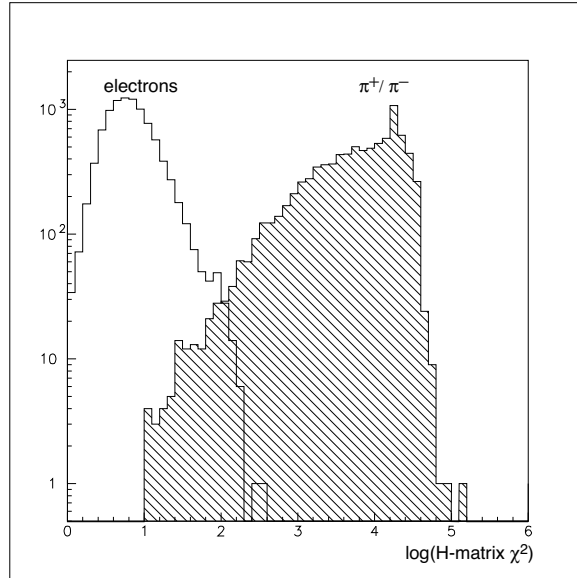


Figure 4.2: Distribution of H-matrix χ^2 for the EM clusters in a MC electron and pion samples [131].

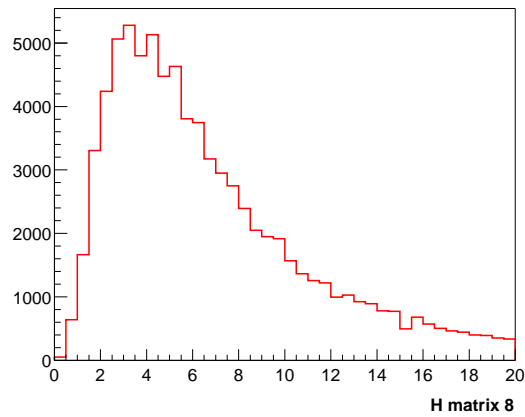


Figure 4.3: Distribution of H-matrix χ^2 for the EM clusters in a MC $\gamma^*/Z \rightarrow ee$ sample.

4.2.3 Electromagnetic cluster isolation

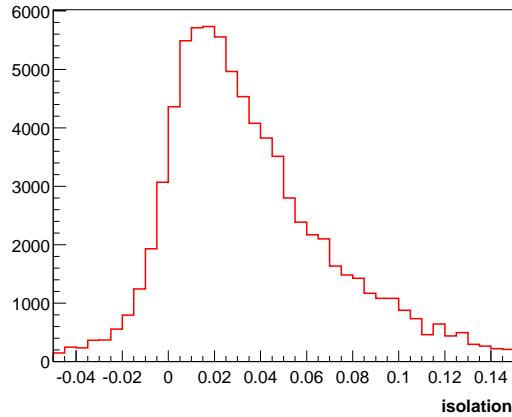


Figure 4.4: Distribution of isolation for the EM clusters in a MC $\gamma^*/Z \rightarrow ee$ sample.

To select an isolated electron we use a cut on a parameter called isolation and defined by comparing the electromagnetic energy within a cone of radius

$$\sqrt{\Delta\eta^2 + \Delta\varphi^2} = 0.2$$

centered around the electron [$E_{\text{EM}}(\mathcal{R} < 0.2)$] to the total energy contained within a concentric cone of radius 0.4 [$E_{\text{tot}}(\mathcal{R} < 0.4)$]

$$f_{\text{iso}} = \frac{E_{\text{tot}}(\mathcal{R} < 0.4) - E_{\text{EM}}(\mathcal{R} < 0.2)}{E_{\text{EM}}(\mathcal{R} < 0.2)}$$

Figure 4.4 shows the distribution of the isolation parameter for the MC $\gamma^*/Z \rightarrow ee$ event sample.

4.2.4 Sequential electron selection in the data

Electron candidates are selected by requiring that

$$f_{\text{EM}} > 0.9 \quad \text{and} \quad \chi^2 < 20 \quad . \quad (4.2)$$

Additionally, the cluster is required to be isolated:

$$f_{\text{iso}} < 0.15 \quad (4.3)$$

The choice of the cuts and the global efficiency estimation has been performed on an unbiased data sample of electrons from Z decays where one is use for tagging purposes and the other to evaluate the efficiency [90]. The fraction of electrons satisfying these cuts is

$$\varepsilon_{\text{em-candidate}} = 0.892 \pm 0.026 \quad (4.4)$$

4.3 Association of EM clusters with central tracks

Although the EM cluster selection is very discriminant, QCD backgrounds contaminate the electron sample. That is due, for instance, to the Compton QCD processes in which photons are produced in conjunction with a coplanar jet or jets production when one of them meets the EM identification (ID) selection criteria. As it will be demonstrated in Chapter 8, this background is the dominant one in the events with isolated EM candidate clusters.

In order to reduce this background, the cluster is required to be associated to a track. Due to the progressive commissioning of the CFT and SMT during the data taking period reported in present thesis, several types of reconstructed tracks are available. In summary there are

- "global" tracks built using the combined information of both trackers (SMT + CFT). For these tracks, the three parameters (p_T, φ, η) are best measured.
- "SMT only" tracks built with the SMT information when the CFT was not fully operated or equipped. They yield accurate measurements for (φ, η) only, as the magnetic field does not bend much the high- p_T tracks over its ~ 10 cm length to give a sensible measurement for high p_T tracks.
- "CFT only" tracks built when no SMT information is available. Their quality is similar to that of global tracks except when only axial information is available. In that case, there is no longitudinal measurement, i.e. no η information.

For each EM cluster candidate and each available track, a χ^2 defined according to the type of track (G = global, S = SMT, C = CFT) as

$$\chi_G^2 = \left(\frac{\delta\varphi}{\sigma_{\varphi G}} \right)^2 + \left(\frac{\delta z}{\sigma_{z G}} \right)^2 + \left(\frac{E_T/p_T - 1}{\sigma_{E/p G}} \right)^2 \quad (4.5)$$

$$\chi_S^2 = \left(\frac{\delta\varphi}{\sigma_{\varphi S}} \right)^2 + \left(\frac{\delta z}{\sigma_{z S}} \right)^2 \quad (4.6)$$

$$\chi_C^2 = \left(\frac{\delta\varphi}{\sigma_{\varphi C}} \right)^2 + \left(\frac{E_T/p_T - 1}{\sigma_{E/p C}} \right)^2 \quad (4.7)$$

is computed [132]. In these expressions,

- $\delta\varphi$ (resp. δz) denotes the difference between φ (resp. z) of the track at impact at EM3 floor and φ (resp. z) of the cluster position measured in the same floor
- E_T/p_T is the ratio of the measured transverse energy of the cluster to the measured p_T of the track
- σ_{φ} , σ_z and $\sigma_{E/p}$ are the rms of the experimental distributions of the 3 associated quantities (φ , z and E_T/p_T) for the 3 types of tracks (G, S and C). Figure 4.5 shows

the distributions of these variables for the global tracks. Typical measured values are

$$\sigma_{\varphi G} = 5 \text{ mrad}, \quad \sigma_z G = 7 \text{ mm}, \quad \sigma_{E/p G} = 0.21, \quad (4.8)$$

$$\sigma_{\varphi C} = 6.5 \text{ mrad}, \quad \sigma_{E/p C} = 0.22, \quad (4.9)$$

$$\sigma_{\varphi S} = 7 \text{ mrad}, \quad \sigma_z S = 9 \text{ mm}. \quad (4.10)$$

A cluster is matched when the condition on the χ^2 probability $P(\chi^2, n_D) < 1\%$ is met by at least one track ($n_D = 2$ for CFT and SMT or 3 for global).

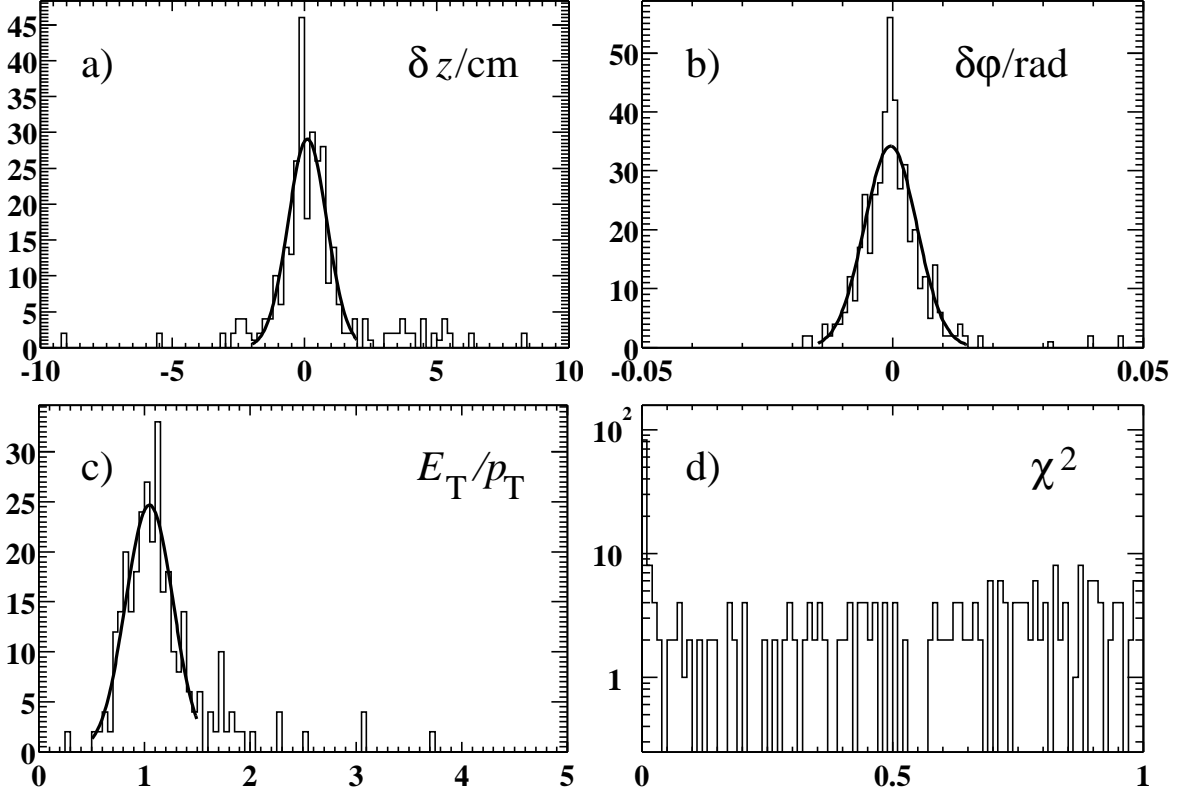


Figure 4.5: Electromagnetic cluster-track matching distributions in the Z Run II data sample. a) δz , b) $\delta\varphi$, c) E_T/p_T and d) χ^2 probability [132].

Taking advantage of the relatively low background in the di-EM candidate sample, as demonstrated in Figure 4.6, the track matching efficiency ε_{trk} is computed using the clusters in the Z sample. Both electrons are required to lie within the EM triggering region ($|\eta_{\text{det}}| < 0.8$). The efficiency is obtained as the ratio of the number of clusters which are successfully matched to a track to the total number of clusters (twice the number of Z events) in the $[80, 100]$ GeV/c^2 mass range. If Z_0 , Z_1 and Z_2 denotes the numbers of Z events in which no, one or both clusters are matched to a track, this efficiency reads

$$\varepsilon_{\text{trk}} = \frac{Z_1/2 + Z_2}{Z_0 + Z_1 + Z_2}. \quad (4.11)$$

Although the background is rather low, its contribution must be corrected for. In a first method to evaluate it, the e^+e^- spectra for all clusters and for the matched ones are fitted to a Breit-Wigner function convoluted with a gaussian plus an exponential function used to estimate the number of background events. In a second method, the background contribution is defined as a half of the events number in the [60-80] and [100-120] GeV side bands. Numbers obtained by both methods agree within statistical errors and for definiteness, the average is taken. To account for the large uncertainty on the assessment of the background fraction, a systematic uncertainty of half the background estimation is assigned. Figure 4.6 displays the invariant mass distribution of the di-EM pairs for events with 0, 1 or 2 EM clusters matched with a central track (details of the used data and EM selection will be explained in Chapter 8). After background subtraction, the following track matching efficiency is obtained:

$$\varepsilon_{\text{trk}} = 0.60 \pm 0.06 \quad (4.12)$$

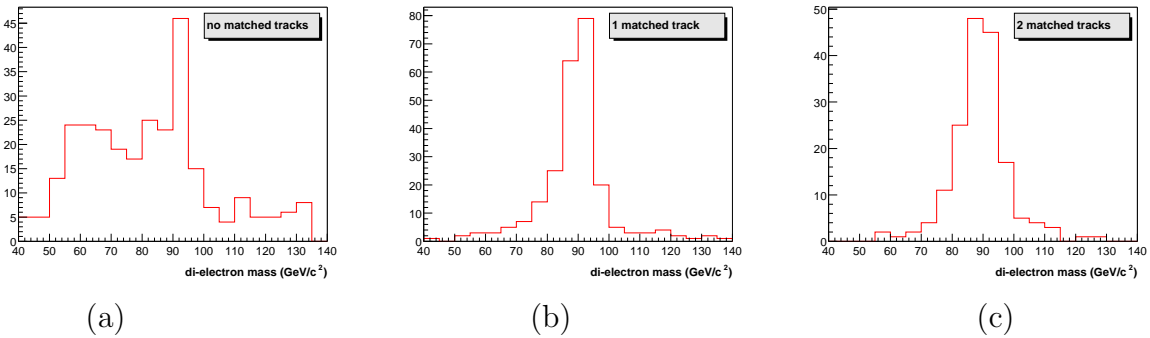


Figure 4.6: Invariant mass distributions for di-electron pairs in Run II data if a) no cluster is matched to a track, b) one and only one cluster is matched to a track and c) when both clusters are matched to a track.

4.4 Neyman–Pearson test

To maximize the background rejection power for any desired efficiency the *Neyman–Pearson* test was implemented in the $D\bar{O}$ reconstruction program [133]. Using this test for two hypotheses H , signal ($H = e$) and background ($H = b$), an EM cluster is considered an electron if it passes the test

$$\frac{p(x|b)}{p(x|e)} < k,$$

where $p(x|H)$ is the probability density for an observable x in the hypothesis H is true and k is determined by the desired efficiency.

4.4.1 Probability distributions

We construct the probability $p(x|e)$ from simulated single electron samples.

The probability $p(x|b)$ for the background can be written as

$$p(x|b) = f_h p(x|h) + f_{ee} p(x|ee),$$

where f_h is the fraction of hadron overlaps in the background, $p(x|h)$ the probability to observe x for hadron overlap, $f_{ee} = 1 - f_h$ is the fraction of conversions in the background, and $p(x|ee)$ the probability to observe x for conversions. To estimate these probabilities separately for hadrons overlaps and conversions one can use simulated jet sample and single photon sample. Finally, the electron likelihood test looks like

$$\mathcal{R}(f_h) \equiv \frac{f_h p(x|h) + f_{ee} p(x|ee)}{p(x|e)} < k.$$

The best efficiencies and rejections can be achieved only if the probability distributions accurately reproduce the data and if the composition of the background (i.e., f_h) is known.

Apart EM energy fraction, H-matrix χ^2 two additional variables have been considered as explained in the following two subsections.

4.4.2 E/p discriminating variable

The presence of the central magnetic field in the upgraded DØ detector allows the determination the momentum of charged particles. As it was shown in [134] an improvement in the low energy pions rejection can be achieved due to E/p cut. So this parameter was also taken into account.

4.4.3 Using the deposited in the preshower detectors

Unfortunately the central magnetic field allows a good momentum resolution only in region of $|\eta| < 2.0$, so for the other part of the detector we have to use additional variables.

The forward preshower detector makes it possible to determine energy loss per unit path length (dE/dx) in the region beyond $|\eta| \approx 2.0$.

The energy loss of heavy charged particles like charged hadrons is mainly due to collisions with atomic electrons and is described by the Bethe–Bloch formula. For $\beta \approx 0.96$ dE/dx is smallest and almost the same for all particles with the same charge. Such particles are called *minimum ionizing*. At lower velocities dE/dx can be substantially larger, but at higher velocities it increases only logarithmically with energy. Pions are minimum ionizing at energies of several hundred MeV, so most charged particles that are detected in DØ are at or beyond the minimum ionizing point and expected to have small energy loss in the preshower system.

In the case of electrons and positrons the energy transfer is between particles of equal mass and therefore larger than for heavy charged particles. Thus for the same velocity dE/dx for electrons is expected to be larger than for heavy charged particles.

Electron–positron pairs from photons which pair–convert are often not resolved and thus result in a single track with twice the expected dE/dx .

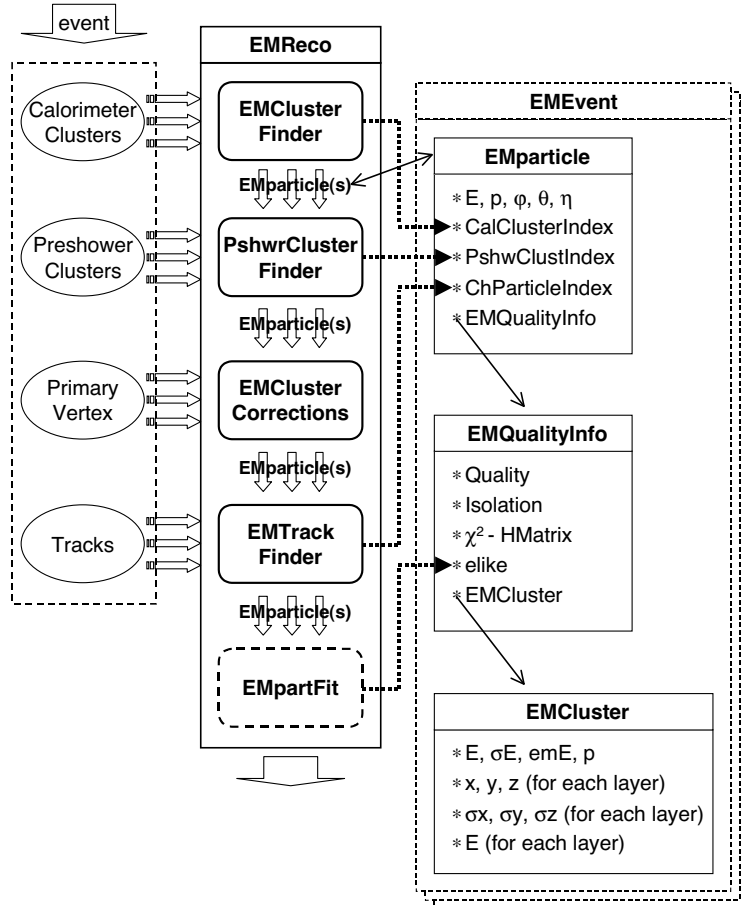


Figure 4.7: General structure of the $DØ$ electron reconstruction program $EMReco$.

4.4.4 Implementation of Neyman–Pearson test in $DØ$ reconstruction program

The part of the $DØ$ event reconstruction program responsible for electron identification is called $EMReco$. General structure and data flow of the package are shown in Fig. 4.7.

The first module of the $EMReco$ package is called *Electromagnetic Cluster Finder*. It uses the described cuts on the f_{iso} , f_{EM} and P_T to select a calorimeter cluster which looks like electron candidate.

The next two modules which are called *Preshower Cluster Finder* and *Track Finder* find the closest to the selected electromagnetic cluster preshower system cluster and track.

For each electron candidate the program creates an instance of the type $EMparticle$ that stores pointer to the calorimeter cluster, the preshower detector cluster and the track.

The last module is called $EMpartFit$. It uses the described Neyman–Pearson test for final fit of the electron candidate. Till date the reconstruction software was well developed only for central region of the detector ($|\eta| < 2.0$). Therefore at the present

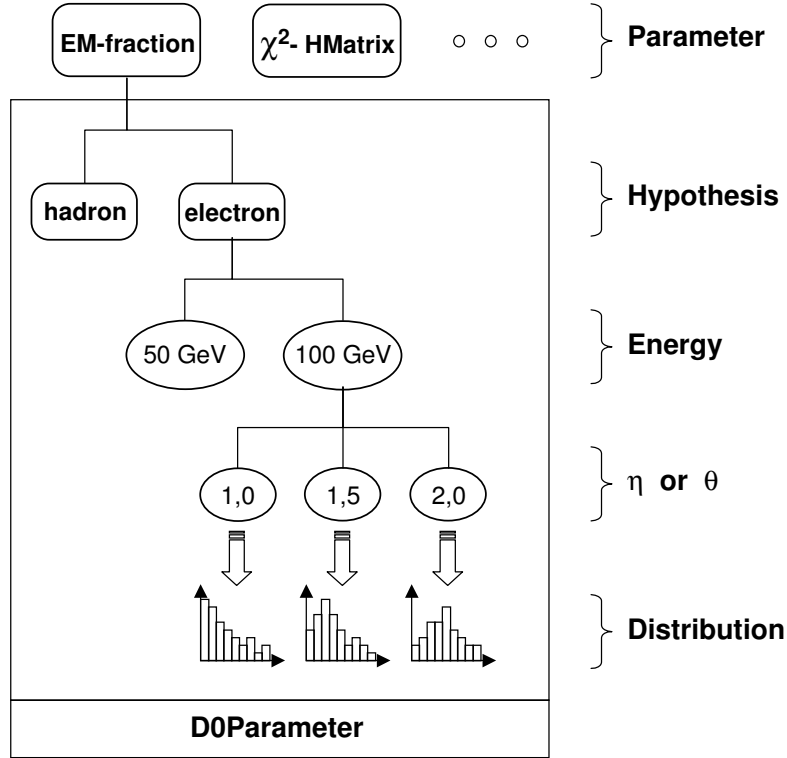


Figure 4.8: Database structure for storing probability distributions for the EM likelihood.

time EMpartFit uses only three variables: H–matrix χ^2 , E/p and EM energy fraction f_{EM} . So the probability was factorized using those variables:

$$p(x|H) = p_1(\chi^2|H) \times p_2(E/p|H) \times p_3(f_{EM}|H)$$

for $H = e, h, ee$. When more information coming from the reconstruction program will be available the number of the variables will be increased.

The process for constructing the probabilities for different ranges of energy and pseudorapidity consists of four main steps of DØ physics analysis:

- events simulation by Monte Carlo methods (single e^- , single π^\pm , jets);
- detector response simulation;
- extraction (calculation) of parameters and probability distributions production.

The first three steps use the standard DØ programs. The program for the last step was specially developed because it needs some calculations which were not implemented in the present general DØ software. All the received probability distributions are ordered and stored in structure shown in Figure 4.8. The structure is organised per variable (f_{EM} , H–matrix χ^2 , ...), then per hypothesis (hadron or electron), per bins in energy, per bins in η and per bins in ϕ . The number of bins is a compromise between rejection capability and necessary MC statistic to produce accurate probability distributions.

4.5 Electron misidentification rate

There are several possible ways to calculate the rate of expected fake electrons. The estimate can be based on the number of events or alternatively on the structure and the objects contained in these events. Both methods will be discussed in this section.

Fake electron rate per event

To study a fake electron rate per event, a sample with similar properties as the data sample is needed. If the kinematics and the structure of the events in the data sample and the sample used for the fake study are similar one can expect a good prediction for the fake rate. The main problem with this method is finding a sample with high enough statistics and a well understood or negligible background of extra electrons.

The most convenient sample for such a study is the Z -sample, because Z -events are well defined by the existence of two high energetic electrons. In the region of the Z mass peak the production of Z clearly dominates all backgrounds. Still using the Z sample for a fake electron rate study is impossible at the current stage of the experiment due to small statistics.

Fake electron rate per EM-candidate

The estimate of the electron fake rate will be more reliable if one uses more of the information contained in the events. If the exact structure of the events is used the estimate should describe reality better. In order to use most of the information contained in the event a fake electron rate per EM-candidate in the event will be calculated in this subsection.

To define the fake electron rate the following strategy has been used: for an inclusive multijet sample, fill one histogram with the E_T spectrum of all the jets in this sample, fill another histogram with the E_T spectrum of all the EM objects in this sample passing certain EM object quality cuts, and then define the E_T -dependent jet rate as the (bin-by-bin) ratio of the two histograms.

The problem arises from the fact that the current jet energy corrections do not distinguish between the EM jets and hadronic jets when making. However, a jet faking an electron must have high EM fraction, so its energy has to be corrected differently from an average hadronic jet. Since we divide histograms bin-by-bin, it is necessary to ensure that the same scale is used for both histograms. Therefore, the two logical possibilities to define the fake rate are:

1. Use EM energy when filling the EM candidate histogram and then use the uncorrected jet energy for the jet histogram;
2. Use corrected jet energy for the jet histogram, and use similar corrected energy of the jet matching the EM object when filling the EM candidate histogram.

Both methods are self-consistent and should give similar results. The latter definition is used for consistency purposes (*i.e.* always use corrected jet energy).

Two simplifying assumptions could be made (driven by the Run I experience) when defining fake electron rate f :

- η -dependence within each part of the calorimeter is consistent with being constant. So, the rate is defined separately for the central and forward calorimeters: f_{CC} and f_{EC} ;
- The electrons of interest in this thesis are highly isolated, so the fake electrons are assumed to be jets with nearly entire energy fluctuated in the EM energy, *i.e.* the E_T of the fake electron is close to the original jet E_T . This assumption worked well in Run I, and it is expected to be reasonable in Run II as well. It allows to define the E_T -dependent fake rate by dividing bin-by-bin the E_T spectra of EM-candidates by the corresponding jet energy spectra.

An additional complication arises from the jet trigger/reconstruction/selection threshold effects. For the corrected jet energies these effects are rather large, especially in the forward part of the calorimeter, due to the size of energy corrections. That would lead to the significant threshold effect in the fake electron rate: below certain energies the rate would fall because more and more jets in the given bin would have non-corrected jet energy below the different trigger threshold. As it will be shown by the study of the fake electron rate obtained using the ratio of uncorrected jet energies (the first method), the fake electron rate for high E_T can be extrapolated to the low- E_T region.

Two independent samples were used to evaluate the rate. One selected by using the muon-only triggers and the other was based on jet triggers. Sample of jet events with Level 3 trigger thresholds at 25, 45, 65, and 95 GeV were used. The results obtained from jet triggers are consistent with those obtained from muon-only triggers (see below). Since the jet triggered sample contains more events, it was used to obtain more precise results.

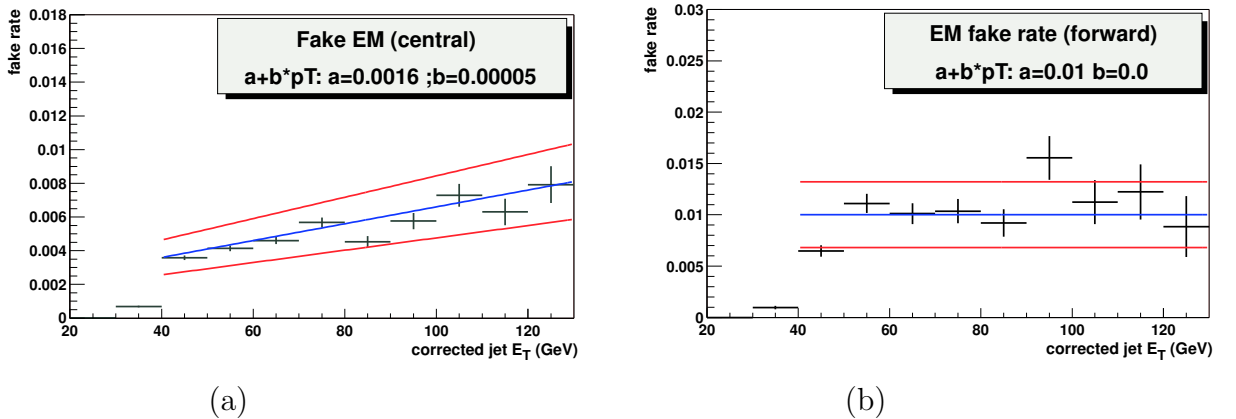


Figure 4.9: Nominal fake electron rate obtained from the jet triggers for central (a) and forward (b) region. Low-energy "turn-off" is the artifact of the various thresholds, amplified by jet energy corrections.

The results based on the high-statistics jet triggers are shown in Figure 4.9. The following fake rates corresponding to the standard EM ID certified cuts v2.0 [90], with

the $\chi^2(\text{HM8}) < 20$ cut, were obtained:

$$\begin{aligned} f_{\text{CC}} &= (1.6 \pm 0.3) \times 10^{-3} + (5.0 \pm 0.5) \times 10^{-5} \times E_T/\text{GeV}; \\ f_{\text{EC}} &= (1.0 \pm 0.2) \times 10^{-2}. \end{aligned}$$

The quoted error is dominated by statistics; the overall $\pm 25\%$ error to the fake rates is assumed. This reflects both the statistical error and the additional systematics to cover small differences using different cross checks, *e.g.* data obtained via (unbiased) muon triggers.

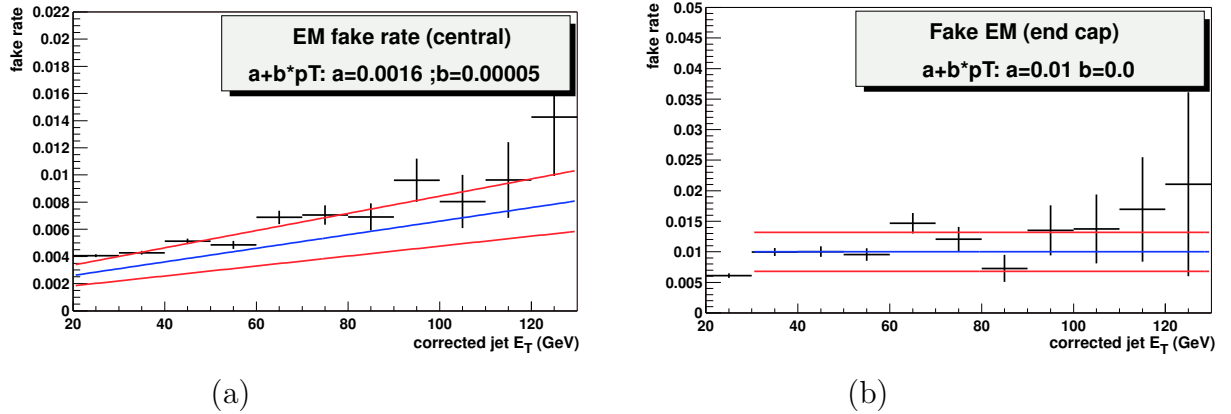


Figure 4.10: Comparison of the nominal fake electron rate obtained using the corrected-energy ratio with that for the uncorrected ratio for central (a) and forward (b) region.

To prove that the extrapolation in the low- E_T region works well, the fake rate obtained using the ratio of uncorrected jet energies was studied. Figure 4.10 shows this rate as a function of jet E_T with the above best fit overlaid. The agreement is good over the entire range. This allows to extrapolate the fake rate to E_T^{jet} as low as 20 GeV.

As another cross check, the above fake electron rate is overlaid with the estimate obtained by the same method using the muon-only triggers, which are expected to be completely unbiased toward EM-candidate. Again, the good agreement is obtained, as shown in Figure 4.11.

Requirement of an EM-candidate to be matched with a central track results in a much lower electron fake rate which is shown in Figure 4.12. The fake electron rates obtained from the fit to the above histograms are:

$$\begin{aligned} f(\text{matched})_{\text{CC}} &= (1.5 \pm 0.2) \times 10^{-4}; \\ f(\text{matched})_{\text{EC}} &= (1.4 \pm 0.7) \times 10^{-4}. \end{aligned}$$

Due to the difficulty to get an unbiased estimate of the electron fake rate several groups have developed their own algorithm [137]. The different estimates are very useful to understand systematics.

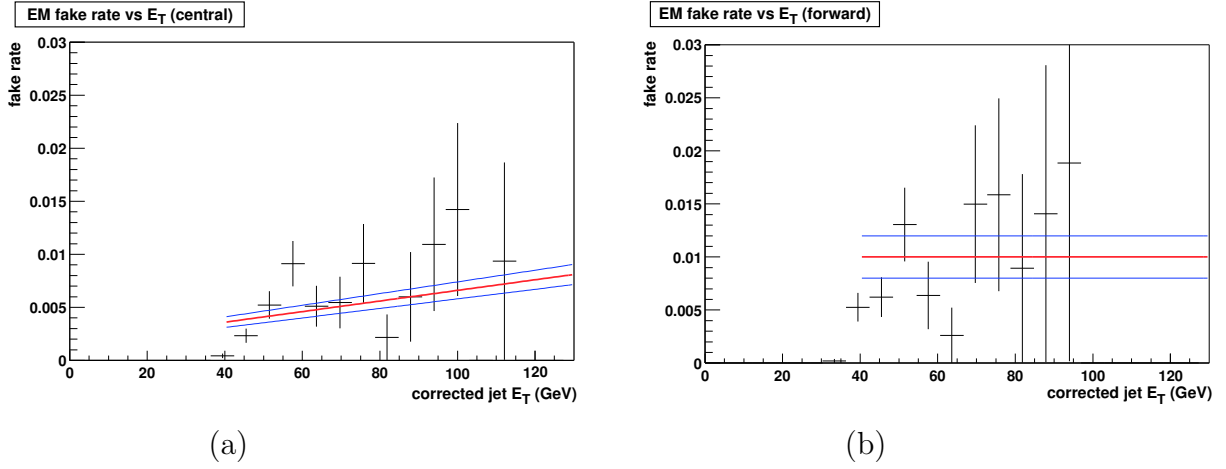


Figure 4.11: Comparison of the nominal fake electron rates with the ones obtained from the muon triggers for central (a) and forward (b) region. Low-energy "turn-off" is the artifact of the various thresholds, amplified by jet energy corrections.

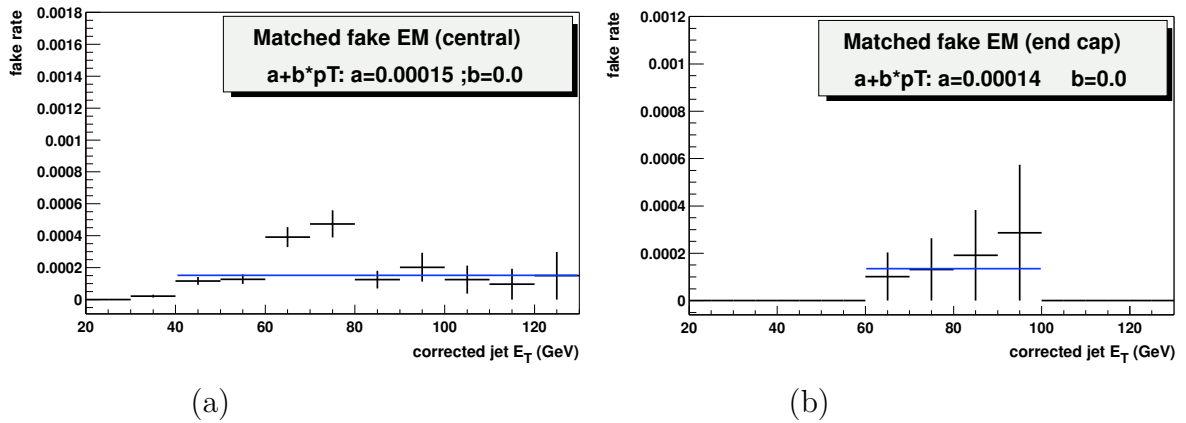


Figure 4.12: Electron fake rate with central track matching condition for central (a) and forward (b) region.

4.6 Electron energy corrections

The energies of the objects reconstructed by DØReco need to be corrected for various effects prior to the physics analysis. The following sections briefly discuss the various corrections.

Energy corrections for geometry effects Due to material in front of the calorimeter, gap between the calorimeter cells, uninstrumented regions, the electron energy reconstructed in the calorimeter is lower than the initial one. So, a parametrized correction $\Delta E(\eta, E_{\text{reconstructed}}) = E_{\text{initial}} - E_{\text{reconstructed}}$ has been determined for both central and forward calorimeters as a function of eta and energy using single electron MC [138].

Electromagnetic energy scale corrections A sampling calorimeter measures only a fraction of the energy it absorbs. Data from a test beam, where the response of calorimeter modules from electrons and pions of known energies is measured, are used for basic calibration and determination of the sampling weights. Those weights have to be redefined for the Run II data because of the modification of the material in front of the calorimeter. As it is impossible to put the calorimeter in test beam and the effects due to intercalibration between groups of crates cannot be simulated, the weights have to be deduced from the real data and in particular using e^+e^- resonances at known masses [139].

The relation between the energy E and the measured ADC counts, a_i of an electromagnetic object in the floor n is given by

$$E = \alpha \sum_i^n \beta_i a_i + \gamma \quad (4.13)$$

where α is the overall energy scale, β_i are the sampling fractions ($\sum_i^n \beta_i = 1$) and γ is the bias [140, 141].

In principle all the parameters depend on η and Φ . The purpose of the energy scale correction is to adjust α which can vary in time: $\alpha(t) = \alpha(0) \cdot (1 + X)$. One expect that this correction X is of the order of few percents.

These corrections are determined from very pure samples of $Z \rightarrow ee$ events. Since the mass of the Z has been measured accurately at LEP, the EM energy scale is just the correction factor to take their masses measured by the calorimeter to the correct values.

Presently, the EM energy scale correction factors X_i ($i = 1 \dots 6$; $E_{\text{corrected}} = (1 + X_i) \cdot E_{\text{uncorrected}}$) are determined for 6 regions in the calorimeter using the real data samples of $Z \rightarrow ee$ events. The following regions have been considered:

- One region per forward calorimeter;
- Four regions in the central calorimeter ($z > 0, z < 0, \cos(\phi) > 0, \cos(\phi) < 0$).

The di-electron mass distributions were fitted with Breit-Wigner function folded with gaussian and the maximum likelihood method was used to determine the X_i coefficients to adjust data on Monte-Carlo. Presently all the factors X_i are below 0.03 [142].

Chapter 5

Muon identification

The muon identification in the spectrometer is carried out in several successive stages. Information coming from the detector is initially translated into usable physical quantities (wires hits, drift time, etc.). The wires hits are associated with drift times (hit reconstruction). Straight line segments combine then several close hits (segment reconstruction). And the segments are associated by pairs of each side of the toroid to form the tracks. These various stages are described in more details in this chapter.

The reconstruction programs are written in C++ language. They should be fast enough (less than 50 ms per event) to work equally as part of the level 3 trigger.

The information from the muon detector can then be combined with information coming from other detectors like the tracking system or the calorimeter in order to complete the identification.

5.1 Muon hit reconstruction

As explained in Chapter 2, the central part of the muon detector consists of three layers of proportional drift tubes (PDT) and two layers of scintillator (cosmic counters and $A-\varphi$ counters). In the forward part the detector has three layers of mini drift tubes (MDT) and each layer has a layer of scintillator added, called pixels. Due to their different nature, the hit reconstruction for each type of detectors (PDT, MDT and scintillator, also known as MSC) is specific. The available hit information is also different for the different detectors.

5.1.1 PDT hit reconstruction

The measured axial drift time can easily be converted to an axial distance with a linear time to distance relationship, using the signal speed along the wire. There is no such linear relationship between the drift time and the drift distance to the wire; this relationship depends on factors like the gas used and the angle of the track, and has to be measured experimentally. Because of the dependence of the drift distance on the angle of the track, it is not possible at hit reconstruction level to give a definite position of the hit. Therefore, an angle of zero (measured from the normal to the plane in which the wires are located) is assumed. When the segments are reconstructed, the angle of the segment can be measured

and used for more precise determination of the drift distance, and thus of the position of the hit.

5.1.2 MDT hit reconstruction

The wires of MDT are not linked to their neighbors, as it is the case for the PDT, that is why in the forward system it is not possible to make a distinction between the drift time and the axial time based on the information of the time when the wire was touched. Because of the lack of this information, the hit is placed in the middle of the wire at the hit reconstruction step. The drift time can be calculated later. By associating of wire with the information of the scintillators it will be possible, at the level of the segments reconstruction, to measure the track position along the wire and to determine more precisely the drift time. Because of the square profile of the MDT cells, the relation between the drift time and the drift distance is practically linear and does not depend on the angle of the track (in the approximation of small incidence angles in the forward direction).

From this the time it took the signal to travel along the wire to the pre-amplifier can be deduced, and the remaining time is taken to be the drift time of the hit.

5.1.3 MSC hit reconstruction

In both the central and the forward system, the scintillators provide timing information. In the forward system they serve for better position resolution along the wire (and hence better drift time resolution). The scintillators are read out by photomultiplier tubes (PMT), which are linked to a clock giving the arrival time of the signal. The T_0 of this clock is taken to be the collision time, given by the machine, plus the time it takes a particle, traveling in a straight path with the speed of light, from the origin to the center of the scintillator. Some of the scintillators are read out by two PMT's for redundancy. In the hit reconstruction step, the position of the hit is taken to be the center of the scintillator, while the position resolution of the hit is equal to the size of the scintillator.

5.2 Muon segment reconstruction

After their reconstruction in the different parts of the detector the PDT or MDT hits are combined chamber by chamber. And a straight line, called a segment, is fitted through the combined hits. The magnetic field is negligible at the chambers level (see Figure 5.1). Then the found segments are associated with the scintillators to obtain the timing information.

For the segment reconstruction algorithm, the muon detector is split into two parts, each of which is again split in two parts:

- Central system (WAMUS)
 - Octants 0, 3, 4 and 7
 - Octants 1, 2, 5 and 6

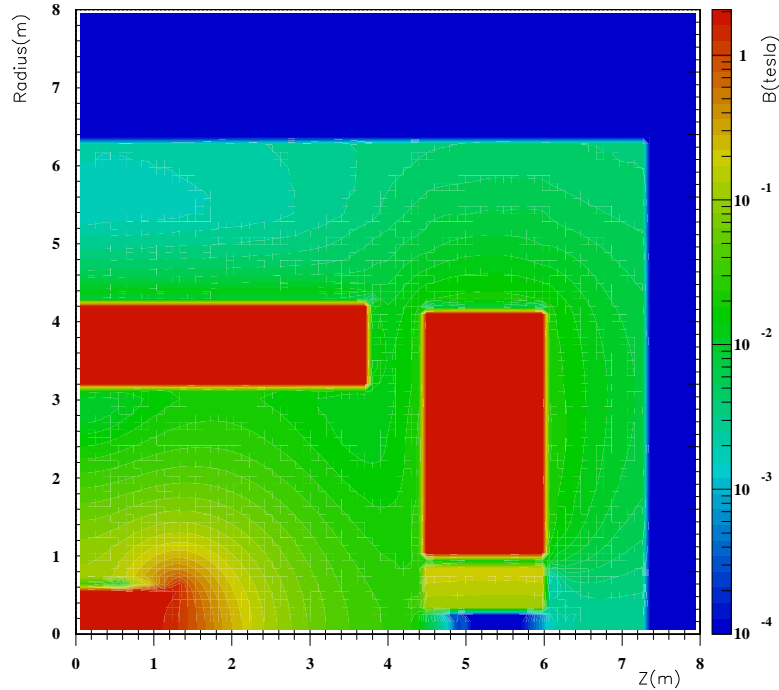


Figure 5.1: Magnetic field map in the DØ detector calculated by the TOSCA program [144].

- Forward system (FAMUS)
 - Octants 0, 3, 4 and 7
 - Octants 1, 2, 5 and 6

This division is based on the difference in geometry between these parts. Both in the WAMUS and FAMUS, the wires are oriented along the y -axis (octants 0, 3, 4 and 7) or along the x -axis (octants 1, 2, 5 and 6). The octants are numbered in the trigonometric sense (with positive sign for ascending angles) starting with octant 0 at $x > 0$ and $y > 0$ (Figure 5.2). However, in the WAMUS, the wire plane is in the x - z or y - z plane, while in the FAMUS this is the x - y plane. To overcome this division, and still be able to have a common algorithm for all different parts, the pattern recognition is not done in the global system but in a local system. This requires a transformation of the reconstructed hits into the local system.

Another problem arises from the fact that the wire hits in the central system (PDT hits) and the wire hits in the forward system (MDT hits) behave differently. The PDT hits need to be updated with the angle to calculate the correct drift distance from the drift time, while the MDT hits need to be updated with a pixel hit for the axial position (and better drift time) information. This is reflected in the algorithm.

The algorithm is divided in 6 steps:

- Transformation of 'global' hits to 'local' hits
- Creation of links between hits

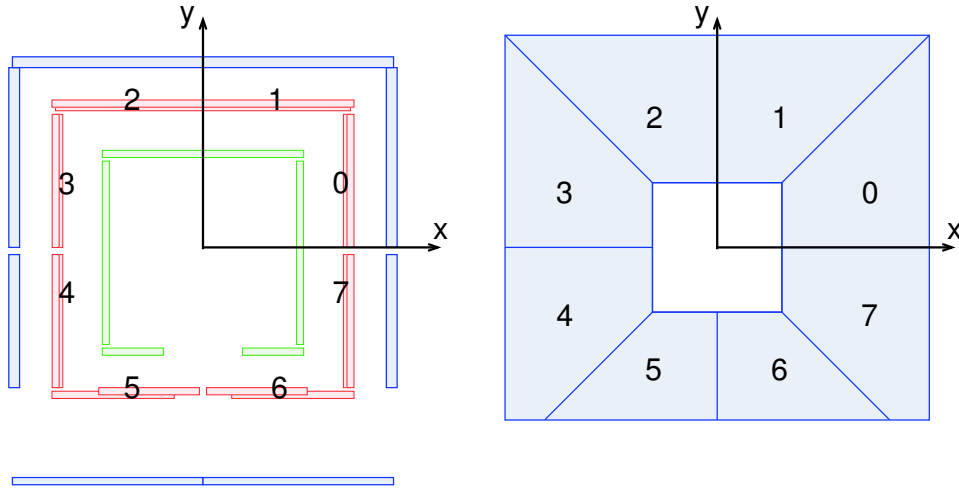


Figure 5.2: View of the chambers of the muon spectrometer in the central (on the left) and in the forward (on the right) region. The digits indicate the octants numbers.

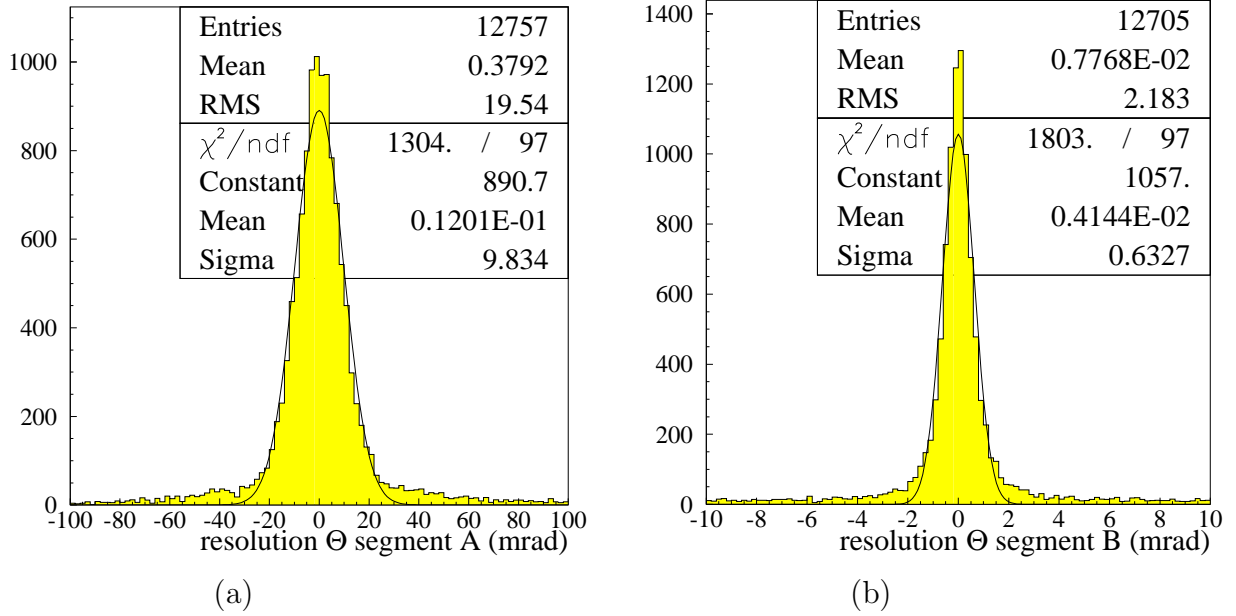


Figure 5.3: Angular resolution (in mrad) of the segments deviation for the layer A (a) and layers BC (b) [143].

- Matching of links into local segments
- Fitting of local segments
- Filtering of local segments based on the fit χ^2 and on the number of hits per segment.
- Fitting of local segments in one layer to local segments in other layers and transformation back to global system

The Figure 5.3 shows the resolution of the segment angle in the deviation plane. The resolution is better in the BC layers than in the A layer as a result of larger lever arm for the BC layers where the hits from the layer B are associated with those from the layer C:

$$\begin{aligned}\sigma_{|\theta_{\text{seg A}} - \theta_{\text{simulated A}}|} &\approx 10 \text{ mrad} \\ \sigma_{|\theta_{\text{seg BC}} - \theta_{\text{simulated BC}}|} &\approx 0.6 \text{ mrad}\end{aligned}$$

5.3 Local track reconstruction

Track segments reconstructed inside and outside the toroid serve as input to the track finding and fitting algorithm. The result of this procedure is a muon track reconstructed in three dimensions, in the muon system.

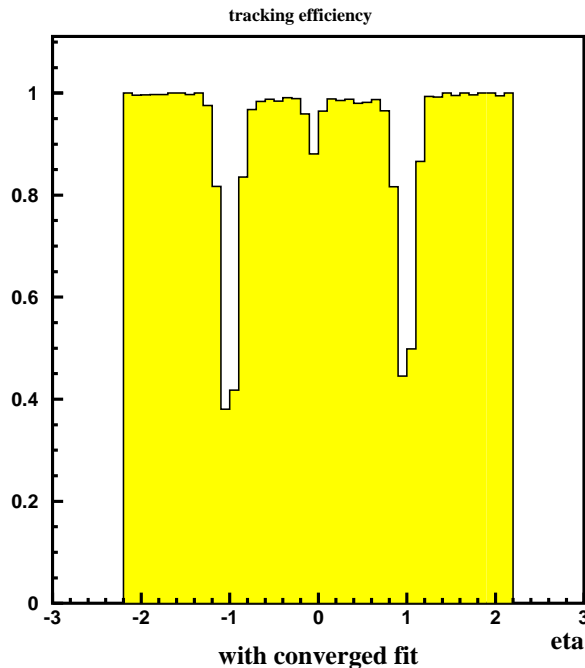


Figure 5.4: Local track reconstruction efficiency as a function of η [143].

Figure 5.4 shows the track reconstruction efficiency as a function of η . This efficiency is defined as a number of found tracks over number of events containing two reconstructed segments, one before and one after the toroid. The mean efficiency to find a track is 81 %.

In the MC events, 78 % of tracks which does not converge with the segments are in the $0.7 \leq |\eta| \leq 1.3$ region. The efficiency drops around $|\eta| = 1$. A possible explanation is that it is not possible to associate the segments coming from different regions (a segment PDT with a segment MDT for example). The same problem exists for the segment reconstruction which does not associate the hits appearing in the different detectors. The segments around $|\eta| = 1$ possess less hits and this affects the resolution.

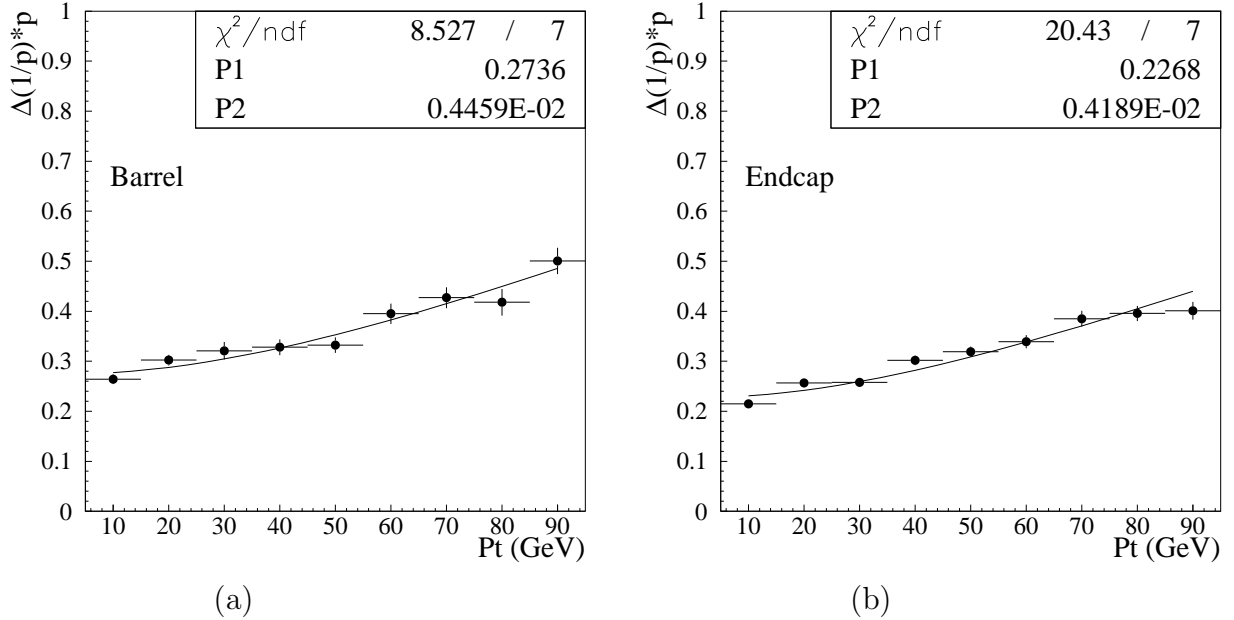


Figure 5.5: Transverse momentum resolution of the reconstructed local track for central (a) and forward (b) region [143].

Figure 5.5 shows the momentum resolution of the reconstructed local tracks for central and forward part of the detector. The momentum dependency of the resolution obtained from the fit to the above histograms is:

$$\begin{aligned} \Delta P_T/P_T &= (27 + 0.44 \times P_T/\text{GeV}) \% \text{ for the central region;} \\ \Delta P_T/P_T &= (23 + 0.42 \times P_T/\text{GeV}) \% \text{ for the forward region.} \end{aligned}$$

The reconstructed track momentum resolution depends also on η . For the same reasons leading to the low track reconstruction efficiency around $|\eta| \approx 1$ the momentum resolution degrades in this region. The momentum resolution as a function of η is shown on the Figure 5.6.

The local muon tracks will be matched with the central tracks (SMT + CFT). A global fit will be made which will result into a better p_T resolution.

5.4 Muon background

Primary background to muon candidates is the cosmic rays. In Figure 5.7 a typical cosmic muon is shown. The most important information used to reject the cosmic background

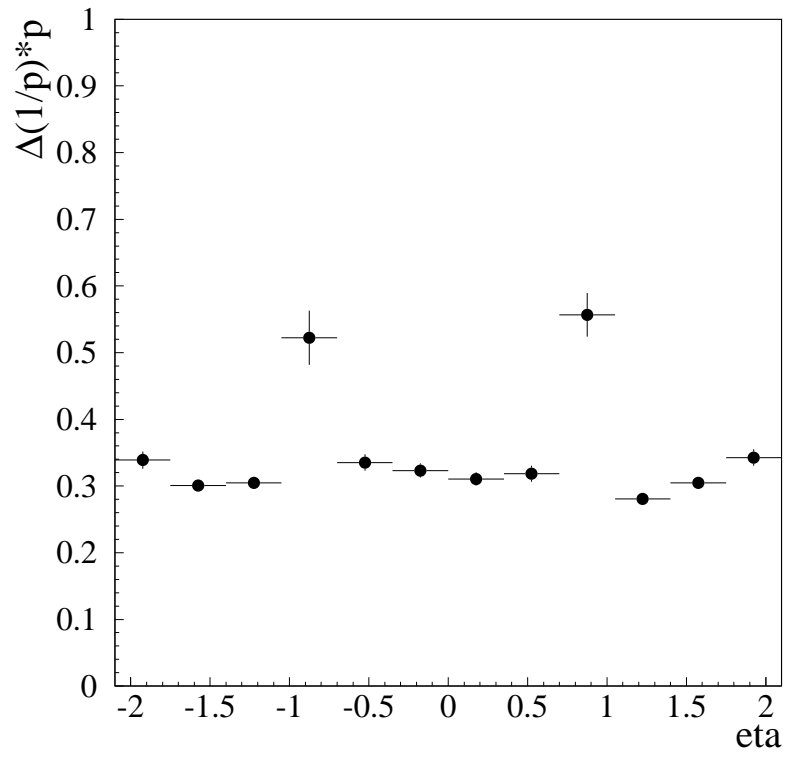
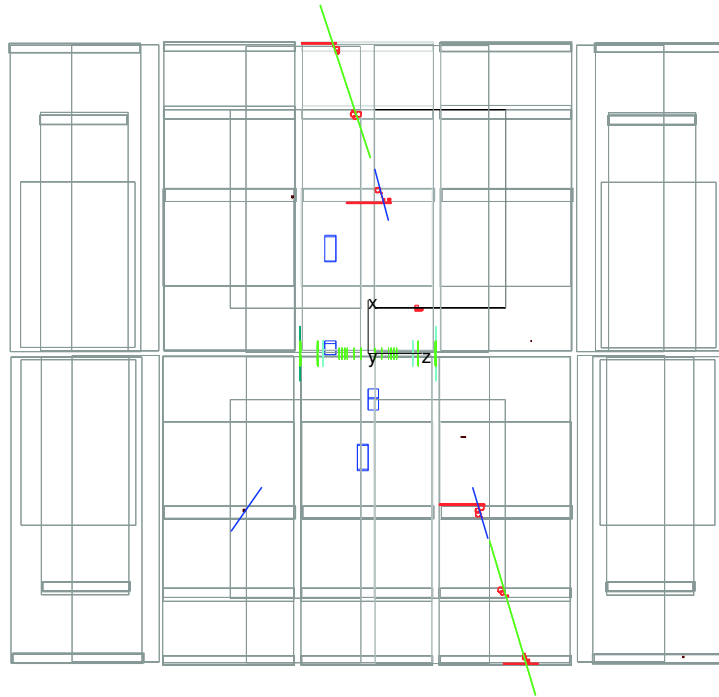


Figure 5.6: Track transverse momentum resolution as a function of η for reconstructed local muon tracks [143].



View 3, Plan (X-Z)

Figure 5.7: Event display of a typical cosmic muon.

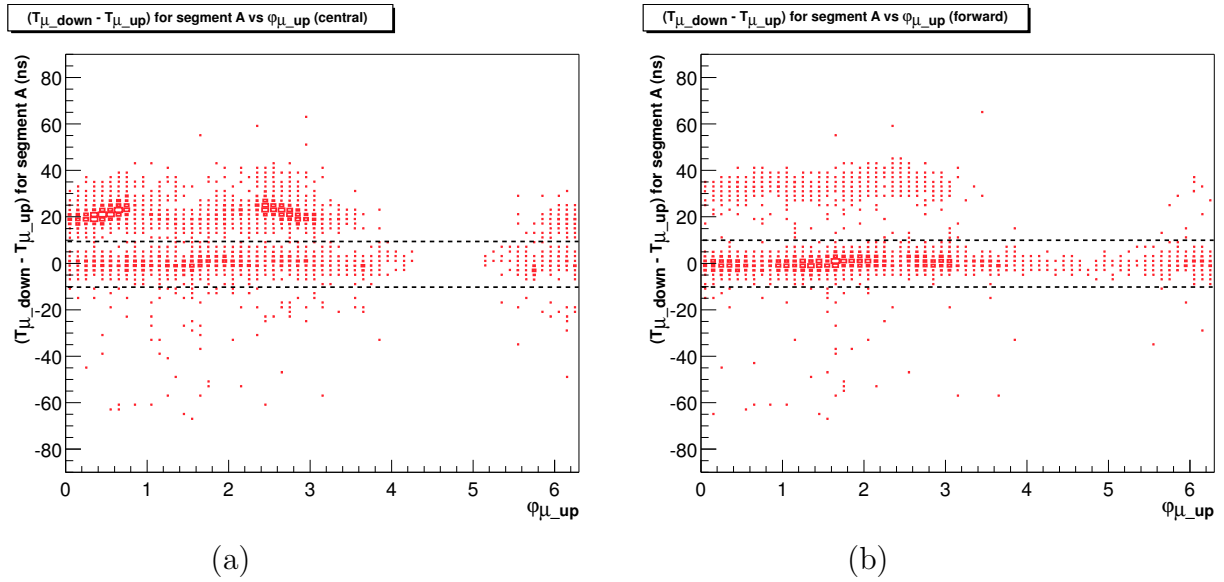


Figure 5.8: Difference between the arrival time of upward muon and downward muon for central (a) and forward (b) region.

is the timing information from the muon detector scintillators. The difference between the arrival time in the A and in the BC layers can be used to reject these events. There are two possibilities for a cosmic muon to be reconstructed by the muon identification software. It can be reconstructed as two local tracks in both parts of the muon detector or as only one local track.

Cosmic muon reconstructed as two local tracks Assuming that a cosmic muon moves with the speed of light and that the distance between opposite parts of the muon detector is ≈ 6 m in the central region and ≈ 9 m in the forward region it will take a cosmic muon between about 20 ns and 30 ns to cross the detector. Figure 5.8 shows difference between the arrival time of upward muon candidate and downward muon candidate (time is measured in the layer A). As it is expected the local tracks with the arrival time difference around 0 are coming from the interaction point, those with the arrival time difference of about 20 ns are cosmic muons crossing the central part of the muon detector and those with the arrival time difference 30 ns are cosmic muons crossing the forward part. As it can be seen from the plots the following cut should efficiently remove the cosmic muons events:

$$|T_{\mu 1} - T_{\mu 2}| < 10 \text{ ns} \quad (5.1)$$

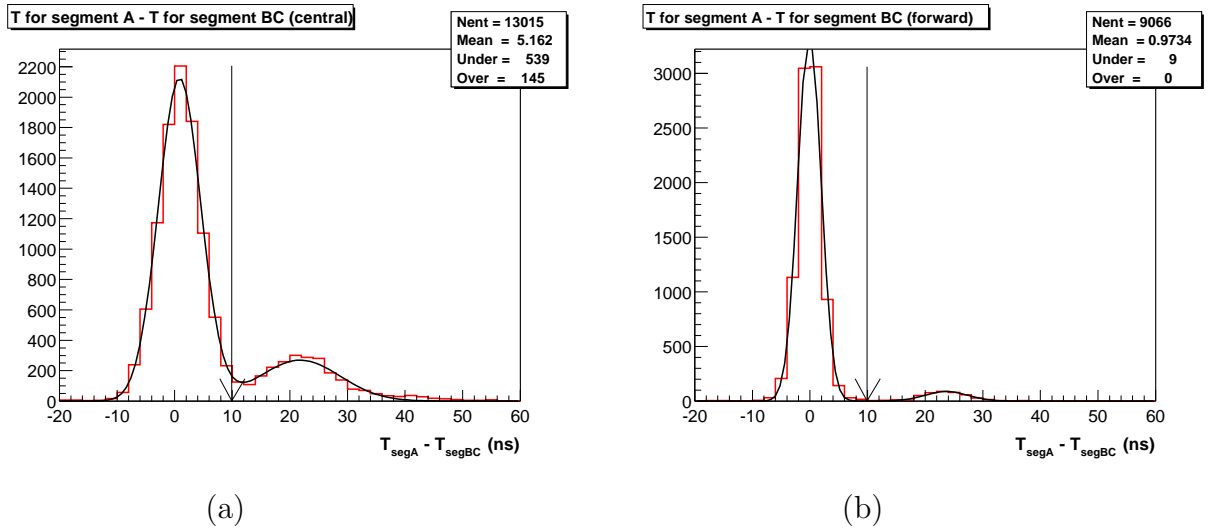


Figure 5.9: Difference between the muon arrival time in the A and in the BC layers for central (a) and forward (b) region.

Cosmic muon reconstructed as one local track Due to acceptance effects some cosmic muons are reconstructed as one local track (the bottom of the $D\bar{O}$ detector is partially covered with muon chambers). To check whether a single reconstructed muon is cosmic the difference between the muon arrival time in the A and in the BC layers can be used. The distance between the A and BC layers of the muon detector is ≈ 3 m both in the central region and in the forward region. It will take a muon about 10 ns to cross this

distance. The timings for A and BC layers are calibrated so that $\langle T_A - T_{BC} \rangle \approx 0$ ns for the muons coming from the interaction point. With this calibration the muons coming from the outside of the detector are expected to have a time difference $\langle T_A - T_{BC} \rangle \approx 20$ ns. Figure 5.9 shows difference between the muon arrival time in the A and in the BC layers.

To eliminate the cosmic muon background two possible selections which can be applied sequentially are proposed:

- time difference calculated for the layer A and for all possible pairs of local tracks should be $|T_{\mu 1} - T_{\mu 2}| < 10$ ns;
- time difference between A and BC layers for all local track should be $T_A - T_{BC} < 10$ ns.

5.5 Conclusion

The DØ muon systems has a good hermeticity. The curvature in the toroide allows the determination of the momentum of the local muon tracks. The p_T resolution of these tracks is improved if they have a matching central track. The timing information allows an efficient rejection of the cosmic rays background.

Chapter 6

Identification of b -quark jets

6.1 Introduction

The study of b -hadrons and processes involving production of b -quarks is one of the main goals of DØ at Run II. In addition to the direct interest in b -quark properties, many particles searched at DØ, like Higgs boson or top quark, have at least one b -quark among their decay products. b -hadrons are also present in the decay of supersymmetric particles and in particular in the hypothesis of R-parity violation by a λ' or λ'' coupling. However the production of b -hadrons at $p\bar{p}$ colliders is hidden in the large background coming from lighter quarks. Thus an efficient technique to select the events with b -hadrons is required.

Run I b -tagging at DØ was based on the detection of soft muon coming from semileptonic decay of a b , in particular muon P_T relative to the jet axis distribution was used [145].

Run II upgraded DØ detector includes a *silicon microstrip tracker* allowing precise reconstruction of long-lived particles decay vertices. We include this feature into the tagging algorithm.

The methods implemented to identify the jets coming from the b -quark fragmentation are presented in this chapter.

6.2 Particularities of the b -quarks jets

The identification of the jets coming from b -quark can use many specific properties of the b -hadrons:

- The lifetimes of b -hadrons are around 1.6 ps . Due to their energy which is typically of the order of few tens of GeV they travel on a significant distance (some millimeters) inside the detector before they decay. Moreover, the b -hadrons disintegrate mainly to the c -hadrons which have as well a lifetime which increases furthermore the travel distance.
- The masses of the b -hadrons are higher than those of other hadrons. The decay products have a larger P_T relative to their flight direction than ordinary hadrons.
- The fragmentation is hard: the b -hadrons carry away a large fraction of the quark energy.

- The b -hadrons have a $\approx 10\%$ probability of decaying to electrons (and similarly for decays to muons).

The flight distance is very an important parameter for the b -tagging. Other features of the event are also sensitive to b -quarks, and some of them are also used together with the flight distance information to construct a combined tag. For example, for a b -hadron which decays semileptonically one can use the presence of an electron or muon with a relative p_T of the order of 1 GeV/ c . On its own, the high- p_T lepton tag would have too low efficiency for many b -quark studies, but the presence of such a lepton is a useful information which can be combined with the long flight distance property. The combined tag also makes use of other variables which have significantly different distributions for b -quark and light quarks, *e.g.* the track rapidities with respect to the jet axis.

6.3 Topological tagging

Regardless of the importance of all other properties, the most crucial one for the selection of b -hadrons is their lifetime. The hadron is moving several millimeters in relation to the point of interaction, its disintegration products do not point anymore towards the primary vertex. An event with a b -jet will have therefore a more rich vertexes structure. Furthermore, the decay tracks from a b -hadron have non-zero impact parameter, *i.e.* when extrapolated backwards in space they do not pass exactly through the primary vertex (see Section 6.3.1).

It is the topology which must be recognized (at least partially) to identify the searched events. There exist essentially two ways to proceed:

- The first one consists in reconstructing all vertexes of the event or at least in a jet. The jet is identified as b -jet if it presents at least one vertex distinct from the primary vertex (criteria is based on its decay length significance $L_{\text{decay}}/\sigma_{L_{\text{decay}}}$). The method requires an excellent reconstruction of the tracks and vertexes parameters to be efficient.
- In the second method the reconstruction of all vertexes is not necessary. To spot tracks inconsistent with the primary vertex the track impact parameter or the distance of closest approach to the interaction point is used.

Both methods have relative merits and disadvantages, which both depend critically on the tracking performance in jets. The dense track environment of jets may lead to high fake track rates and/or low tracking efficiencies in data (the tracking performance of jets in data still needs to be assessed, so these effects are for the most part unknown as of yet). If tracking efficiencies are low, it will be difficult to reconstruct secondary vertices efficiently (especially fully reconstructed secondary vertices), and thus the impact-parameter tag method has the advantage in such a situation that it makes full use of information associated with all tracks in the jet. If fake track rate is high, however, the efficiency of the impact-parameter tag method will be significantly degraded. Thus, the secondary vertex tag may then have an advantage because fake tracks generally do not form good vertexes, and thus probably would not significantly degrade the performance of the tag.

6.3.1 Impact Parameter tag

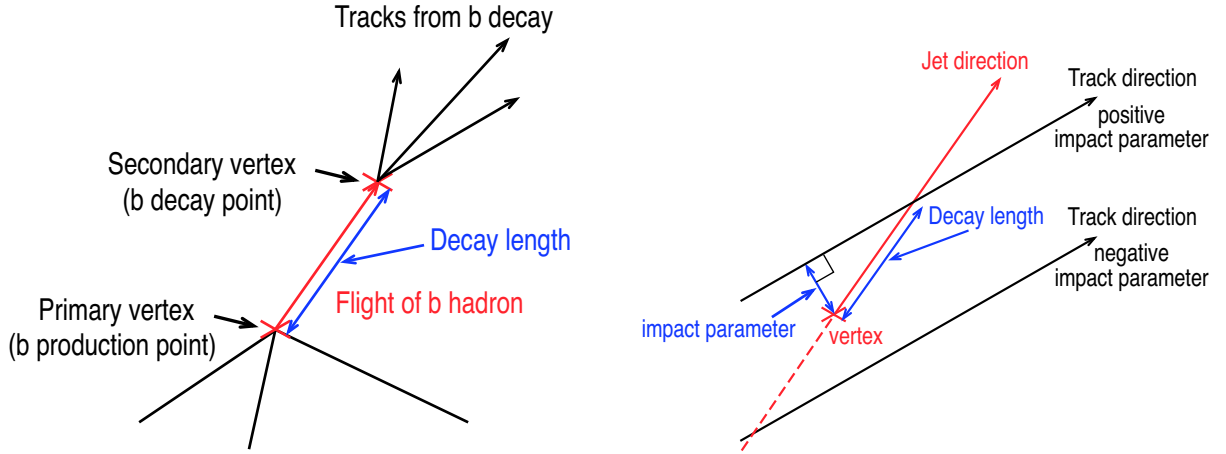


Figure 6.1: Schematic decay pattern of a b -hadron (left) and representation of the signed impact parameter with respect to primary vertex (right).

The impact parameter (IP) is the minimal distance between the reconstructed primary interaction point and the track trajectory. The decay of a long-lived particle produces tracks with large impact parameters, which is not the case for particles from the primary interaction.

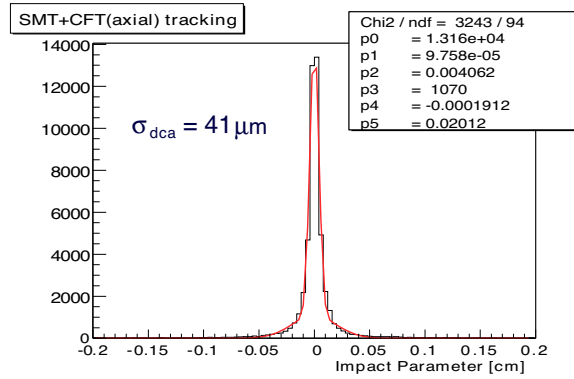


Figure 6.2: Resolution of the impact parameter in the transverse plane [146]

The scale of these impact parameters is $c\tau \approx 400 \mu m$. This is to be compared with the DØ experimental resolution σ (Figure 6.2) of about $\sigma = 41 \mu m$ [146]. This is for the impact parameter (IP) in the plane perpendicular to the beam; along the beam direction, the resolution is slightly worse.

Although in general the IP is defined in 3-dimensional space, for b -tagging the IP projections on the $R\phi$ and Rz planes are used. The main reason for this separation is that the measurement of the particle trajectory in DØ is performed independently in these 2 planes with rather different precision. This is due to the geometry of the Silicon Microstrip

Tracker (described in Section 2.4) and also to the worst precision of the reconstructed vertex in the z direction. The separate treatment of the IP projections provides the freedom to reject outliers in the Rz plane, while keeping useful $R\varphi$ information.

The impact parameter in the $R\varphi$ plane is defined as the minimal distance between the primary vertex (PV) and the track trajectory projected onto the plane perpendicular to the beam direction (Figure 6.1). The point of the closest approach (P_C) of the track trajectory to the primary vertex in the $R\varphi$ plane is also used to define the Rz projection of the IP. Then the Rz projection of the track impact parameter is the difference between the z -coordinates of the primary vertex and of the point P_C . Such a definition of the projections reflects the better precision and quality of the $R\varphi$ measurements, as well as the smaller dimensions of the beam in the transverse directions. In addition, it simplifies the equations for computing the impact parameters, allowing a fast linear approximation in the primary vertex fit.

According to these definitions, there are two ingredients in the IP computation: the parameters of the track trajectory, and the position of the primary interaction, applying the standard error propagation formalism, it follows that:

$$\sigma^2(d_{R\varphi}) = (\sigma_{R\varphi}^{trk})^2 + (\sigma_{R\varphi}^{PV})^2 \quad (6.1)$$

where $d_{R\varphi}$ is the IP projection with respect to the primary vertex position, $\sigma_{R\varphi}^{trk}$ is the error coming from the track fit and $\sigma_{R\varphi}^{PV}$ is the error of the PV position. The track significance is defined as:

$$S_{R\varphi} = d_{R\varphi}/\sigma(d_{R\varphi}) \quad (6.2)$$

The track significance thus compares the measured value of the IP with its expected precision. This quantity is used as an input variable for the b -jet tagging.

Probability for a track to come from the primary vertex

The distribution of the negative track impact parameter significance is determined mainly by tracks coming from the PV, including scatters in the detector material, tracks with wrong hit association etc, while the contribution of tracks coming from decays of long-lived particles is relatively small. Figure 6.3 (left) shows the distribution of track impact parameter significance. The negative side of the distribution is folded on the positive side. The excess seen on positive side is attributed to long-lived particles (with a slight contamination coming from K^0). The distribution of the negative track impact parameter significance can thus be used to define the probability $P(S_{R\varphi}^0)$ for a track from the PV to have its measured value of significance equal to or exceeding the value $S_{R\varphi}^0$. This function is obtained by integration of the probability density function of the negative significance $f(S)$ from $S_{R\varphi}^0$ to infinity and assuming that $P(S^0)_{R\varphi}$ is the same for primary tracks with either positive or negative significance:

$$P(S_{R\varphi}^0) = \begin{cases} \int_{S_{R\varphi} < -S_{R\varphi}^0} f(S_{R\varphi}) dS_{R\varphi} & \text{if } S_{R\varphi}^0 < 0, \\ P(-S_{R\varphi}^0) & \text{if } S_{R\varphi}^0 > 0. \end{cases} \quad (6.3)$$

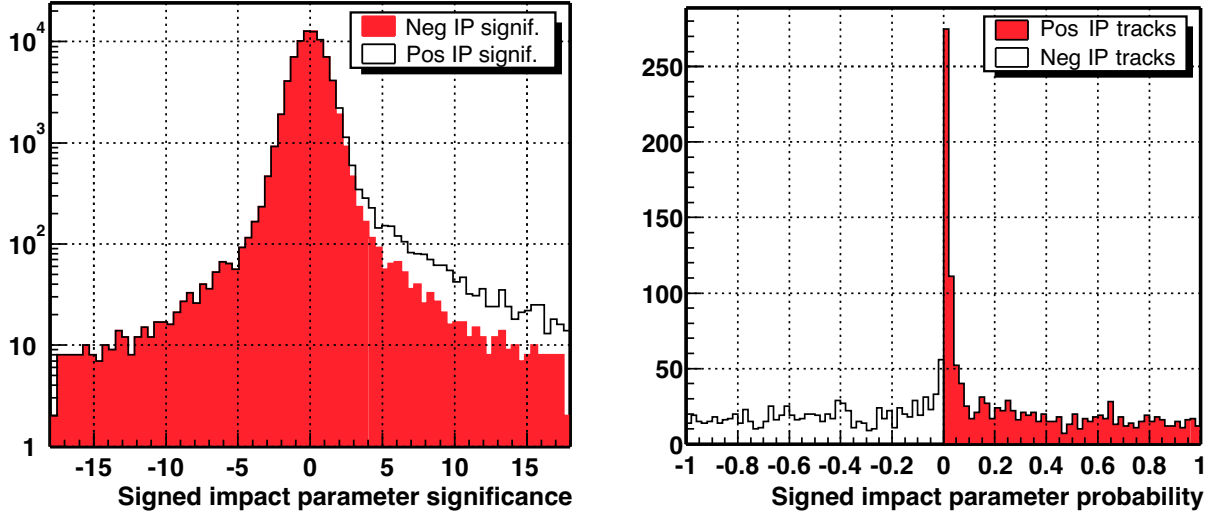


Figure 6.3: Signed track impact parameter significance (left) and track impact parameter probabilities (right) [147].

By definition, tracks from the PV have a flat distribution of $P(S_{R\varphi}^0)$ between 0 and 1, while tracks from decays of long-lived particles have large positive values of $S_{R\varphi}^0$ and receive small values of $P(S_{R\varphi}^0)$, reflecting the small probability for tracks from the primary vertex to have such large values of the IP and hence of $S_{R\varphi}^0$. As an example, Figure 6.3 shows the distribution of $P(S_{R\varphi}^0)$ for tracks with positive and negative IP. The peak at low probability $P(S_{R\varphi}^0)$ for tracks with positive IP corresponds to the tracks which have a large significance and it is produced mainly by the long-lived particles. The transformation of the significance distribution into the track probability is referred to as the calibration of the detector resolution.

Impact parameter discriminant

Track probabilities are directly used to construct a lifetime probability. For any group of N tracks it is defined as:

$$P_N = \prod \cdot \sum_{j=0}^{N_{R\varphi}-1} \frac{(-\ln \prod)^j}{j!} \quad (6.4)$$

$$\prod = \prod_{i=1}^{N_{R\varphi}} P(S_{R\varphi}^i)$$

Here $P(S_{R\varphi}^i)$ is the track probability and $N_{R\varphi}$, is the number of $R\varphi$ measurements used in the tagging. The proof that this variable behaves as a probability is given in [148].

The variable P_N has a simple and straightforward definition and can be computed for any group of tracks (*e.g.* a jet, hemisphere or whole event) which makes it flexible and easily adjustable to different physics applications. It is a very useful variable, accumulating the discriminating power of all tracks considered.

The meaning of the variable P_N is very similar to that of track probability: it is the probability for N tracks coming from the PV to have their product of significances equal to or exceeding the observed value. P_N really behaves as a probability: it varies between 0 and 1 and has a flat distribution for any group of N uncorrelated tracks coming from the PV. (The definition of P_N thus ignores the small off-diagonal elements of the IP error matrix, coming from the use of some of the tracks in defining the PV.)

An attractive feature of lifetime tagging is that it is constructed using only the track impact parameters. This provides the possibility to achieve a good b -tagging efficiency by the accurate tuning of the track resolution with simulated data.

This tagging method has been applied to Monte-Carlo samples. More specifically, the conditions applied to the tracks are as follows. All tracks with positive IP and at least 4 measurements in the SMT are used for lifetime tagging.

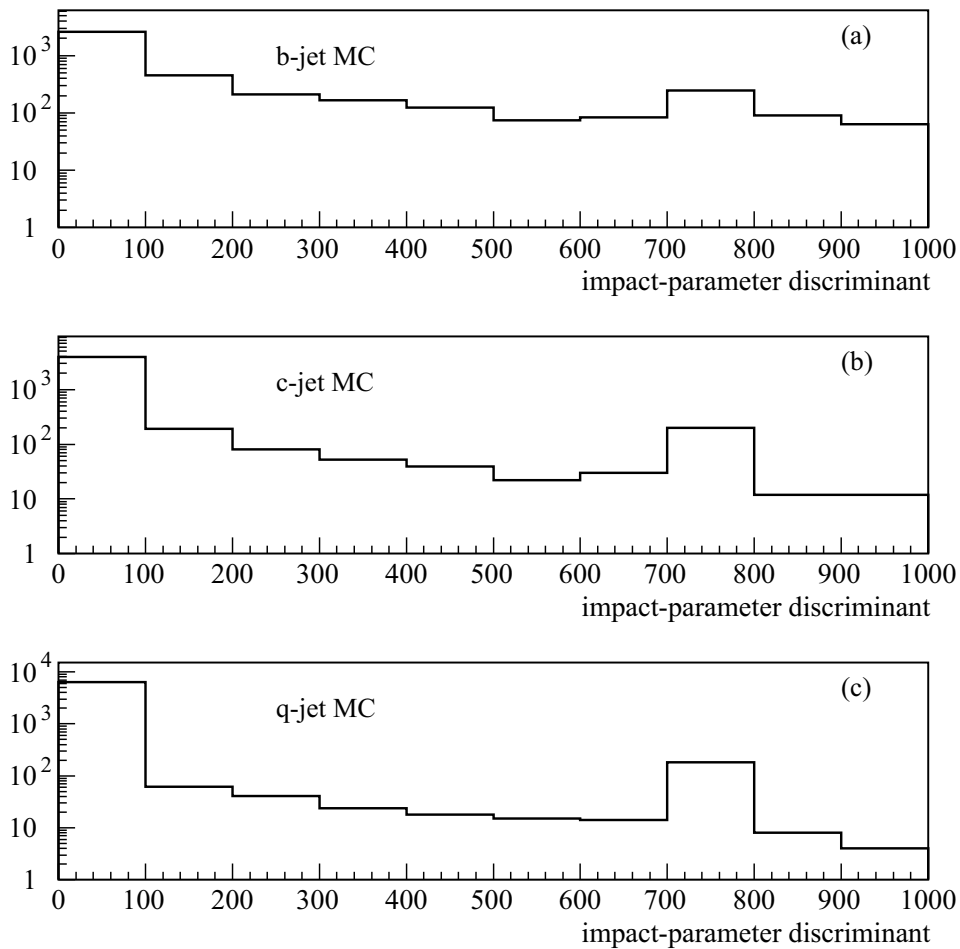


Figure 6.4: Impact-parameter discriminant ($-\ln(P_N)$) distributions for b , c , and light-quark jets in the Monte Carlo samples ("non-taggable" jets due to a dearth of reconstructed tracks have a discriminant of zero, and are included in the plot) [149].

Figure 6.4 shows the IP discriminant ($-\ln(P_N)$) distribution for b , c , and light-quark jets in the Monte Carlo samples ("non-taggable" jets due to a dearth of reconstructed

tracks have a discriminant of zero, and are included in the plot) [149]. The b quark jets tend to have, on average, larger IP discriminants than c jets, which in turn tend, on average, to have larger IP discriminants than light-quark jets.

6.3.2 Secondary vertex tag

Figure 6.5 shows the $\Delta R(\text{jet}, \text{vtx}) = \sqrt{\Delta\varphi^2 + \Delta\eta^2}$ of the reconstructed secondary with respect to the jet axis, for a $b\bar{b}$ MC sample. To associate a secondary vertex with a particular jet, the vertex has to be within

$$\Delta R(\text{jet}, \text{vtx}) < 0.3.$$

where vtx is the direction to the secondary vertex defined as line joining the primary and the secondary vertexes. The reconstructed secondary vertex is required to contain at least 2 tracks and at least one of the tracks with $p_T > 1.5 \text{ GeV}/c$ [150].

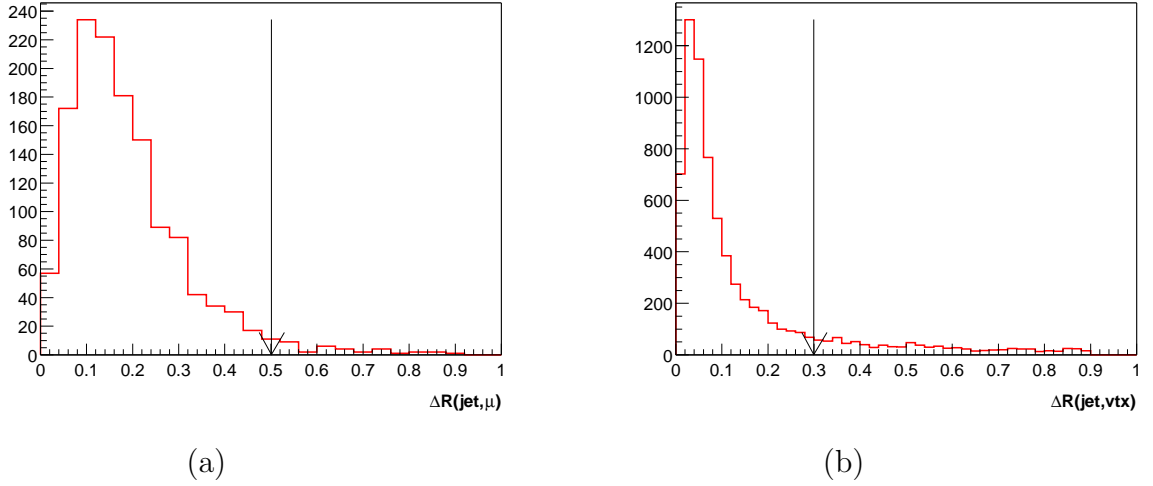


Figure 6.5: $\Delta R(\text{jet}, \mu) = \sqrt{\Delta\varphi^2 + \Delta\eta^2}$ between jet and muon (a), and jet and secondary vertex (b) for a $b\bar{b}$ MC sample. Chosen cuts are shown as vertical arrows.

The decay length significance is calculated in the transverse plane to the beam in the following way:

$$\frac{L_{xy}}{\sigma_{L_{xy}}} = \frac{(x_0 - x_1)^2 + (y_0 - y_1)^2}{\sqrt{(x_0 - x_1)^2(\sigma_{x_0}^2 + \sigma_{x_1}^2) + (y_0 - y_1)^2(\sigma_{y_0}^2 + \sigma_{y_1}^2)}} \quad (6.5)$$

where x_0, y_0 and x_1, y_1 are the coordinates of the primary vertex and the secondary vertex respectively. Finally, the secondary vertex discriminant is defined as [150]:

$$D_{svx} = \begin{cases} 1 & \text{if } \frac{L_{xy}}{\sigma_{L_{xy}}} > 3 \text{ for any of the associated vertexes,} \\ 0 & \text{otherwise.} \end{cases} \quad (6.6)$$

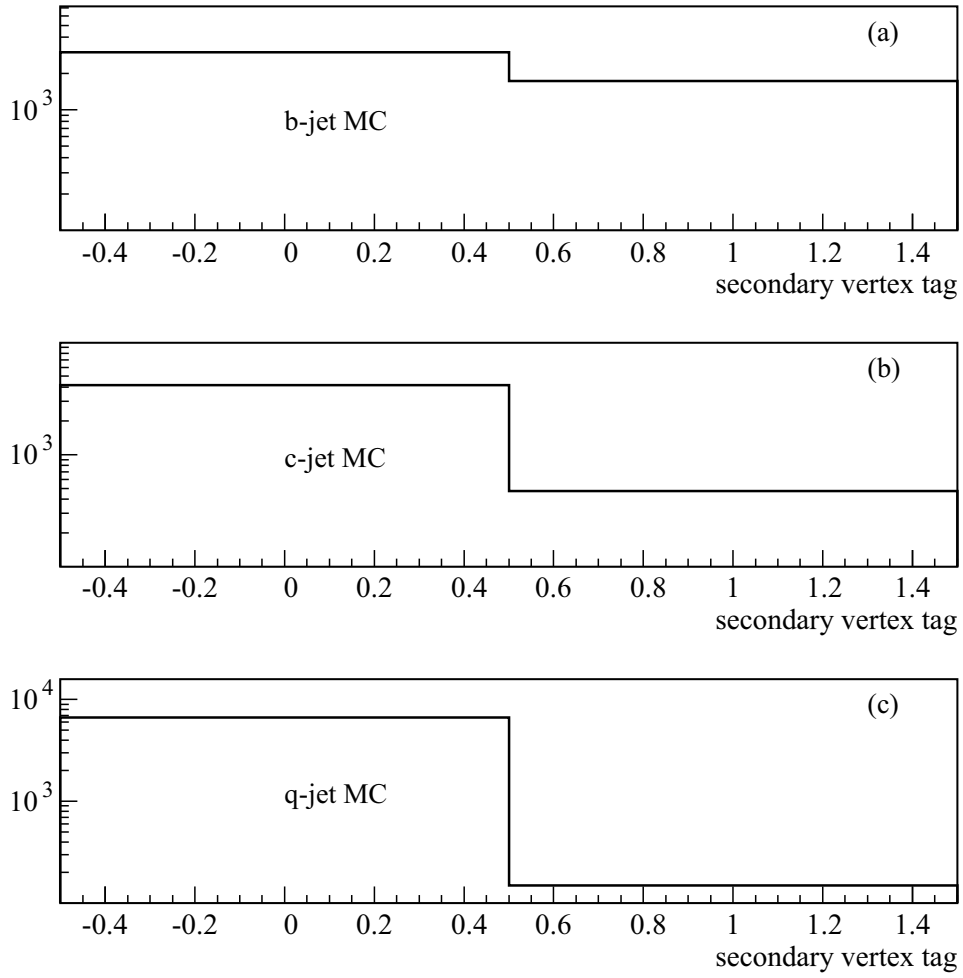


Figure 6.6: Secondary-vertex tag distributions for b , c , and light-quark jets in the Monte Carlo samples.

Figure 6.6 shows the secondary vertex tag distribution for b , c , and light-quark jets in the Monte Carlo samples. Again, the b quark jets tend to be, on average, more probable to pass this tag than c jets, which in turn tend to be more probable to pass the tag than light-quark jets.

6.4 Tagging with muons

The identification with muons leans on the following properties of b -hadrons: the lepton coming from the semi-leptonic decay of a b -hadron have indeed high transverse momentum. For an hadronic collider where the environment is dominated by the QCD processes it is an interesting signature: for example, CDF has measured that 90 % of electrons with $p_T > 12$ GeV/ c come from b -hadrons (after subtraction of the production by W and Z) [151].

The method however is not very efficient, on the one hand because of $Br(b \rightarrow l) \approx 18\%$ ($l =$ electron and muon) and because the lepton which is near/inside the jet must be identified. In order to obtain an acceptable efficiency, the lepton p_T cut (p_T^{min}) relative to the jet has to be rather low. Identification is particularly difficult for electron. Specific method called "road method" [152] to reconstruct electron near jet has been developed by the Orsay laboratory (LAL). The work is not so challenging for muons which are reconstructed in the muon system. Nevertheless, it is necessary to match them with the tracking system in order to have a precise determination of their direction and momentum.

Figure 6.5 shows the $\Delta R(jet, \mu) = \sqrt{\Delta\varphi^2 + \Delta\eta^2}$ of the reconstructed muon with respect to the jet axis, for a $b\bar{b}$ MC sample. To associate a muon with a particular jet, the muon has to be within

$$\Delta R(jet, \mu) = \sqrt{\Delta\varphi^2 + \Delta\eta^2} < 0.5. \quad (6.7)$$

The P_{Trel} between the muon and the jet is defined as the relative momentum of the muon with respect to the combined muon + jet axis, as is shown in Figure 6.7. The higher P_{Trel} is a consequence of the higher mass of the b -quark with respect to the c and lighter quarks. This variable has been used successfully in Run I to tag b -jet in order to measure b -jet cross section and is expected to give even better results in Run II due to the improvements of the muon and the tracking systems.

Figure 6.8 shows the P_{Trel} distribution for the three different MC samples, QCD, $c\bar{c}$ and $b\bar{b}$ [153]. A clear distinction can be made between background and the $b\bar{b}$ sample. The best discriminant to distinguish b -jets from c -jets and light quark jets is currently the muon momentum transverse to the jet direction (P_{Trel}) variable.

To tag b -jets using the P_{Trel} variable, one needs to define a value above which a jet is defined as being a b -jet. Both the efficiency and the miss-identification rate of the method depend on this value. Figure 6.9 shows the tagging efficiency as a function of the P_{Trel} cut applied, in the top plot, for the $b\bar{b}$ sample. This efficiency is normalized to the number of b -jets in the sample, and consequently is a convolution of a number of efficiencies:

$$\epsilon_{method} = \epsilon_{b \rightarrow \mu} \cdot \epsilon_{reco} \cdot \epsilon_{P_{Trel}} \quad (6.8)$$

where:

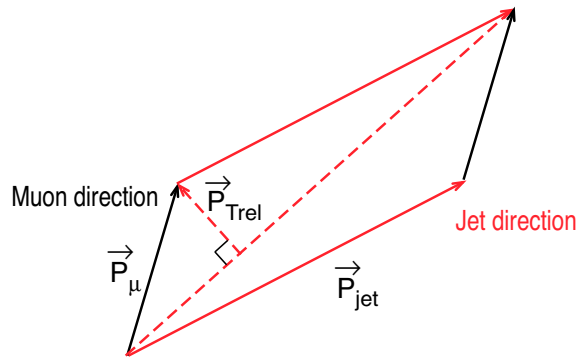


Figure 6.7: P_{Trel} definition.

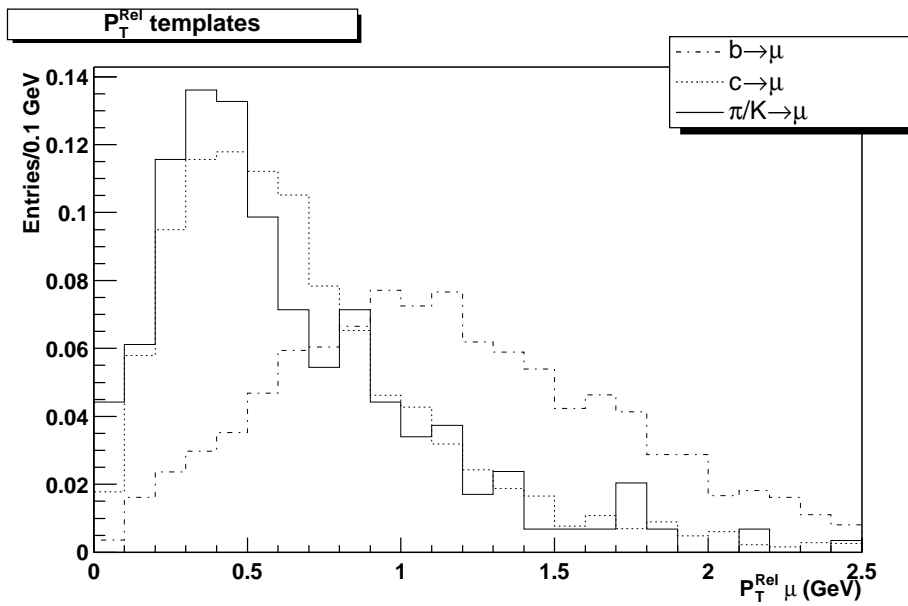


Figure 6.8: Muon P_{Trel} distribution of three MC samples. Solid is QCD, dotted $c\bar{c}$, dashed $b\bar{b}$ [153].

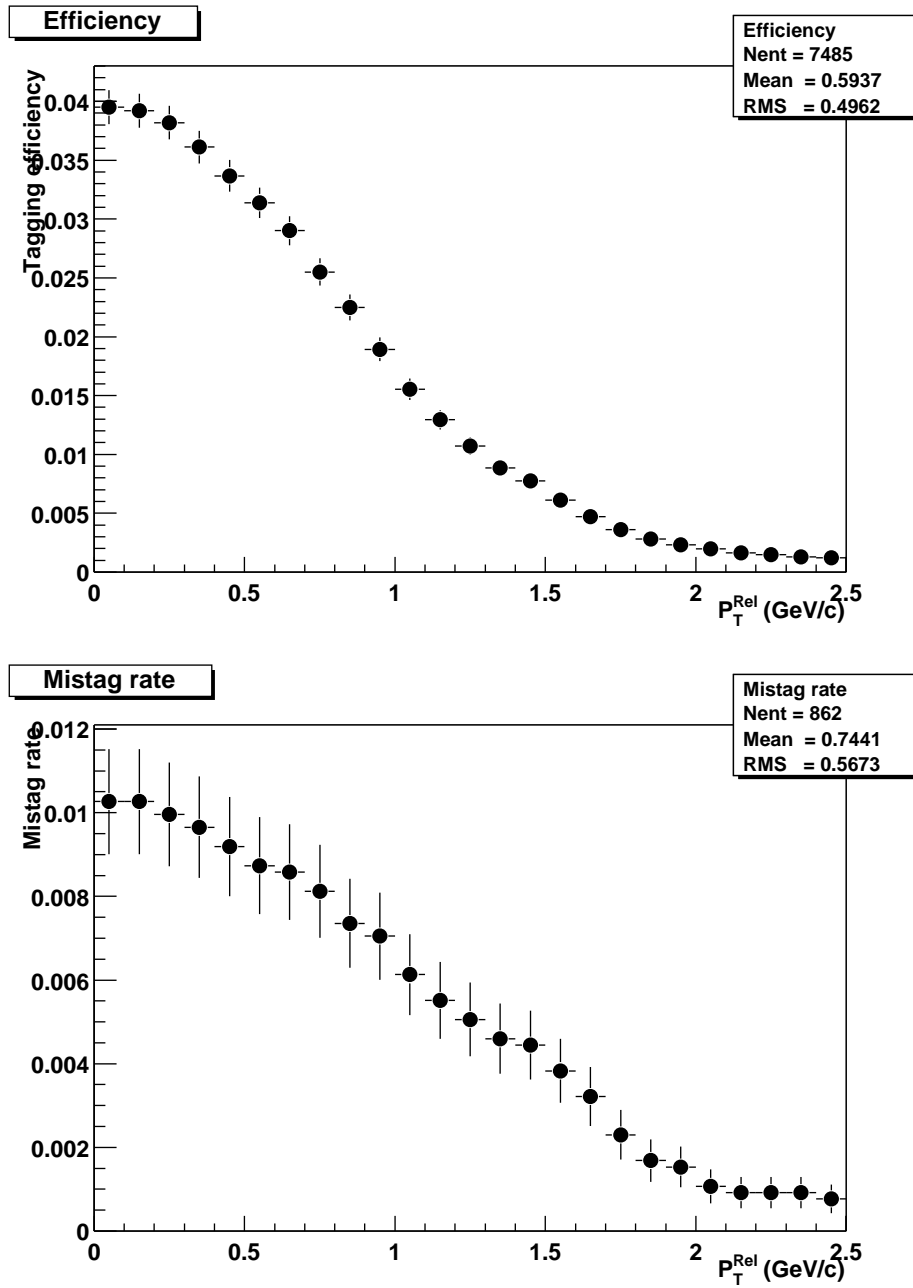


Figure 6.9: The top plot shows the efficiency to tag a b -jet in the $b\bar{b}$ sample as function of the P_{Trel} cut applied. The bottom plot shows the efficiency to tag a light jet in the sample. There is no requirement on an associated muon present with the jet.

- ϵ_{method} — the efficiency to tag a b -jet, ~ 0.02 ;
- $\epsilon_{b \rightarrow \mu}$ — the probability of having a muon in the b -jet from direct b -decay, ~ 0.1 ;
- ϵ_{reco} — the efficiency to reconstruct the muon and identify it as a tight muon, ~ 0.47
- $\epsilon_{P_{Trel}}$ — the efficiency of the P_{Trel} cut, ~ 0.5 for a $P_{Trel} > 1$ GeV/ c .

The bottom plot in Figure 6.9 shows the efficiency to tag a light (non b) jet in the same $b\bar{b}$ sample as a b -jet. This efficiency is normalized to all light jets in the sample. One sees that the tagging rate is around a factor of four higher than the mis-identification rate.

6.5 Combined tagging

Efficient utilization of different properties of b -hadrons requires the development of a technique for their combination into a single tagging variable. The simplest solution is a system of cuts on different discriminating variables. But the method was shown to be not satisfactory due to a significant overlap between the signal and background for some of the discriminating variables. Instead, a likelihood ratio method of a combination of variables is more adapted for the DØ experiment. This approach has the important advantage of being technically very simple while at the same time providing a powerful separation of signal and background. For independent variables, it gives optimal tagging [154]. It can easily be extended to any number of discriminating variables, and can deal with different number of variables in different events. However, its practical application requires the careful selection of variables with reduced correlations among them. The description of this likelihood ratio method, the set of variables used and the performance of the combined b -tagging is given below.

6.5.1 Description of the method

The combined tagging variable y in the likelihood ratio method is defined as:

$$y = \frac{f^{bgd}(x_1; \dots; x_n)}{f^{sig}(x_1; \dots; x_n)} \quad (6.9)$$

where $f^{bgd}(x_1; \dots; x_n)$, $f^{sig}(x_1; \dots; x_n)$ are the probability density functions of $x_1; \dots; x_n$ discriminating variables for the background and the signal respectively. The selection of all events with $y < y_0$ gives the optimal tagging of the signal. It should be stressed that such tagging is absolutely the best for a given set $x_1; \dots; x_n$ of variables.

In practical applications the determination and utilisation of multidimensional probability density functions is quite difficult for $n > 2$. The solution consists in a special selection of discriminating variables having reduced correlations among them. In the limit of independent variables, expression (6.9) becomes:

$$y = \prod_{i=1}^n \frac{f^{bgd}(x_i)}{f^{sig}(x_i)} = \prod_{i=1}^n y_i \quad (6.10)$$

where $f_i^{bgd}(x_i)$, $f_i^{sig}(x_i)$ are probability density functions of each individual variable x_i for the background and signal, and are determined from simulation.

This scheme is used to construct the combined b -jet tag. For each individual variable x_i the value y_i is computed; the combined tag y is defined as the product of the y_i . It is not absolutely optimal any more, because the discriminating variables are not independent, but due to their special selection the correlations between them are small enough so that the resulting tagging is very close to optimal.

All discriminating variables and the likelihood ratio itself are computed independently for each jet in an event, where ideally all tracks coming from the fragmentation of the b -quark and from the decay of the b -hadron are combined in one jet by a jet clustering algorithm. In this case the background for the b quark selection can be separated in two different parts - jets generated by c -quarks and by light ($q = u; d; s$) quarks. These two parts are independent and have very different distributions of discriminating variables.

To define the extra discriminating variables for the b -tagging, tracks are selected so as to come preferentially from b -hadron decay. For this purpose all jets in an event are classified into 3 categories:

- In the first category all jets with one or more reconstructed secondary vertices are included. A reconstructed secondary vertex provides a clean selection of b -hadron decay products and a number of discriminating variables can be defined in this case.
- If the secondary vertex is not reconstructed, the particles from a b -hadron decay are selected by requiring the track significance probability to be less than 0.05, and the second category includes all jets with at least 2 such tracks. This criterion is less strong, allowing more background jets to pass the cut.
- Finally, if the number of tracks with significance less than 0.05 is less than 2, the jet is included in the third category and in this case only the reduced set of inclusive discriminating variables, like the jet probability (see Section 6.3), is used.

The modified tagging variable y_α for each category α is defined as:

$$y_\alpha = n_\alpha^c/n_\alpha^b \prod_{i=1}^n y_{i,\alpha}^c + n_\alpha^q/n_\alpha^b \prod_{i=1}^n y_{i,\alpha}^q \quad (6.11)$$

$$y_{i,\alpha}^{(c,q)} = f_\alpha^{(c,q)}(x_i)/f_\alpha^b(x_i)$$

where $f_\alpha^q(x_i)$, $f_\alpha^c(x_i)$, $f_\alpha^b(x_i)$ are the probability density functions of x_i in jet category α generated by uds , c and b quarks respectively and n_α^q , n_α^c and n_α^b are their normalised rates, such that $\sum n_\alpha^q = R_q$, $\sum n_\alpha^c = R_c$, and $\sum n_\alpha^b = R_b$. R_q , R_c and R_b are the normalised production rates of different flavors and $R_q + R_c + R_b = 1$

As can be seen from (6.11), the classification into different categories effectively works as an additional discriminating variable with the discrete probabilities given by $n_\alpha^{(q,b,c)}$. However, the primary purpose of this separation is to allow the clean definition of a large set of discriminating variables, which is only possible when the secondary vertex is reconstructed. The search for the secondary b -hadron decay vertex is thus an important ingredient of b -tagging.

6.5.2 Tagging algorithm

The present version of likelihood b -tagging algorithm is applied to secondary vertices and muons within a jet.

A secondary vertex is associated to a jet if

$$\Delta R(\text{jet}, \text{vtx}) = \sqrt{\Delta\varphi^2 + \Delta\eta^2} < 0.3.$$

The reconstructed secondary vertex is required to contain at least 2 tracks not compatible with primary vertex and to have $p_T > 0.5 \text{ GeV}/c$.

A muon is associated with a jet if

$$\Delta R(\text{jet}, \mu) = \sqrt{\Delta\varphi^2 + \Delta\eta^2} < 0.5.$$

The algorithm combines the transverse momentum of identified muons with the variables based on the vertex mass and relatively long decay length of the b -hadron. All the available information is combined using multivariate techniques. The lifetime information exploits the large distance between primary and secondary vertices together with a search for secondary and tertiary vertices based on their invariant masses.

The density distribution $f_\alpha^l(x_i)$ ($l = q, c, b$) is modeled by a training sample of simulated events that is different and tuned for each data set. The probability that a jet comes from b quark is

$$\mathcal{P}_\alpha^b = \frac{1}{1 + y_\alpha} \quad (6.12)$$

The output is closer to 1 for "signal-like" events and to 0 for "background-like" events.

6.5.3 Discriminating variables

In this section the discriminating variables used in the b -tagging are described. All definitions are given for jets with reconstructed secondary vertices. The distributions of all discriminating variables, except the jet probability discussed in Section 6.3, are shown in Figure 6.10. These distributions are shown for b quark jets and for uds quark jets, which constitute the main background for b -tagging.

6.5.4 Decay length significance

The decay length significance is calculated in the transverse plane to the beam as shown in (6.5).

Secondary vertex mass

The large masses of the b -hadrons relative to light-flavor hadrons make it possible to distinguish b -hadron decay vertices from those found in light flavors events. However, due to the missing particles, M_{vtx} cannot be fully determined. We shall define a vertex invariant mass "à la SLD", M_{vtx} [156]. In the rest frame of the decaying hadron, M_B can be written as

$$M_B = \sqrt{M_{ch}^2 + P_{ch\perp}^2 + P_{ch\parallel}^2} + \sqrt{M_0^2 + P_{0\perp}^2 + P_{0\parallel}^2} \quad (6.13)$$

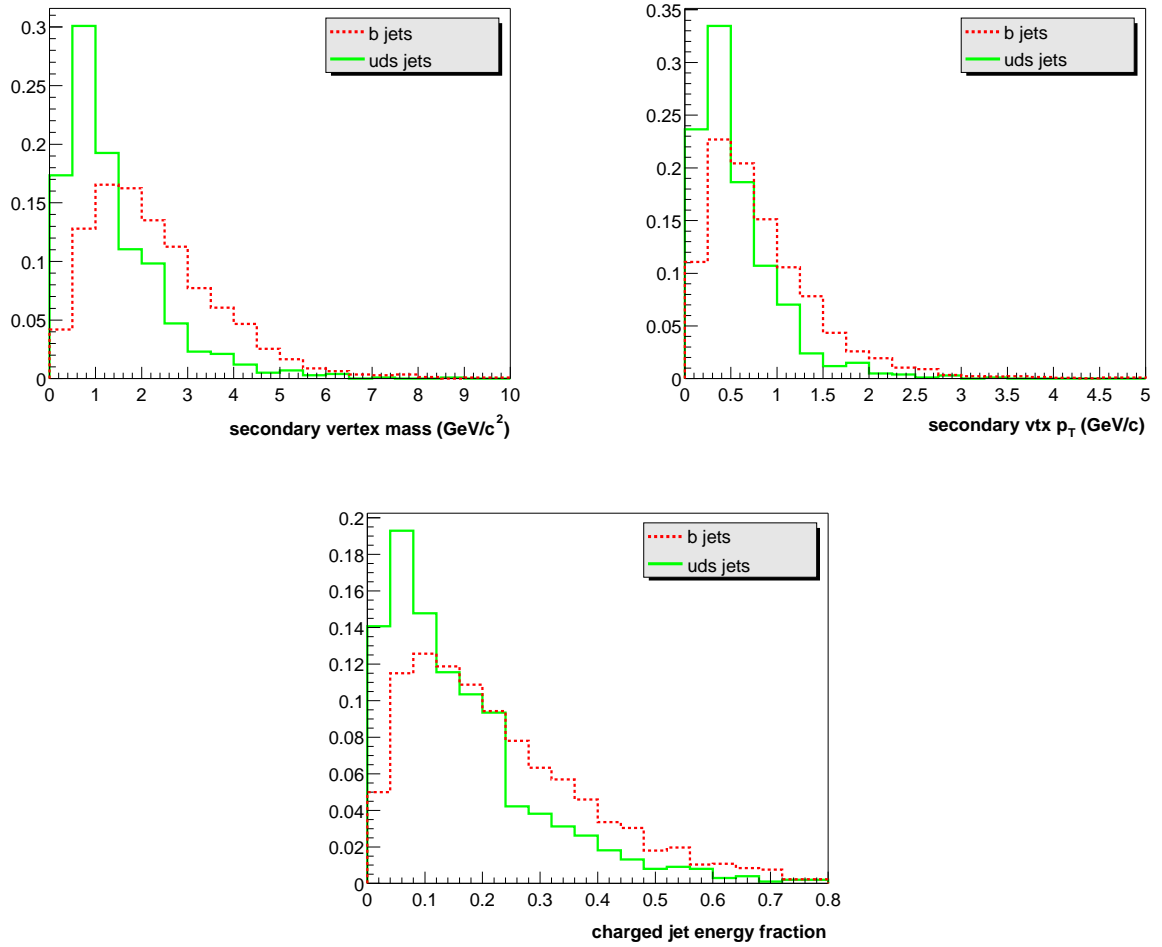


Figure 6.10: Distribution of discriminating variables for *uds* and *b*-quark jets.

where M_{ch} and M_0 are the total invariant masses of the set of vertex-associated tracks and the set of missing particles, respectively. $P_{ch\perp}$ is the total charged track momentum transverse to the b -hadron flight direction, which is identical to the transverse momentum of the set of missing particles $P_{0\perp}$ by momentum conservation. $P_{ch\parallel}$ and $P_{0\parallel}$ are the respective momenta along the b -hadron flight direction. In the b -hadron rest frame, $P_{ch\parallel} = P_{0\parallel}$. Using the set of vertex-associated charged tracks, we calculate the total momentum vector \vec{P}_{ch} , the total energy E_{ch} and the invariant mass M_{ch} , assuming the charged pion mass for each track. The b -hadron flight direction is defined by the line joining the primary and the secondary vertex. The lower bound for the mass of the decaying hadron

$$M_{vtx} = \sqrt{M_{ch}^2 + P_{ch\perp}^2} + |P_{ch\parallel}|$$

is used as the discriminating variable. The mass of the secondary vertex for c -jets is limited by the mass of D -mesons, and above $M_{vtx} = 1.8 \text{ GeV}/c^2$ the number of c -jets decreases sharply, while for b -jets the mass distribution extends up to $7 \text{ GeV}/c^2$ due to detector resolution.

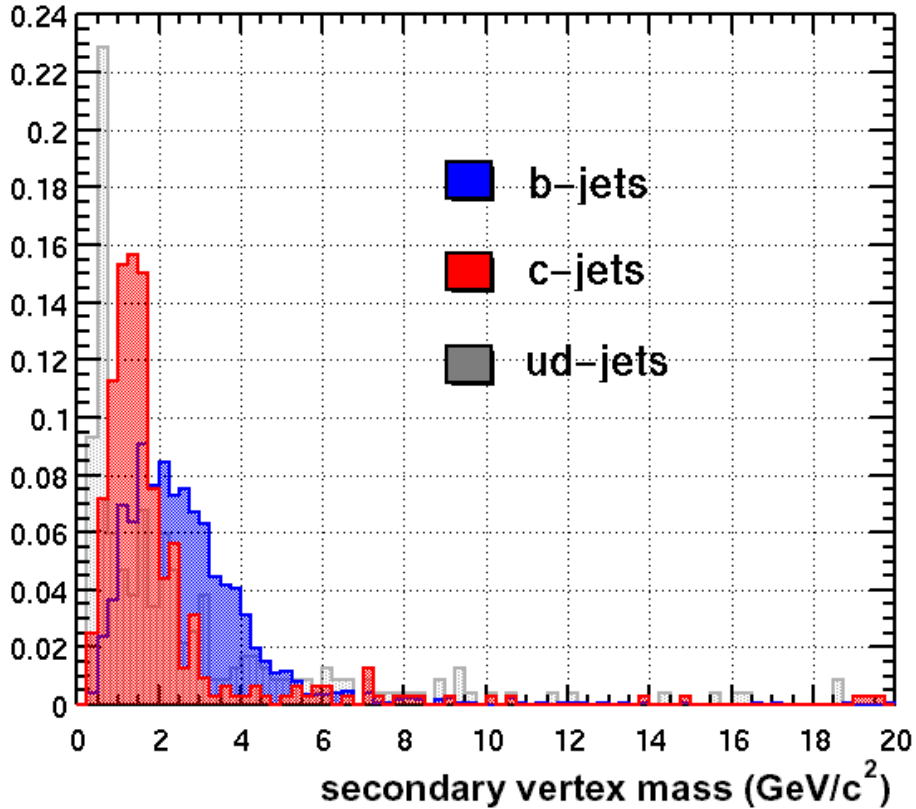


Figure 6.11: Distribution of the secondary vertex invariant mass for uds , c and b -quark jets.

Charged jet energy fraction

The fraction of the charged jet energy included in the secondary vertex, X_{ch} , reflects the differences in the fragmentation properties of different flavors. The fragmentation function for the c -quark is softer than for the b -quark, as seen in the distribution of X_{ch} in Figure 6.10.

Secondary vertex transverse momentum

The transverse momentum at the secondary vertex, $P_{T_{svtx}}$, first introduced by the SLD collaboration [156], takes into account missing particles not included in the secondary vertex definition. $P_{T_{svtx}}$ is defined as the resultant transverse momentum (with respect to the b -hadron estimated flight direction) of all particles attached to secondary vertex. The missing particles can be neutrinos from semileptonic decay, all neutral particles or non-reconstructed charged particles. In all cases, due to the high mass of the b -hadron, the value of $P_{T_{svtx}}$ for b -quark jets is higher, as can be seen from Figure 6.10.

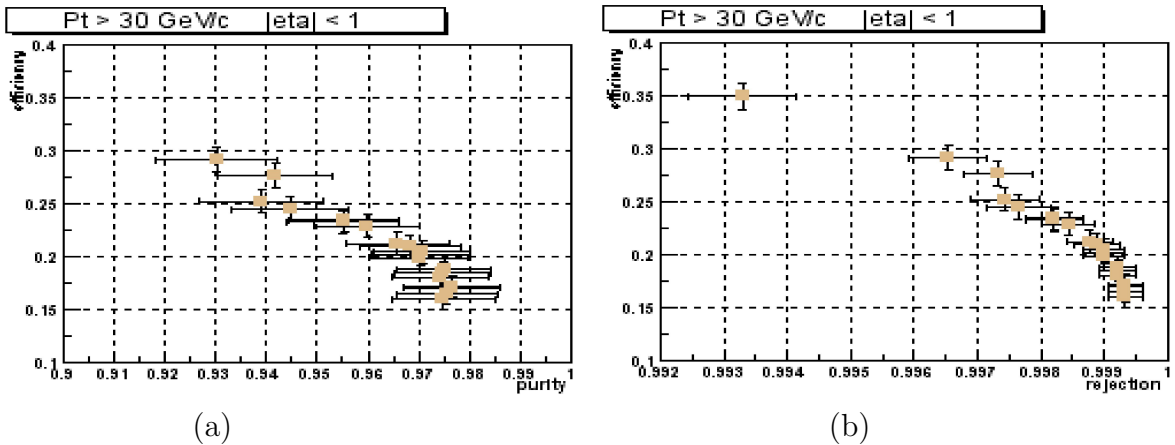


Figure 6.12: Tagging efficiency as a function of the purity of the tagged sample (a) and as a function of the background rejection ratio (b).

Muon transverse momentum

The muon momentum transverse to the jet direction is defined as it is explained in Section 6.4.

6.5.5 Performance of the combined tag

The performance of the method can be described by the following three parameters:

$$\text{efficiency: } \mathit{eff}_{b\text{-tag}} = \frac{\text{correctly tagged } b\text{-jets}}{\text{all } b\text{-jets}} \quad (6.14)$$

$$\text{purity: } \mathit{pur}_{b\text{-tag}} = \frac{\text{correctly tagged } b\text{-jets}}{\text{all jets tagged as } b} \quad (6.15)$$

$$\text{rejection: } \mathit{rej}_{bkg} = \frac{\text{non tagged } uds\text{-jets}}{\text{all } uds\text{-jets}} \quad (6.16)$$

$$(6.17)$$

By varying the cut on y_α defined in (6.11) one obtains the plots of efficiency vs purity (Figure 6.12 (a)) and efficiency vs rejection (Figure 6.12 (b)). With the present reconstruction performance one gets a 20 % efficiency for a purity of 97 % and almost constant rejection factor of 99 %

6.6 Conclusion

A program for discriminating b -jets against possible background using combined tagging algorithm is implemented into the DØ software environment. This method highly depends on the performance of the muon identification and secondary vertex and reconstruction which depends critically on the tracking performance in jets. The effects of the track reconstruction performance in jets are for the most part unknown as of yet. With low tracking efficiencies and high fake track rates it is difficult to reconstruct secondary vertices efficiently and the impact-parameter method does not perform well yet. Due to these problems the method was not used for the data analysis described in this thesis.

As the next step, when the performance of the track reconstruction will achieve an acceptable level, the possible background coming mostly from light quark jets and c -jets have to be studied in more details and the probability density tables have to be produced for each type of background. And then the algorithm can be used for the DØ data analysis in particular in the hypothesis of R-parity violation by a λ' or λ'' coupling where b -hadrons are present in the decay of supersymmetric particles.

Chapter 7

Phenomenology of the \mathcal{R}_p signal and expected exclusion limits

In the hypothesis that the R-parity is not conserved, the Lightest Supersymmetric Particle decays in standard particles. As explained in Chapter 1, in the superpotential 3 terms couple supersymmetric particles to standard particles. In this analysis, we are concerned with the term of the superpotential, which couples sleptons to leptons and in particular λ_{121} .

7.1 Consequences of an \mathcal{R}_p coupling

The running of these new Yukawa couplings has to be taken into account into RGE evolution. Assuming that one coupling dominates all the others, the effects of the \mathcal{R}_p terms on the phenomenology leads to two scenarios:

- \mathcal{R}_p couplings are small enough, so that as in case of the supersymmetry with conserved R-parity, the sparticles are produced in pairs. The only difference is coming from the effects in the decay of the supersymmetric particles in which the λ_{ijk} , λ'_{ijk} or λ''_{ijk} couplings are involved;
- \mathcal{R}_p couplings are dominant with respect to the gauge couplings. The mass spectrum and branching ratio of the supersymmetric particle could be affected depending on the magnitude of the couplings. In that case, one generally searches for specific processes involving the couplings at the production, for example resonant production of the sparticles [128, 143].

These effects have been experimentally searched for at the Tevatron collider and a brief review can be found in Section 1.6.4. The analysis described in this thesis assumes the first scenario.

7.2 SUSYGEN a \mathcal{R}_p Generator

In this thesis the generation of SUSY particles has been done with SUSYGEN. SUSYGEN [157] has been developed for e^+e^- colliders and has been intensively used in the

SUSY analysis at LEP. E. Perez from Saclay has recently developed a $p\bar{p}$ version [158]. SUSYGEN generates all the \mathcal{R}_p processes: resonant production and pair production. All the branching ratios of the SUSY particles are included. This program is interfaced with Suspect [159] which computes the RGE. The hadronisation of the particles is done with PYTHIA [160].

7.3 Effects of the R-parity violating couplings in the decay

Neutralinos $\tilde{\chi}_{1,2,3,4}^0$ and charginos $\tilde{\chi}_{1,2}^\pm$ are gauginos that can be produced in pair in $p\bar{p}$ collisions via the ordinary couplings from supersymmetry with conserved R-parity [70]. In the s -channel, the gauginos are produced via the exchange of W or Z (Figure 7.1).

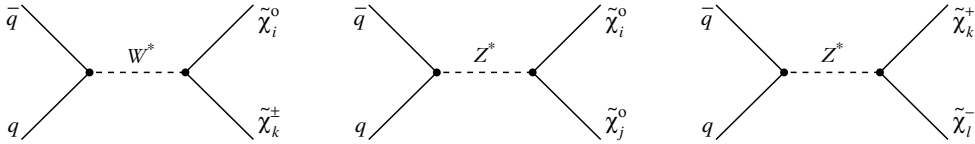


Figure 7.1: Gaugino pair production diagrams ($i, j = 1 \dots 4$; $k, l = 1, 2$) at the Tevatron.

Figure 7.2 shows the cross sections for pair production of different SUSY particles ($\tilde{\chi}^0\tilde{\chi}^0$, $\tilde{\chi}^0\tilde{\chi}^\pm$, $\tilde{\chi}^\pm\tilde{\chi}^\pm$, $\tilde{q}\tilde{q}$, $\tilde{q}\tilde{g}$, $\tilde{g}\tilde{g}$, $\tilde{l}\tilde{l}$) as function of $m_{1/2}$, for $m_0 = 100 \text{ GeV}/c^2$ and for two values of $\tan\beta$ (5 and 15) and for positive and negative μ . Figure 7.3 shows the cross sections for pair production for $m_0 = 300 \text{ GeV}/c^2$ [75]. From these curves one draws the following comments:

- parameter $m_{1/2}$ is the most significant. For $m_{1/2} \gtrsim 350 \text{ GeV}/c^2$ the total cross section is always less than 0.01 pb that makes the exploration of this region extremely difficult at the Tevatron.
- $\tilde{\chi}^0\tilde{\chi}^\pm$ pair production always dominates.
- squark pair production may be significant for low m_0 ($m_0 \lesssim 100 \text{ GeV}/c^2$).
- slepton pair production is practically negligible in relation to other processes with an exception of the low m_0 region ($m_0 \lesssim 100 \text{ GeV}/c^2$) and high $m_{1/2}$ ($m_{1/2} \gtrsim 350 \text{ GeV}/c^2$).
- total cross section is always higher for $\mu > 0$ than it is for $\mu < 0$.

In the presence of \mathcal{R}_p terms in the superpotential, the lightest neutralino $\tilde{\chi}_1^0$, usually considered as the LSP can decay into a fermion and its virtual supersymmetric partner which then decays via the \mathcal{R}_p couplings into two fermions. This decay chain gives rise to 3 fermions in the final state. For pair produced supersymmetric particles like $\tilde{\chi}_2^0$ and $\tilde{\chi}_{1,2}^\pm$ all heavier than the LSP $\tilde{\chi}_1^0$, the \mathcal{R}_p decays can be classified into 2 categories:

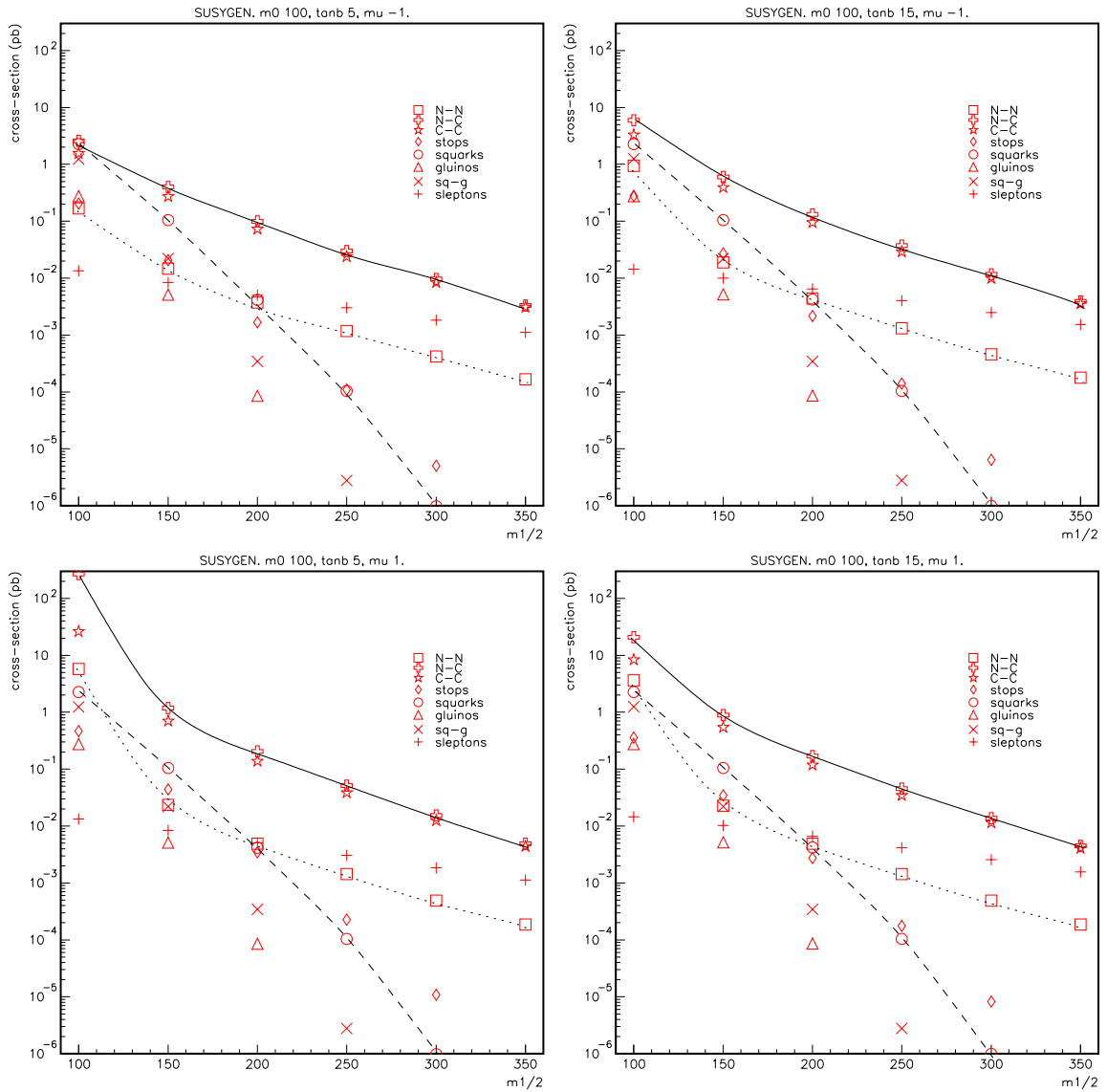


Figure 7.2: Susygen: cross sections (pb) of the supersymmetric particles pairs production as function of $m_{1/2}$ [75]. $m_0=100$ GeV; $\tan\beta=5$ (left) and $\tan\beta=15$ (right); $\mu < 0$ (up) and $\mu > 0$ (down); $A_0=0$.

Neutralinos (NN, squares and dotted lines);
 Neutralino-chargino (NC, crosses and solid lines);
 Charginos (CC, stars);
 stops (diamonds);
 squarks except stops (circles and dashed lines);
 gluinos (triangles);
 squark-gluino (\times signs);
 sleptons (+ signs).

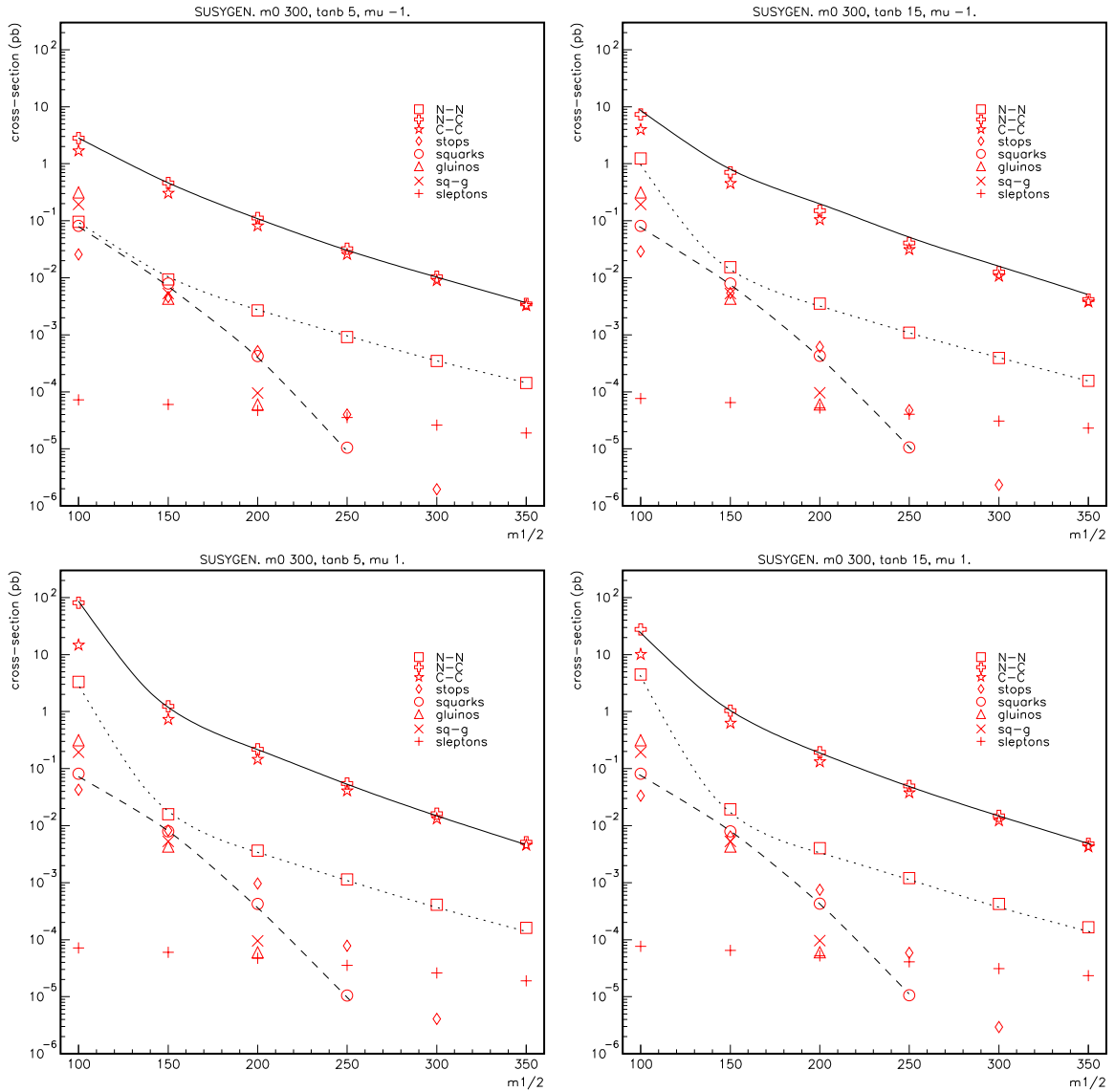


Figure 7.3: Susygen: cross sections (pb) of the supersymmetric particles pairs production as function of $m_{1/2}$ [75]. $m_0 = 300$ GeV; $\tan\beta=5$ (left) and $\tan\beta = 15$ (right); $\mu < 0$ (up) and $\mu > 0$ (down); $A_0 = 0$.

Neutralinos (NN, squares and dotted lines);
 Neutralino-chargino (NC, crosses and solid lines);
 Charginos (CC, stars);
 stops (diamonds);
 squarks except stops (circles and dashed lines);
 gluinos (triangles);
 squark-gluino (\times signs);
 sleptons (+ signs).

- indirect \mathcal{R}_p (or cascade) decays. The supersymmetric particle first decays through a R-parity conserving vertex to an on-shell supersymmetric particle till the LSP $\tilde{\chi}_1^0$ which then decays, as described above, via one \mathcal{R}_p coupling.
- direct \mathcal{R}_p decays. The supersymmetric particle decays directly to standard particles through one \mathcal{R}_p coupling.

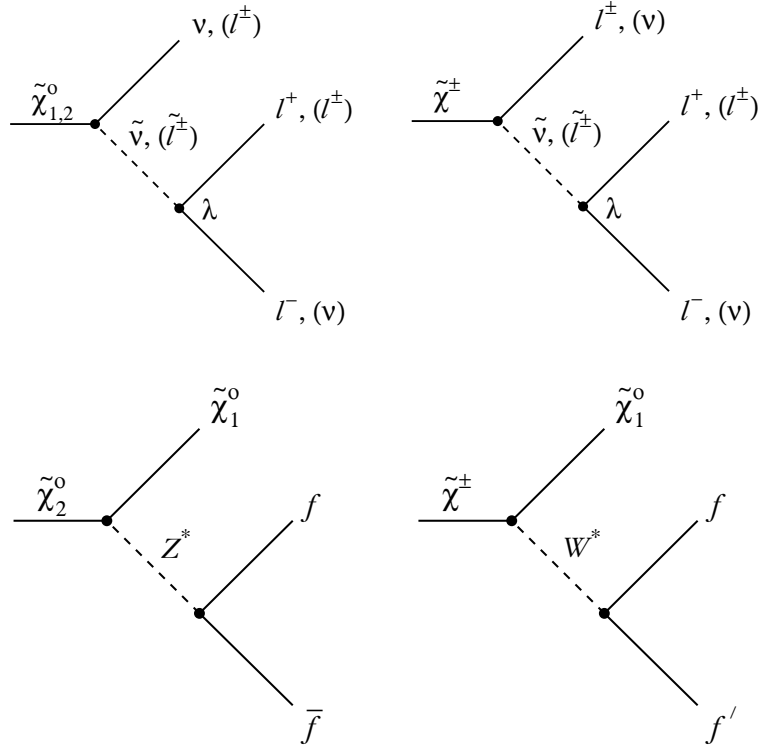


Figure 7.4: Gaugino direct (upper part) and indirect (lower part) decay diagrams for a λ_{ijk} coupling.

Some examples of direct and indirect decays of gauginos, when λ_{ijk} couplings are involved, are shown in Figure 7.4 and the corresponding possible signatures are given in Table 7.1. Decay of supersymmetric particles via λ_{ijk} couplings give rise in general to leptonic topologies although one can see in Table 7.1 that jets may be present in the final states in case of indirect gaugino decays. In case of a dominant λ_{ijk} coupling, the sleptons couple to the leptons, and the gauginos decay into charged leptons and neutrinos. The decay of the lightest neutralino leads to one neutrino and two charged leptons (Figure 7.4, upper part). The heavier neutralinos and the charginos, depending on their mass difference with $\tilde{\chi}_1^0$ can either decay directly into 3 standard fermions, or decay to $\tilde{\chi}_1^0$, via for example virtual Z or W , as illustrated on Figure 7.4, lower part.

In the analysis described in this thesis, the hypothesis of the λ_{121} dominant coupling was made. In this case, the leptons from \mathcal{R}_p decay are electrons and muons. Assuming

final states	direct decay of	indirect decay of
$2l + \cancel{E}$	$\tilde{\chi}_1^+ \tilde{\chi}_1^-$	
$4l + \cancel{E}$	$\tilde{\chi}_1^0 \tilde{\chi}_1^0, \tilde{\chi}_1^+ \tilde{\chi}_1^-$	$\tilde{\chi}_2^0 \tilde{\chi}_1^0$
$6l$	$\tilde{\chi}_1^+ \tilde{\chi}_1^-$	
$6l + \cancel{E}$		$\tilde{\chi}_1^+ \tilde{\chi}_1^-, \tilde{\chi}_2^0 \tilde{\chi}_1^0$
$4l + 2 \text{ jets} + \cancel{E}$		$\tilde{\chi}_2^0 \tilde{\chi}_1^0$
$4l + 4 \text{ jets} + \cancel{E}$		$\tilde{\chi}_1^+ \tilde{\chi}_1^-$
$5l + 2 \text{ jets} + \cancel{E}$		$\tilde{\chi}_1^+ \tilde{\chi}_1^-$

Table 7.1: Final states in gaugino pair production when a λ_{ijk} coupling is dominant

slepton mass degeneracy, the branching ratio in each of the two final states of (7.1) is 50 % independent of the $\tilde{\chi}_1^0$ composition.

$$\tilde{\chi}_1^0 \xrightarrow{\lambda_{121}} \begin{cases} ee\nu_\mu \\ e\mu\nu_e \end{cases} \quad (7.1)$$

7.4 Study of the \cancel{R}_p signal with fast MC simulation

This section presents the results of an analysis with fast detector simulation in order to obtain the exclusion contours in the mSUGRA parameter space for different values of the Tevatron integrated luminosity that can be achieved during the Run II. The supersymmetrical particles are produced in pair with conserved R-parity. The R-parity is violated by the λ_{121} coupling. And its values is chosen to be equal 0.04 slightly below its present limit. As long as its value is not too small so that the LSP decays in the detector, the analysis is almost insensitive to it.

7.4.1 PGS. Fast DØ detector response simulation

SUSYGEN and PYTHIA have been interfaced with the PGS detector simulation package [72], which has been tuned to mimic the DØ Run II detector performance.

In PGS the detector effects are simulated by smearing the generated quantities with gaussian. The parameters of the gaussian have been tuned in order to reproduce the DØ full simulation. Fiducial cuts are applied on the various object to simulate the DØ instrumented regions. The main parameters which were adjusted are:

- Primary vertex $\sigma_z = 28$ cm;
- Calorimeter resolution is described by the following formula:

$$\left(\frac{\sigma_E}{E}\right)^2 = C^2 + \frac{S^2}{E} + \frac{N^2}{E^2} \quad (7.2)$$

where, for the electromagnetic calorimeter:

$$\begin{aligned} C &= 0.003 \\ S &= 0.170 \\ N &= 0.140 \end{aligned} \tag{7.3}$$

and for the hadronic calorimeter:

$$\begin{aligned} C &= 0.032 \\ S &= 0.500 \\ N &= 1.28 \end{aligned} \tag{7.4}$$

- The cracks between cells are considered as holes (around 1/4 of the 2π acceptance is removed);
- Tracks are reconstructed in $|\eta| < 1.1$ with an efficacy of 98 %;
- EM candidates should satisfy the following criteria:

$$pT > 5 \text{ GeV} \tag{7.5}$$

$$|\eta| < 1.1 \tag{7.6}$$

$$\text{isolation} < 0.10 \tag{7.7}$$

$$0.5 < E/p < 1.5 \tag{7.8}$$

$$EM_{frac} > 90\% \tag{7.9}$$

$$\tag{7.10}$$

and a reconstruction efficiency factor of 85 % was applied to them.

- Jets are reconstructed with a cone algorithm ($\Delta R = 0.7$) with an initial seed of 3 GeV. The jet electromagnetic energy fraction should be $f_{EM} < 0.9$.

7.4.2 Signal simulation

Events with \tilde{R}_p decay of gauginos were produced using SUSYGEN Monte Carlo program [157] for a wide range of m_0 , $m_{1/2}$ masses. More than 700 points in the plane $m_0 - m_{1/2}$ with a statistics of 1000 events per point have been generated and simulated:

$$\begin{aligned} m_0 &= 80 \div 500 \text{ step } 20 \text{ GeV} \\ m_{1/2} &= 100 \div 360 \text{ step } 20 \text{ GeV} \\ \text{sign } \mu &= +1, -1 \\ \tan \beta &= 5 \\ A_0 &= 0 \end{aligned} \tag{7.11}$$

These parameters were selected to be in the typical region accessible for the Run II of the Tevatron. The values of $\tan \beta < 2$ are excluded by the LEP experiments (Higgs boson search results) [71].

7.4.3 Background simulation

The Standard Model background processes have been simulated using the PYTHIA event generator [160]. The following processes have been considered:

- $t\bar{t}$ production where electrons may arise from $t \rightarrow bW$ followed by $W^- \rightarrow e\nu$;
- single boson production ($\gamma^*/Z, W$);
- double boson production (ZZ, ZW, WW);

The characteristics of these processes and the equivalent integrated luminosity of the produced samples are shown in Table 7.2.

For the tri-lepton search considered in this thesis, there are physics sources of background. First, the 4 leptons signal, which can be generated by the ZZ and $t\bar{t}$ productions, appears as a 3 leptons signature if one of the leptons is missed. Besides, the processes $p\bar{p} \rightarrow Z + X$, Drell-Yan + X would mimic a tri-electron signal if X fakes a electron. Monte Carlo simulations using simplified detector simulation, like PGS [72] in the present study, cannot give a reliable estimate of this background. A knowledge of the details of the detector response as well as the jet fragmentation is necessary in order to determinate the probability to fake a lepton. In [73], using standard cuts the background coming from $p\bar{p} \rightarrow Z + X$, Drell-Yan + X , X faking an electron has been estimated to be of order 2 fb at the Tevatron with $\sqrt{s} = 2$ TeV. The authors of [73] have also estimated the background cross section from the three-jet events faking tripleton signals to be around 10^{-3} fb.

7.5 Tri-electron selection and its effect on the signal and on the background

In the 100 pb^{-1} analyzed in Run I, no four lepton event have been observed by $D\bar{O}$. As the present data analyzed in this thesis is around 10 pb^{-1} , one does not expect 4 lepton event either (this will be confirmed in Chapter 8). So the study was done with three leptons assuming that the fourth was not identified. The selection conditions were:

- there should be at least three isolated electron in event with $p_T > 10 \text{ GeV}/c$;
- there should be at least two electrons in the central $|\eta(\text{EM-candidate})| < 1.0$;

The kinematic cuts were chosen after studying the effect of these cuts on signal as well as on various backgrounds. As it can be seen from Tables 7.2 and 7.3, these criteria allow to effectively eliminate the background events and still keep a sufficient amount of signal events. Further optimization of the selection should be done with more precise detector simulation.

Tri-electron events have been identified in $\gamma^*/Z \rightarrow ee$, ZZ and WZ backgrounds. The dominant contributions are from Drell-Yan where the third electron is coming from radiated γ reconstructed as an electron (no matching with central track is required at this level). The contributions from all processes are below one event for 200 pb^{-1} . Table 7.2 combines the results of the SM background study using MC samples.

bkg process	σ , pb	$\mathcal{L}_{\text{equiv}}$, pb $^{-1}$	cut eff, %	bkg contrib for 200 pb $^{-1}$
$\gamma^*/Z \rightarrow ee$ (2 – 60 GeV/c 2)	580	3.5×10^1	0	0
$\gamma^*/Z \rightarrow ee$ (60 – 130 GeV/c 2)	186	1.1×10^2	0.5×10^{-2}	1.9 \pm 0.2
$\gamma^*/Z \rightarrow ee$ (130 – 250 GeV/c 2)	1.4	1.4×10^4	0.2×10^{-1}	0.42 \pm 0.03
$\gamma^*/Z \rightarrow ee$ (250 – 500 GeV/c 2)	0.13	1.6×10^6	0.2×10^{-1}	0.37 \pm 0.03
WZ	2.7	7.5×10^3	0.5×10^{-1}	0.24 \pm 0.02
ZZ	1.3	1.5×10^4	0.6×10^{-1}	0.14 \pm 0.01
WW	8.5	2.4×10^3	0	0
$t\bar{t}$	6.4	3.1×10^3	0	0
$\gamma^*/Z \rightarrow \tau\tau$ (2 – 60 GeV/c 2)	580	3.5×10^1	0	0
$\gamma^*/Z \rightarrow \tau\tau$ (60 – 130 GeV/c 2)	186	1.1×10^2	0	0
$\gamma^*/Z \rightarrow \tau\tau$ (130 – 250 GeV/c 2)	1.4	1.4×10^4	0	0
$\gamma^*/Z \rightarrow \tau\tau$ (250 – 500 GeV/c 2)	0.13	1.6×10^6	0	0

Table 7.2: Tri-electron channel SM background.

$m_0 = 300, A_0 = 0$ $\tan\beta = 5$	σ , pb	cut eff, %	signal contrib for 200 pb $^{-1}$
$m_{1/2} = 140, \mu < 0$	1.11	14.3	31 \pm 2
$m_{1/2} = 140, \mu > 0$	3.08	11.9	73 \pm 5
$m_{1/2} = 200, \mu < 0$	0.196	15.3	6.3 \pm 0.4
$m_{1/2} = 200, \mu > 0$	0.369	16.2	11.2 \pm 0.6
$m_{1/2} = 260, \mu < 0$	0.0468	18.1	1.17 \pm 0.06
$m_{1/2} = 260, \mu > 0$	0.0753	17.3	2.21 \pm 0.15
$m_{1/2} = 320, \mu < 0$	0.0127	20.1	0.53 \pm 0.03
$m_{1/2} = 320, \mu > 0$	0.0187	18.0	0.62 \pm 0.04

Table 7.3: Tri-electron selection effect on the signal.

7.6 Limit in the m_0 - $m_{1/2}$ Plane

The 95% confidence level upper limits can be calculated using either a frequentist or a Bayesian algorithm. In the present analysis limits are calculated by the frequentist algorithm implemented in POILIM.F program [74].

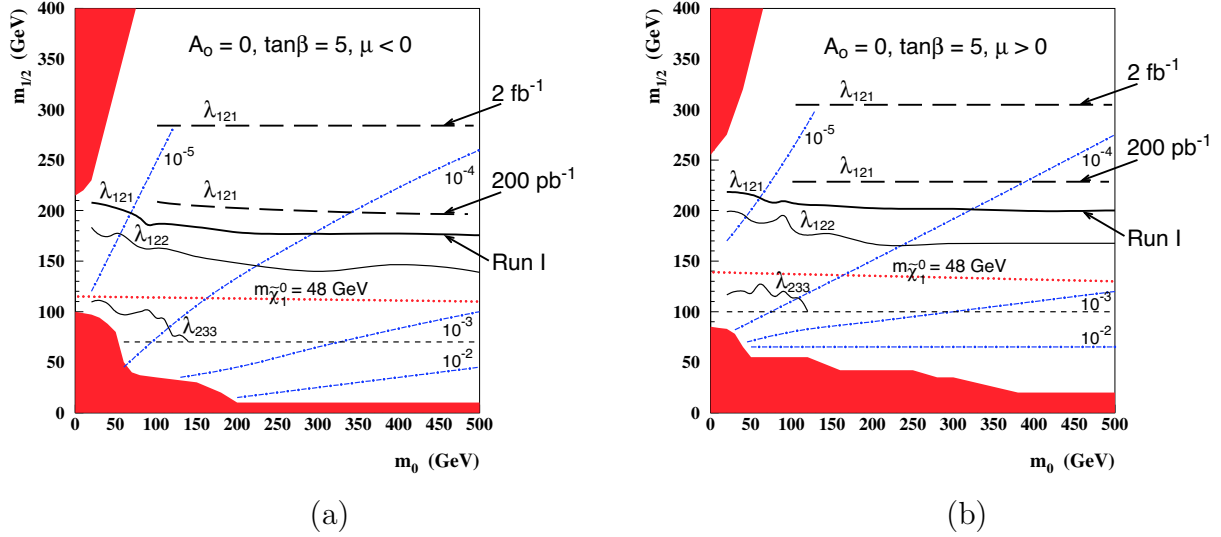


Figure 7.5: Exclusion contour in the $m_0 - m_{1/2}$ plane for $A_0 = 0$, $\tan \beta = 5$, $\mu < 0$ (a) and $\mu > 0$ (b) and for the case of finite λ_{121} , λ_{122} and λ_{233} couplings. The Run I limits [76] are shown as solid lines. For the case of λ_{121} coupling expected limits for different integrated luminosity (200 pb^{-1} and 2 fb^{-1}) are shown as bold dashed lines. The exclusion regions at 95% C.L. correspond to the spaces below the lines labelled with the coupling types, and above the dash-dotted curves specifying the numerical values of λ .

With no excess of events over Standard Model backgrounds, upper limits on the cross section are calculated. These limits indicate the reach of the experiment. Models that predict cross sections greater than the upper limit can be ruled out. Lower limits on the m_0 and $m_{1/2}$ mSUGRA parameters can then be inferred from the upper cross section limits. Limits on m_0 and $m_{1/2}$ induce lower mass limits for squarks and gluinos as explained in Chapter 1 (Figure 1.8)

The acceptance uncertainty of 10 % and statistical errors on the numbers of expected background events are used as input for the POILIM.F program. For more correct estimation of the uncertainties the following sources should be considered:

- Theoretical uncertainties. Effects which influence the cross section of the signal and background processes:
 - error resulting from the uncertainty of the structure function;
 - cross sections calculation errors of the MC generators like PYTHIA or SUSY-GEN.

- Systematic uncertainties. Effects which change the acceptance or which are due to detector effects or statistics:
 - statistics of the MC generation. The error on the acceptance of the MC SUSY sample could be estimated as the statistical error for the scenario with the worst acceptance;
 - the luminosity of the analyzed sample (one of the main sources when analyzing the real data);
 - electron identification efficiencies;
 - trigger efficiency.

Figure 7.5 shows the expected exclusion contours (bold dashed lines) in the m_0 - $m_{1/2}$ plane for the λ_{121} coupling, for $\tan\beta = 5$ and for both signs of μ , the value of A_0 is fixed to zero. The limits were calculated for two values of the integrated luminosity (200 pb^{-1} and 2 fb^{-1}). These limits are superposed with results of the similar Run I analysis [76]. The shaded areas indicate the regions where there is no electroweak symmetry breaking or where the LSP is not the lightest neutralino.

7.7 Conclusion

By the end of Run II the Tevatron is expected to deliver an integrated luminosity of at least 2 fb^{-1} , which is about a factor of twenty more than what was recorded during Run I. This allows to probe new regions of the parameter space. It can be seen from Figure 7.5 that for $\tan(\beta) = 5$ and $A_0 = 0$ scenarios the limits obtained during Run I will be significantly improved. With the expected luminosity it will be possible to probe scenarios with values of $m_{1/2}$ up to more than 300 GeV.

In order to obtain reliable limits the fast simulation should be done with PMCS (Parameterized MC Simulation) [77] much more complete and realistic than PGS. PMCS is 2000 faster than DØGSTAR and will allow a detailed exploration of the SUSY parameter space.

The Tevatron is now running and an integrated luminosity of around 2 fb^{-1} is expected in 2004. Since the luminosity plays a major role in the limit determination more stringent limits will be obtained in the future.

Chapter 8

Run II Data Analysis and Background Estimation

In this chapter, the analysis of the data in the R-parity violating scenario is discussed. The search for multi-lepton events in the $5.2 \pm 0.8 \text{ pb}^{-1}$ data taken between February and June 2002 is described. As it is explained in Chapter 7 this topology is expected in the processes with *R*-parity violation via leptonic λ Yukawa couplings. The chapter begins with a description of the data sample. The online trigger and the offline selection requirements used for this analysis are then described with their justifications. This is followed by a discussion of the background modeling and the method adopted for their estimation. This chapter also describes the consistency checks made to establish the validity of the background modeling.

With any triggering system, one runs the risk of discarding potentially interesting physics events. The trigger and filter requirements are thus made as loose as the bandwidth allows, and so data samples that (perhaps) contain signal events may be heavily contaminated with uninteresting background events. Further event selection criteria or cuts are placed on the data to select the events that could be signal.

The signal efficiency is the fraction of signal events the cuts accept. Similarly, the background rejection rate is the fraction of background events not accepted by the cuts. The idea is to design a set of requirements that keeps most of the signal (high signal efficiency) while reducing the background contamination as much as possible (large background rejection).

Monte Carlo (MC) simulations are used to determine the characteristics of signal and backgrounds. Some backgrounds are estimated with the real data. The cuts exploit well understood differences between the signal and backgrounds. In this chapter, Section 8.3 details the cuts that are applied to the data and the differences between signal and background events that justify them. The backgrounds to this analysis will be presented in Section 8.4. Section 8.3.2 discusses the effects of the cuts on the collider data passing the analysis filter. The events that pass are the candidates. Since this candidate sample is still contaminated with background events, the background contribution to the data is estimated using MC and collider data. That procedure is described in Section 8.4.2.

8.1 Data Sample

The data collected by the DØ detector during the February – June 2002 has been used in this analysis. Runs during which the detector system or the data acquisition system had problems were excluded. The resulting data sample corresponds to an integrated luminosity of $5.2 \pm 0.8 \text{ pb}^{-1}$, where the quoted uncertainty of 15 % includes the error on Level 0 trigger efficiency and the error on the inelastic scattering cross section (used to compute the luminosity). The data set used for this study consists of all runs taken with trigger global_CalMuon of version 3.3 or higher. The range of run numbers is 145035 to 153879, reconstructed with the release version p10.15.01.

8.2 Selection of reliable data sample at early stage of the experiment

The DØ experiment is still at its early stage and neither common criteria for the data quality estimation nor common selection criteria were developed. The following explains how these questions have been addressed in the present analysis.

The online trigger and offline selection criteria are chosen after studying the features of both the signal and background processes in order to retain a sizeable fraction of signal events and also to reduce the background significantly.

8.2.1 Runs selection for tri-electron channel analysis

For the tri-electron channel study all the runs known to have problems with tracking and/or calorimetry were removed. The following sources of information have been used:

- DØ Offline Run Quality Database:
 - SMT bad runs;
 - CFT bad runs;
 - Calorimeter bad runs.
- Bad runs list (ver. 1.4, ver. 1.5) provided by the Jet and Missing E_T Identification Group. The selection is based on the uniformity of the missing transverse energy (ME_T) and the scalar sum of the transverse energy in the event (SE_T) spectra [163]. The mean value of these 2 quantities should be stable in time. The off-line monitoring of these parameters is a powerful tool to remove bad runs.
- DØ Shift Captain reports. All runs mentioned as "bad", "useless" and "uncertain".
- DØ Offline Run Database:
 - Runs with "prescale panic" for the Level 1 trigger which is used for CEM20, EM_HI and EM_MX triggers at Level 3;
 - Runs with less than 1000 events. The small size of a run indicates that it was stopped after less than 2 minutes due to detector or DAQ problems.

8.2.2 Runs for di-electron one muon channel analysis

In addition to the tracking and calorimetry quality requirements of the tri-electron selection this analysis requires reasonable data from the muon detectors. This information was obtained from the runs quality list provided by the Muon Identification Group [164]. Following the group recommendations bad runs were rejected.

8.2.3 Single electron trigger efficiency

To be selected by the trigger system an event must be accepted by three levels of requirements.

During winter/spring 2002, the third level rejection was operational for only part of the data, the second level trigger was not operational and the first level trigger thresholds have been changed several times. To accurately account for these changes, an effective trigger efficiency is computed with simultaneous Level 1 and Level 3 rejections folded in.

In order to measure a luminosity and thereafter a cross section, a set of relevant triggers must be chosen. If the choice is more than one, it is crucial to account for overlaps. In the present analysis only one trigger is considered, corresponding to the unrescaled Level 1 requirement with the lowest possible threshold (the trigger flags used are indicated in Table 8.1).

To compute the trigger efficiency, an unbiased sub-sample of single EM-candidate events having fired any single or double muon Level 1 trigger is used. The single EM-candidates satisfy the criteria explained in Section 8.2.4. The Level 1 muon trigger uses terms like $muNptxYtxx$, where N is the number of muons found by the trigger, ptx indicates that only muons with a p_T above a threshold x are counted. As x is not set any muons are counted for the time being. The variable Y can take the following values: a = all/any ($|\eta| < 2$), b = between ($1 < |\eta| < 2$), c = central ($|\eta| < 1$), w = wide ($|\eta| < 1.5$). Finally, the txx indicates the trigger is looking for a t = tight (not loose) muon while xx are the quality criteria of the wire chambers in the trigger and possible additional future option (such as muon sign ...), respectively.

The EM trigger efficiency is then measured as the fraction of those events in the sub-sample which have also fired the relevant EM trigger.

$$\epsilon_{\text{EMtrigger}}(E_T^{\text{EM-candidate}}) = \frac{N_{(muNptxYtxx) \text{ and (EM trigger)}}(E_T^{\text{EM-candidate}})}{N_{(muNptxYtxx)}(E_T^{\text{EM-candidate}})} \quad (8.1)$$

To calculate the efficiency and its uncertainty the EFFIC program has been used [165]. Figure 8.1 shows the resulting efficiency for the combined EM trigger. The overall effective trigger efficiency for EM particles with E_T larger than 30 GeV/c is:

$$\epsilon_{\text{trig}} = (90 \pm 6)\%. \quad (8.2)$$

The loss with respect to full efficiency is due to level 1 trigger towers which are temporarily suppressed. The loss of efficiency at low E_T is due to the use of the higher threshold CEM20 trigger at the beginning of the data taking period.

Trigger	Run numbers	Trigger version	level 1	level 3
CEM20	144998 – 145597	3.30 – 4.00	CEM(1,20)	
EM_HI	145626 – 149222	4.10 – 4.20	CEM(1,15)	$E_T > 12$ GeV
EM_MX	149269 – 155605	5.00 – 7.20	CEM(1,15)	$E_T > 12$ GeV

Table 8.1: Trigger types used in the analysis.

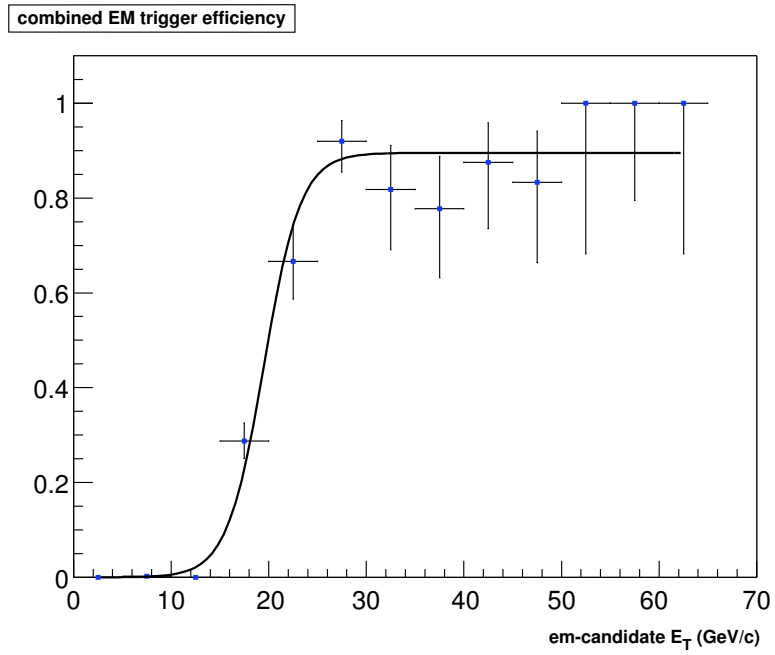


Figure 8.1: Trigger efficiency as a function of the EM-candidate energy.

The measured efficiency was fitted with the expression

$$\epsilon(E_T^{em-candidate}) = \frac{a}{1 + e^{(b \cdot E_T^{em-candidate} - c)}}$$

The resulting fit parameters are summarized in Table 8.2. This efficiency will be applied to the MC data events.

trigger	a	b	c
combined EM	0.90 ± 0.06	-0.5 ± 0.2	-10 ± 4

Table 8.2: Result of the 3-parameter fit applied to the measured turn-on curve for the combined EM trigger.

8.2.4 Selection of reconstructed physics objects

The physics objects identification in the DØ detector is described in more details in Chapters 3, 4 and 5. The following is a brief description of the criteria used in the present analysis.

For object definitions the certified criteria of the EM ID (ver. 1.9) [166, 167], Jet/MET (ver. 2.1) [168] and Muon ID (ver. 1.1) [169] group are used:

- EM-candidate: the EM calorimeter clusters reconstructed with simple cone algorithm have been used to define EM objects, with
 - id = 10 OR |id| = 11
 - EM Fraction > 0.9, where EM Fraction is the energy fraction of the EM-candidate in the electromagnetic calorimeter with respect to the total EM-candidate energy.
 - iso = $\frac{E_{tot}(\mathcal{R}<0.4) - E_{EM}(\mathcal{R}<0.2)}{E_{EM}(\mathcal{R}<0.2)} < 0.15$, where iso is the isolation of the EM-candidate, $E_{EM}(\mathcal{R} < 0.2)$ is the electromagnetic energy within a cone of radius $\mathcal{R} = \sqrt{\Delta\eta^2 + \Delta\varphi^2} = 0.2$ centered around the EM-candidate, $E_{tot}(\mathcal{R} < 0.4)$ is the total energy contained within a concentric cone of radius $\mathcal{R} = 0.4$;
 - HMx8 < 20, where HMx8 is a H-matrix χ^2 based on the comparison of the values of the energy deposited in each layer of the EM calorimeter and the total energy of the shower with average distributions obtained from Monte Carlo (calculated without energies deposited in the preshower detector whose information was not available at the time of the data taking). In the present analysis the matrix is 8-dimensional. The H-matrix technique is described in more details in Section 4.2.2.
- Jets: the Run II cone (of radius $\mathcal{R} = \sqrt{\Delta\eta^2 + \Delta\varphi^2} = 0.7$) algorithm has been used, with
 - $0.05 < \text{EM Fraction} < 0.95$, where EM Fraction is the energy fraction of the jet in the electromagnetic calorimeter with respect to the total jet energy;

- CHF < 0.4, where CHF is the energy fraction of the jet in the coarse hadronic calorimeter with respect to the total jet energy;
 - HotF < 10, where HotF is the ratio highest and next-highest cell ET of the jet;
 - n90 > 1, where n90 is the number of cells which contain 90% of the jet energy;
 - $E_T > 10$ GeV.
- Muons: defined as medium quality local tracks in the muon detector, with
 - at least 2 wire hits in the A segment;
 - at least 1 scintillator hit in the A segment;
 - at least 2 wire hits in the BC segment;
 - at least 1 scintillator hit in the BC segment.

8.2.5 Di-lepton Event Selection Criteria

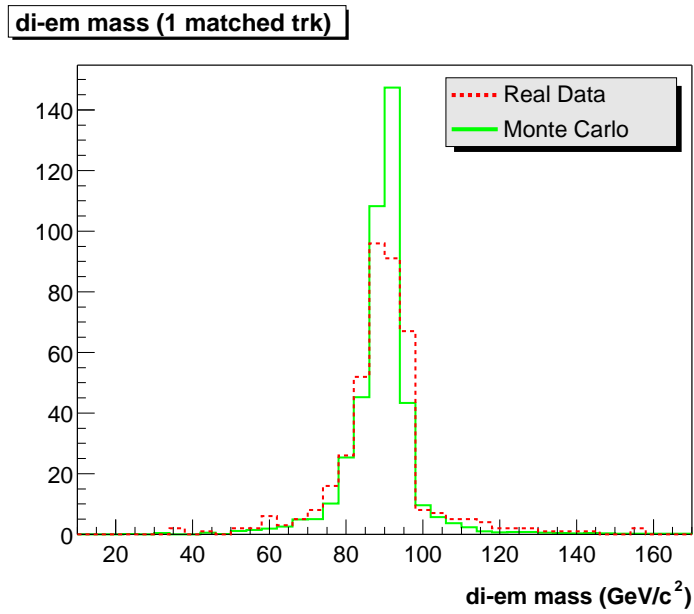
Events with at least two electrons (EM-candidates) or one electron and at least one muon (μ -candidate) which pass the following cuts have been retained:

- EM-candidate: criteria of section 8.2.4 and $E_T > 6$ GeV;
- μ -candidate: criteria of section 8.2.4 and $p_T > 4$ GeV/c.

20 870 events satisfied those conditions.

The number of background events in the two lepton sample is much too high to identify any SUSY signal contribution in this sample. It is used to cross-check the analysis and show that the background is well understood. In the sample there are 9 253 events containing two or more electrons and 11 617 containing one electron and one or more muon. The invariant mass of the di-electron from this sample is shown in Figure 8.2. At least one electron is required to be matched with a track from the central tracking detector. It can be clearly seen that the simulation does not reproduce the data: slight disagreement in number of events and narrower peak in MC. The possible sources of errors are:

- calculation of the integrated luminosity. As it was noted in Section 3.2 the integrated luminosity calculation depends on effective $p\bar{p}$ cross section and for this analysis the value adopted at the end of Run IB was chosen. As the efficiency and acceptance of the detector are different and the \sqrt{s} is larger the present effective $p\bar{p}$ cross section may differ from one of Run IB more than it is expected.
- detector simulation. The present version does not reproduce the real behavior of the calorimeter electronics. Recent studies have shown that the electron energy in the MC has to be smeared by an additional constant term of 4 % in order to reproduce the data [132].



	$n_{\text{candidates}}$ (78 – 102 GeV/c ²)	$\langle m_Z \rangle$, GeV/c ²	width , GeV/c ²
Real Data	$(3.4 \pm 0.3) \cdot 10^2$	89.1 ± 0.4	5.8 ± 0.4
Monte Carlo	$(3.8 \pm 0.4) \cdot 10^2$	89.8 ± 0.3	4.7 ± 0.3

Figure 8.2: Invariant mass distributions for dielectron pairs.

8.3 Tri-lepton selection

For the final tri-lepton selection, events were required to be triggered with CEM20, EM_HI or EM_MX trigger depending on the data taking period. This sample corresponds to a recorded luminosity of $5.2 \pm 0.8 \text{ pb}^{-1}$ for the events with electrons only and $4.6 \pm 0.7 \text{ pb}^{-1}$ if the presence of a muon is required. This type of trigger enrich the final sample in electrons.

In addition to electron and muon quality cuts the following kinematic cuts are applied to further reduce the background and to improve the signal to background ratio.

- To be certain that an event passes the single EM trigger there should be at least one EM-candidate passing the quality cuts with $p_T(\text{EM-candidate}) > 30 \text{ GeV}/c$ and $|\eta(\text{EM-candidate})| < 0.8$ (the EM trigger region has been extended to $|\eta| < 2.6$ in July 2002);
- other EM-candidate satisfying the quality cuts should have $p_T(\text{EM-candidate}) > 15 \text{ GeV}/c$ and $\Delta R > 0.7$ is required between any pair of leptons;
- $p_T(\mu\text{-candidates}) > 5 \text{ GeV}/c$, where p_T is the local track transverse momentum measured in the muon detector and $\Delta R > 0.7$ between the muon and any jet.
- In order to correctly calculate the sample luminosity only the events corresponding to the good luminosity blocks were selected (Section 3.2).

8.3.1 Effect of the selection criteria on the signal and on the background

The kinematic cuts described above were chosen after studying the effect of these cuts on signal as well as on various backgrounds. This study was done using simulated events for both signal and backgrounds. In this section, we justify the above cuts. For the signal, a typical point in the mSUGRA parameter space, $m_0 = 200 \text{ GeV}/c^2$ and $m_{1/2} = 260 \text{ GeV}/c^2$ has been chosen for illustration. In making these plots no trigger requirements were imposed. All the distributions are normalised to an integrated luminosity of 200 pb^{-1} .

Figure 8.3 shows the p_T distribution of the electron with the highest p_T arising from various sources of backgrounds and signal. It is clear that a cut of $p_T > 30 \text{ GeV}/c$ still does not remove significant amount of signal and it is not effective in removing backgrounds from any of the sources discussed here. But this cut is very important, because otherwise many other sources *e.g.* QCD heavy quark (b or c) events where the heavy quark decays to electrons are likely to contribute to the background. The instrumental background is also expected to be higher (not shown in the figure). The η distribution of the electron with the highest p_T is shown in Figure 8.4. It can be seen that a cut of $|\eta| < 0.8$ due to the limited region covered by the trigger has a good efficiency for the signal and remove roughly half of the $\gamma^*/Z \rightarrow ee$, γZ , γW and WZ background.

Figure 8.5 shows the p_T distribution of the electron with the third highest p_T from various sources of background and the signal. A cut at $p_T > 15 \text{ GeV}/c$ removes the γW and a good fraction of the $\gamma^*/Z \rightarrow ee$ background.

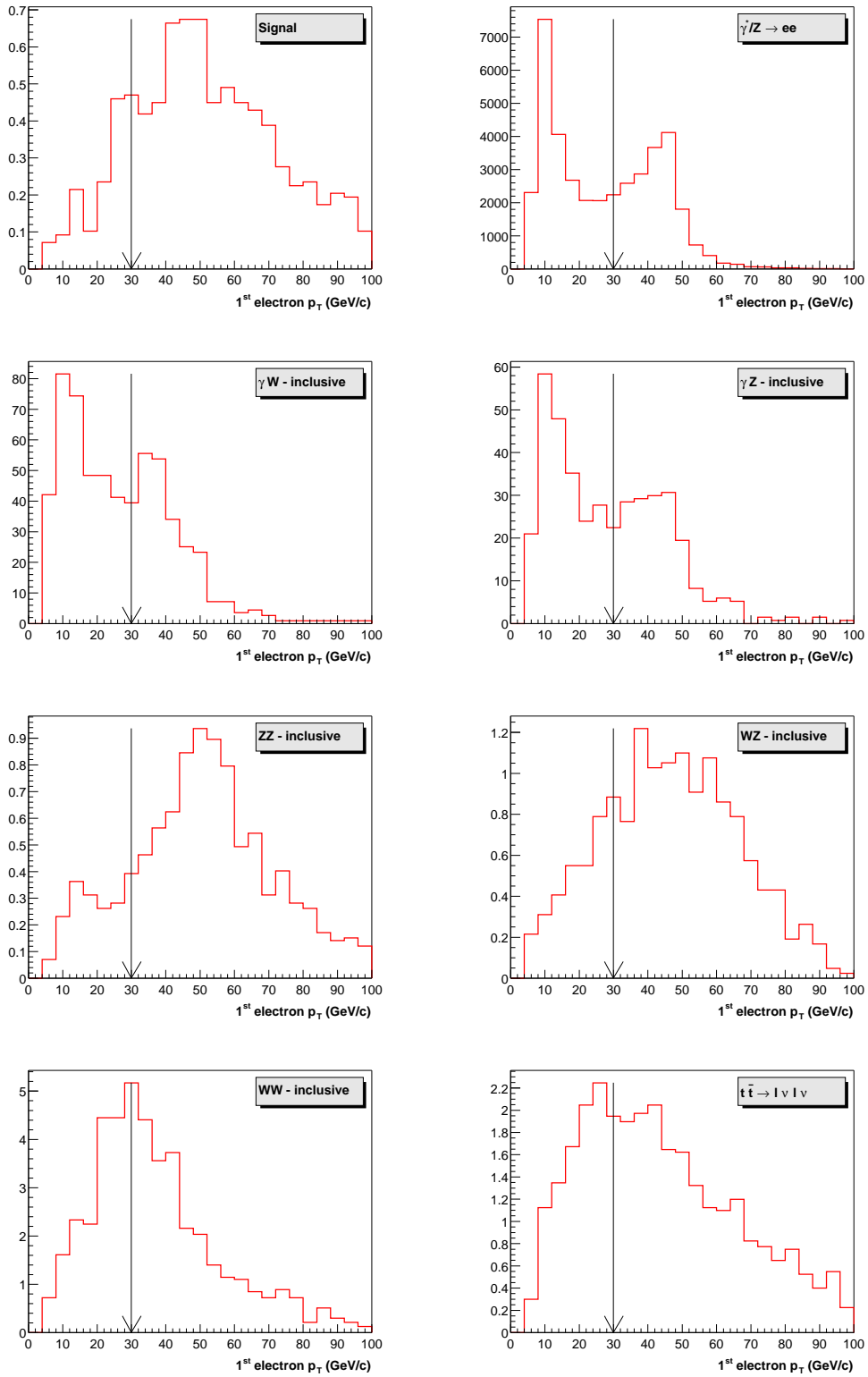


Figure 8.3: p_T distributions of the first highest p_T electron and the chosen cut (shown as vertical arrow). For the signal, a typical point in the mSUGRA parameter space, $m_0 = 200 \text{ GeV}/c^2$ and $m_{1/2} = 260 \text{ GeV}/c^2$ has been chosen.

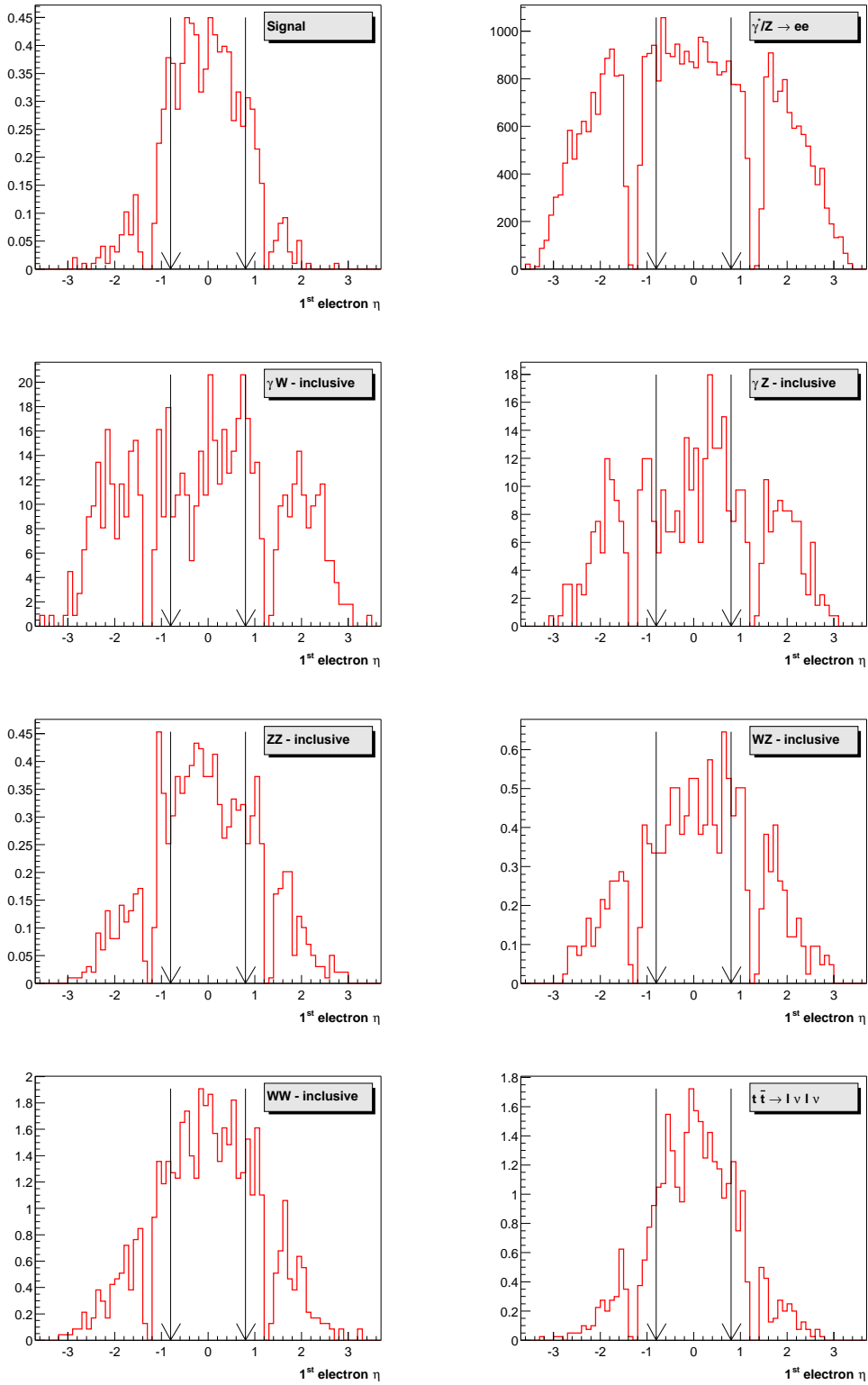


Figure 8.4: η distributions of the first highest p_T electron and the chosen cut (shown as vertical arrow). For the signal, a typical point in the mSUGRA parameter space, $m_0 = 200 \text{ GeV}/c^2$ and $m_{1/2} = 260 \text{ GeV}/c^2$ has been chosen.

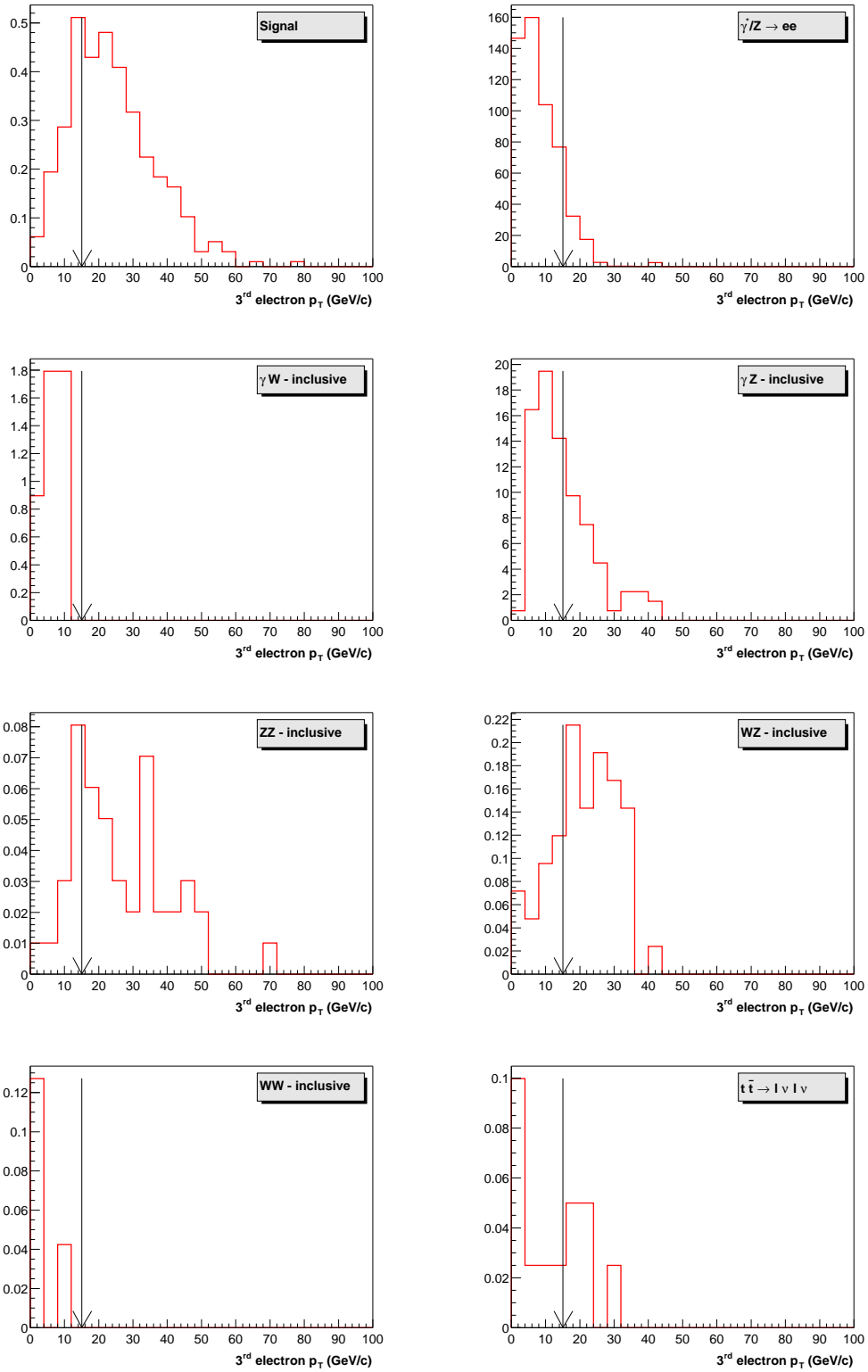


Figure 8.5: p_T distributions of the third highest p_T electron and the chosen cut (shown as vertical arrow). For the signal, a typical point in the mSUGRA parameter space, $m_0 = 200 \text{ GeV}/c^2$ and $m_{1/2} = 260 \text{ GeV}/c^2$ has been chosen.

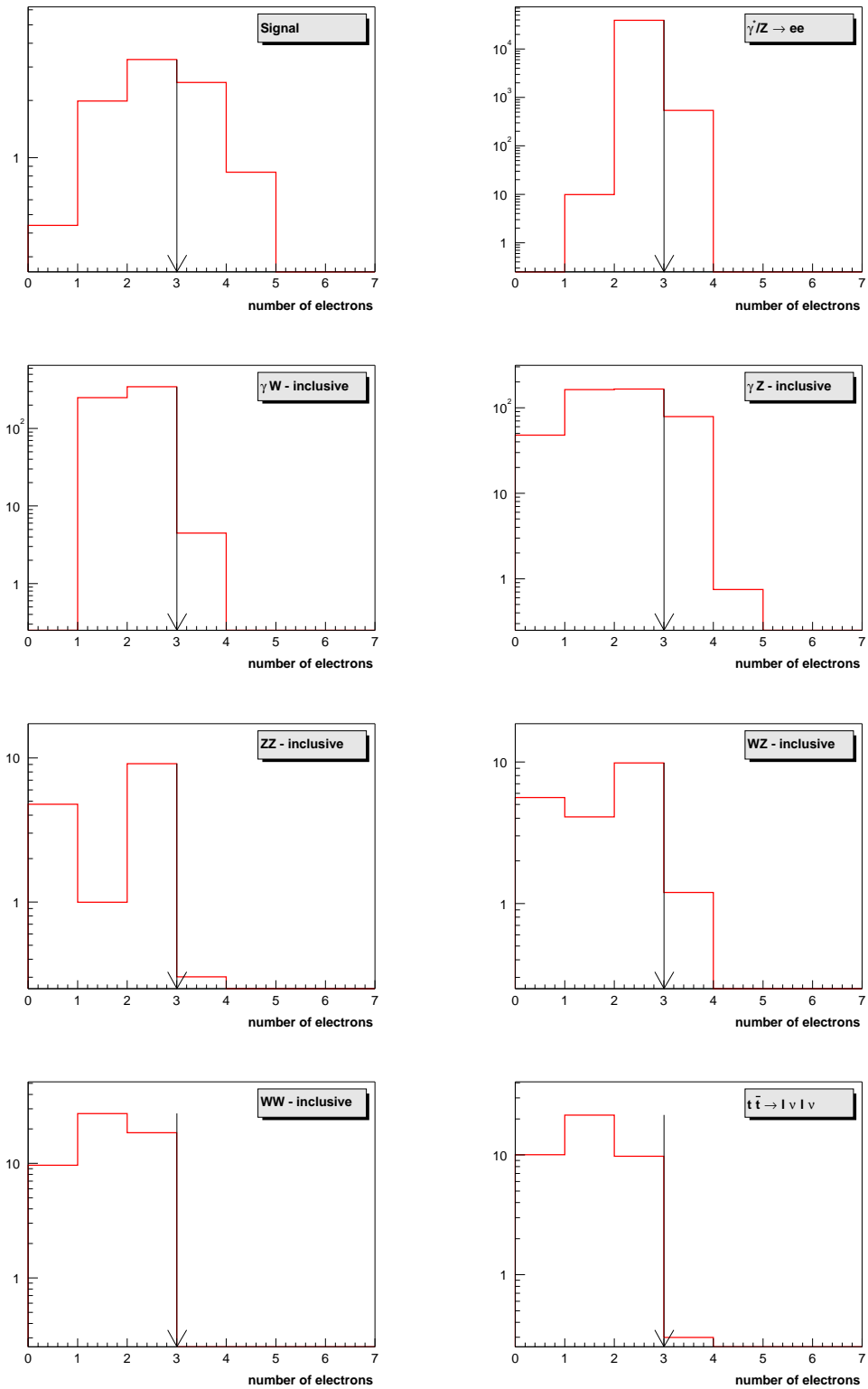


Figure 8.6: Distributions of the number of electrons ($p_T > 15$ GeV) and the chosen cut (shown as vertical arrow). For the signal, a typical point in the mSUGRA parameter space, $m_0 = 200$ GeV/ c^2 and $m_{1/2} = 260$ GeV/ c^2 has been chosen.

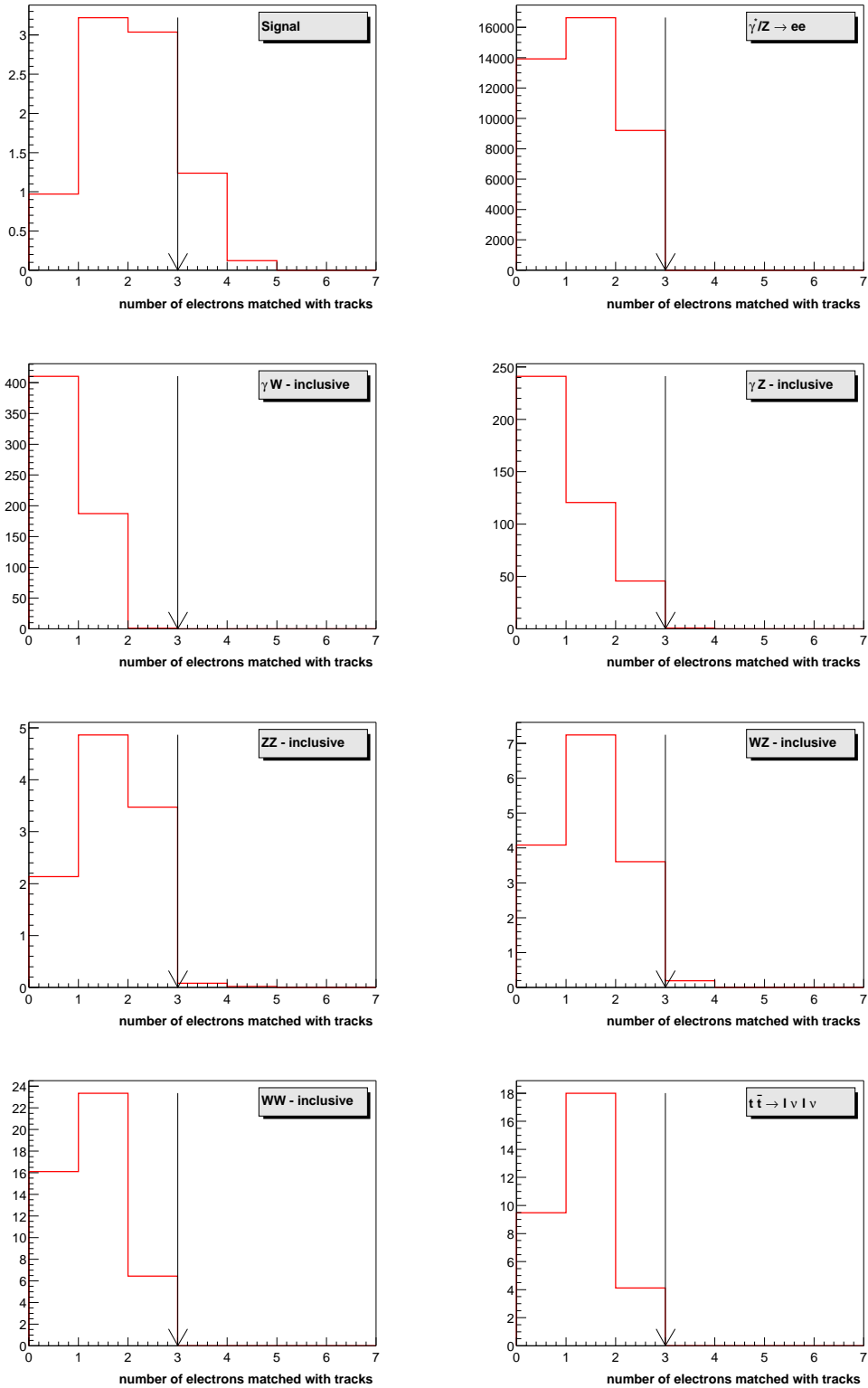


Figure 8.7: Distributions of the number of electrons ($p_T > 15$ GeV) matched with a central track and the chosen cut (shown as vertical arrow). For the signal, a typical point in the mSUGRA parameter space, $m_0 = 200$ GeV/ c^2 and $m_{1/2} = 260$ GeV/ c^2 has been chosen.

Figure 8.6 shows the distribution in the number of electrons with $p_T > 15$ GeV/c and with quality cuts (described in Section 8.2.4) imposed on them for different processes. This cut kills the ZZ and almost all the $t\bar{t}$ background.

Figure 8.7 shows the distribution in the number of electrons with $p_T > 15$ GeV/c and with quality cuts imposed on them for different processes and with the track matching requirement. It can be seen from these two figures that these cuts are effective in suppressing the background from all the sources. Moreover, it was shown in Section 4.5, that the electron fake rate is about two order of magnitude lower for the EM candidates matched with tracks from the central tracking system than for candidates without matching track.

8.3.2 Candidate events

The number of events satisfying the described cuts is given in Table 8.3. Corresponding run and event numbers are given in the Table 8.4. Figure 8.8 presents an event display of one of two tri-electron candidates. The only $ee\mu$ candidate is shown in Figure 8.9.

Event categories	eee	$ee\mu$
$\mathcal{L}_{\text{int}}, \text{ pb}^{-1}$	5.2 ± 0.8	4.6 ± 0.7
Observed events	2	1
Background events	1.9 ± 0.4	0.9 ± 0.2

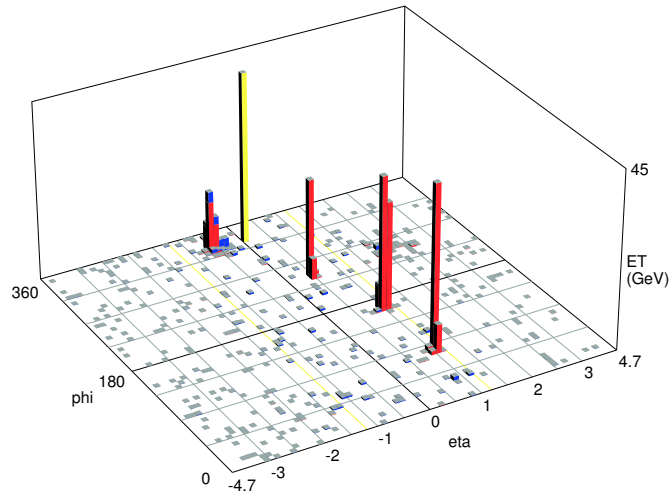
Table 8.3: The results of the search for a tri-lepton signature at DØ.

eee		$ee\mu$	
run number	evt number	run number	evt number
152243	35119440	148847	4747032
153408	1256282		

Table 8.4: Run and event numbers of the selected tri-lepton candidates.

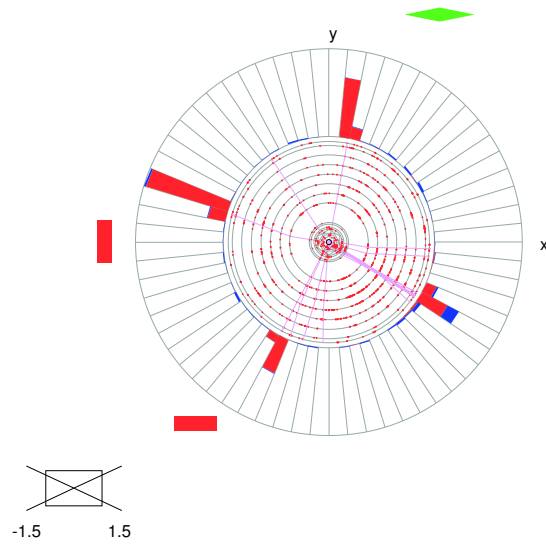
8.4 Estimation of the background

As shown in the previous section, 2 eee and 1 $ee\mu$ events survive all described requirements. Thus 3 events constitute the final data set. In order to investigate further the origin of these events first an estimation of the contribution from various physics processes as well as due to misidentification of certain objects is needed. In principle any known process that gives rise to an event with two or more electrons and one or more muon satisfying the selected cuts, could constitute a background. These can be classified as background from Standard Model processes (SM backgrounds) and instrumental background due to imperfections in the detector and misidentification of some jets as electrons and misidentified muons. The various physics backgrounds are estimated using



(a)

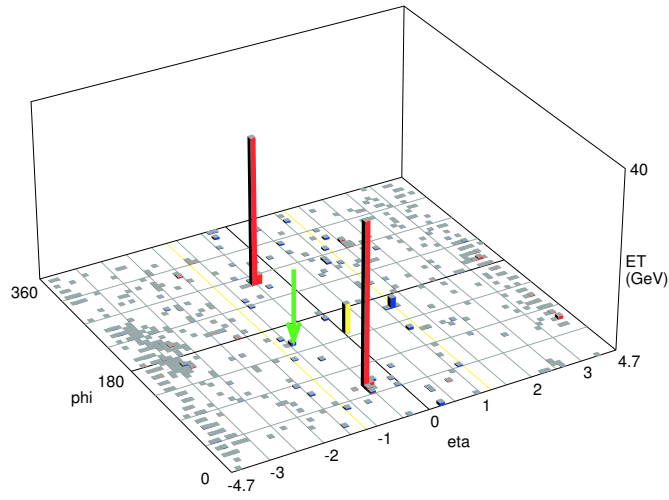
ET scale: 64 GeV



(b)

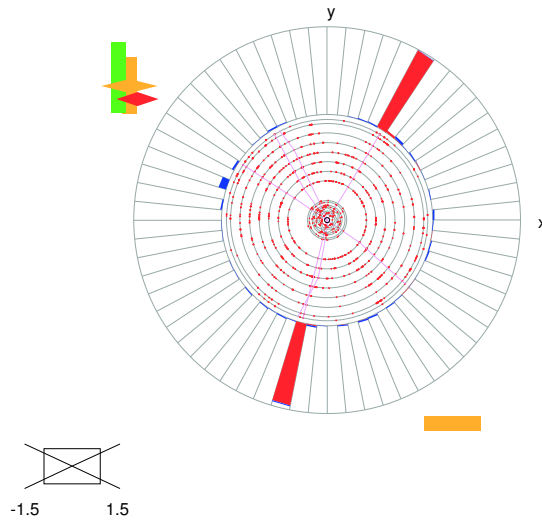
e_1	e_2	e_3
$p_T(\text{cal}) = 76.0 \text{ GeV}/c$	$p_T(\text{cal}) = 56.0 \text{ GeV}/c$	$p_T(\text{cal}) = 33.4 \text{ GeV}/c$
$\eta = 1.12$	$\eta = 1.15$	$\eta = 0.65$
$\varphi = 2.8$	$\varphi = 1.4$	$\varphi = 4.2$
no track match	charge = -1	charge = -1
$m_{e_1 e_2} = 86.6 \text{ GeV}/c^2$	$m_{e_1 e_3} = 68.9 \text{ GeV}/c^2$	$m_{e_2 e_3} = 88.3 \text{ GeV}/c^2$
$m_{e_1 e_2 e_3} = 142 \text{ GeV}/c^2$		$ME_T = 10.2 \text{ GeV}$

Figure 8.8: $\eta - \varphi$ lego plot (a), $x - y$ view (b) and properties of an example tri-electron candidate.



(a)

ET scale: 38 GeV



(b)

e_1	e_2	μ
$p_T(\text{cal}) = 46.5 \text{ GeV}/c$	$p_T(\text{cal}) = 43.5 \text{ GeV}/c$	$p_T = 12.9 \text{ GeV}/c$
$\eta = -0.36$	$\eta = -0.33$	$\eta = -0.92$
$\varphi = 1.02$	$\varphi = 4.47$	$\varphi = 2.59$
no track match	no track match	charge = -1
$m_{e_1 e_2} = 88.9 \text{ GeV}/c^2$		$ME_T = 11.9 \text{ GeV}$

Figure 8.9: $\eta - \varphi$ lego plot (a), $x - y$ view (b) and properties of an example $e + e + \mu$ candidate.

Monte Carlo simulation, whereas the instrumental background is estimated directly from data.

The main source of three lepton events will be processes with two real leptons, where a jet passes all lepton requirements and is misidentified as a lepton. This is the more probable as the lepton cuts used in this analysis are very loose. In this chapter the SM backgrounds to the signal will be investigated. First the number of three lepton events expected from MC will be investigated. Then the main background, the fake leptons will be considered.

8.4.1 Standard Model Background

The production of three real high p_T leptons in one event is a very rare occurrence in the SM. Processes that can produce three real high p_T leptons have either a small cross-section (ZZ , WZ , γZ) or a small branching fraction into leptons (top-pair production). In the rare cases in which an event contains four real leptons they will not necessarily all be seen. They can hit an uninstrumented area of the detector or their energy can be too low for them to be detected.

To determine how many events with three real leptons are expected in the data a large number of background MC was studied. All simulated processes can produce events with three real leptons. All except Drell-Yan, $W\gamma$ and WW can produce events with three real leptons.

- $t\bar{t}$ ($m_t = 175 \text{ GeV}/c^2$)
- di-bosons (ZZ , WZ)

In order to determine the contribution of real leptons from SM processes to the signal channel the full statistics of the MC data produced by the DØ physics working groups was used.

Drell-Yan Production

The cross section for Drell-Yan MC production depends strongly on the mass of the γ^*/Z . Four sets of Monte Carlo events, corresponding to the following γ^*/Z mass ranges were produced using the Pythia event simulation package:

- $2 - 60 \text{ GeV}/c^2$
- $60 - 130 \text{ GeV}/c^2$
- $130 - 250 \text{ GeV}/c^2$
- $250 - 500 \text{ GeV}/c^2$

Events were not generated for invariant mass $< 2\text{GeV}/c^2$ because electrons produced in such events would be too soft to pass the offline energy cut. No events were generated for invariant mass $> 500\text{GeV}/c^2$ because the cross section is expected to be small, and their contribution to background negligible. For each of the MC samples, the equivalent

integrated luminosity was more than a factor 3 higher than the luminosity recorded by $D\bar{O}$ and used for the present analysis. Events were then passed through the detector simulation package $D\bar{O}GSTAR$ and $D\bar{O}Reco$ (version p10.11.00).

$t\bar{t}$ Production

To estimate background due to top quark production, events were generated using the Pythia event generation package. Direct top production with a top mass set to $m_t = 175 \text{ GeV}/c^2$ was considered. All events containing at least 2 leptons and two neutrinos were processed by the detector simulation. In total a number of events corresponding to 8.1 fb^{-1} were investigated.

Di-boson Production

Events containing ZZ , WZ , WW , $Z\gamma$, $W\gamma$ were generated in 5 separate samples.

For each sample the transverse momentum of the interaction was required to be $q > 5.0 \text{ GeV}/c$.

There were no additional cuts at generator level. The equivalent integrated luminosity for each of the MC samples was more than 20 times the analyzed luminosity. Due to the small cross section for diboson production only few events pass the requirements. Only the ZZ , WZ and $Z\gamma$ channels produce events containing three or more leptons.

A summary of the Monte Carlo events considered in this analysis and their contribution to the background are given in Table 8.5 and Table 8.6.

Total SM background

For tri-lepton channel, the dominant contributions are from Drell-Yan, Z , γZ . The contributions from all processes are below one event. Summing up one expects a total of 0.9 ± 0.2 tri-electron events.

For di-electron with one muon events also the dominant contributions are from Drell-Yan and Z . A total of 0.13 ± 0.08 di-electron with one muon events are expected.

8.4.2 Instrumental Background

The instrumental background for electrons arises mainly from misidentification of jets as electrons. This is due to fluctuations in the energy deposition patterns of jets, and is difficult to estimate by simulation. Primary background to muon candidates is the cosmic rays and it is also difficult to simulate. That is why the collider data were therefore used for this purpose.

Background coming from jet that mimics an electron

The details on the EM fake rate estimation methods can be found in Section 4.5 and [170]. In this section the background expected from events with one em-fake is discussed. Two samples of events have been used:

- $e + e + \text{jets}$ for eee selection;

bkg process	number of evts	σ , pb	$\mathcal{L}_{\text{equiv}}$, pb ⁻¹	bkg contrib	
$\gamma^*/Z \rightarrow ee$ (60 – 130 GeV/c ²) *	15 000	184	81.5	0.40	\pm 0.18
γZ	9 750	36.5	267	0.45	\pm 0.15
$\gamma^*/Z \rightarrow ee$ (130 – 250 GeV/c ²) *	13 000	1.36	9 560	0.028	\pm 0.010
WZ	20 250	2.42	8 370	0.014	\pm 0.006
$\gamma^*/Z \rightarrow ee$ (250 – 500 GeV/c ²) *	22 500	0.12	186 000	0.004	\pm 0.001
ZZ	21 250	1.07	19 900	0.004	\pm 0.001
$t\bar{t} \rightarrow l\nu + l\nu$ *	5 000	0.62	8 060	0	
WW *	37 750	8	4 720	0	
γW *	10 000	44.8	223	0	
$\gamma^*/Z \rightarrow ee$ (2 – 60 GeV/c ²) *	11 000	569	19.3	0	
$\gamma^*/Z \rightarrow \tau\tau$ (all mass bins) *	50 000			0	
Total non-em-fake background:				0.9	\pm 0.2
$e + e + \text{em-fakes}$:				1.0	\pm 0.3
Data:				2	

Table 8.5: Contributions to the tri-electron channel background (* in this background a γ has been radiated).

bkg process	number of evts	σ , pb	$\mathcal{L}_{\text{equiv}}$, pb ⁻¹	bkg contrib	
$\gamma^*/Z \rightarrow ee$ (60 – 130 GeV/c ²)	15 000	184	81.5	0.11	\pm 0.08
$t\bar{t} \rightarrow l\nu + l\nu$	5 000	0.62	8 060	0.014	\pm 0.014
WZ	20 250	2.42	8 370	0.004	\pm 0.002
ZZ	21 250	1.07	19 900	0.004	\pm 0.002
$\gamma^*/Z \rightarrow ee$ (130 – 250 GeV/c ²)	13 000	1.36	9 560	0.002	\pm 0.001
γW	10 000	44.8	223	0	
$\gamma^*/Z \rightarrow ee$ (2 – 60 GeV/c ²)	11 000	569	19.3	0	
$\gamma^*/Z \rightarrow ee$ (250 – 500 GeV/c ²)	22 500	0.12	186 000	0	
$\gamma^*/Z \rightarrow \mu\mu$ (all mass bins)	49 500			0	
$\gamma^*/Z \rightarrow \tau\tau$ (all mass bins)	50 000			0	
Total non-em-fake background:				0.13	\pm 0.08
$e + \mu + \text{em-fakes}$:				0.6	\pm 0.2
$e + e + \text{cosmic } \mu$:				0.145	\pm 0.014
Data:				1	

Table 8.6: Contributions to the di-electron one muon channel background.

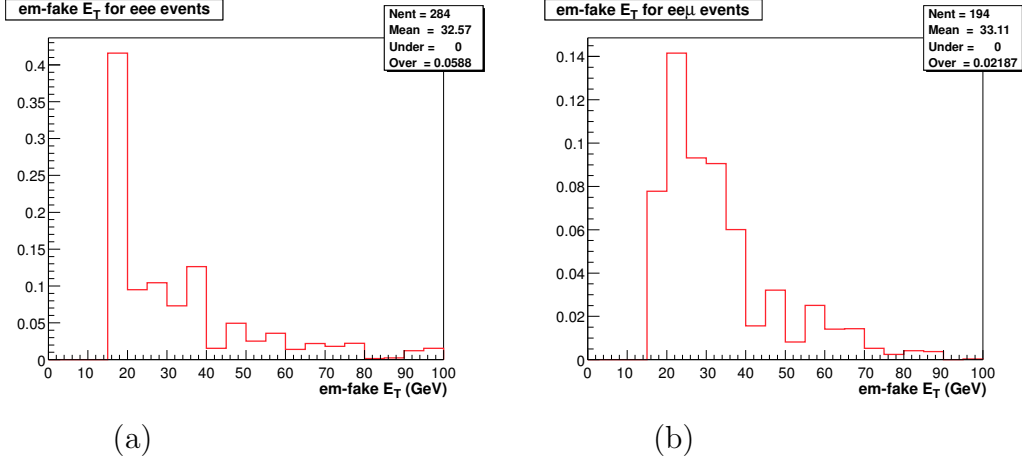


Figure 8.10: Number of expected events $e + e + \text{EM-fake}$ for $\mathcal{L}_{\text{int}} = 5.2 \pm 0.8 \text{ pb}^{-1}$ (a) and $e + \text{EM-fake} + \mu$ $\mathcal{L}_{\text{int}} = 4.6 \pm 0.7 \text{ pb}^{-1}$ (b) versus p_T of the EM-fake

- $e + \mu + \text{jets}$ for $ee\mu$ selection.

In each case, the fake EM rate has been applied to the inclusive E_T spectrum of the jets in the sample (Figure 8.10). The fake rate was set to $(1.6 \pm 0.3) \cdot 10^{-3} + (5.0 \pm 0.5) \cdot 10^{-5} \cdot E_T$ in the Central Calorimeter region and $(1.0 \pm 0.2) \cdot 10^{-2}$ in the End-Cap Calorimeter region.

Background coming from cosmic muons

There are several possible ways to calculate the rate of expected fakes. The estimate can be based on the number of events or alternatively on the structure and the objects contained in these events. In the present analysis the event based rate has been used.

Assuming that the single cosmic muon rate does not depend on the event structure the single electron events has been chosen (*i.e.* $\frac{N_{e+e+\text{cosmic } \mu}}{N_{e+e}} = \frac{N_{e+\text{cosmic } \mu}}{N_e}$). The selected sample consists of events with CEM20, EM_HI or EM_MX trigger and at least one loose EM-candidate with $E_T > 10 \text{ GeV}$. Total number of the selected events is $N_e = 346\,192$.

The events with one μ with $T_A - T_{BC} > 10 \text{ ns}$ has been selected as cosmic (for more details on cosmic μ see Section 5.4). Having obtained the number of events with one cosmic muon $N_{e+\text{cosmic } \mu} = 68 \pm 9$ the fake rate can be calculated by dividing this number by the total number of single electron events:

$$\text{cosmic } \mu \text{ rate} = \frac{N_{e+\text{cosmic } \mu}}{N_e} = (2.0 \pm 0.2) \cdot 10^{-4} \text{ (per event)}. \quad (8.3)$$

To estimate the contribution of di-EM-candidate events with one cosmic muon the $e + e$ sample of events has been used. The cosmic muon rate has been applied to the total number of di-EM-candidate events $N_{ee} = 724$. The expected number of $ee\mu$ coming from this type of background is 0.145 ± 0.014 and is shown in Table 8.6.

Possible interpretation of the candidate events

Figure 8.8 presents an event display of one of two tri-electron candidates. For this event the tri-EM-candidate invariant mass is close to that of Z . This event can be interpreted as $Z \rightarrow ee$ where one the EM-candidates is a radiated γ .

The $ee\mu$ candidate contains a tight local track in the forward muon detector, the di-em-candidate invariant mass is in the Z region. From Figure 8.9 it is clearly seen that there is a possible continuation of the muon track in the central tracking detector and this track looks like a straight line crossing the detector. This could be an indication that in this event a Z was produced and a cosmic muon traversed the detector. However during winter/spring 2002, the timing of the muon detector was not completely calibrated, especially in the beginning of the period when this event was recorded. Therefore the event cannot be safely identified as a Z superposed by a cosmic muon. As was shown in this section, without using timing information we expect 0.145 ± 0.014 events of this type. This highlight the necessity to have a precise timing calibration for the muon system.

8.5 Conclusion

The search for multi-lepton events in the $5.2 \pm 0.8 \text{ pb}^{-1}$ data taken between February and June 2002 was described. In the eee channel 2 events were found for 0.9 ± 0.2 events expected from the Standard Model background and 1.0 ± 0.3 from the instrumental background and in the $ee\mu$ channel 1 event was found for for 0.13 ± 0.08 events expected from the Standard Model background and 0.8 ± 0.2 from the instrumental background.

Due to the very limited statistics, no attempt to deduce an exclusion plot in the mSUGRA parameter space has been done.

Chapter 9

Conclusion and Outlook

This thesis describes the search for R-parity violating SUSY in the multi-lepton channel in the $5.2 \pm 0.8 \text{ pb}^{-1}$ data taken between February and June 2002 by the DØ Collaboration at the Tevatron.

In the eee channel 2 events were found for 0.9 ± 0.2 events expected from the Standard Model background and 1.0 ± 0.3 from the instrumental background and in the $ee\mu$ channel 1 event was found for 0.13 ± 0.08 events expected from the Standard Model background and 0.8 ± 0.2 from the instrumental background. No four-lepton events were found.

Due to the very limited statistics for the data, no attempt to deduce an exclusion plot in the mSUGRA parameter space has been made.

A perspective study has been done using a fast simulation program and exclusion limits have been obtained in the m_0 - $m_{1/2}$ mSUGRA parameters space for several expected integrated luminosities 200 pb^{-1} (twice Run I luminosity) and 2 fb^{-1} (Run IIa luminosity).

By the end of Run II the Tevatron is expected to deliver an integrated luminosity of at least 2 fb^{-1} , which is about a factor of twenty more than what was recorded during Run I. Moreover, it is planned to continue the run further and accumulate as much luminosity as possible (15 fb^{-1} expected in 2007). With the increased luminosity and the upgraded detector, new regions of the parameter space can be explored. It was demonstrated that for $\tan(\beta) = 5$ and $A_0 = 0$ scenarios the limits obtained during Run I will be significantly improved. With the expected luminosity it will be possible to probe scenarios with values of $m_{1/2}$ up to more than 300 GeV.

Of course, the hope is that someday a new particle will be observed. There are still plenty of chances with the Tevatron Run II and the LHC. Until that day, the SUSY parameter space will be further constrained by other SUSY searches. With the Minimal Supergravity models, the results from many searches for sparticles can be easily combined, improving limits obtained by any one analysis. DØ searches for R-parity violating SUSY in the multi-lepton are underway as are searches within di-lepton multi-jets channels. The work is still not finished if a sparticle is discovered, the correct SUSY model must still be determined. Theorists and experimentalists will worry about that exciting problem if that time comes.

Bibliography

- [1] F. Abe *et al.*, Phys. Rev. Lett. 74, 2626 (1995).
- [2] S. Abachi *et al.*, Phys. Rev. Lett. 74, 2632 (1995).
- [3] S.L. Glashow, Nucl. Phys. 22, 579 (1961);
S. Weinberg, Phys. Rev. Lett. 19, 1264 (1967);
A. Salam, in Elementary Particle Theory, edited by N. Svartholm (Almquist and Wiksells, Stockholm, 1968).
- [4] O.W. Greenberg, Phys. Rev. Lett. 13, 598 (1964).
- [5] ALEPH, DEPHI, L3, and OPAL Collaborations, Electroweak parameters of the Z0 resonance and the Standard Model, Phys. Lett. B276, 247 (1992).
- [6] UA1 Collaboration, GTJ Arnison *et al.*, Phys. Lett. B 122 (1983) 103-116;
UA1 Collaboration, GTJ Arnison *et al.*, Phys. Lett. B 126 (1983) 398-410;
UA2 Collaboration, M. Banner *et al.*, Phys. Lett. B 122 (1983) 476-485;
UA2 Collaboration, M. Banner *et al.*, Phys. Lett. B 129 (1983) 130-140.
- [7] G. 't Hooft, Under the Spell of the Gauge Principle, Advanced Series in Mathematical Physics, Vol. 19 (University of Utrecht, The Netherlands, 1994).
- [8] M.E. Peskin, Beyond the Standard Model, SLAC-PUB-7479, 1997.
- [9] V. Barger and R. Phillips, Collider Physics (Addison-Wesley, New York, 1987).
- [10] R. Mohapatra, Unification and Supersymmetry (Springer-Verlag, New York, 1992).
- [11] K. Lane, Two lectures on Technicolor, hep-ph/0202255 (2002);
J. Ellis, G.L. Fogli and E. Lisi, Technicolour and precision electroweak data revisited, Phys. Lett. B343 (1995) 282-290.
- [12] H.E. Haber and G.L. Kane, Phys. Rep. 117, 75 (1985).
- [13] H.P. Nilles, Phys. Rep. 110, 1 (1984).
- [14] J. Wess and B. Zumino, Nucl. Phys. B70, 39 (1974);
J. Wess and B. Zumino, Phys. Lett. B49, 52 (1974).
- [15] A.L. Lyon, "The Basics of Supersymmetry", DØ Internal Note 2523, 1994 (unpublished).

- [16] S. Dimopolous and H. Georgi, Nucl. Phys. B193, 150 (1981);
 N. Sakai, Z. Phys. C11, 153 (1981);
 J. Amundson *et al.*, "Report of the Supersymmetry Theory Subgroup", Snowmass 1996 proceedings;
 G.L. Kane, C. Kolda, L. Roszkowski and J.D. Wells, Phys. Rev. D49, 6173 (1994).
- [17] J.L. Lopez, Rep. Prog. Phys. 59, 819 (1996).
- [18] J. Ellis *et al.*, Nucl. Phys. B238, 453 (1984).
- [19] S. Weinberg, Phys. Rev. D26, 287 (1982);
 N. Sakai, T. Yanagida, Nucl. Phys. B197, 133 (1982).
- [20] J. L. Goity and M. Sher, Phys. Lett. B346, 69 (1995).
- [21] R. Barbier *et al.*, Report of the GDR working group on the R-parity violation, hep-ph/9810232;
 H. Dreiner, Perspectives on Supersymmetry, ed. G. L. Kane, World Scientific, hep-ph/9707435;
 J.W.F. Valle, Physics beyond the standard model, In: 8th Jorge Andre Swieca Summer School: Particles and Fields, Rio de Janeiro, Brazil, 5 – 18 February 1995. World Scientific, Singapore, 1996, pp.3-77, hep-ph/9603307;
 J.W.F. Valle, Supersymmetry without R-parity, International Workshop on Quantum Effects in the MSSM, Barcelona, Spain, 9 – 13 September 1997, World Scientific, Singapore, 1998, pp. 302-317, hep-ph/9802292;
 V. Bednyakov *et al.*, On present status of R-parity violating supersymmetry, hep-ph/9904414.
- [22] S. Dimopoulos and D. Sutter, Nucl. Phys. B452, 496 (1995).
- [23] J. Ellis, D.V. Nanopolous and K. Tamvakis, Phys. Lett. 121B, 123 (1983);
 L. Ibanez, Phys. Lett. 118B, 73 (1982);
 L. Alvarez-Gaume, J. Polchinski, and M.B. Wise, Nucl. Phys. B221, 495 (1983);
 K. Inoue *et al.*, Prog. Theor. Phys. 68, 927 (1982).
- [24] A. Chamseddine, R. Arnowitt and P. Nath, Phys. Rev. Lett. 49, 970 (1982);
 R. Barbieri, S. Ferrara and C. Savoy, Phys. Lett. B119, 343 (1982);
 L.J. Hall, J. Lykken and S. Weinberg, Phys. Rev. D27, 2359 (1983);
 H. Baer, C. Kao and X. Tata, Phys. Rev. D48, 2978 (1993).
- [25] S. Park, in 10th Topical Workshop on Proton – Anti-proton Collider Physics, edited by R. Raja and J. Yoh (AIP, Woodbury, NY, 1996).
- [26] M. Dine *et al.*, Phys. Rev. D53, 2658 (1996).
- [27] S. Dimopoulos, M. Dine, S. Raby and S. Thomas, Phys. Rev. Lett. 76, 3494 (1996);
 S. Ambrosanio *et al.*, Phys. Rev. Lett. 76, 3498 (1996).
- [28] F. Ledroit-Guillon, DELPHI Internal Note 2002-045-CONF-579.

- [29] ALEPH Collaboration, A. Heister *et al.*, Eur. Phys. J. C. 25 (2002) 1-12, CERN-EP/2001-094 and Contributed paper to ICHEP 2002 abstract 618.
- [30] T. Papadopoulou, results presented at ICHEP 2002 Conference, parallel session Beyond standard Model ,
<http://www.ichep02.nl/index-new.html>
- [31] H. Dreiner and G.G. Ross, Nucl. Phys. B410 (1993) 188.
- [32] C. Carlson, P. Roy and M. Sher, Phys. Lett. B357 (1995) 99.
- [33] A.Y. Smirnov and F. Vissani, Phys. Lett. B380 (1996) 317.
- [34] F. Zwirner, Phys. Lett. B132 (1983) 103.
- [35] J.L. Goity and M. Sher, Phys. Lett. B346 (1995) 69.
- [36] S. Dimopoulos and L.J. Hall, Phys. Lett. B207 (1987) 210.
- [37] R.M. Godbole, P. Roy and X. Tata, Nucl. Phys. B401 (1993) 67.
- [38] R.N. Mohapatra, Phys. Rev. D34 (1986) 3457.
- [39] M. Hirsch, H.V. Klapdor-Kleingrothaus, S.G. Kovalenko, Phys. Rev. Lett. 75 (1995) 17.
- [40] K.S. Babu and R.N. Mohapatra, Phys. Rev. Lett. 75 (1995) 2276.
- [41] V. Barger, G.F. Giudice and T. Han, Phys. Rev. D40 (1989) 2987.
- [42] Particle Data Group, Phys. Rev. D50 (1994) 1173.
- [43] K. Agashe and M. Graesser, Phys. Rev. D 54 (1996) 4445, hep-ph/9510439.
- [44] G. Bhattacharyya and D. Choudhury, Mod. Phys. Lett. A10 (1995) 1699.
- [45] G. Bhattacharyya, J. Ellis and K. Sridhar, Mod. Phys. Lett. A10 (1995) 1583.
- [46] G. Bhattacharyya, D. Choudhury and K. Sridhar, Phys. Lett. B355 (1995) 193.
- [47] H1 Collaboration, S. Aid *et al.*, Z. Phys. C71 (1996) 211.
- [48] KARMEN Collaboration, B. Armbruster *et al.*, Phys. Lett. B 348 (1995) 19.
- [49] D. Choudhury and S. Sarkar, Phys. Lett. B374 (1996) 87.
- [50] R. Maschuw, talk given at WIN'99, Cape Town 1999.
- [51] D. Choudhury *et al.*, hep-ph/9911365.
- [52] The LEP Electroweak Working Group report, preprint CERN-PPE/94-187 (1994).
- [53] B. Brahmachari and P. Roy, Phys. Rev. D50 (1994) 39.

- [54] The OPAL Collaboration, P.D. Acton *et al.*, Phys. Lett. B313 (1993) 333.
- [55] The ALEPH Collaboration, D. Buskulic *et al.*, Phys. Lett. B349 (1995) 238.
- [56] G. Bhattacharyya and A. Raychaudhuri, Phys. Lett. B374 (1996) 93.
- [57] D. Choudhury, Phys. Lett. B376 (1996) 201.
- [58] D.P. Roy, Phys. Lett. B283 (1992) 270.
- [59] DØ Collaboration, B. Abbott *et al.*, Phys. Rev. Lett. 83 (1999) 4476.
- [60] DØ Collaboration, V.M. Abazov *et al.*, Phys. Rev. Lett. 89 (2002) 171801.
- [61] DØ Collaboration, V.M. Abazov *et al.*, hep-ex/0207100, submitted to Phys. Rev. Lett.
- [62] CDF Collaboration, F. Abe *et al.*, Phys. Rev. Lett. 83 (1999) 2133.
- [63] B. Allanach *et al.*, Searching for R-parity Violation at Run II of the Tevatron, hep-ph/9906224.
- [64] ATLAS Detector and Physics Performance Technical Design Report, LHC 99-14/15.
- [65] Hirsch *et al.*, Phys. Rev. D53 (1996) 1329.
- [66] F. Ledroit and G. Sajot, Indirect limits on SUSY R-parity violating couplings λ and λ' , GDR-S-008, 1998.
- [67] Allanach *et al.*, hep-ph/9906209, Phys. Rev. D60 (1999) 075014.
- [68] V. Bednyakov, A. Faessler *et al.* S. Kovalenko, On present status of R-Parity violating supersymmetry, hep-ph/9904414, 1999.
- [69] J. M. Yang, R_b and R_l in MSSM without R-Parity, hep-ph/9905486, TU-566, (1999)
- [70] GDR SUSY, Report of the group on the MSSM, <http://www.lpm.univ-montp2.fr:7082/~djouadi/GDR/resume.ps>
- [71] D. Fouchez, ALEPH, DELPHI, L3 and OPAL Collaborations, results presented at the Moriond Conference, 2002, http://moriond.in2p3.fr/EW/2002/transparencies/4_Wednesday/evening/D_Fouchez/D_Fouchez.pdf
- [72] J. Conway, Simple simulation package for generic collider detectors, <http://www.physics.rutgers.edu/~jconway/soft/pgs/pgs.html>
- [73] T. Kamon, J.L. Lopez, P. McIntyre and J.T. White, Phys. Rev. D50 (1994) 5676.
- [74] J. Conway, K. Maeshima, Upper Limits on Poisson Processes Incorporating Uncertainties in Acceptance and Background, CDF Internal Note 4476, 1998.

- [75] A. Besson, Ph.D. Thesis, University Grenoble I, Etude des événements di-leptons + 4 jets dans Run II de l'expérience DØ à Fermilab., 2002.
- [76] DØ Collaboration, B. Abbott *et al.*, Phys. Rev. D62 (2000) 071701.
- [77] http://www-d0.fnal.gov/~sceno/pmcs_doc/pmcs.html
- [78] The Large Hadron Collider, <http://lhc.web.cern.ch/lhc/>.
- [79] M. Witherell, DØ Collaboration meeting, 22-26 April 2002, http://d0server1.fnal.gov/projects/meetings/collab_april_2002/witherell_talk.pdf
- [80] DØ Collaboration, DØ Silicon Tracker Technical Design Report, DØ Internal Note 2169, 1994, http://d0server1.fnal.gov/projects/silicon/www/tdr_final.ps
- [81] DØ Collaboration, DØ Central Fiber Tracker, http://d0server1.fnal.gov/projects/SciFi/cft_home.html
- [82] M.D. Petroff and M.G. Staplebroek, IEEE Trans. Nucl. Sci., **36**, No. 1 (1989) 158; M.D. Petroff and M. Attac, IEEE Trans. Nucl. Sci., **36**, No. 1 (1989) 163.
- [83] J. Ellison, For the DØ Collaboration, The DØ Detector Upgrade and Physics Program, hep-ex/0101048, 2001.
- [84] M. Adams *et al.*, A Detailed Study of Plastic Scintillating Strips with Axial Wavelength Shifting Fiber and VLPC Readout, Nucl. Instrum. Meth. A366 (1995) 263.
- [85] DØ Collaboration, P. Baringer *et al.*, Cosmic Ray Tests of the DØ Preshower Detector, Nucl. Instrum. Meth. A469 (2001) 295.
- [86] DØ Collaboration, A. Gordeev *et al.*, Technical Design Report of the Forward Preshower Detector for the DØ Upgrade, DØ Internal Note 3445, 1998.
- [87] DØ Collaboration, The DØ Upgrade: Forward Preshower, Muon System, Level 2 Trigger, FNAL PAC Report, DØ Internal Note 2834, 1996.
- [88] DØ Collaboration, S. Abachi *et al.*, Nucl. Instr. Methods Phys. Res. A338 (1994) 185 and references therein.
- [89] DØ Collaboration, Calorimeter Electronics Upgrade for Run 2, <http://www-d0.fnal.gov/~d0upgrad/calelec/intro/tdr/tdr17.pdf>
- [90] DØ EM Identification Group, Certification Results Version 2.0, http://www-d0.fnal.gov/phys_id/emid/d0_private/certification/main_v2_0.html;
- [91] R. Chiche, C. de la Taille, Y. Jacquier, G. Martin, P. Petroff, M. Ridet, Optimisation of the DØ Online Calorimeter Calibration for RunII, DØ Internal Note 3914, 2001.

- [92] U. Bassler, Wave form measurements,
[http://www-d0.fnal.gov/~d0upgrad/d0private/software/calorimeter/
/talks011030/waveforms.ppt](http://www-d0.fnal.gov/~d0upgrad/d0private/software/calorimeter/talks011030/waveforms.ppt), October 2001.
- [93] B. Olivier, Ph.D. Thesis, Universities Paris VI and VII, Search for the Top Quark Supersymmetric Partner and Improvement of the DØ Experiment Calorimetry for the Tevatron Run II, (Chapter 5: La calibration en ligne du calorimetre), 2000.
- [94] R. Zitoun, Study of the Non Linearity of the DØ Calorimeter Readout Chain, DØ Internal Note 3997, 2002.
- [95] DØ Collaboration, Technical Design of the Central Muon System, DØ Internal Note 3365, 1997.
- [96] DØ Collaboration, Technical Design Report for the DØ Forward Muon Tracking Detector Based on Mini-drift Tubes, DØ Internal Note 3366, 1997.
- [97] DØ Collaboration, Technical Design Report for the DØ Forward Trigger Scintillator Counters, DØ Internal Note 3237, 1997.
- [98] A. Brandt *et al.*, A Forward Proton Detector at DØ, FERMILAB-Pub-97/377.
- [99] C.-C. Miao, R. Partridge, Study of the Run II Luminosity Monitor Counter Design, DØ Internal Note 3319, 1998.
- [100] A. Lo, C.-C. Miao, R. Partridge, Luminosity Monitor Technical Design Report, DØ Internal Note 3320, 1997.
- [101] C.-C. Miao, The DØ Run II Luminosity Monitor, Nucl. Phys. Proc. Suppl., 78 (1999) 342-347.
- [102] J. Bantly *et al.*, The Level 0 trigger for the DØ Detector, DØ Internal Note 1996, 1994.
- [103] M. A. Tartaglia, D. P. Owen, A Comparison of FastZ and SlowZ Luminosity Monitors, DØ Internal Note 2879, 1996.
- [104] D. Edmunds *et al.*, Level 1 Trigger OR's with Pseudo-AND/OR Terms, DØ Internal Note 3683, 1999.
- [105] M. Martens, P. Bagley, Luminosity Distribution During Collider Run II, DØ Internal Note 3515, 1998.
- [106] S. H. Ahn *et al.*, DØ Luminosity in Run 2: Delivered, DØ Internal Note 3970, 2002.
- [107] S. H. Ahn *et al.*, DØ Luminosity in Run 2: Triggered, DØ Internal Note 3971, 2002.
- [108] S. H. Ahn *et al.*, DØ Luminosity in Run 2: Recorded, DØ Internal Note 3972, 2002.
- [109] J. Bantly *et al.*, DØ Luminosity Monitor Constant for the 1994—1996 Tevatron Run, DØ Internal Note 3199, 1997.

- [110] D. Edmunds *et al.*, Online measurement of Beam Luminosity and Exposed Luminosity for Run II, 1997.
- [111] M. Abolins *et al.*, DØ Run II Level 1 Trigger Framework Technical Design Report, http://www.pa.msu.edu/hep/d0/ftp/l1/framework/l1fw_tdr_05june98.txt
- [112] H. Schellman *et al.*, Summary of the Luminosity Workshop — September 17-18, 1998, DØ Internal Note 3523.
- [113] G.C. Blazey, The DØ Run II Trigger, <http://niuhep.physics.niu.edu/~blazey/rt.ps>.
- [114] F. Borcharding *et al.*, CTT Technical Design Report, DØ Internal Note 3551.
- [115] http://www.pa.msu.edu:80/hep/d0/ftp/run1/l1/caltrig/d0_note_706.txt
http://www.pa.msu.edu:80/hep/d0/ftp/run1/l1/caltrig/d0_note_1680.txt
- [116] M. Klute and A. Quadt, Measurement of Level 1 Trigger Efficiencies from DØ Data, DØ Internal Note 3949 (2002).
- [117] R.D. Martin, Design of the DØ Run II Level 2 Trigger, <http://hepalphal1.phy.uic.edu/l2cal/overview/chep133.ps>
- [118] D. Baden *et al.*, Specification of the Level2 Central Tracking Trigger Preprocessing Crate, http://www.nhn.ou.edu/~abbott/L2Trigger/l2ctt_documentation_02.ps
- [119] M. Adams *et al.*, Level-2 Calorimeter Preprocessor Technical Design Report, http://hepalphal1.phy.uic.edu/l2cal/l2cal_tdr_v1_5.ps
- [120] L. Phaf, Electron + jet triggers for top physics, DØ Internal Note 4017.
- [121] B. Abbott *et al.*, Fixed Cone Jet Definitions in DØ and R_{sep} , FERMILAB-Pub-97/242-E.
- [122] S. Protopopescu, S. Baffioni, E. Nagy, Thumbnail a compact data format, DØ Internal Note 3979 (2002).
- [123] A. Milder, R.V. Astur, DØ Internal Note 1595, 1989.
- [124] I. Bertram *et al.*, Proposal for DZero Regional Analysis Centers, DØ Internal Note 3984 (2002).
- [125] T. Ferbel, Experimental Techniques in High-Energy Nuclear and Particle Physics, Second Edition, World Scientific Publishing Company, 1991.
- [126] L. Dufлот, Simple cone preclustering for cone jets, DØ Internal Note 3749, 2000.
- [127] S. Protopopescu, EMReco Algorithm, 1999, <http://www-d0.fnal.gov/d0dist/dist/releases/current/emreco/doc/EMReco.ps>

- [128] A. Abdesselam, Ph.D. Thesis, University Paris VI, Recherche de production resonante de sleptons au Run I de DØ. Identification et mesure des electrons au Run II, 2001.
- [129] R. Engelmann *et al.*, Nucl. Instr. Meth. 216, 45 (1983);
R. Raja, H–Matrix analysis of top \rightarrow lepton + jets – MC Physics Workshop II, DØ Internal Note 1192, 1991.
- [130] M. Jaffre, H-Matrix Reconstruction Status, EM Identification Vertical Review, 2000,
http://www-d0.fnal.gov/~d0upgrad/d0_private/software/emid/vreview/michel_hmreco_000330.pdf
- [131] F. Touze, A. Abdesselam, P. Petroff, M. Jaffre, H-Matrix Status, results presented at DØ Collaboration Workshop, 1 July 1999,
http://www-d0.fnal.gov/phys_id/emid/d0_private/minutes/070199michel.ps
- [132] M. Kado and R. Zitoun, Measurement of the Z and W boson production cross sections in the electron mode in $p\bar{p}$ collisions at $\sqrt{s} = 1.96$ TeV, DØ Internal Note 4003, 2002.
- [133] S. Crépe-Renaudin *et al.*, Electron Identification Likelihood, EM Identification Vertical Review, 2000,
http://www-d0.fnal.gov/~d0upgrad/d0_private/software/emid/vreview/sabine_000330.pdf
- [134] N. Denisenko, Electron identification in the DØ detector, DØ Internal Note 1885, 1993.
- [135] Y. Fisyak, J. Womersley, DØ GEANT Simulation of the Total Apparatus Response, DØ Internal Note 3191, 1997.
- [136] GEANT – Detector Description and Simulation Tool, CERN, Geneva, 1993.
- [137] T. Vu Anh, EM Identification Group meeting, 17 July 2002,
http://www-d0.fnal.gov/phys_id/emid/d0_private/minutes/min20020717.html
- [138] S. Crépe-Renaudin, Energy corrections for geometry effects for electrons in Run II, DØ Internal Note 4023 (2002).
- [139] J. Womersley, EM Calorimeter Calibration for the DØ Upgrade, DØ Internal Note 2377.
- [140] E. Nagy and S. Negroni, Simultaneous Calibration of Various Parts of the DØ Electromagnetic Calorimeter, DØ Internal Note 3758 (2000).

- [141] S. Negroni, Ph.D. Thesis, Université de la Méditerranée Aix-Marseille II, Etude de la détection de la supersymétrie par production de quark top en singlet. Détermination de l'échelle d'énergie des calorimètres électromagnétiques auprès des collisionneurs hadroniques, 2000.
- [142] A. Cothenet, EM Energy Scale Corrections, DØ EM Identification Group meeting, 10 July 2002, http://www-d0.fnal.gov/phys_id/emid/d0_private/minutes/20020710alexis.ps
- [143] F. Deliot, Ph.D. Thesis, University Paris VII, Reconstruction et identification des muons dans l'expérience DØ. Etude de la production résonnante de sleptons, 2002.
- [144] Yamada, Ostiguy and Mesin, 2-D and 3-D Display and Plotting of 3-D Magnetic Field Calculation for Upgraded DØ Detector, DØ Internal Note 2023.
- [145] DØ Collaboration, B. Abbott *et al.*, Phys. Rev. Lett. 85 (2000) 5068.
- [146] B. Wijngaarden, *b*-ID Impact Parameter Certification Results, 2002, http://www-d0.fnal.gov/phys_id/bid/d0_private/certification/impltag_v1p0/impltag_v1p0.html
- [147] B. Wijngaarden, Impact Parameter Tagging Status, results presented at DØ Collaboration Workshop, 10 July 2002, http://www-d0.fnal.gov/phys_id/bid/d0_private/meetings02/wijngaarden-0710.ps
- [148] D. Brown, M. Frank, Tagging *B* Hadrons Using Track Impact Parameters, ALEPH Internal Note 92-135 (1992).
- [149] S. Towers, Performance comparison of Impact-Parameter and Secondary Vertex *b*-Quark Jet Tags in Data, DØ Internal Note 4031 (2002).
- [150] A. Schwartzman and M. Narain, Secondary Vertex *b*-tagging using the Kalman Filter Algorithm, DØ Internal Note 3909 (2001).
- [151] CDF Collaboration, F. Abe *et al.*, Phys. Rev. Lett. 71 (1993) 500504.
- [152] F. Beaudette and J.-F. Grivaz, The road method, DØ Internal Note 3976 (2002); F. Beaudette and J.-F. Grivaz, Electron identification and *b*-tagging with the road method, DØ Internal Note 4032 (2002).
- [153] O. Peters, Certification of *b*-jet tagging with a muon, 2002, http://www-d0.fnal.gov/phys_id/bid/d0_private/certification/\muon_btag_cert_v1p0.pdf
- [154] G.V. Borisov, Combined *b*-tagging, DELPHI Internal Note 97-94 PHYS 716 (1997).
- [155] M. Boonekamp, *b*-tagging with high p_T leptons, DELPHI Internal Note 98-54 PHYS 779 (1998).

- [156] SLD Collaboration, K. Abe *et al.*, Measurement of R_b Using a Vertex Mass Tag, Phys. Rev. Lett. 80 (1998) 660.
- [157] S. Katsanevas and P. Morawitz, A Monte Carlo Event Generator for MSSM Sparticle Production at e^+e^- Colliders, IC/HEP/97-5, IFAE-UAB/97-01, LYCEN 9744;
- [158] N. Ghodbane, S. Katsanevas, P. Morawitz, E. Perez, Susygen 3, hep-ph/9909499, <http://lyoinfo.in2p3.fr/susygen/susygen3.html>
- [159] A. Djouadi *et al.*, Suspect, <http://www.lpm.univ-montp2.fr:7082/~kneur/suspect.html>
- [160] H. U. Bengtsson, T. Sjöstrand, Pythia v5.6, CERN Program Library Long Writeup, CERN (1991).
- [161] B. Anderson, G. Gustafson, G. Ingelman and T. Sjöstrand, Phys. Rep. 97 (1983) 33.
- [162] <http://www-d0.fnal.gov/computing/MonteCarlo/simulation/d0sim.html>
- [163] G. Bernardi, Jets and Missing ET Run Selection, http://www-d0.fnal.gov/~d0upgrad/d0_private/software/jetid/certification/Macros/runsel.html
- [164] H.T. Diehl, V.M. Abazov, R. McCroskey, Good and Bad Muon Global Runs Early in Run II, DØ Internal Note 3938 (2002).
- [165] M. Paterno, Calculating Efficiencies and Their Uncertainties, DØ Internal Note 2861 (1996).
- [166] EM Identification Group, Certification Results Version 1.9, http://www-d0.fnal.gov/phys_id/emid/d0_private/certification/main_v1_9.html;
- [167] EM Identification Group, Certification Results Version 2.0, http://www-d0.fnal.gov/phys_id/emid/d0_private/certification/main_v2_0.html;
- [168] Jets and Missing Energy Group, Certification Results, http://www-d0.fnal.gov/d0upgrad/d0_private/software/jetid/certification/certif.html;
- [169] Muon Identification Group, Certification for Moriond 2002, http://www-d0.fnal.gov/phys_id/muon_id/d0_private/muonid_302.ps;
- [170] S. Fu, O. Kouznetsov, G. Landsberg, A. Melnitchouk, G. Sajot, V. Zutshi, Studies of the EM Object Fake Rate for v2.0 EM Certified Objects, DØ Internal Note 4010 (2002).